Radionuclide Dosimetry at Microscopic and Macroscopic Level in a Thyroid Model

Chuamsaamarkkee, Krisanat

Awarding institution:
King's College London

Radionuclide Dosimetry at Microscopic and Macroscopic Level in a Thyroid Model

A thesis submitted to King's College London

for the degree of

Doctor of Philosophy in Imaging Sciences and Radiation Biology

Krisanat Chuamsaamarkkee

Division of Imaging Sciences and Biomedical Engineering

King's College London

2016

Abstract

This study proposes to evaluate dosimetrically the feasibility of using rhenium isotopes (^{186}Re and ^{188}Re) in the form of perrhenate (which is also a substrate of the sodium iodide symporter, NIS) for the treatment of benign nodular thyroid disease and non-thyroidal NIS expressing tumours. While radioiodine (^{131}I-NaI) has practical limitations, there is a window in which rhenium isotopes might offer greater therapeutic advantages. For instance, ^{186}Re and ^{188}Re-perrhenate have shorter half-life, higher energy beta particles, longer range and less abundant gamma photons thus reducing effective dose to the whole body and members of the public and family. Generally, dosimetry in nuclear medicine is considered only at macroscopic level with radionuclide uptake assumed to have a uniform distribution throughout the organ. However, this assumption is not always correct as radionuclides may or may not get incorporated into intracellular structures which, depending on the particular energy transfer mechanisms, may be influential. . Therefore, an aim of this thesis was to study the effect of tracer localisation on microscopic and macroscopic dosimetry by using the thyroid as a model.

First, a basic performance evaluation of preclinical imaging systems was carried out. The image-based quantification accuracy of SPECT radionuclides (^{99m}Tc, ^{123}I and ^{188}Re) and PET (^{18}F) with regard to effect of object size, acquisition time and reconstruction parameters (number of iterations) were examined with a mouse-size micro-hollow sphere phantom. Quantification accuracy in small objects was attempted to be improved using phantom-derived correction factors (Chapter 2). Then, a series of *in vivo* experiments was carried out aimed at spatio-temporal quantification with the available SPECT NIS-radiotracers (^{99m}Tc-pertechnetate, ^{123}I-NaI, ^{131}I-NaI and ^{188}Re-perrhenate) and a forthcoming clinical PET radiotracer (^{18}F-tetrafluoroborate). These data demonstrated distinct differences of uptake patterns between metabolised (^{123}I- and ^{131}I-NaI) and non-metabolised tracers (^{18}F-tetrafluoroborate, ^{99m}Tc-pertechnetate and ^{188}Re-perrhenate), and also subtle differences between the non-metabolised tracers. Human-equivalent effective dose calculations for diagnostic use of these radiotracers were reported in this study. Dose estimations were conducted on the same strain sex- and age-matched animals to allow approximate comparison. Dosimetric estimations relevant to treatment of benign nodular thyroid disease indicated that rhenium isotopes were equally effective when excluding the highly variable uptake in the stomach and urinary bladder. The effective dose per unit of administered activity from ^{186}Re and ^{188}Re was lower than conventional radioiodine. Also red marrow absorbed dose

was about 1.5 and 3 times (for ^{186}Re and ^{188}Re respectively) lower than that produced by radioiodine. In xenograft bearing non-thyroidal NIS adenocarcinoma tumour (human NIS-engineered model), our data indicated that both rhenium isotopes delivered higher absorbed dose to the tumour (6.33 and 8.68 times higher for ^{186}Re and ^{188}Re) compared to ^{131}I-NaI. Additionally, the therapy indexes (tumour to effective dose and tumour to thyroid ratio) for both rhenium isotopes were greater than ^{131}I-NaI. An investigation of the radionuclide distribution at the microscopic level in thyroid tissue with electron microscopy and micro-autoradiography techniques illustrated that non-metabolised tracers were only located in thyrocytes whereas iodide was detected in the colloid. This information (thyroid geometrical model and tracer distribution) were used as an input for small-scale pilot dosimetry using the MCNPx (Monte Carlo N-particle extended) platform. The simulation results indicated that the mode of absorbed dose when ^{188}Re distributed in thyrocytes was higher and more uniform when compared with ^{131}I being located in the colloid.

In conclusion, dose delivered to the thyroid is dependent on cellular distribution of radiotracers. The work presented in this thesis has been an important step for initial dosimetric estimates of the therapeutic potential of these radiotracers to inform future translation with pilot studies in humans.

Statement of Authorship

I, the undersigned, hereby confirm that:

- This submission is my own work and that to the best of my knowledge.
- This work was done wholly or mainly while in candidature for a research degree at this university.
- I have fully acknowledged and referenced the ideas and work of others, whether published or unpublished, in my thesis.
- I have prepared my thesis specifically for the degree of Doctor of Philosophy, while under supervision at this university.
- My thesis does not contain work extracted from a thesis, dissertation or research paper previously presented for another degree or diploma at this or any other university.

(Mr. Krisanat Chuamsaamarkkee)

Date

Table of Contents

Table of Figures

Table of Tables

“Dedicated to my beloved mum for her love and support from the Heaven”

Acknowledgements

Frist and foremost, I would like to thank my supervisor Dr Lefteris Livieratos for his support and encouragement during this project and also when I was in the hospital. I have been extremely lucky to have a supervisor who cared so much about my work, my life, my health and who responded to my questions and queries so promptly. I am also grateful for his efforts and patient to correct my endless grammatical mistakes, which taught me a lot and helped improve my writings.

My special thanks go to my second supervisor Prof. Phil Blower for his guidance, for all the invested time in the supervision of my thesis and for his keenness for scientific discussion. In addition, I acknowledge the very interesting point he proposed for my thesis and the critical comments on this work. At many stages in the course of this research project I benefited from his advices, particularly, when exploring new ideas.

I owe special thanks to Dr. Jim Ballinger, Dr. Greg Mullen, Prof. Paul Marsden, Prof. Val Lewington for great advices for my thesis. I am grateful to my post graduated co-ordinator, Prof. Steve Keevil and Dr. Andrew Reader, for his kindly consideration of my progression over 4 years. Special thanks also go to my colleagues and friends in Imaging Biology and Chemistry, Dr. Seckou Diocou, Dr. Levente Meszaros, Dr.Ehsan Sharif-Paghaleh, Dr. Florian Kampmeier, Dr. Istvan Szanda, Dr. Michelle Ma, Dr. Maite Jauregui-Osoro, Dr. Zaitulhusna Md Safee, Dr. Kazumi Chia, Dr. Julia Blower, Dr. Samantha Terry, Muhumad Bin Othman (soon to be Dr) and Julia Bagunya Torres (soon to be Dr). I must express my gratitude to my lab manager David Thakor who helps me with radiation and instrumental issues and great organise of laboratory in Imaging Chemistry. I would also like to mention and thanks to Dr. Kavitha Sunassee, Stephen Clark, Barry Crook, Dr. Karen Shaw for their help in the lab. Thanks all of you for a friendly environment with happy times we spent together in the lab and social life. I have very fond memories of my time in London.

Thanks also go to Prof. Alice Warley, Centre for Ultrastructural Imaging, KCL for her help with electron microscope. I would like to thank Dr. Antigoni Divoli, Institute of Cancer Research (ICR) and the Royal Marsden NHS foundation Trust for her helps with MC simulation and small-scale dosimetry. I would also like to thank Dr. Adam Badar (Centre for Advanced Biomedical Imaging, UCL) for high-energy multi-pinhole collimator. My thanks go to radiopharmacists and

medical physicists team, Nuclear Medicine Department, Guy's & St. Thomas's NHS foundation Trust for their helps with instruments and radiotracers in this thesis.

I would like to thank Prof. Alan Perkins from University of Nottingham and Dr. Glenn Flux from Institute of Cancer Research (ICR) and the Royal Marsden NHS foundation Trust for being my thesis examiner committee. Their valuable suggestions and corrections to this work, greatly helped me to improve in various aspects.

Millions of thanks go to Dr. Putthiporn Charoenphun (who seem to be like my elder sister), for all her sincere helps with my lab, life and health. I looking forward to work with you in Thailand, hope we have many great projects together. A very special mention and thanks goes to Dr. Kankamol Jaisin (Pompam) for her unremitting encouragements, advices and supports, she is wonderful in so many ways. I am so glad that we met and you make me look forward to tomorrow.

Massive thanks go to all my friends in UK, Dr. Duantida, Dr. Pirada, Dr. Arkom, Dr. Palittiya, Dr. Theeranan, Dr. Chinnavuth, Dr. Saijai and also my friends in Thailand, Natthaporn, Dr. Chayanit, Dr. Sakdithep, Mongkol, Sorranat, Pakkinee, Arnon for their support. I always feel that I am not alone when I faced a problem.

I gratefully acknowledge the funding received towards my PhD from the Faculty of Medicine Ramathibodi Hospital, Mahidol University, Thailand. I am also grateful to my colleagues at Nuclear Medicine, Department of Radiology, Ramathibodi Hospital for their support during my study leave.

Last but not least, I take this opportunity to express the profound gratitude from my deep heart to my beloved dad, brothers, aunties, uncles. It is not possible to complete this work with your warm supports and encouragements from Thailand. Finally, this thesis is especially dedicated to my beloved mum and grand-mum for their forever love, encouragement and support from the heaven. Until we meet again.

Krisanat Chuamsaamarkkee

May 2016

Abbreviations

BSU	biological service unit
CFOV	centre field of view
CPM	count per minute
CPS	count per second
CT	computed tomography
CV	coefficient of variance
DIT	di-iodotyrosine
EBRT	external beam radiotherapy
EDS	Energy Dispersive Spectroscopy
EDX	Energy Dispersive X-ray Spectroscopy
EM	electron microscopy
eV	electron volt
FDG	fluorodeoxyglucose
FOV	field of view
FWHM	full width at half maximum
g	gram
GBq	giga Becquerel
GMP	good manufacturing practice
HAADF	High Angle Annular Dark Field
ICRP	International Commission on Radiation Protection
ICRU	International Commission on Radiation Unit
ID	injected dose
ID/g	injected dose per gram
IM	intra muscular injection
IV	intra venous injection
keV	kilo electron volt
LET	linear energy transfer
MAR	micro-autoradiography

MBq	mega Becquerel
MC	Monte Carlo
MCNP	Monte Carlo N-Particle
MeV	mega electron volt
MHS	micro hollow sphere phantom
MIP	maximum intensifying projection
MIRD	medical internal radiation dose
MIT	mono-iodotyrosine
MMP	multiplexed multi-pinhole
MRI	magnetic resonance imaging
NEMA	National Electrical Manufacturers Association
NIS	sodium iodide symporter
NPL	National Physics Laboratory
OCT	Optimal Cutting Temperature
OLINDA	Organ Level Internal Dose Assessment
OSEM	ordered-subsets expectation maximisation
PBS	phosphate buffer saline
PET	positron emission tomography
PI	post injection
PSF	point spread function
PVE	partial volume error
RAIT	radioactive iodine treatment
ROI	region of interest
SD	standard deviation
SE	standard error
SEM	scanning electron microscopy
SG	salivary glands
SIMS	secondary ion mass spectroscopy
SNM	Society of Nuclear Medicine

SPECT	single photon emission tomography
SUV	standard uptake value
T3	triiodothyronine
T4	thyroxine
TAC	time-activity curve
TEM	transmission electron microscopy
TEW	triple energy window
TFB	tetrafluoroborate
TG	thyroglobulin
TLC	thin layer chromatography
TPO	thyroperoxidase
TSH	thyroid stimulating hormone
VOI	volume of interest
WB	whole body
W_R	radiation weighting factor

Chapter 1 Introduction

1.1 Introduction

In nuclear medicine, unsealed radiation sources are administered to patients for diagnostic and therapeutic purposes. Dosimetry is intended to predict the risks of radiation in diagnosis and also the effectiveness and treatment outcome in therapeutic nuclear medicine. The term of dosimetry generally reflects only the macroscopic level but the information at this level is not always adequate to explain the complexity of inhomogeneous distribution of radiotracer and also the effect of Auger electrons and other secondary emissions (Sgouros, 2005; Stabin et al., 1999). Thus, it is important to study the distribution of tracer at cellular and subcellular level in order to obtain realistic dosimetry maps. Consequently, this knowledge is important in further understanding of biological effects from internal emitting radiation in nuclear medicine (Puncher and Blower, 1994a). This research will use the thyroid as a model for studying the dosimetry at macroscopic and microscopic levels.

Radioactive iodine treatment (RAIT) is a standard methodology to treat benign and malignant disease of the thyroid gland. The administration of radioiodine (^{131}I-iodide) for therapeutic purposes has been commonly accepted for the treatment of benign and malignant disease of the thyroid gland since the 1940s and still continues in the therapy of thyroid diseases today (Cooper et al., 2006; Tuttle et al., 2010). In the case of benign disease, RAIT is used in treatment of hyperthyroidism such as Grave's disease, toxic nodular goitre or toxic autonomous goitre. Additionally, RAIT is also used to decrease the size of nodule and also for suppressing the function of thyroid gland in non-toxic diffuse goitre and euthyroid multi nodular goitre. In thyroid cancer, RAIT is used to ablate thyroid gland after thyroidectomy and/or to treat metastasis lesion (Aschebrook-Kilfoy et al., 2010; Pacini).

In normal thyroid, the thyroid cells are formed by "colloid" surrounded by a single layer of follicular cells (thyrocytes) (as shown in figure 1-1). Radioiodine is trapped into follicular cells via the sodium iodide symporter (NIS) glycoprotein. Then, iodide is metabolized to thyroid hormones in the colloid. These are the molecular mechanisms of thyroid radioiodine therapy (Lazar et al., 1999). The disadvantages of radioiodine thyroid treatment can be attributable to the long physical half-life of 8.02 days and the beta-particles emitted by ^{131}I-iodide are quite low energy ($E_{average}$ = 0.18 MeV) which have a mean range in soft tissue of only 0.39 mm (Haymart et al., 2011). In particular, the abundant high-energy gamma rays (0.36 MeV, abundance 81.7%) emitted at the

same time as the beta emissions cause a large fraction of the whole body radiation dose as well as strongly influencing radiation protection associated with RAIT.

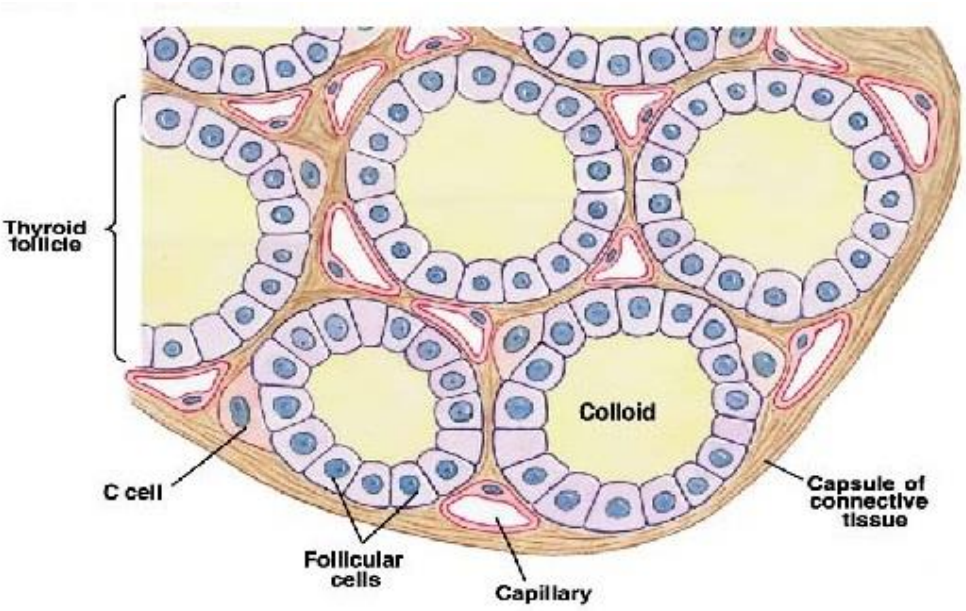

Figure 1-1 Schematic diagram shows section of thyroid gland, thyroid follicular cells are formed from "colloid" surround by a shell of follicular cells (Modified from (Champion et al., 2007b; Elbast et al., 2008a))

In this research, we propose to evaluate novel radionuclide therapy agents ^{186}Re- and ^{188}Re- perrhenate, which are also a substrate of NIS but not metabolised in processes of thyroid hormone production. Radiopharmaceuticals labelled with rhenium isotopes have been proposed for therapeutic use of non-thyroidal NIS-expressing tumours, for example palliation of skeletal bone pain (^{188}Re-,^{188}Re-HEDP), hepatic tumour (^{188}Re-lipiodol) and neuroendocrine tumour (labelled with peptides) (Spitzweg and Morris, 2009). ^{188}Re-perrhenate may offer several potential advantages over ^{131}I-iodide for radionuclide therapy of the thyroid.

The radioactive ^{188}Re-perrhenate is easily eluted from an ^{188}W/^{188}Re generator system which has a shelf-life of about 6 months. ^{188}Re-perrhenate has a physical half-life of 16.7 h and emits more energetic beta-particles ($E_{average}$ = 0.76 MeV) when compared with I-131 ($E_{average}$ = 0.18 MeV). The higher beta energy of ^{188}Re may offer more radiobiologically effective treatment when treating larger tumours (the mean beta-particle range in soft tissue of ^{188}Re-perrhenate is 3.10 mm when compared with ^{131}I-iodide of 0.39 mm) and may also enable cross-fire irradiation effects. However, the increased range may be also a disadvantage, hence this requires further understanding of cellular/subcellular tracer distribution and also small-scale dosimetry. In terms of imaging, the gamma photon of 0.15 MeV (15%) emitted by ^{188}Re is less abundant than 0.36 MeV (81.7%) by ^{131}I-iodide. This means ^{188}Re-perrhenate is still suitable for imaging but imparts

less whole body radiation dose when compared with conventional ^{131}I-iodide (Chung et al., 2010a; Ferro-Flores and Arteaga de Murphy, 2008a; Jeong and Chung, 2003). In the case of ^{186}Re, it has a physical half-life of 90.6 h, $E_{average}$ 0.346 MeV, E_{max}1.070 MeV. Imaging is possible for the gamma emission of 0.137 Mev with 9.4 % abundance.^{186}Re can be produced by either cyclotron or reactor which make this tracer less available when compared with generator based production of ^{188}Re. However, it is still a tracer of choice for therapeutic NIS applications. Also for both rhenium isotopes, the cost of radiation protection and management will be reduced due to less demanding aspects of shielding and waste management owing to their gentler gamma profiles emitted from both rhenium isotopes and shorter half-life.

According to these potential advantages, the proposed treatment may potentially offer a significant therapeutic improvement to patient quality of life and treatment cost effectiveness (Cyr et al., 2007; Verburg et al., 2011). However, these issues require further studies in order to confirm the radiation dose profiles and clinical advantages. The studies in this thesis are designed to assess the hypothesis that rhenium isotopes might offer greater therapeutic advantages for treatment of thyroid diseases and non-thyroidal NIS expressing tumour. Hence, the micro-scale dosimetry is one way to predict and answer these topics. These clinical relevant therapeutic decisions and questions, coupled with the well-defined tissue/cell geometry and uptake mechanisms associated with thyroid, make the thyroid therapy model an ideal one to introduce and evaluate micro-scale dosimetry theory.

1.2 Thyroid

As mentioned in the introduction, this project aims to use the thyroid as the model to study microscopic and macroscopic dosimetry. Thyroid is a good model because there is a lot of clinical data available, together with well-defined cell geometry and potential clear cut differences in micro-distribution of the various radiotracers. Therefore, these make the thyroid therapy model an ideal one to introduce and evaluate the role of small-scale dosimetry. The following part will provide the literature research of thyroid anatomy, histology, physiology and the role of nuclear medicine in the management of thyroid disease.

1.2.1 Thyroid Anatomy

The thyroid gland is part of the endocrine system which secretes hormones into the bloodstream. The thyroid gland is composed of two cone-like lobes connected via the isthmus. The anatomical form of thyroid is a butterfly-shape located in the anterior of lower neck, below the larynx. The posterior side of thyroid is reaching to the oesophagus and carotid sheath. The upper border is limited by crico-thyroid muscle to thyroid cartilage. The lower border extends to approximately the 5th or 6th tracheal ring which move during swallowing (Marine, 1922).

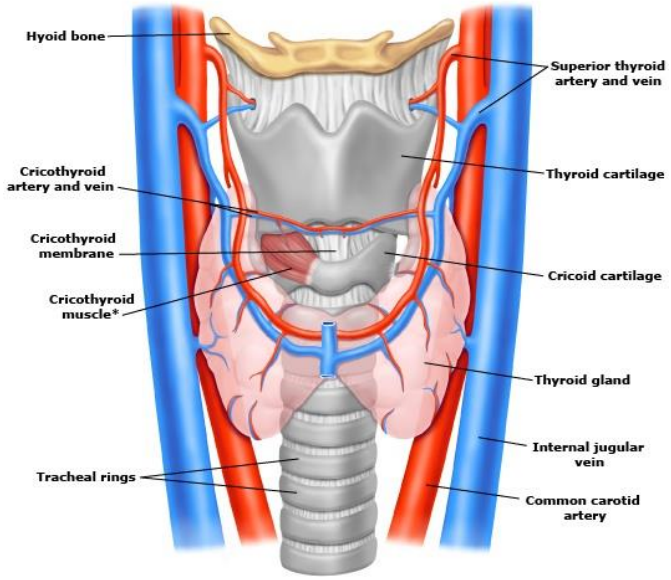

Figure 1-2 The thyroid gland gross anatomy and blood supply system (Modified from Netter, 1997)

1.2.2 Thyroid Histology

The thyroid gland contains two types of cells: follicular cells, which are responsible for the production of thyroid hormones, and C-cells, which synthesize calcitonin, a hormone that controls calcium metabolism. The C-cells are greatly outnumbered by follicular cells. The thyroid follicle is composed of a layer of simple epithelium follicular cells surrounding a gel-like pinkish material called “colloid”. The follicular cell is responsible for synthesizing the thyroid hormones and thyroglobulin (T_g). After the synthesis processes, thyroid hormones are stored as part of the thyroglobulin in the colloid which serves as a reservoir of materials for thyroid hormone production. The variation in follicular size and height depend on cell activity: squamous shape cells indicate a relative inactivity whereas cuboidal to columnar cells show more activity in removing the hormone from the stored form (McMullen and Delbridge, 2009; Weigel, 2008).

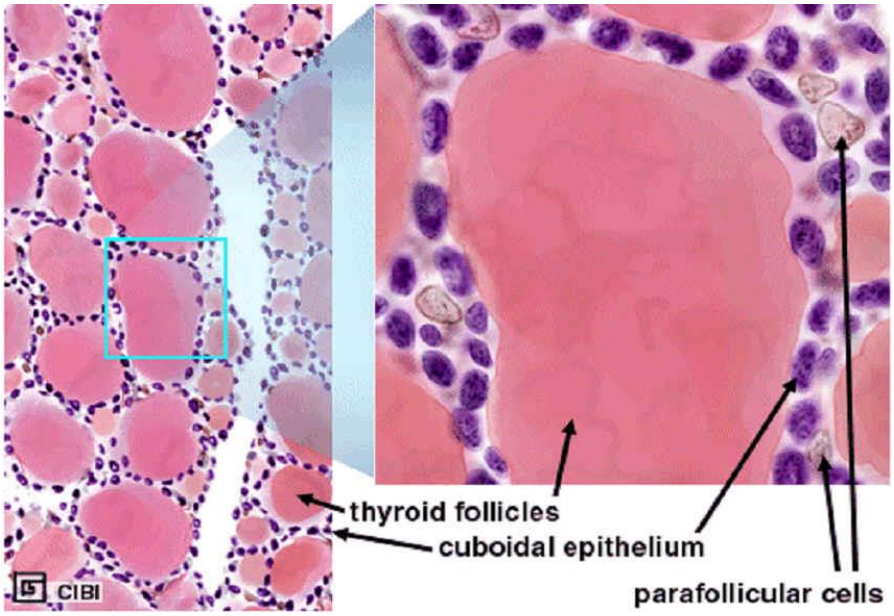

Figure 1-3 normal thyroid gland composed of thyroid follicles (follicular epithelial cells and colloid) and parafollicular C-cells Modified from (McMullen and Delbridge, 2009; Weigel, 2008)

The C-cells (clear cells) are another type of cell in the thyroid gland which usually appears large and clear because their cytoplasm and nucleus does not take up stain with H&E (hematoxylin and eosin). The C-cells are located in spaces between the follicles, so they are sometimes called “parafollicular cells”. Parafollicular cells secrete calcitonin, a hormone that lowers the level of calcium in the bloodstream (McMullen and Delbridge, 2009; Pacini et al., 2010; Weigel, 2008).

1.2.3 Thyroid Hormones Synthesis and Physiology

Thyroid hormones are synthesised from tyrosine. The key element in the synthesis of thyroid hormone is iodine. There are two thyroid hormones; thyroxine (T4) and 3,5,3'-triiodothyronine (T3). T4 contains four iodine atoms while T3 is identical to T4, but it has only three atoms of iodine per molecule. Thyroid hormones are synthesized by the follicular cells together with colloid under regulation by TSH (thyroid stimulating hormone).

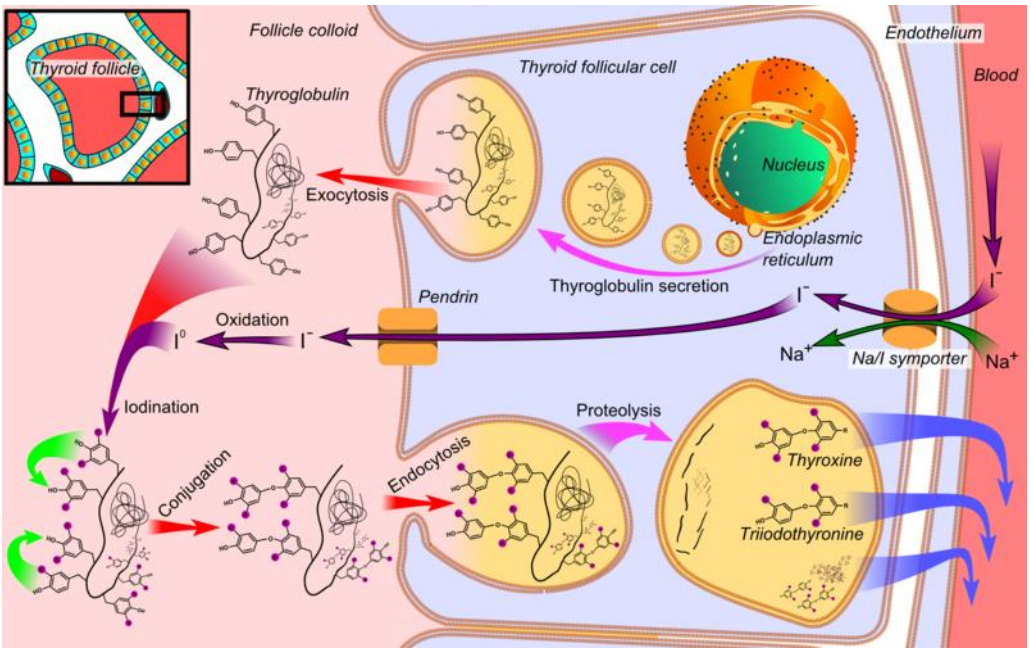

Figure 1-4 Schematic diagram of thyroid hormones synthesis (Modified from (Häggström, 2014))

There are 5 main steps in synthesis of thyroid hormones.

"Trapping" – Iodide is trapping from bloodstream into follicular cell by active transport via NIS (sodium-iodide symporter). NIS action is stimulated by TSH and can also concentrate other ions such as perrhenate, perchlorate, astatide or bromide. In this process, iodide is co-transported with sodium from basal to apical membrane by ion-gradient. Then, iodide is exported into colloid via the exporter protein pendrin.

"Organification"– Iodide is oxidised to iodine and then iodinated to tyrosyl residues in thyroglobulin. According to this process, two molecules are formed: MIT (mono-iodotyrosine) and DIT (di-iodotyrosine). This process is controlled by thyroperoxidase (TPO) which is an enzyme stimulated by TSH.

"Coupling" –The linking process of iodotyrosines occurs within the Tg molecule to form the thyroid hormones. Linking two molecules of DIT produces T4, whereas, linking one molecule of DIT and MIT produces T3.

"Proteolysis" – After endocytosis to follicular cells, the Tg glycoprotein is digested releasing the hormones T3, T4 and iodotyrosine. Thyroid hormones are secreted into the bloodstream binding to plasma proteins, only 0.04% of T4 and 0.4% of T3 are free form.

"Intrathyroidal deiodination" – The deiodination processes of iodotyrosine (MIT or DIT) occurs in follicular cell in order to use this iodide again as thyroidal hormones material. This process also deiodinate the remaining excess thyroid hormones.

Thyroid hormones affect almost every cell in our body. The major roles of thyroid hormones are:

Metabolism

- Increases the basal metabolic rate
- Increases carbohydrate, lipid and vitamins metabolism
- Protein synthesis
- Regulate body temperature

Growth and Development

- Neuronal maturation
- Essential for proper development and differentiation of all cells
- Long bone growth

Other System

- Cardiovascular – increase heart rate and cardiac output
- Increase sensitivity to catecholamine (e.g. adrenaline)

In addition, the thyroid gland also produces calcitonin by parafollicular C-cell. The action of this hormone is related to calcium and phosphorus metabolism. There are many functions of calcitonin such as inhibition of Ca^{2+} absorption by the intestines, inhibition of osteoclast activity in bones, inhibition of resorption of Ca^{2+} in kidney and vitamin D regulation (McMullen and Delbridge, 2009; Weigel, 2008).

1.2.4 Iodine Kinetics and Sodium Iodide Symporter (NIS)

The glycoprotein responsible for iodide transport is the sodium iodide symporter or NIS which is located at the baso-lateral plasma membrane of thyroid follicular cells. NIS accumulates both Na+ and I- into the cell by active transport. Electrophysiological analysis of NIS indicates that it transports a 2:1 ratio of Na+ and I- , which results in a steady-state inward gradient from basal to apical membrane. The maintenance of the Na+ gradient is caused by Na+-K+-ATPase. Therefore, the iodide transport is energy-dependent. Human NIS is the sodium/iodide co-transport glycoprotein coded as SLC5A5 which is located on chromosome 19 and codes for a protein of 643 amino-acids with a molecular weight of approximately 70-90 kDa and 13 transmembrane domains (De la Vieja et al., 2000; Dohán et al., 2003; Spitzweg et al., 1998).

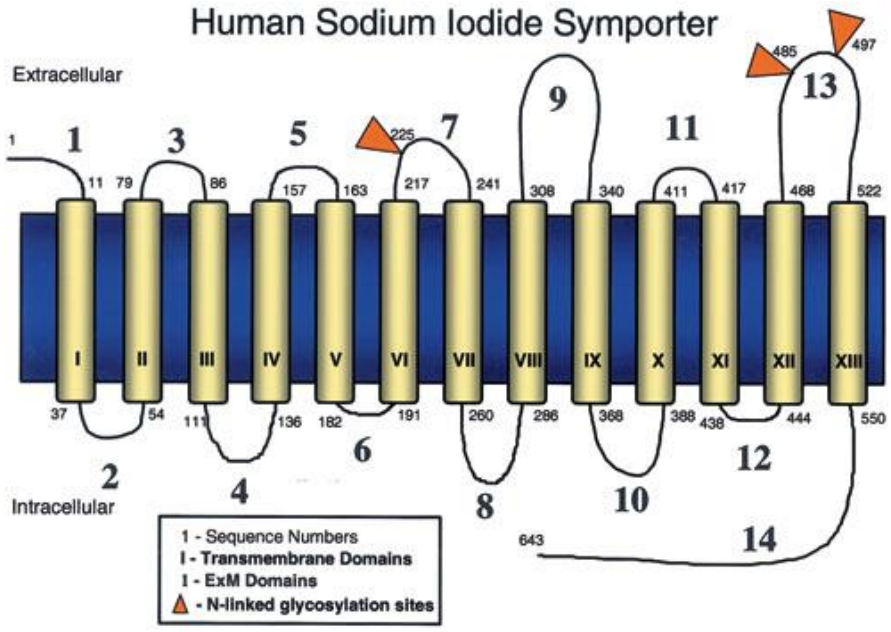

Figure 1-5 Schematic of human NIS with 13 transmembrane domains (Modified from (Dohán et al., 2003))

1.2.5 Radionuclide Imaging of Thyroid Gland

The thyroid gland can be imaged with several modalities such as conventional radiography, computed tomography (CT), magnetic resonance imaging (MRI) or nuclear medicine e.g. planar scintigraphy, positron emission tomography (PET) or single photon computed tomography (SPECT).

In conventional radiography, CT or MRI, thyroid imaging from these modalities accesses only the anatomical aspects and some abnormal pathology but does not inform about the function of the organ (Filetti et al., 1999). Nevertheless, the most common cause of thyroid disease occurs due to abnormal metabolic function. Therefore, nuclear medicine provides appropriate functional imaging based on the physiological properties of radiopharmaceuticals. There are several types of radiopharmaceuticals that can be used.

For SPECT imaging, the most common and practical application is using ^{99m}Tc-pertechnetate. Pertechnetate ($^{99m}TcO4-$) has physiochemical characteristics similar to iodide but is not organified to produce thyroid hormones. (Dadachova and Carrasco, 2004; Dohán and Carrasco, 2003a). The ^{99m}Tc-pertechnetate produces good quality images thanks to the properties of ^{99m}Tc but does not indicate all of the aspects of thyroid function. In addition, ^{99m}Tc-sestamibi or -tetrofosmin may help as thyroid tumour seeking tracers in some diseases such as differentiated thyroid carcinoma (Giordano et al., 2003). A better physiological approach of thyroid imaging would involve the use of radioisotopes of iodine as it is both trapped and organified by thyroid cell. ^{123}I-iodide is ideal tracer for diagnostic imaging, the energy of gamma photons of 159 keV with abundance of 83.4 % is suited for sodium iodide (NaI) crystal detectors used in SPECT. ^{123}I-iodide has physical half-life of 13.3 h, which is appropriate for 24 h iodine uptake studies but ^{123}I-iodide is expensive and not-available worldwide. ^{131}I-iodide has lower cost however it has several disadvantages over ^{123}I-iodide. For the same administered activity, ^{131}I-iodide gives more radiation dose and lower count rate (lower image quality) when compared with ^{123}I-iodide (Park, 2002).

For thyroid PET imaging, most tracers are aimed for use in diagnosis and management of thyroid cancer. ^{18}F- fluorodeoxyglucose (FDG) has been used widely in oncology. In thyroid, Sundram FX suggested the use of ^{18}F-FDG in patients with high risk disease, adverse histology, rising Tg with unknown anatomical source and Hurthle cell carcinoma. Authors also noted that combining ^{18}F-FDG PET with ^{131}I-iodide whole body scans had higher diagnostic sensitivity to 95% (Sundram et al, 2003). Additionally, M. Jauregui-Osiro et al synthesised and evaluated 18F-

tetrafluoroborate (TFB) for thyroid disease and reported gene imaging of NIS. The preclinical evaluation of the tracer in animals has been reported and the work is being translated as a clinical study. Hence, ^{18}F-TFB will be another forthcoming PET tracer in thyroid disease (Jauregui-Osoro et al., 2010a). For PET iodine isotopes, ^{124}I-iodide can be used for imaging and has presented better sensitivity than SPECT. However, ^{124}I-iodide has several disadvantages such as low positron yield (23%), long half-life (4.18 days), high positron energy (E_{max}=2.14 MeV), high energy and abundance of gamma emissions (gamma ray abundance exceeds 90% per disintegration) (Pentlow et al., 1996). Freudenberg et al suggested that ^{124}I-iodide can be used for improved treatment planning and patient specific dosimetry in thyroid cancer of 131I-iodide due to better spatial resolution than SPECT (Freudenberg et al., 2004).

1.2.6 Radionuclide Therapeutic of Thyroid Gland

For therapeutic purposes, ^{131}I-iodide has been used for therapy of thyroid diseases since 1940s. As mentioned in previous sections, radioactive iodine treatment (RAIT) is used to ablate thyroid remnant after thyroidectomy in thyroid cancer. In addition, RAIT can be used for treatment of Grave's disease, toxic multi-nodular goitre or toxic autonomously thyroid nodule and also for suppression of thyroid function in hyperthyroidism. NIS is the fundamental molecular basis for the use of radioactive iodine for treatment. Consequently, NIS has also been shown to transport other structurally similar anions like ClO_3-, $SCN-$, $SeCN-$, NO_3-, $Br-$, TcO_4- or ReO_4-.

^{188}Re-perrhenate (^{188}ReO4−) is also a substrate of NIS but not metabolised in processes of thyroid hormone production. Radiopharmaceuticals labelled with ^{188}Re have been used for therapeutic applications in non-thyroidal tissue. NIS gene transfers for non-thyroidal human cancer have been of interest to many groups in cancer researcher. Kogai et al observed NIS expression and radioiodine concentration in breast cancer cell line caused by retinoic acid (RA). The authors concluded that RA could induce iodide uptake in breast cancer cells and might be a potential application for patients whom standard treatments are not effective (Kogai et al., 2000). Spitzweg and co-worker also performed experiments in human prostatic adeno-carcinoma cell lines (Spitzweg et al., 1999). This study presented another step towards gene therapy of cancer with radioiodine. In vivo studies also showed the possibility for this method. Dadachova et al. studied the role of ^{131}I and ^{188}Re for treatment of mammary cancer in a mouse model. They concluded that NIS expression in the breast cancer animal model is efficient and safe treatment with several radionuclides transported by NIS. (Dadachova et al., 2005).

In addition, ^{211}At is proposed as new therapeutic radiotracer for thyroid cancer and metastatic which emits high energy alpha particles. The physical properties of ^{211}At are promising however currently it is only available at a few centres (Chung et al., 2010b). In addition, the method to calculate dosimetry for alpha particles must consider energy deposition at the cellular and subcellular level as these particles have high linear energy transfer (LET) and high relative biological effectiveness (RBE) (Brady et al., 2013).

Further details on radionuclide therapy of thyroid diseases are provided in chapter 4 of this thesis.

1.3 Microscopic and Macroscopic dosimetry in Nuclear Medicine

Radiation dosimetry in nuclear medicine aims to estimate radiation risks or benefits from unsealed radiation sources that administered to patients. Traditionally, nuclear medicine has been focused mainly on a diagnostic radiopharmaceutical. The absorbed dose calculation is based on an average organ dose for risks assessment. However with increasing development of new radiopharmaceuticals for therapeutic applications, the dosimetry in nuclear medicine needs to be determined on a scale comparable to the range of emission and target cell and organelle of interest.

In general, there are 2 levels of dosimetry described in the literature; microscopic and macroscopic. Macroscopic dosimetry is considered in non-stochastic approaches while microscopic aims to quantify the energy deposited at small scale with stochastic approaches (Bardies and Pihet, 2000; Stabin, 2006). Therefore, the following section will provide the general overview of macroscopic and microscopic dosimetry in nuclear medicine.

1.3.1 Macroscopic Dosimetry in Nuclear Medicine

Macroscopic dosimetry in nuclear medicine deals with the energy deposited by internal emitted radionuclide to organ, tissue or whole body level. To state the macroscopic quantity, the absorbed dose is usually used. The absorbed dose for each tissue is the energy absorbed per unit mass. The direct measurement of absorbed dose for internalised emitting radionuclide is difficult to perform, and the absorbed dose in nuclear medicine is usually determined indirectly by calculation (Zanzonico, 2000). Mostly of clinical nuclear medicine dosimetry are relied on macroscopic dosimetry with calculated by MIRD (Medical Internal Radiation Dose) method. This method is sufficient to estimate absorbed dose by using 2 fundamental quantities; the source-target geometry factor (also called S-factor) and activity distribution as a function of time (Speer, 2012). The details of this method, the assumptions and their limitations are extensively discussed in chapter 4.

1.3.2 Microscopic Dosimetry in Nuclear Medicine

Microscopic dosimetry most generally means measuring the energy deposited on a microscopic scale and a sub-millimetre scales which below the resolution of the scanner. More distinctively, microscopic dosimetry studies the number, size, spatial, temporal and energy-spectral distributions of individual energy imparted in cellular and sub-cellular structures (Attix, 2007; Rossi and Zaider, 1991). Furthermore, dosimetry at microscopic scale takes into account

the stochastic fluctuations in the micro volume. This contrasts with macroscopic dosimetry, where the radiation absorbed dose is obtained by dividing the total energy deposited by the mass of that volume (i.e. averaging out inhomogeneity within that volume). The calculation does not include the stochastic effects because of the large target volume of interest. Consequently, the individual cell dose can be over or under estimated due to stochastic nature of radiation and because of the inhomogeneous distribution of radionuclides within the volume.

Another consideration point for macroscopic dosimetry is the assumption of the radionuclide distribution is homogeneously to all cells over the entire organ. However, this assumption is not always correct as some cell populations in the organ may contain very different amounts of radioactivity, and even some cells may not uptake radiotracer. (Farragi et al., 1994; Humm et al., 1993a). In addition, the microscopic dosimetry is increasingly of interest because the clinical application of high LET radionuclides has become increasingly widespread e.g. alpha therapy. The conventional macroscopic dosimetry are inadequate, also, the understanding of microscopic dosimetry is important for the diagnostic radiopharmaceutical due to their Auger electrons e.g. ^{67}Ga, ^{99m}Tc, ^{201}Tl (Humm et al., 1993b; Roeske et al., 2008a).

The details of microscopic dosimetry including methods for estimation, assumptions and their limitations are explored in chapter 5.

1.4 Thesis Overview

The major aim of this work is to study the connecting paths of micro- and macro-dosimetry using the thyroid as a model. We also aim to evaluate novel radionuclide therapy agents ^{186}Re- and ^{188}Re-perrhenate and to compare these radiotracers with conventional radioiodine (^{131}I-NaI) using preclinical data. Several experiments have been undertaken for this work. The overview of the work is summarised below.

Chapter 1 contains an introduction and general literature review.

Chapter 2 investigates the quantification accuracy of preclinical imaging systems (nanoScan SPECT/CT and nanoScan PET/CT)

Chapter 3 explores the capabilities of preclinical imaging systems to quantify the spatio-temporal distribution of NIS radiotracers (^{99m}Tc-pertechnetate, ^{123}I-NaI, ^{131}I-NaI ^{188}Re-perrhenate and ^{18}F-tetrafluoroborate) in healthy model and NIS-expressing tumour model (rat adenocarcinoma engineered-hNIS).

Chapter 4 examines the macro-dosimetry of the potential radiopharmaceuticals by using MIRD (Medical Internal Radiation Dose) formalism with the OLINDA dosimetry software. The kinetic data are based on quantitative preclinical imaging from the previous chapter. We estimate the effective dose of diagnostic NIS-radiotracers and also investigate the dosimetric feasibility of using ^{186}Re- and ^{188}Re-perrhenate in treatment of benign nodular thyroid disease in comparison with conventional ^{131}I-NaI and explore using these new therapeutic radiotracers in NIS-expressing tumours. We also examine the impact of quantification accuracy on dosimetry calculations from preclinical studies.

Chapter 5 investigates methods for measurement of tracer distribution at the microscopic level. Tracer distribution in thyroid is examined using micro-autoradiography (MAR) and electron microscopy (EM) techniques. The distribution and cell geometry are used as input for pilot micro-scale dosimetry. Then, the micro-scale dosimetry is used to estimate the dose at cellular level using the Monte Carlo MCNPx platform.

Chapter 6 concludes with overall discussion, future perspectives and conclusion of this work.

Chapter 2 Quantitative Imaging with the nanoScan SPECT/CT

2.1 Introduction

SPECT/CT is an essential tool for accessing the distribution of radioactivity in biomedical research. The SPECT (Single Photon Emission Tomography) modality offers a tool for visualisation of radiotracer accumulation but can also provide quantitative information. *In vivo* image quantification is crucial for many applications, especially for image-based dosimetry, where the absolute activity within the tissue/organ permits the calculation of absorbed dose. There are many intricate processes and limitations related to SPECT instrumentation and methodology which can affect the accuracy of quantification (Franc et al., 2008; Ritt and Kuwert, 2013; Walrand, 2014). The following figure outlines the factors and correction methods for quantitative SPECT in clinical applications.

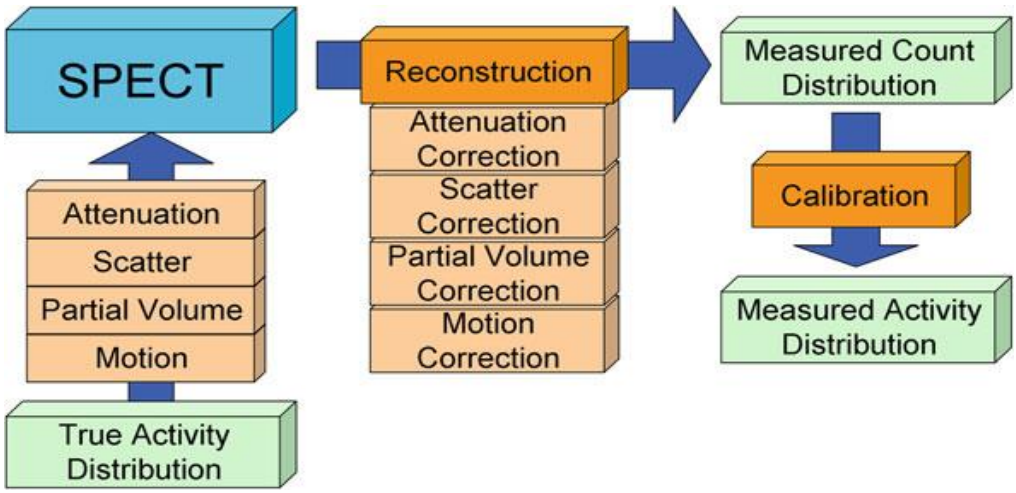

Figure 2-1 The flow chart shows the process of measuring the activity distribution in clinical SPECT. Imaged activity distribution is influenced by many factors (attenuation, scatter, Partial Volume Effect (PVE) and motion). In SPECT, the pre- or during reconstruction processes can correct for these effects. Then, the measured count distribution can be converted to the measured activity distribution via an equipment calibration factor. (Modified from Quantitative SPECT) (Ritt and Kuwert, 2013)

The main factors limiting the accuracy of quantitative SPECT are photon attenuation and scatter of gamma photons as they pass different layers of tissue or surrounding material (e.g. collimators) before entering the detector. Additionally, the relatively poor intrinsic resolution of the scanner can blur the activity distribution with strong influence on quantification when the dimensions of object are comparable or smaller than the spatial resolution of the imaging instrument; this called “Partial Volume Effect” (PVE) (Franc et al., 2008; Jaszczak et al., 1981). The PVE and its influence on quantification are discussed in more detail in the following sections.

In preclinical research, high spatial resolution is required for small animal imaging. The use of dedicated multi-pinhole collimators enables sub-millimetre resolution in a small field of view (due to the small aperture of collimation and high magnification factor) along with preserved sensitivity (by the use of multiple apertures per collimator) for *in vivo* molecular imaging. However, the preclinical SPECT is not a scaled down version of clinical SPECT. For example, the PVE in preclinical imaging may be a more crucial factor as the size of organs is much smaller when compared to the resolution of the scanner. However, less influence from photon attenuation characterises small animal imaging due to the shorter track of photons as they pass through tissue(Deleye et al., 2013; Franc et al., 2008; Mannheim et al., 2012).

In this work, we propose to study the magnitude of quantification errors in preclinical SPECT with ^{99m}Tc, ^{123}I and ^{188}Re. The main goal of this chapter aims to evaluate, quality control of preclinical SPECT and to evaluate the accuracy of nanoScan SPECT/CT in quantification, correction of small-objects/organs.

2.2 Pre-clinical Imaging

2.2.1 System Description of the nanoScan SPECT/CT

This work makes substantial use of preclinical imaging systems which are introduced in this and the next section. Preclinical nanoScan SPECT/CT (Mediso, Hungary) is a dual imaging modality system which combines the functional SPECT and anatomical CT at high resolution for small animal imaging. SPECT is composed of fours NaI(Tl) detectors (215×230 mm^2) with pixel size less than 1 mm^2. The multiplexed multi-pinhole (MMP) collimator magnifies images through many pinholes simultaneously with high resolution (1.0 mm-aperture offers FWHM of < 0.75 mm.) and high sensitivity levels (≥ 1200 cps/MBq for whole-body imaging with trans-axial field-of-view (TFOV) ≥ 30mm.

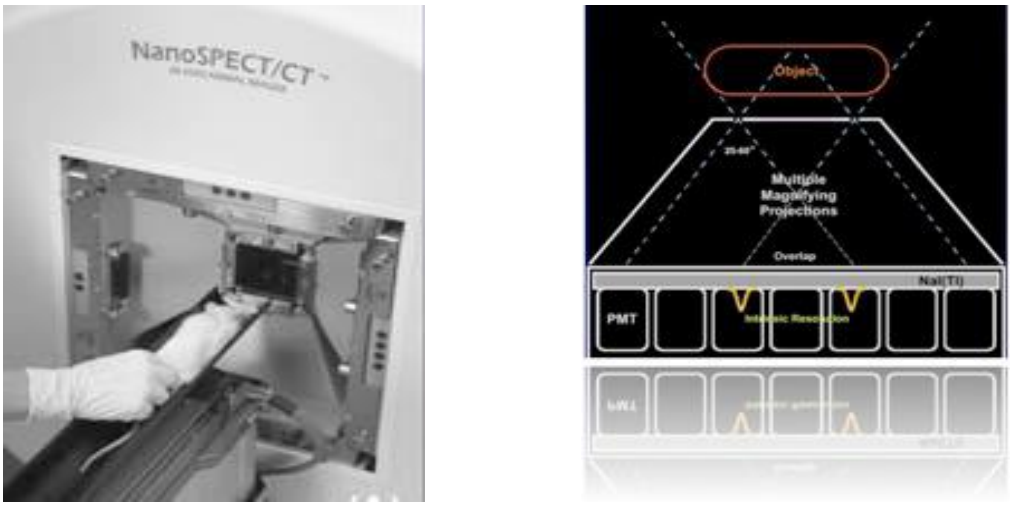

Figure 2-2 (Left) Four detectors NaI (Tl) system surround the animal for fast and dynamic acquisition (Right) Multiplexed Multi-Pinhole (MMP) collimator for magnification the image with ultra-high resolution (modified from the nanoScan SPECT/CT user manual)

For reconstruction, all SPECT tomographic projections are reconstructed using HiSPECT™ software (supplied with the camera). An iterative Ordered-Subsets Expectation Maximisation (OSEM) algorithm is used in this software. This software does not correct for either attenuation or scatter. There are 3 settings for reconstructing the tomographic projections;

- Fast Reconstruction – 6 iterations with 35% Gaussian Smoothing Filter
- Standard Reconstruction - 9 iterations with 35% Gaussian Smoothing Filter
- Phantom Reconstruction - 24 iterations with 25% Gaussian Smoothing Filter

Images are visualised with VivoQuant image and analysis software. This software has a user defined calibration factor (details and methods for obtaining calibration factor in chapter 3) to convert image counts to units of radioactivity concentration (MBq or kBq per voxel). VivoQuant

also includes software for image quantification, post processing and image co-registration with CT (when modalities are not spatially aligned).

The CT system of nanoScan SPECT/CT is used for scout scanning and anatomical imaging. It comprises a standard micro-focus X-ray source (5-8 μm spot size) with an operating voltage range of 30 – 90 keV and tube current of 0.09-0.18 mA. The CT system provides a low-dose X-ray system and relatively high tissue contrast imaging.

2.2.2 System Description of nanoScan PET/CT

Preclinical nanoScan PET/CT is a dual-modality PET and CT system with high resolution and high efficiency for *in vivo* small animal imaging. The PET component comprises twelve detector arrays of 85 x 39 LYSO:Ce crystals of 1.12 x 1.12 x 13 mm^3 each. The effective FOV is 123 mm (axial). The trans-axial FOV is 94 mm with the spatial resolution of the system at central FOV (CFOV) less than 1.2 mm (for filtered back projection) and sensitivity at CFOV of 8.3 % (for 250 – 750 keV window). Acquisition is possible in list mode with the option of 3D reconstruction using CT for attenuation correction.

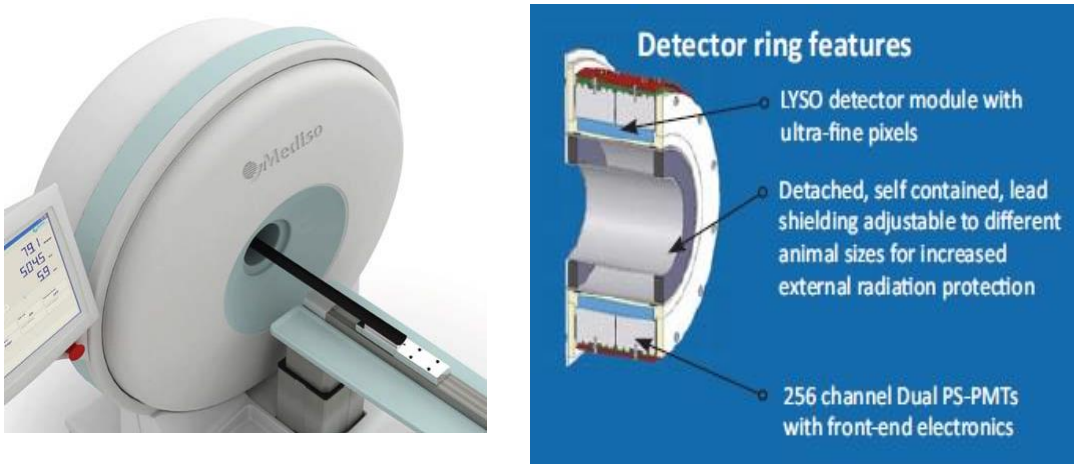

Figure 2-3 (Left) nanoScan PET/CT (Right) LYSO Detector ring system of PET (modified from nanoScan PET/CT user manual)

The CT images of nanoScan PET/CT are used for scout scanning, anatomical imaging and deriving an attenuation map for attenuation correction. The X-ray CT is acquired using helical scanning with volumetric cone-beam technology and a micro-focus source (5-9 μm spot size). The operating voltage can be varied from 35-90 keV with maximum tube current of 0.18 mA.

2.3 Tomographic Uniformity with Mouse-Size Phantom

Tomographic uniformity is a basic test to indicate the overall performance of the imaging system (Deleye et al., 2013). Basically, tomographic uniformity is the uniformity of the image after reconstruction. Hence, the tomographic uniformity includes the effects of reconstruction as well as the attenuation and scatter correction performance of the imaging system.

2.3.1 Aim

The aim of this experiment is to evaluate tomographic uniformity of nanoScan SPECT/CT with ^{99m}Tc, ^{123}I and ^{188}Re. We also analysed the data with all available reconstructing options: fast, standard and phantom. In addition, the line profile was obtained to compare the effects of attenuation for each isotope.

2.3.2 Materials and Methods

2.3.2.1 Phantom

The 30 ml universal tube (Thermo Scientific, UK) was selected to use as a uniformity phantom. This tube has a diameter of 3.1 cm and is 9.4 cm long (as seen in figure 2-2A). The phantom was filled with well mixed radionuclide solution with activity range from 37 -74 MBq as recommended by the manufacturer.

2.3.2.2 Experiment Protocol

The phantom was scanned for 50 s per projection with 40 projections on a sampling matrix of 256 × 256 pixels, which resulted in approximately 30 minute scanning time. The scan was performed with the following energy-window settings; ^{99m}Tc (20% window centred over the 140 keV photo-peak), ^{123}I (20% window centred over the 159 keV photo-peak) and ^{188}Re (20% window centred over the 155 keV photo-peak). All projection data were reconstructed in HiSPECT© (Scivis, GmbH, Gottingen, Germany) version 1.4.1876 with; fast (OSEM - ordered subset maximum likelihood expectation maximisation, 6 iterations with 35% smoothing), standard reconstruction parameters (OSEM, 9 iterations with 35% smoothing) and ‘phantom’ reconstruction parameters (OSEM, 24 iterations with 25% smoothing)

2.3.2.3 Uniformity Analysis

Uniformity was quantitatively measured by drawing a cylindrical volume of interest (VOI) with diameter of 10% of the diameter of the phantom (diameter of VOI approximately 3 mm.) at the centre of uniformity area in the phantom (figure 2-4 right) using the VivoQuant analysis software version 2.0 (InVicro, USA). A small VOI was defined (figure 2-4 right) in order to avoid

effects related to photon attenuation, however, this could be at the cost of a large standard deviation about the mean. The uniformity of the tomographic image was computed using the NEMA (National Electrical Manufacturers Association) formula (equation 2-1) (Deleye et al., 2013).

$$Uniformity\ (\%) = \frac{Max\ Count - Min\ Count}{Max\ Count + Min\ Count} \times 100 \qquad \text{Equation 2-1}$$

We also calculated the coefficient of variation (%CV) using the data from the same VOI. Additionally, we compared the uniformity value and %CV for each set of reconstruction parameters (fast, standard and phantom).

$$\%CV(\%) = \frac{SD}{Mean} \times 100 \qquad \text{Equation 2-2}$$

The VOI was repeatedly drawn on 3 separate occasions to obtain a measure of deviation of the measurement.

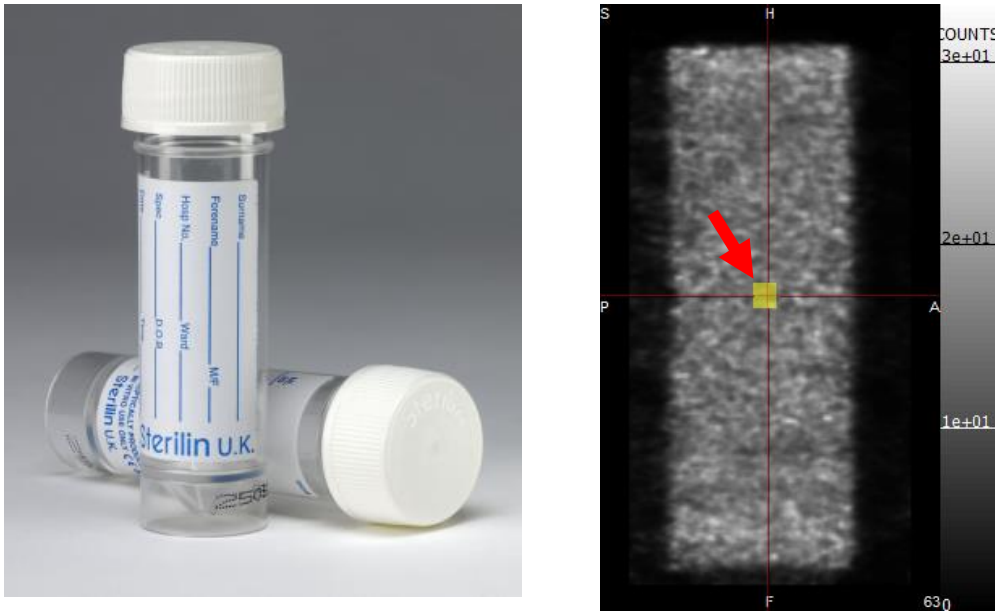

Figure 2-4 (Left) 30 ml universal tube used as a phantom in this study (Right) Cylinder VOI placed on the centre of the uniform area to obtain the uniformity and %CV

2.3.2.4 Line Profile

The middle axial slices across the Z-axis of the scanner filed-of-view were compressed (40 axial planes in total for each data set) using ImageJ software version 1.48v (National Institutes of Health, USA) to avoid the noisy signal in each single slice. Line profiles across the X-axis of the tomographic image (for standard reconstruction algorithm) were obtained and plotted against axial position for each isotope.

2.3.3 Results and Discussion

For the tomographic uniformity, the results were calculated from the mouse-size cylindrical phantom. The maximum, minimum, SD and mean values for each VOI were obtained from VivoQuant. The uniformity and percentage coefficient of variation were expressed as mean ± SD in the table 2.1 below. The SD in this experiment was obtained from repeatedly-drawn VOI 3 times on the same data set.

Table 2-1 Percentage non-uniformity and percentage coefficient of variation (%CV) from tomographic image of nanoScan SPECT/CT (mean ± SD)

Syringe	Reconstruction Protocol	% Non-Uniformity	% CV
^{99m}Tc	Fast	12.71 ± 0.54	5.22 ± 0.40
	Standard	22.00 ± 1.03	8.27 ± 0.12
	Phantom	77.83 ± 5.29	31.57 ± 0.69
^{123}I	Fast	12.17 ± 0.68	4.98 ± 1.16
	Standard	19.07 ± 1.66	6.60 ± 0.26
	Phantom	64.79 ± 2.84	22.28 ± 0.18
^{188}Re	Fast	18.74 ± 1.40	6.44 ± 0.45
	Standard	29.04 ± 5.38	9.79 ± 0.76
	Phantom	91.92 ± 1.82	44.20 ± 1.96

Based on the results, the tomographic uniformity and %CV changed with the reconstruction algorithm. The images were less uniform and %CV increased at high iteration numbers (a lower number indicates better uniformity). For the standard reconstruction parameters (as we used this reconstruction protocol for all *in vivo* studies), the tomographic uniformity for ^{99m}Tc (22.00 ± 1.03 %) was found to be similar to ^{123}I (19.07 ± 1.66). Slightly improved uniformity with ^{123}I might be due to higher energetic gammas compared with ^{99m}Tc, thus slightly reduced photon attenuated, although we deliberately chose a small centrally-defined VOI to avoid influence from photon attenuation. As this version of nanoScan SPECT/CT reconstruction platform does not include correction for attenuation, we can see a drop in the activity at the centre of the phantom from uniformity calculations and the line profile (in the following section). The tomographic uniformity of ^{188}Re was found to be 29.04 ± 5.38 % with 9.79 ± 0.76 %CV for standard reconstruction. The non-uniform result of ^{188}Re (compared with ^{99m}Tc and ^{123}I) can be explained

by the high event of Bremsrahlung backscattered caused from high-energy beta (extending up to 2 MeV), down-scatter from high-energy photons penetrate collimator septa (creating background elevated in the image) (Shcherbinin et al., 2014). We did not apply any corrections at this stage due to lack of provision for re-importing corrected projection files into the reconstruction platform.

For the 'phantom' reconstruction parameter set, the uniformity and % CV values were very high (non-uniform) as expected. Due to the nature of OSEM reconstruction it is widely reported that noise in the images increases as iteration increase (Leong et al., 2001).

Plots of line profiles from the compressed middle axial slides of the uniformity phantom are shown in figure 2-5 below. As stated earlier, this version of nanoScan SPECT/CT does not include correction for attenuation. To investigate this effect, we compared the line profiles of ^{99m}Tc and ^{123}I. It can be seen that the drop of activity at the middle of ^{99m}Tc phantom was larger than ^{123}I. In the case of the ^{188}Re line profile, the background counts outside the object are observed at around 5000 counts whereas for ^{99m}Tc and ^{123}I the background counts outside the object fall to almost zero. This poses a difficulty with quantification due to high background for ^{188}Re. ^{188}Re quantification also influence by scatter, this will discuss in more detail in quantification section with micro-hollow sphere phantom.

Also, it was important to note that a ^{99m}Tc correction flood was used for all studies rather than a flood specific to the radionuclde under study.

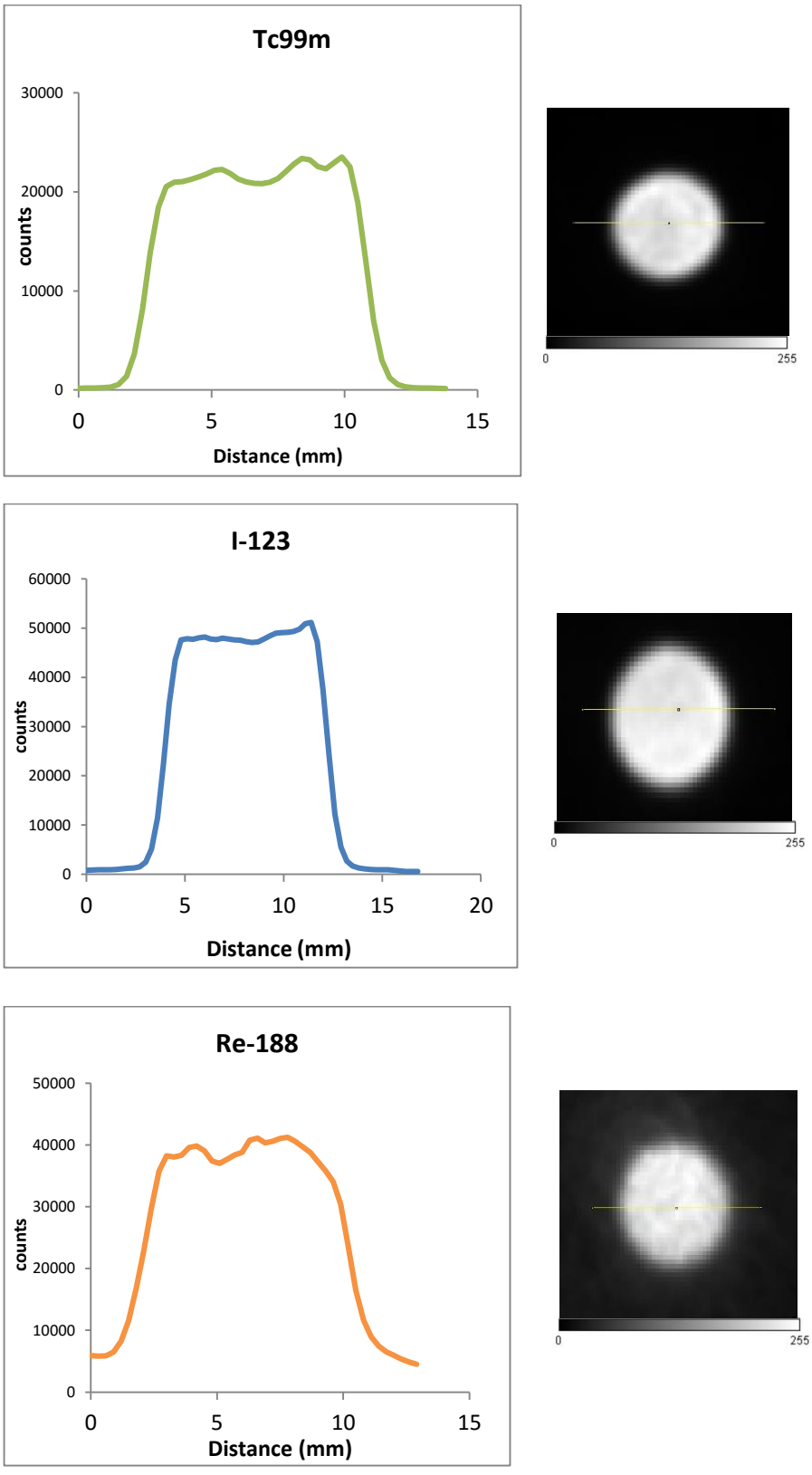

Figure 2-5 Line profile plots and line ROIs from uniform area across X-axis of the scanner for ^{99m}Tc, ^{123}I and ^{188}Re (Activity in phantom were in the range prescribed by manufacturer 37-74 MBq)

2.4 System Calibration

System calibration is an important step to determine absolute amounts of radioactivity from the images. To obtain this, the number of counts per voxel needs to be convert to activity or activity concentration. This conversion factor may be referred to as system calibration factor or system sensitivity (for example counts/MBq/s). The calibration factor is specific for each radionuclide as well as the collimator apertures and thicknesses. Also, the protocol for obtaining this factor is specific to the data acquisition and reconstruction parameters as well as any attenuation compensation and scatter correction (if available) used in the experimental study.

2.4.1 Aim

The aim of this experiment was to evaluate the calibration factor of the nanoScan SPECT/CT using the radionuclide activity calibrator (Capintec CRC® - 25R, Ramsey, NJ, USA) as a standard reference device. The radionuclide activity is annually calibrated against the NPL (National Physics Laboratory) as primary standard. Hence, we aim to establish calibration factors for ^{99m}Tc, ^{123}I, and ^{188}Re with a low energy multi-pinhole collimator aperture of 1 mm and for ^{131}I using high energy collimator with aperture of 1 mm.

2.4.2 Materials and Methods

2.4.2.1 Calibration Phantom

The mouse-sized quantification phantom is illustrated in figure 2-4. A 3 ml syringe (diameter of 9.83 mm) filled with 1.5 ml of the radiotracer solution, aiming for an activity of 37-74 MBq. The activity was measured in the radionuclide activity calibrator, and the time of the measurement noted. Then, the syringe was inserted into a 2.5 cm diameter water-filled Perspex cylinder phantom in order to simulate photon attenuation and scattering conditions caused by the body of the mouse.

Figure 2 6 Perspex Quantification Phantom with a 3 ml syringe inserted with activity of 37-74 MBq in a volume of 1.5 ml for obtaining a calibration factor

2.4.3 Experimental Protocol

The phantom was acquired for a minimum of 50,000 counts per frame according to manufacturer recommendations. The scan projections were processed using the standard reconstruction protocol. A 3D VOI was drawn using VivoScope© analysis software, then the number of counts, time and activity of the syringe measured in the radionuclide activity calibrator were inputted to the software for calculation of the calibration factor.

2.4.4 Results

The quantification factors for the radionuclides used are shown in Table 2-2. The quantification factors were dependent on collimator type (thickness), aperture size and isotope emissions. These factors were stored for subsequent use to convert count rates to activity in mega-Becquerel in the VivoScope© software.

Table 2-2 Calibration factors (± SD) with photo-peak and window width of ^{99m}Tc, ^{123}I and ^{188}Re for the low energy collimator with aperture 1 mm, ^{131}I for high energy pinhole collimator.

Radionuclides	Photo-peak (keV)	Width (%)	Calibration Factor (Conversion of count to MBq)
^{99m}Tc	140.0	20	0.00304 ± 0.00021
^{123}I	159.0	20	0.00440 ± 0.00044
^{131}I	364.0	20	0.01214 ± 0.00112
^{188}Re	155.0	20	0.01901 ± 0.00279

2.5 Linearity of nanoScan SPECT/CT

As this work focused on longitudinal imaging studies, quantitative accuracy over a wide dynamic range was critical for following the time course of the tracer from the initially high amount of radioactivity injected and over a period permitted by the effective half-life and the animal licence restrictions. Since in vivo activity distribution will be followed until the later time-points leading to relatively low activity levels, the linearity of the system was tested over the entire intended activity range.

2.5.1 Aim

The aim of this experiment was to examine the linearity response and dead time performance of nanoScan SPECT/CT over a range of activity levels using the decay method.

2.5.2 Materials and Methods

The quantification phantom described previously (in chapter 2.3) was used to test linearity respond and dead-time correction of the system. A 3 ml syringe was filled with 1.5 ml of ^{99m}Tc, aiming for a high activity of approximately 200 MBq (similar to the highest activity permitted to be injected into the mouse in the lab facility). Higher activity ranges were considered unrealistic for the pre-clinical imaging setting both due to associated absorbed radiation dose (e.g. potential biological radiation effects, especially in longitudinal studies) and the specific activity and injected volume limitations. The activity was measured in the radionuclide activity calibrator, and then the syringe was placed into the water-filled Perspex cylindrical phantom. The phantom was scanned with an acquisition time of 50 s/projection (40 projections on a sampling matrix of 256 × 256 pixels) for a total scanning time of approximately 40 minutes. The activity in the phantom was scanned at various time points over 3 consecutive days. All projection data were reconstructed using the standard reconstruction protocol (OSEM, 9 iterations with 35% smoothing). The images were viewed and analysed using VivoQuant© software.

2.5.3 Results and Discussion

The linearity and count rate tests on the nanoScan SPECT/CT were performed by scanning a 1.5 ml syringe inserted into a plexiglass quantification phantom. The activity in the phantom was measured and recorded with the radionuclide activity calibrator prior to scan, with total activity in the syringe of 208.80 MBq. Data were acquired over a period of about 3 days in order to allow activity in the phantom to decay to approximately 1 MBq. Activity measured in the radionuclide activity calibrator was decayed for the isotope's physical half-live and plotted against

the quantification results obtained from the nanoScan SPECT/CT in a semi-logarithmic scale (Figure 2-5).

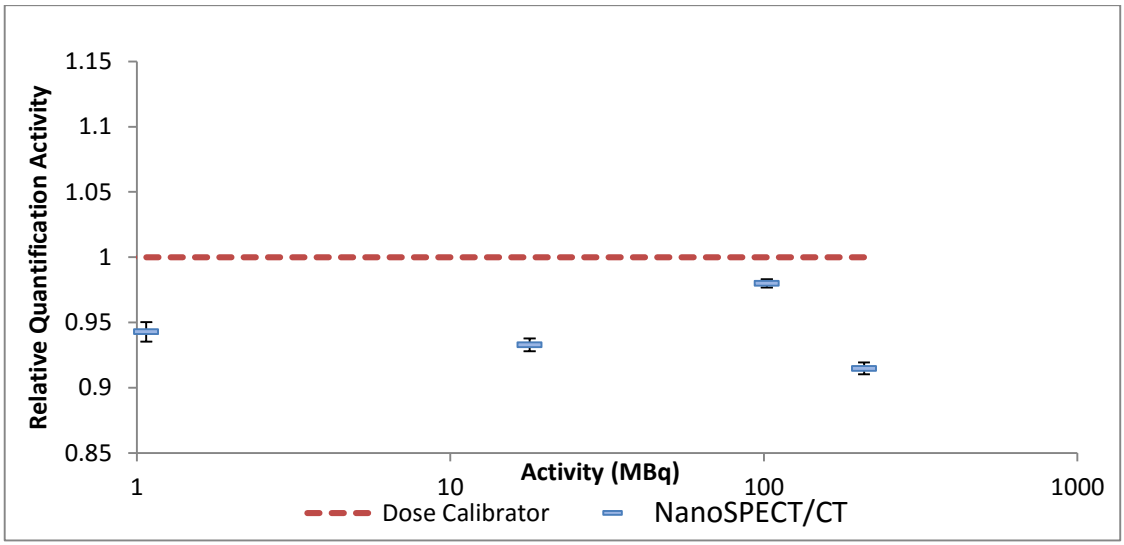

Figure 2-6 Linearity of nanoScan SPECT/CT obtained with ^{99m}Tc by using quantification phantom. The relative quantification activity were the measured activity from nanoScan SPECT/CT normalised to initial activity measured in radionuclide activity calibrator then plotted against activity of phantom

From the results, it can be seen that the relationship between the quantified activities from nanoScan SPECT/CT with ^{99m}Tc was within 10% from the radionuclide activity calibrator derived radioactivity over the range assessed. At high activities, the quantified activity showed the highest discrepancy at approximately 10 % (relative quantified value 0.915 ± 0.005). The quantified activity was within reasonable range from the measured activity from the radionuclide activity calibrator at lower activities with underestimated to within 5 – 6 %, the quantified value deviated from the unity line at 0.933 ± 0.005, 0.943 ± 0.007 and 0.949 ± 0.003 for 0.530, 1.072 and 17.904 MBq respectively. These activity levels up to 100MBq represent a realistic range of small-animal scans from the full maximum injected activity in the scanner field-of-view to decayed levels in longitudinal dynamic imaging studies. It should be noted that other non-instrumentation related limitations, such as those related to the achieved specific activity injected into small animals, are also good reasons to avoid higher injected activities (Hume et al., 1998).

2.6 Accuracy of nanoScan SPECT/CT in Quantification of Small Objects

Image quantitative accuracy in emission tomography (PET and SPECT) is hampered by the finite spatial resolution capability of the scanner which results in blurring the activity distribution and limiting tissue sampling (each individual voxel can in principle contain 2 or more tissue types at the boundary of regions). This is called the partial volume effect or PVE. This problem can be more severe when quantifying small objects/organs with size less than 2-3 times the scanner's spatial resolution, which is measured in terms of the full width at half maximum (FWHM) (Hoffman et al., 1979; Hwang et al., 2008; Soret et al., 2007).

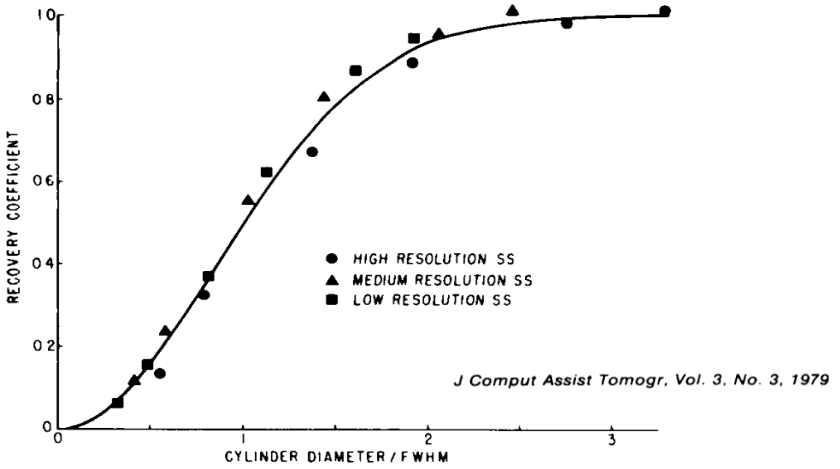

Figure 2-7 Graph demonstrating the relationship between the recovery coefficient and diameter of the cylindrical object in terms of units of FWHM of the emission scanner. There is not a linear relationship between the image-derived and true activity concentration when object size is less than 2 times of system FWHM (modified from (Hoffman et al., 1979))

The quantification of activity in the region can be either under- or overestimated, depending on the cause of spill-in or spill-out effects (Soret et al., 2007). In case of spread of activity from outside the region of interest (ROI), then the derived value inside the ROI is overestimated and this effect is called "spill-in". On the other hand, "spill-out" refers to activity spreading out of the region, consequently the activity inside the ROI is erroneously decreased (underestimated). These effects (spill-in and spill-out) can happen at the same time, for example (as illustrated in figure 2-7) spill in to structure X from background (fig C) occurred at the same as spill-out from background to structure X (fig B). Hence, the resulting image is the sum of spill-in and –out (also termed as "spill-over") and typically it is not balanced and difficult to predict. The

equilibrium is seen only if the object has similar activity concentration to background (Erlandsson et al., 2012; Mannheim et al., 2012; Soret et al., 2007).

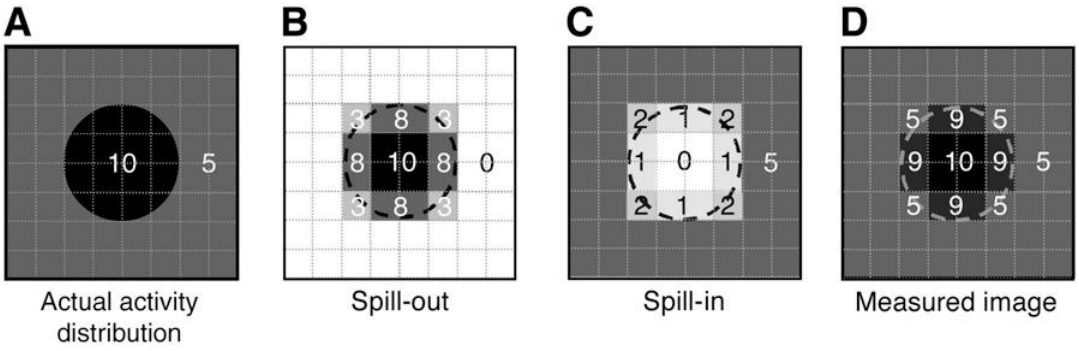

Figure 2-8. Image A is the actual activity distribution (value of 10 is lesion and 5 is background). The measured image D is the sum of spill-out B (spilling out of lesion to background) and spill-in C (spilling of background to lesion) from the imaging system (Modified from (Soret et al., 2007))

Furthermore, the PVE is related to the finite dimensions of the voxel. A larger voxel size has a high chance to contain mixed type of tissues. Thus, the displayed signal will be composed of the average of mixed confounding signals. This effect can be better observed at the boundary of the organ/tissue. It is also called “tissue fraction”. This effect can be improved by decreasing the voxel size of the imaging facility (Soret et al., 2007).

There are several existing techniques to correct partial volume errors published in the literature. These techniques have been applied with different strategies and implementation. Correction methods can be categorised in 3 main strategies (a) anatomical based correction (b) reconstruction based correction and (c) phantom based correction.

First approach, the anatomical based partial volume correction method uses the anatomical information from other available modalities (CT, MRI) to correct the emission data. Since most of modern imaging facilities are equipped with high spatial resolution anatomical imaging systems such as in dual-modality SPECT/CT, PET/CT, SPECT/MRI, PET/MRI or tri-modality SPECT-PET/MRI. Basically, this correction method utilises the anatomical information by assuming that those images are perfectly registered and segmented into physiological compartments. Then the magnitude of the spill-over between the regions can be mathematically calculated and used to correct the partial volume error in the emission images. However, a major limitation of this method is that it only uses the anatomical information at a snapshot of the functional process assuming uniform activity and equilibrium partial volume effect within each region.

For reconstruction-based correction, the reconstruction algorithms together with PSF (point spread function) modelling are performed to resolve PVE. The basic concept of this approach is an improved overall spatial resolution of the scanner, thus the partial volume error can be limited. For instance, Rapisarda E et al (2010) implemented the 3D OSMLEM (ordered subset maximum likelihood expectation maximisation) reconstruction with modelling of PSF incorporated in image space, thus the result of this technique found high contrast, lower noise and improved the quantitative accuracy (Rapisarda et al., 2010). For details of reconstruction based during- and post-reconstruction of SPECT, the review by Erlandsson et al. described many techniques from several groups, mostly applied to clinical imaging (Erlandsson et al., 2012). We have also investigated the effects of HiSPECT™ iterative OSEM reconstruction which is commercially supplied together with the nanoScan SPECT/CT camera. The details are described in the following section.

Another approach to diminish the partial volume error is multiplication of image-derived measurements by pre-defined correction factors (also called “recovery coefficient”). The correction factor can be derived and measured from a relevant physical phantom. Principally, this factor is the ratio of apparent activity from the measured image to true activity in the object. Once phantom measurements of standard shape geometries (sphere, cylinder) are experimentally performed, then the recovery coefficient over a range of physical dimensions of those objects can be plotted (also called “recovery curve”). Subsequently, the recovery coefficient can then be applied and consequently used to estimate the true activity in such objects. This concept of recovery coefficient was first introduced by Hoffman EJ et al. (1979). Based on Hoffman’s report, the effect of object size and the quantitative capability of PET were measured. This work reported the recovery curve of simple test objects, for example line, cylinder, bar and wedge in low-activity background. The work by Kessler et al. (1984) extended Hoffman’s concept by investigating the effects of neighbouring activity, and also defined the terms HRSC (hot lesion in a cold background), CSRC (cold lesion in a hot background) and CRC (contrast recovery coefficient-ratio of image to object contrast). However, this methodology has some limitations; for example, the simple geometrical shape may not always be a suitable approximation for all anatomical structures. Furthermore, the uniformity of the activity distributed in the target and background is not always a valid assumption. However, this approach is simple to achieve and can be used as a starting correction method to improve quantification accuracy.

2.6.1 Aim

The aim of this experiment was to understand the magnitude of error in quantification of small-objects/organs with nanoScan SPECT/CT. We also intended to plot the recovery curve and calculate the recovery coefficient for ^{99m}Tc, ^{123}I and ^{188}Re with the micro hollow sphere (MHS) phantom in order to correct the *in vivo* data in the following chapter. Additionally, this study also aims to investigate the effects of acquisition time and reconstruction protocol on quantification accuracy.

2.6.2 Materials and Methods

2.6.2.1 Micro Hollow Sphere Phantom

A fillable micro hollow sphere (MHS) phantom (Bartec Tech, UK) was selected to use in this study as the only commercially available option for object dimensions considered in the *in vivo* studies. The MHS phantom consists with 4 micro-spheres with the nominal volumes of 31.3, 62.5,125 and 250 µl. These micro-spheres correspond to diameters of 3.9, 4.8, 6.0 and 7.8 mm with the wall thickness approximately 1 mm (diagram in figure 2-8). The details are given below.

Table 2-3 Dimensions of each micro-sphere

Sphere Volume (µl)	Diameter (mm)	Outside Diameter (mm)	Inside Diameter (mm)
250	7.8	9.86	7.86
125	6.0	8.23	6.23
62.5	4.8	6.95	4.95
31.3	3.9	5.95	3.95

The micro-spheres can be mounted onto the cylinder phantom with approximately rat size dimensions (diameter of 51 mm and length of 114 mm). However, our *in vivo* experiments only used mice. Therefore, we adjusted this phantom to mount the spherical inserts into a mouse size cylinder (manufactured by King's College London Workshop, London, UK) with diameter of 25 mm and length of 50 mm. The picture of the phantom and set of microsphere inserts are shown in following figure.

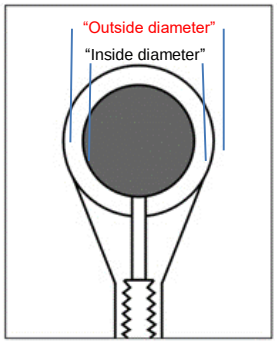

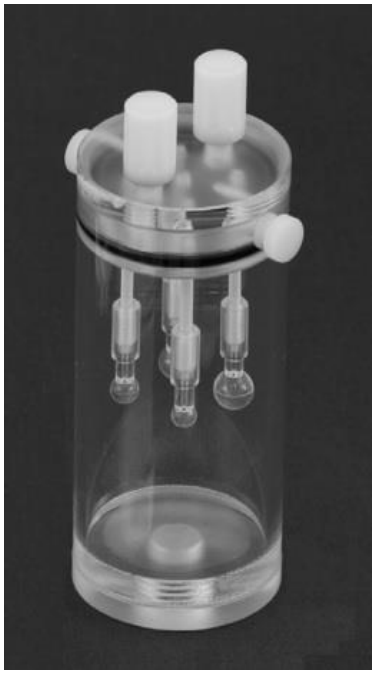

Figure 2-9 (Top Left) Set of microspheres. From left to right, the volumes are 31.3, 62.5, 125 and 250 µl (Bartec Ltd, UK) (Bottom Left) Diagram for each sphere indicates inside and outside diameter as tabulated in table 2-3 (Right) Mouse Size Micro Hollow Sphere Phantom (KCL Workshop, London, UK)

2.6.2.2 Radionuclides

In this experiment, the MHS phantom was filled with different amounts of ^{99m}Tc, ^{123}I or ^{188}Re. The amount of radioactivity in each sphere was measured using a radionuclide activity calibrator (CRC-25R Capintec, USA) prior to imaging. The details of activity are tabulated in the following table. In addition, the amount of radionuclide in the MHS phantom was similar to the activity typically injected to mice in our *in vivo* experiments (see next chapter) in order to investigate performance aspects of the scanner (effects of count rate, acquisition time and/or activity-dependent dead-time correction).

Table 2-4 Amount of radionuclide filled in MHP phantom

Radionuclide	Whole Phantom Activity (MBq)	Activity in Each Microsphere (MBq)			
		31.3 µl Sphere (3.9 mm diameter)	62.5 µl Sphere (4.8 mm diameter)	125 µl Sphere (6.0 mm diameter)	250 µl Sphere (7.8 mm diameter)
^{99m}Tc	206.70	12.60	29.30	61.00	103.80
^{123}I	21.50	1.40	2.89	5.81	11.40
^{188}Re	41.00	2.90	5.49	10.56	22.06

2.6.2.3 Experimental Protocol

To study the partial volume error on quantitative measurements, the MHS phantom was filled with radionuclide with water in the surrounding cylinder (no activity in cylinder). (The term partial volume error is used loosely here to describe object size dependency as typically the term partial volume effect refers to activity concentration).The partial volume error for different contrast ratios was not determined in this work. The MHS phantom was positioned and scanned in the middle of the axial FOV of the scanner. SPECT was acquired using the low energy multi-pinhole collimators (1 mm aperture and 9 pinholes). The acquisition was run in step-and-shoot mode for 25 projections with default acquisition time of 20 seconds per projection.

To study the effects of acquisition time, the time per projection was varied from 5, 10, 20, 50 and 100 seconds per projection. The total accumulated counts from DICOM information noted for each acquisition time and tabulated in the graph.

To study the effects of reconstruction, all data sets from the nanoScan SPECT/CT were reconstructed using HiSPECT OSEM iterative reconstruction software (supplied with the camera). This software does not correct for photon attenuation and there were only 3 optional sets of reconstruction parameters:

- Fast Reconstruction – 6 iterations with 35% Gaussian Smoothing Filter
- Standard Reconstruction - 9 iterations with 35% Gaussian Smoothing Filter
- Phantom Reconstruction - 24 iterations with 25% Gaussian Smoothing Filter

All MHS phantom projection data were reconstructed with these 3 reconstruction options, and the quantification accuracy was calculated and compared to examine its effect.

2.6.2.4 Data Analysis

All images were displayed and analysed using VivoQuant© software (VivoQuant, USA). A large 3D VOI (much larger than observed activity) was manually defined around each microsphere to obtain the total count of radiotracer in each sphere (as illustrated in following figure). This also called “integral method”. We defined a large VOI to include total object activity by setting a threshold of 10% of the maximum count to exclude background. The aim to include all activity in the organ/object was because the main purpose of this work was to study the dosimetry of radiotracer. Consequently, we were interested in the total accumulation of radiotracer in each organ in terms of percentage of injected dose (%ID) and percentage of injected dose per gram of tissue/organ (%ID/g) at a particular time-point. Likewise, we used these values to compare the ratio of tracer accumulated between different organs and also comparing uptake of one tracer with another. This would be a different approach (likely a different VOI definition) to SUV-led (Standard Uptake Value) quantification which relies on activity concentration rather than total activity, hence definition of uniform areas of uptake and avoiding cross boundary effects are critical. Also, it is important to note that the integral approach is only suitable for a low-background situation.

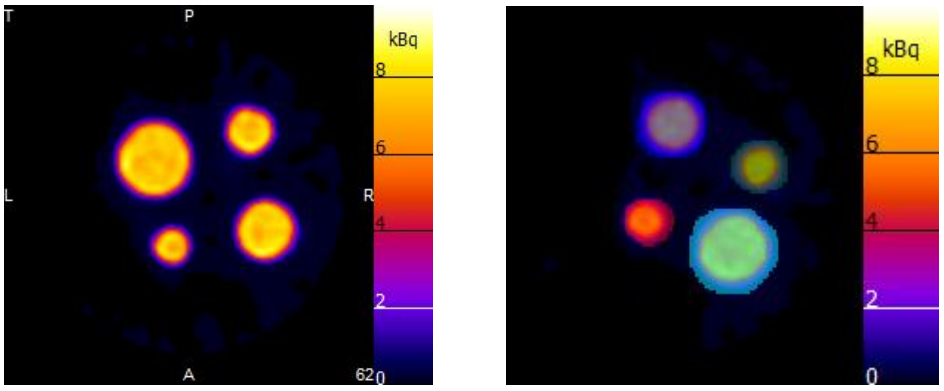

Figure 2-10 (Left) Actual activity of MHS phantom consists 4 spheres (Right) Large VOI defined (by setting a threshold of 10% of the maximum count to exclude background) in VivoQuant to obtain total activity in each sphere

In this study, the total activity in each sphere was taken from VivoQuant© software, all measured data were decay corrected to the radionuclide activity calibrator’s time (as we used the measured activity from radionuclide activity calibrator as a standard). The percentage error (%) and percentage quantification accuracy (%, as a measure for inter-comparison of different reconstruction and acquisition parameters) were calculated using the following formulae where

A_N and A_D are the activity in units of MBq measured from nanoScan SPECT/CT and radionuclide activity calibrator respectively;

$$Percentage\ Quantification\ Error\ (\%) = \frac{(A_N - A_D)}{A_D} \times 100 \quad \text{Equation 2-3}$$

$$Percentage\ Quantification\ Accuracy\ (\%) = 100 - Percentage\ Quantification\ Error\ (\%) \quad \text{Equation 2-4}$$

To calculate relative error, the VOIs were repeatedly drawn in 3 separate occasions one week apart. The mean of measurement and standard deviation (SD) were calculated and plotted (mean ± SD) in order to appreciate the inconsistency of defining the volumes of interest.

In this chapter, we also evaluated effects of the object size on quantification. As mentioned earlier, we used the integral method in our study. However, there is another approach for reporting outcome of biodistribution study. The method is based on the standardised uptake value (SUV) and it is also referred to the dose uptake ratio. In this study, we selected the SUV_{max} (also called "maximum method") which calculates the SUV based on the highest image pixel in the tumour region (Bailey and Willowson, 2013).

To access SUV_{max}, we used the maximum pixel concentration instead of SUV_{max}. The maximum pixel value was taken from VivoQuant. For SUV_{mean} analysis, VOI was automatically drawn using the AMIDE (AMIDE is a Medical Image Data Examiner) software (version 1.0.4, http://amide.sourceforge.net) with 42% of the maximum value set as a threshold (Hong et al., 2007). Then, these values (taken from VivoQuant and AMIDE in units of MBq) were divided by the pixel size which it is 0.3 × 0.3 × 0.3 mm^3 (for nanoScan SPECT/CT, aperture 1 and standard reconstruction algorithm) in order to obtain the maximum pixel concentration and SUV_{mean} in unit of MBq/mm^3. For reference value, the radiotracer concentration was calculated from the stock activity with which we filled in the MHS phantom using the radionuclide activity calibrator as a standard (MBq per volume of tracer in unit of MBq/mm^3). Then, the percentage error (%) and percentage quantification accuracy (%) were calculated as in the integral method using the above equations (Bai et al., 2013).

2.6.3 Results and Discussion

2.6.3.1 Effects of Object Size

For effects of sphere size, the results were analysed by plotting the mean of percentage quantification accuracy as a function of the microsphere diameter (figure 2-10). The percentage quantification accuracy was calculated based on the above equation from the large VOI (integral

method) and compared to the measured activity from radionuclide activity calibrator. We used the radionuclide activity calibrator as the standard as it was annually calibrated to the National Physics Laboratory (NPL) – details of this calibration are provided in appendix A. We also tested for any geometry effects in the radionuclide activity calibrator by filling the same activity concentration in each microsphere. It was found that the measured activities across the 4 microspheres agreed within 1.74 %. Therefore, we further assumed that geometric uncertainty due to different diameters and sizes of microspheres would be negligible.

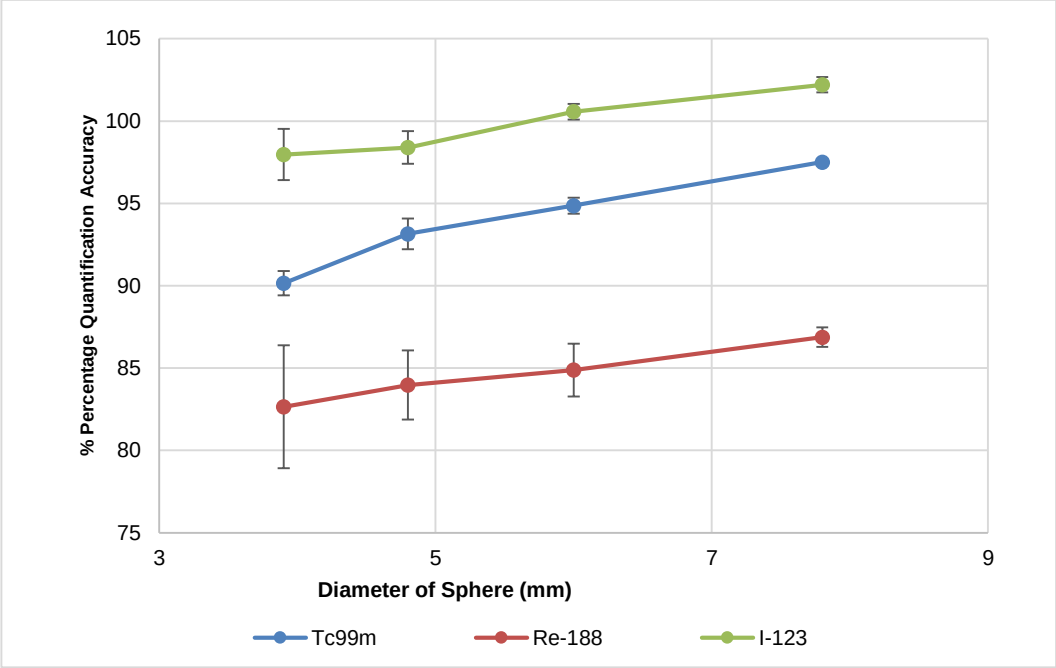

Figure 2-11 Effects of object size: the mean percentage quantification accuracy obtained by integral method (mean ± SD) plotted against diameter of microspheres in millimetres. MHS phantom acquired with 20 seconds per projection and standard reconstruction using nanoScan SPECT/CT. The activity in each sphere was based on defining VOI using the integral method.

These results show that the measurement of smaller objects suffered larger partial volume errors therefore had lower quantification accuracy when compared with larger objects. Based on the results, the quantification accuracy varied also across isotopes. The mean quantification accuracy of ^{99m}Tc and ^{123}I were over 90 %, compared with 82 - 87 % for quantified activity from^{188}Re. The larger errors of ^{188}Re quantification might be a result of the scattered photons contaminating the acquired energy window and also septal penetration from broad spectrum of Bremsstrahlung radiation (up to 2 MeV) and also the higher energy photon emissions of Re-188 (478 and 632 keV). Interestingly, we observed a high variation (SD) in the ^{188}Re small-object quantification. This might be a result from poor signal to noise ratio (low count from only 15% abundant of gamma emission).

For ^{123}I, the results of the two largest spheres (diameters of 7.8 and 6 mm) were overestimated about 2 % which is within the tolerance of the calibrator though it may also reflect differences due to photon attenuation (less attenuated for higher energy gamma of I-123) because this version of reconstruction software does not allow for attenuation correction. In addition, it is unclear whether the PSF and flood uniformity corrections of this preclinical scanner are isotope-specific rather than only based on ^{99m}Tc. Such factors might also influence the quantification of other isotopes. It is important to note that these results may include influence by other factors due to different isotopes (photon energy, attenuation, scatter, PSF model). However, it is important to understand these because in the next chapter we compare the *in vivo* quantification data across isotopes. To eliminate the influence of isotope-related factors, the quantification accuracy was normalised to the value obtained with the largest sphere under the assumption that the effect of photon attenuation (not corrected for SPECT in this implementation) will be of comparable scale across all spheres (similar depth) for the same isotope. The normalised results are plotted in figure 2-12.

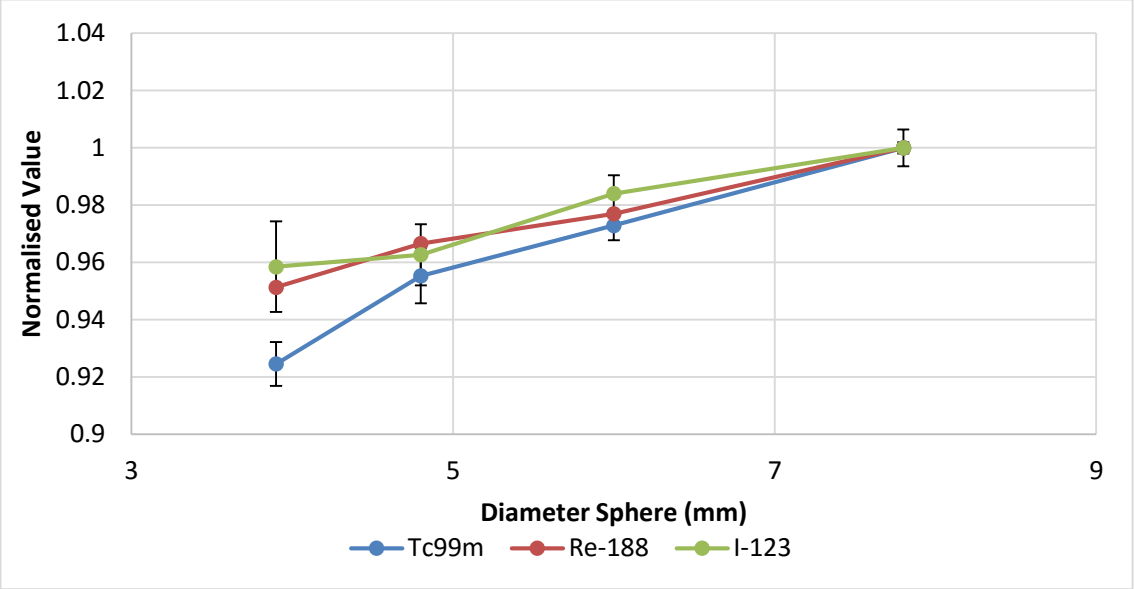

Figure 2-12 Plot of mean of the normalised value to the measured activity in the largest sphere (Mean ± SD) against diameter of object (mm)

From this graph, the errors due to size of the object can be clearly seen. The results indicate comparable PVE effects across the isotopes. These findings are in keeping with the work of McElroy DP et al. which reported that PVEs and spatial resolution were not considerably changed when changing isotopes (McElroy et al., 2002). Also, the septal penetration of the collimator was not significantly changed for those isotopes as primary photon peaks were very similar (^{99m}Tc 140 keV, ^{123}I 159 keV and ^{188}Re- 159 keV). Interestingly, the normalised results

indicated that PVE affected ^{99m}Tc, ^{123}I and ^{188}Re imaging by about 8%, 5% and 4% respectively. The quantification accuracy variation in figure 2-10 likely resulted from other factors such as system calibration factor, scatter and attenuation correction as well.

2.6.3.2 Effects of Object Size on SUV_{max} and SUV_{mean}

The effects of object size on quantification accuracy were additionally examined with $SUV_{max,}$ as this is also used in reporting preclinical imaging data, using the maximum value pixel taken from a large VOI (integral VOI method) and SUV_{mean} using a threshold of 42% of the maximum value. In both cases (SUV_{max} and SUV_{mean}), the initial VOIs were drawn with the size larger than the actual size of the sphere. As mentioned above, quantification accuracy was calculated with respect to the activity concentration obtained from the radionuclide activity calibrator.

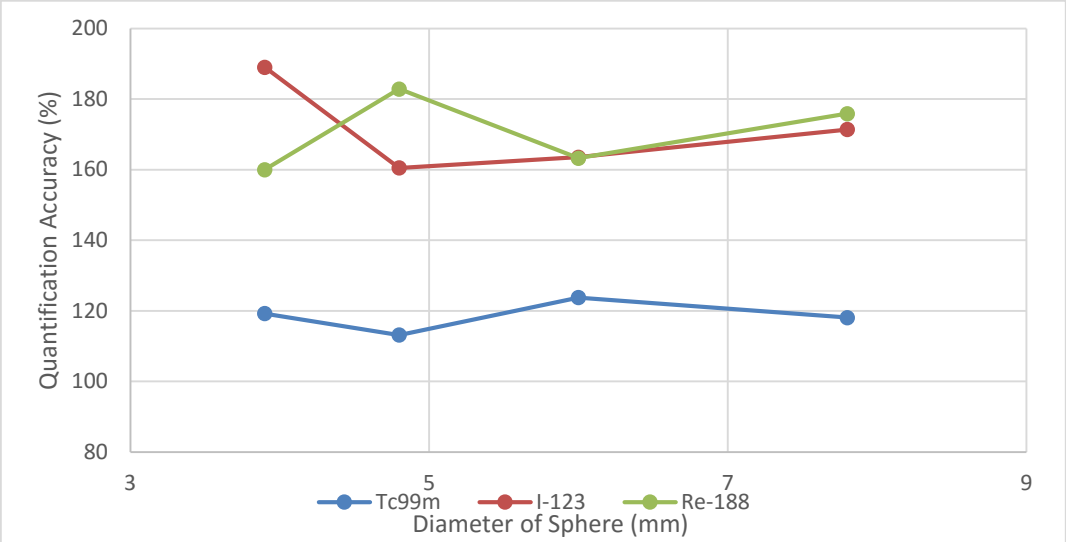

Figure 2-13 Effects of object size and SUV_{max}. The mean percentage quantification accuracy and SD (mean ± SD) plotted against diameter of microspheres in millimetres.

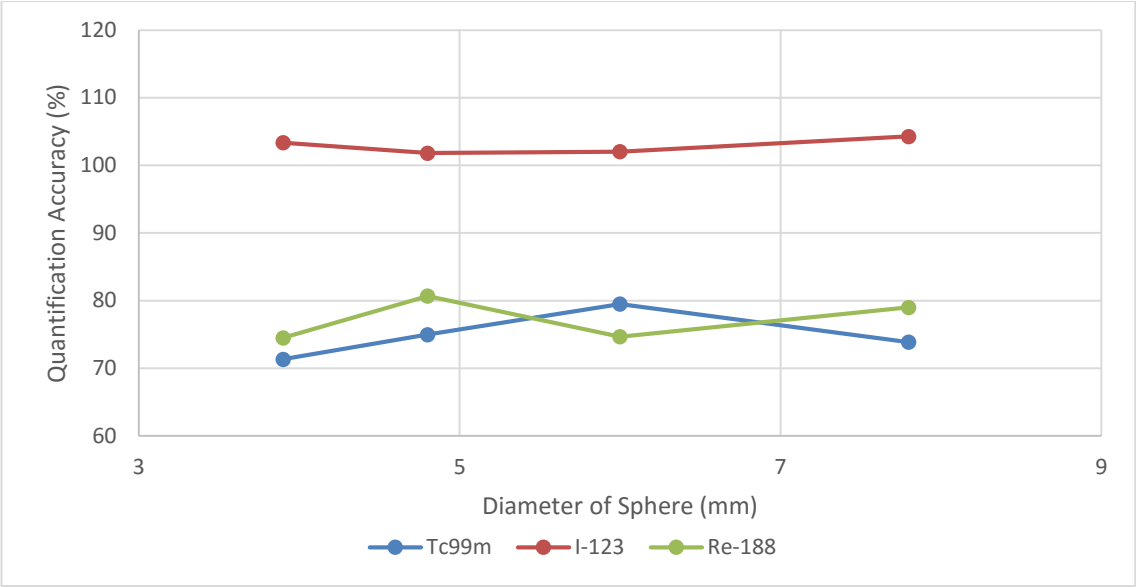

Figure 2-14 Effects of object size and SUV_{mean} (42% thesholding of the maximum value). The mean percentage quantification accuracy and SD (mean ± SD) plotted against diameter of microspheres in millimetre.

As seen from the results, quantification accuracy using SUV_{max} appears excessed overestimated, the quantified values were overestimated about factor of 1.6 to 1.9 from the standard activity measured by radionuclide activity calibrator for ^{123}I and ^{188}Re. For ^{99m}Tc, the SUV_{max} result was overestimated by a factor of about 1.2. Theoretically, it has been reported by many studies that SUV_{max} is robust and less affected by PVE compared to the integral method. However, the weaknesses of maximum SUV method is that it appears more sensitive to noise (Bai et al., 2013). Additionally, this method relies on only the maximum value from one single pixel. This may introduce errors in the preclinical scanner as there may be relatively high levels of noise often in small size structures. For ^{188}Re, the quantified result of the smallest sphere was overestimated about 100%. This might be affected by random noise due to high levels of scattered photons from secondary Bremsstrahlung radiation.

In contrary, the SUV_{mean} results were underestimated by about 20% for ^{99m}Tc and ^{188}Re when using SUV_{mean} with a 42% thresholding. This method has a tendency to underestimate the quantification results because by setting the counting threshold at 42%, some radioactivity below the threshold will be uncounted.

In the same manner as in the integral method, we eliminated other isotope-specific effects (scatter, attenuation, photon energy etc.) by normalising results from each sphere with the value obtained from largest sphere and then plotting as the function of the radius of the diameter of sphere (as shown in figure 2-14 and 2-15 for SUV_{max} and SUV_{mean} respectively)

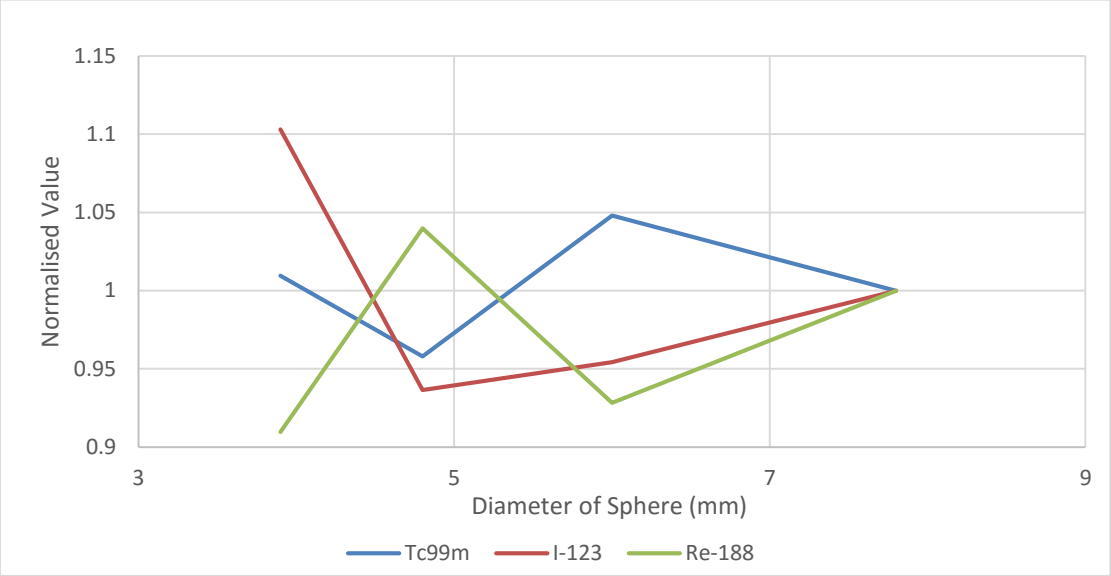

Figure 2-15 SUV_{max} using maximum intensity voxel in VOI. The quantification results were normalised to a value obtained with a largest sphere

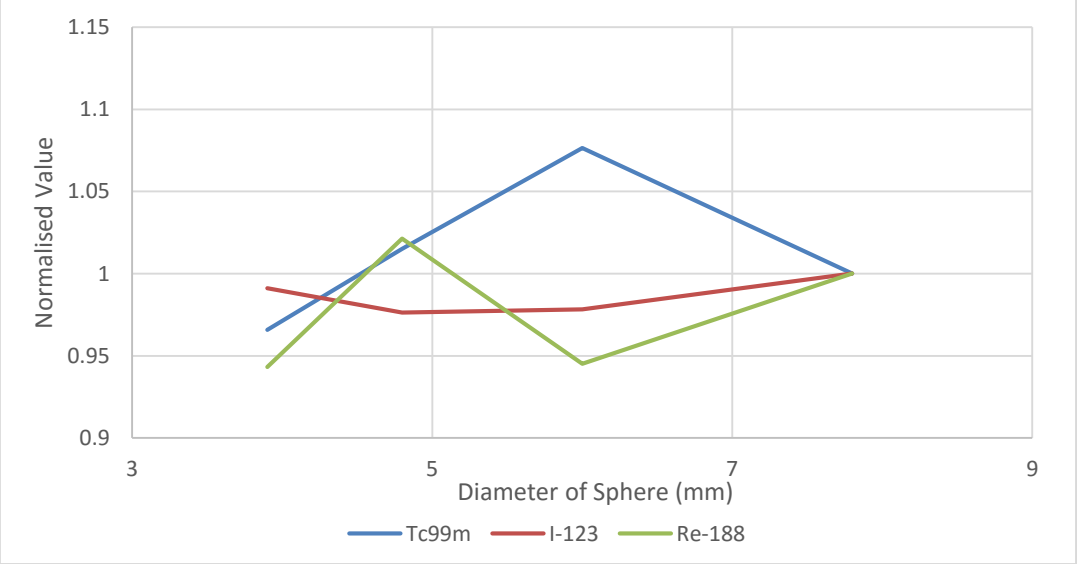

Figure 2-16 SUVmean using 42% thresholding of maximum intensity voxel in VOI. The quantification results were normalised to a value obtained with a largest sphere

As expected, we did not observe a dependency of the PVE for SUV_{max} and SUV_{mean} when decreasing the size of the sphere as we did with the integral method. The quantification accuracy from SUV_{mean} and SUV_{max} seem to be random and difficult to predict whereas the PVE with integral method can be addressed and corrected using this standard phantom.

However, the advantages of these methods are that they are quick and reproducible compared with the more manually-intensive and user-dependent integral method. So, these methods (SUV_{mean} and SUV_{max}) can eliminate the intra- and inter-analyser viability on defining VOI. Whereas, the integral method had an operator-dependent aspect when defining a VOI around the sphere.

2.6.3.3 Effects of Acquisition Time

The effects of acquisition time were studied by varying the time per projection at 5, 10, 20, 50 and 100 seconds per projection. The nanoScan SPECT/CT was set to acquire the standard SPECT mode (25 projections/detector), so these time-varying projections corresponded to total scanning times of 2.08, 4.17, 8.33, 20.83 and 41.67 minutes respectively. This study was performed with 3 isotopes (^{99m}Tc, ^{123}I and ^{188}Re). All projection data were reconstructed with the standard reconstruction parameter set (OSEM, 9 iterations, 35 % smoothing). The graphs of the mean percentage quantification accuracies with SD were plotted versus the time per projection. The total accumulated counts from the DICOM header are also noted for each time-varying condition.

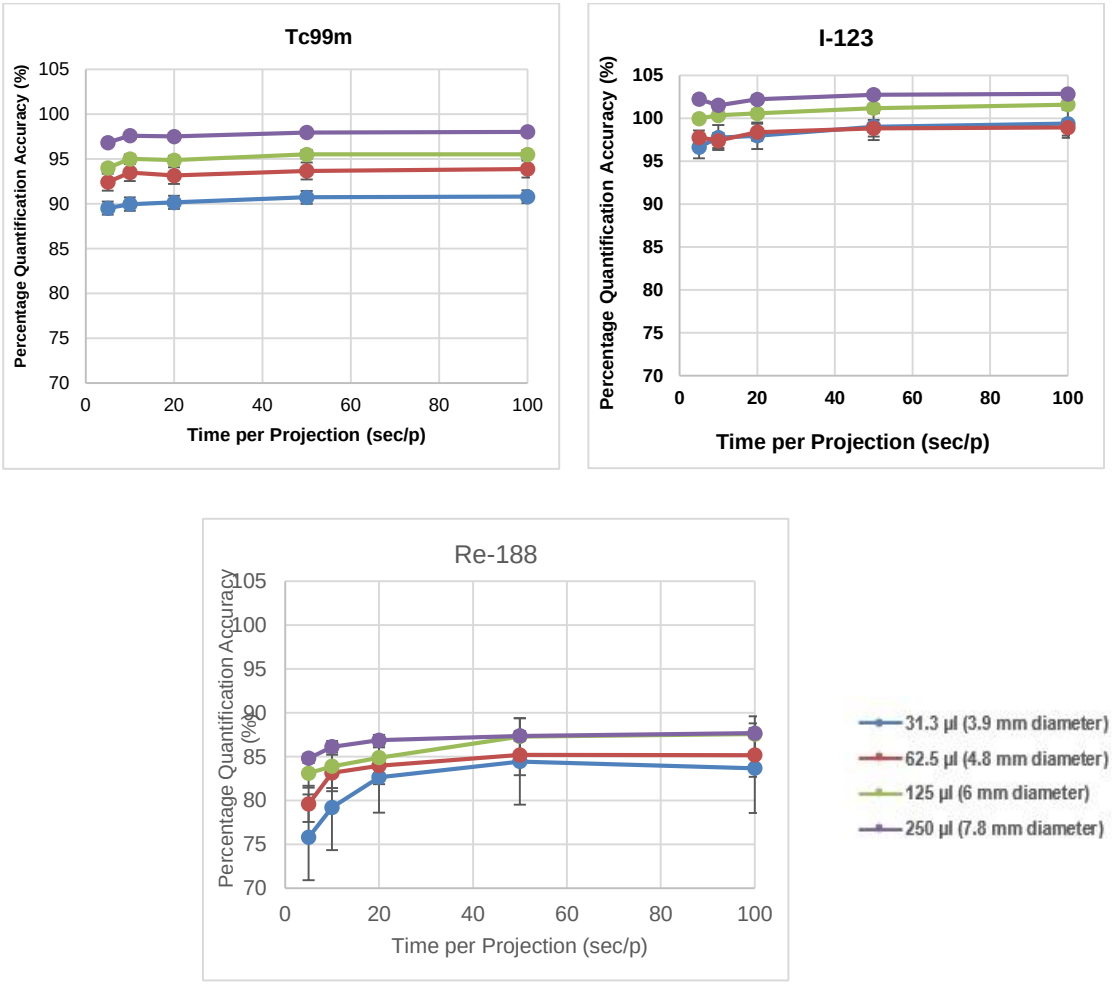

Figure 2-17 Graphs plotted of the mean percentage quantification accuracy (mean ± SD) against the time per projection (sec/p). Top Left: MHS Phantom with ^{99m}Tc; Top Right: MHS Phantom with ^{123}I; Bottom: MHS Phantom with ^{188}Re. All MHS phantom data were reconstructed with the standard algorithm.

As shown in figure 2-16, the quantification accuracy for ^{99m}Tc and ^{123}I were not significantly affected when changing the acquisition time. Even for the smallest microsphere (3.9 mm diameter), the quantification accuracy changed less than 2 % for ^{99m}Tc or ^{123}I. However, the ^{188}Re quantification data were most affected when changing the acquisition time. Especially in the smallest microsphere, the observed accuracy changed from 75.81 ± 4.90 % for 5 s/projection to 83.68 ± 5.11 % for 100 s/projection. The effect of acquisition time was much less influential for larger microspheres. Furthermore, the variation of ^{188}Re quantification accuracy was quite high when compared with ^{99m}Tc and ^{123}I. Therefore, these errors might be related to limited photon counts, as the total accumulated counts of^{99m}Tc and ^{123}I were much higher when compared with ^{188}Re. The total accumulated counts for ^{188}Re were only 0.22 million counts compared with 2.61 and 1.29 million counts for ^{99m}Tc and ^{123}I when acquired for 5 seconds per projection. Low counts can lead to non-Poisson statistics which may introduce bias to the quantification as part of the OSEM reconstruction which is based on the assumption of Poisson statistics.

These results agreed with the study by Finucane CM et al. Their work investigated the accuracy of nanoScan SPECT/CT in quantifying low-count samples. Finucane et al. stated that low counts led to higher levels of deviation and a minimum of 10,000 counts per frame is required for deviation of 10% from true activity values (Finucane et al., 2011). These findings were very important as the dynamic acquisitions of time-activity series for dosimetry are related to a wide dynamic count range. Understanding the quantification errors for different time settings and count levels was necessary for this study. Consequently, this problem is more complicated for *in vivo* (rather than phantom) data as these involve wide dynamic range as tracer distribution changes between organs. However, this study can be applied as a guide protocol for *in vivo* studies in terms of influence of scanning times and injected activity.

2.6.3.4 Effects of Reconstruction Protocol

All SPECT projections were reconstructed using HiSPECT© software supplied with the camera as the only available option for multi-pinhole collimators. This iterative reconstruction software uses the accelerated version of the maximum-likelihood expectation maximisation (MLEM) method, the ordered subsets expectation maximisation (OSEM) for reconstruction of the raw projection data (Hudson and Larkin, 1994). There are only 3 reconstructing parameters available as stated earlier: fast (6 iterations with 35% Gaussian smoothing), standard (9 iterations with 35% Gaussian smoothing) and phantom (24 iterations with 25% Gaussian smoothing).

Plots of mean percentage accuracy against the number of iterations for each microsphere from ^{99m}Tc, ^{123}I and ^{188}Re are illustrated in figures 2-17, 2-18 and 2-19 respectively.

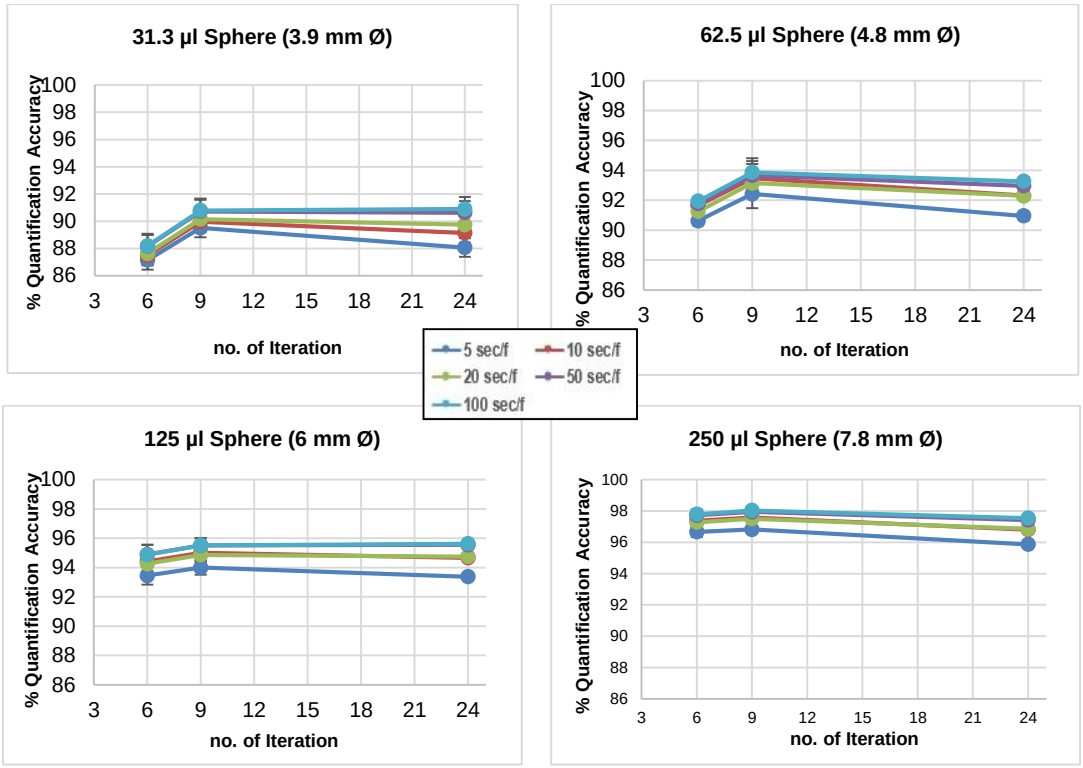

Figure 2-18 Mean of percentage accuracy (mean ± SD) plotted with the number of iterations for ^{99m}Tc, each solid line colour representing different time per projection (5, 10, 20, 50 and 100 s/p)

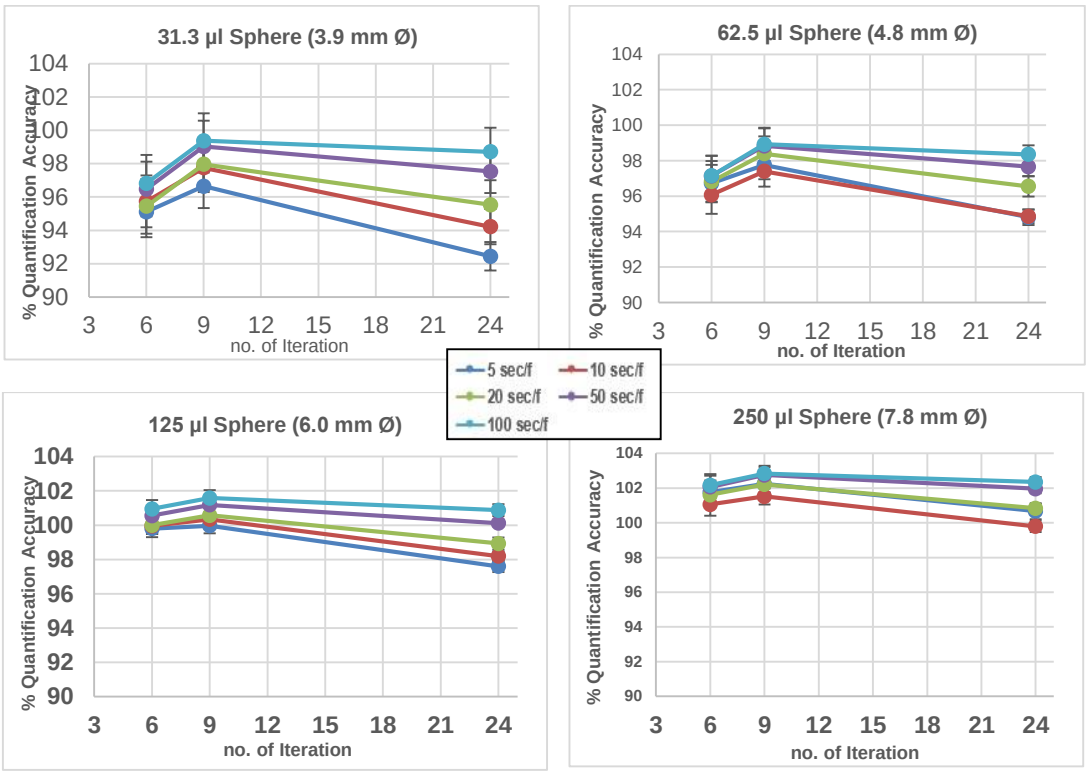

Figure 2-19 Mean of percentage accuracy (mean ± SD) plotted against the number of iterations for ^{123}I, each solid line colour representing a different time per projection (5, 10, 20, 50 and 100 s/p)

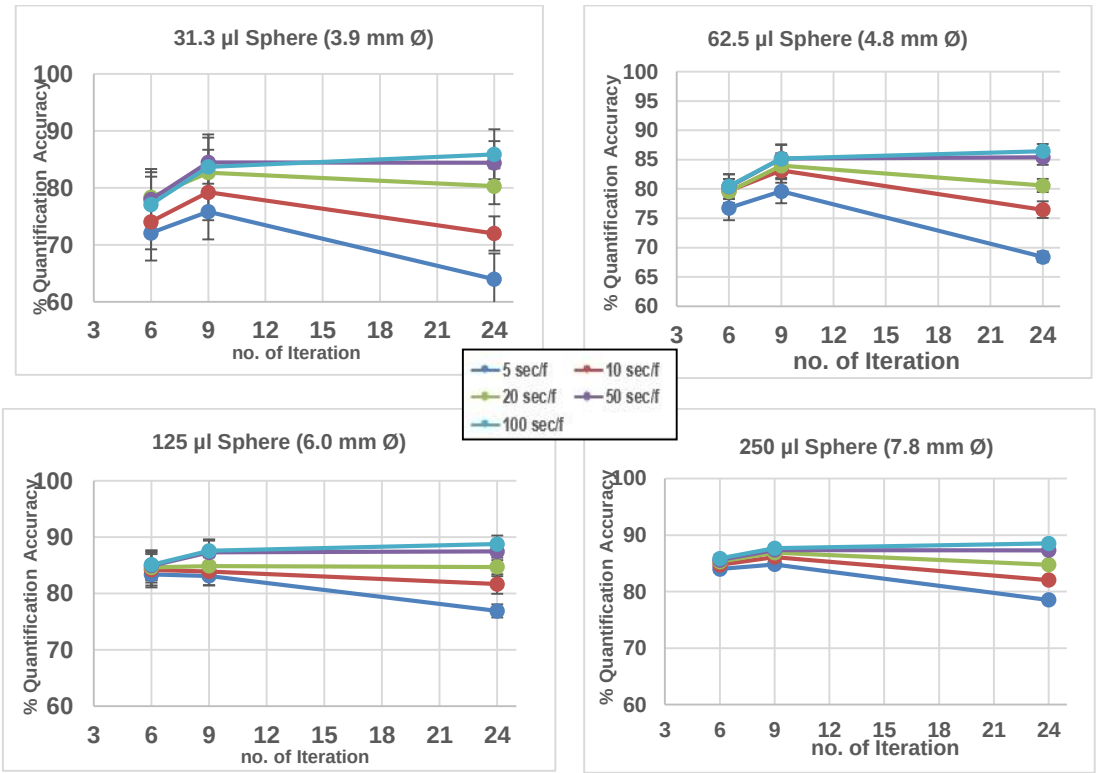

Figure 2-20 Mean of percentage accuracy (mean ± SD) plotted against the number of iterations for ^{188}Re, each solid line colour represented different times per projection (5, 10, 20, 50 and 100 s/p)

The overall results indicate that the quantification accuracies improved when increasing the iteration number from 6 to 9 iterations, probably reflecting a good convergence of the algorithm. However, when increased to 24 iterations, accuracies depended on the scanning time as the quantification was more accurate when the acquisition time per frame was longer (i.e. increased number of counts). As previously mentioned, the reconstruction of nanoScan SPECT/CT is limited to the HISPECT system with only 3 parameters available (fast, standard and phantom). Therefore, a choice from the limited standard reconstruction parameters was made asa compromise between noise and spatial resolution. Furthermore at high number of iterations, the quantification in small objects was affected more by the reconstruction parameters and scanning times, presumably reflecting the influence of both PVE and number of counts in the projections. Interestingly, the variation (SD) observed was larger at higher iterations. This increase of noise levels with increasing iterations is a well-established effect in MLEM/OSEM reconstruction. Therefore, at this particular reconstruction setting, the data were increasingly biased for an image with a lower number of counts. However, there are only 3 option of reconstruction parameters available for this system (fast, standard and phantom). This is important to note as a limitation in this study. Other platforms for reconstructing multi-pinhole projection data may need to be developed in future for further investigation, for example as part of a future extension of the open source STIR software (Fuster et al., 2013) which is currently limited to parallel hole collimation.

2.7 Accuracy of nanoScan PET/CT in Quantification of Small Objects: A Comparison with nanoScan SPECT/CT

In our study, we aim to estimate the dosimetry profile for a forthcoming clinical PET radiotracer, ^{18}F-tetrafluoroborate [BF_4^-]. The initial estimation is to be based on preclinical data and we also intend to compare the effective dose with other well-established NIS imaging radiotracers. Hence, we need to compare the quantitative data from different modalities and isotopes; nanoScan PET/CT (^{18}F-BF_4) and nanoScan SPECT/CT (^{99m}Tc-pertechnetate, ^{123}I-iodide and ^{188}Re-perrhenate). Additionally, our main organ of interest is the thyroid which is particularly small in size and subject to suffer from PVE. It is therefore crucial to understand the magnitude of error and quantification accuracy across these two imaging modalities.

2.7.1 Aim

This experiment aims to evaluate the quantification accuracy for small objects of the nanoScan PET/CT and compare it with the nanoSPECT/CT using the standard MHS phantom.

2.7.2 Materials and Methods

In this experiment, we used the MHS phantom as described in previous sections. The phantom was filled with ^{18}F-NaF, the total activity of phantom was kept below 10 MBq due to limitations of the dead-time correction of the nanoScan PET/CT. The phantom was placed at the centre of the FOV and PET data were acquired for one bed-position in list mode, within a 400-600 keV energy window, a coincidence ratio 1:3 for 30 min followed by CT for attenuation correction. The projection data were reconstructed with 3D Teratomo (supplied with the PET camera) with 0.4 × 0.4 × 0.4 mm^3 voxel size and 8 iterations. Decay, dead-time, attenuation and scatter corrections were applied as part of the reconstruction.

All images were displayed and analysed using VivoQuant following the processing steps described in previous sections in which large VOIs were drawn in order to obtain the activity with the integral and maximum method. The percentage error (%) and percentage quantification accuracy (%) were calculated by equation 2-3 and 2-4 using the radionuclide activity calibrator as the standard. VOIs were repetitively defined for 3 separate occasions to obtain the intra-analyser variability. The SUV_{mean} technique was not employed for PET data due to a technical problem with incomplete header information when transferring DICOM PET data to the AMIDE© software.

2.7.3 Results and Discussion

Based on the graph (as shown in figure 2-20), the quantification results were overestimated for defining VOI with both integral and maximum methods. The quantified result with integral method overestimated 5 - 15 % across all sizes of sphere compared to the activity measured by radionuclide activity calibrator. While, the maximum method generated an error of about 20 – 40%. For the integral method, the smallest compartment (3.90 mm diameter sphere) suffered the largest PVE and the quantification accuracy improved and reached plateau at 6 mm. sphere. The error from the maximum method was difficult to address as this method is very sensitive to noise as mentioned earlier in previous part.

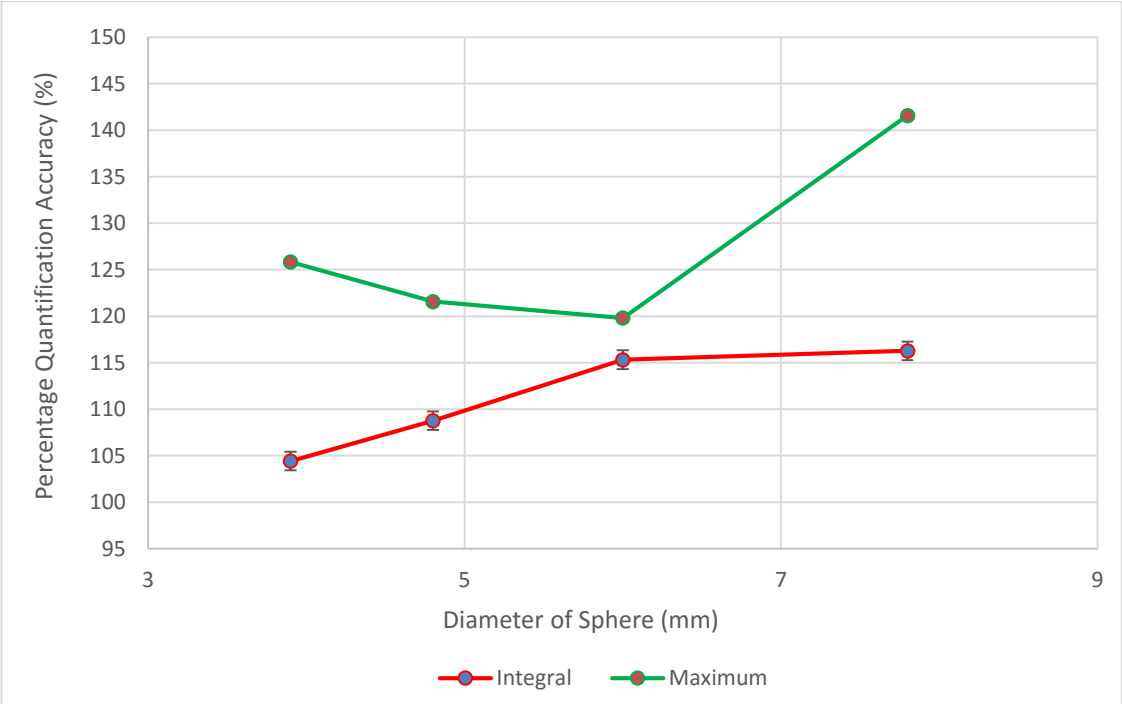

Figure 2-21 Quantification Accuracy of 18F nanoPET/CT with MHS phantom, data showed with 2 different approaches; integral (mean ± 2SD) and maximum method

To compare with SPECT, we used the SPECT data obtained with 20 s/frame with standard reconstruction to compare with PET quantification (as explained earlier). The figures 2-21 below compare the quantification accuracy from the two systems with integral and maximum method.

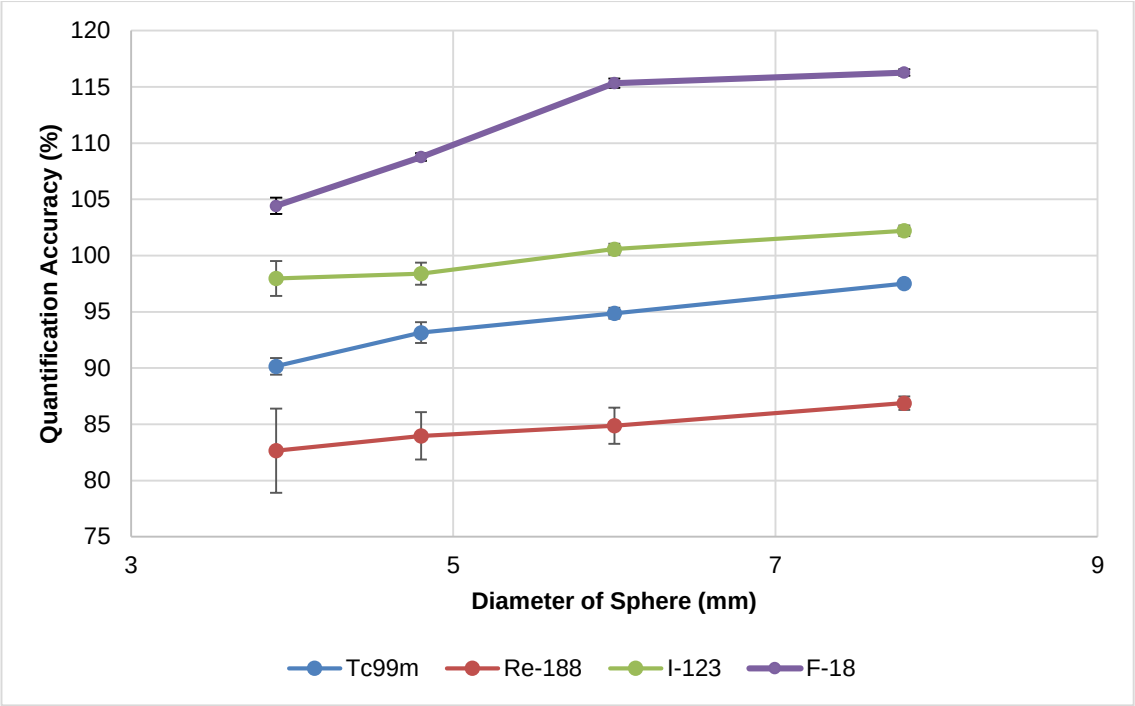

Figure 2-22 Comparison of the quantification accuracy (Integral method) from nanoScan SPECT/CT and nanoScan PET/CT with standard MHS phantom (mean ± SD)

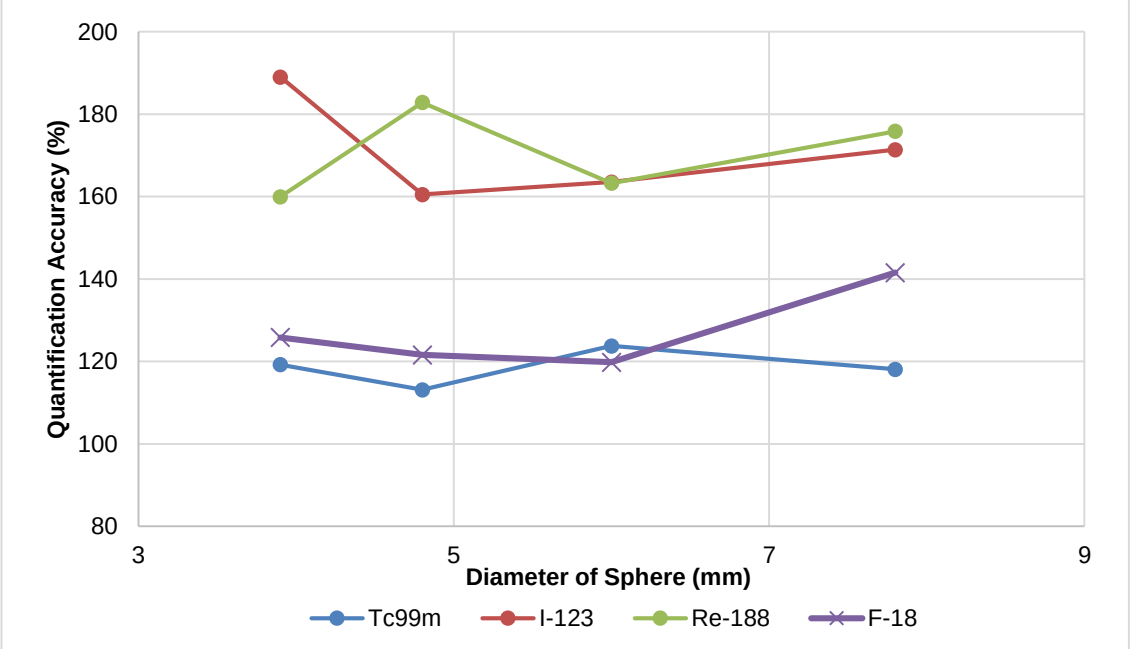

Figure 2-23 Comparison of the quantification accuracy (Maximum method) from nanoScan SPECT/CT and nanoScan PET/CT with standard MHS phantom (mean ± SD)

Results with the integral method demonstrated that PET quantification with ^{18}F was less accurate when compared with SPECT. The mean error from PET quantification of the largest sphere (where we assume less PVE influence) was about +16 % for ^{18}F, whereas results from SPECT were +2, -2.5 and -12 % for ^{123}I, ^{99m}Tc and ^{188}Re respectively. As expected, for smaller objects the quantified activities decreased; however we can use the recovery coefficient to compensate and correct for this phenomenon. On the contrary, the results from the maximum method were difficult to predict. Furthermore, the SUV_{max} method provided a higher error when compared with the integral method.

The nanoScan SPECT/CT has a better spatial resolution than nanoScan PET/CT: according to the scanner specifications, 0.7 mm FWHM at CFOV ^{99m}Tc for nanoScan SPECT/CT vs. 1 mm FMHM at CFOV ^{18}F for nanoScan PET/CT (Szanda et al., 2011). Hence, the quantification of small objects from nanoScan PET/CT might be subject to stronger PVE than nanoScan SPECT/CT. However, the results were seen the other way around. This might mainly result from the correction processes of attenuation, scatter and dead-time, which are employed only in nanoScan PET/CT (as the Teratomo reconstruction software in nanoScan PET/CT is also a more advanced and updated software suite compared to HiSPECT in nanoScan SPECT/CT) (Szanda et al., 2011).

2.8 Conclusion

It has been demonstrated in this chapter that the nanoScan SPECT/CT can be used for quantitative imaging. For general system performance, we have compared the tomographic uniformities with all available reconstruction options. The tomographic uniformity for ^{99m}Tc (22.00 ± 1.03 %) was found to be similar to that for ^{123}I (19.07 ± 1.66) whereas uniformity for ^{188}Re was found to be 29.04 ± 5.38 % for standard reconstruction. The non-uniform result of ^{188}Re (compared with ^{99m}Tc and ^{123}I) can be explained by the high amount of backscattered Bremsrahlung and high-energy photons penetrating collimator septa (creating elevated background in the image).

The linearity of this preclinical SPECT with ^{99m}Tc was found to be within 10 % over the range of activity that we inject into animals in the lab (up to 210 MBq). Deviation was observed at low activity (less than 1 MBq) which might be resulted from a low count. However, discrepancies were still within 10% of radionuclide activity calibrator measurements.

The quantification accuracy is strongly influenced by attenuation and scatter corrections. Unfortunately, our system does not employ these corrections in this current version, however, they have been included and addressed in this study in terms of the quantification accuracy. The MHS phantom was used in this study with 3 SPECT radioisotopes; ^{99m}Tc, ^{123}I and ^{188}Re. We have investigated the effects of object size, acquisition time and reconstruction parameters (number of iterations) on the quantitative accuracy of nanoScan SPECT/CT using the mouse size micro-hollow spheres phantom.

For the effects of object size, we determined the quantification accuracy with 3 different methods; (a) large VOI (by setting a threshold of 10% of the maximum count to exclude background) with integral activity (b) large VOI with SUV_{max} and (c) automatic VOI with 42% thresholding SUV_{mean}. Different methods provided significantly different results for quantification accuracy. However, large VOI with integral activity is the most suitable method for our *in vivo* experiment aiming at relative organ uptake and is aided by the fact that the organs/tissues of interest for the particular tracers are well delineated from each other. Also, it is important to note that the integral approach is only suitable for a low-background situation which is appropriate for this phantom and also for our *in vivo* NIS radiotracer.

Furthermore, the PVE from this method can be addressed and corrected for using phantom-derived correction factors. For the effects of sphere size with the integral method, the PVE and perhaps photon attenuation and photon scatter had a strong influence on the accuracy of quantification (although the last two were not directly assessed but assume that these are the cause of the observed variation). In the smallest compartment (3.9 mm diameter sphere) which is still larger than mouse thyroid, the quantification accuracy with the integral method was found to underestimate uptake by about 18%, 10% and 3% for ^{188}Re, ^{99m}Tc and ^{123}I respectively. Interestingly, the normalised values indicated that changing isotopes does not affect the PVE.

Changing the acquisition time did not alter the quantification accuracy for ^{99m}Tc and ^{123}I. However, ^{188}Re was more affected when acquiring shorter time frames (fewer counts) and the effect was stronger in smaller spheres. These errors are likely to be related to the influence of number of counts per projection on the performance of the EM algorithm.

The effect of reconstruction iterations was also examined in this work. The quantification accuracy improved when changing from 6 to 9 iterations. For changing from 9 to 24 iterations, the accuracies depended on acquisition time (count levels). Also, the quantification accuracy in the smallest microsphere was affected more when changing the reconstructing parameters and acquisition times.

Additionally, we did not perform the quantification accuracy for ^{131}I because our department not own high-energy multi-pinhole collimator and this collimator was not available at the time of phantom study. As we also investigated the *in vivo* kinetic of ^{131}I in next chapter, this is also important issue and need further investigate.

In the last part of this chapter, quantification results from nanoScan SPECT/CT were also compared with the^{18}F data from nanoScan PET/CT. For the integral method, PET quantification with ^{18}F was less accurate when compared with SPECT. The quantification result of nanoScan PET/CT was overestimated about 16 % for ^{18}F, while most of quantification results from nanoScan SPECT/CT were underestimated at -2.5 and -12 % for ^{99m}Tc and ^{188}Re, except for ^{123}I which was overestimated at about 2 %.

Chapter 3 Comparative Spatio-Temporal Quantification of Sodium Iodide Symporter (NIS) Radiotracers in Healthy and Tumour-Bearing Animals

3.1 Introduction

Sodium iodide symporter (NIS) is a membrane glycoprotein responsible for iodide transport which is important for thyroid hormone production. NIS is located at the baso-lateral plasma membrane of the thyroid follicular cells. For the transportation of iodine, NIS pumps 2 sodium ions (Na^+) together with 1 iodide (I^-) using the transmembrane sodium gradient generated by the oubaine-sensitive Na+/K+ ATPase pump as the energy source for this transfer (Ahn, 2012). The activity of NIS at thyroid primarily is controlled by thyroid stimulating hormone (TSH) from the pituitary gland through a dedicated negative feedback loop from the hypothalamus. Intense NIS expression is also normally found in other cell compartments in extra-thyroidal tissues/organs such as gastric lumen/mucosa in stomach, salivary acini/duct lumens in salivary gland, lactating breast and small intestine. However, these expression of NIS in extra-thyroidal tissue are not controlled by TSH (Dohán and Carrasco, 2003b; Portulano et al., 2013).

In research NIS has been important for many years as a molecular target for tracking the distribution, migration, metastasis and survival of cells *in vivo*. Furthermore, NIS has been investigated and used as a reporter gene in several systems such as respiratory, haematopoietic, and neurological systems and for cancer metastasis tracking as well as monitoring treatment response in many preclinical studies (Fruhwirth et al., 2014; Khalil et al., 2011).

In clinical applications several NIS radiotracers are proved as diagnostic radiopharmaceuticals for thyroid diseases in nuclear medicine. For instance, ^{99m}Tc-pertechnetate and ^{123}I-iodide are well known SPECT imaging tracers while PET radiotracers for studying NIS have so far been limited to^{124}I-iodide. However, when compared with ^{18}F, ^{124}I-iodide has several disadvantages such as poor image quality due to low positron yield and higher effective dose due to long physical half-life. ^{18}F-tetrafluoroborate is a forthcoming PET diagnostic agent for thyroid disease and NIS-expressing organs (Jauregui-Osoro et al., 2010b).

In therapeutic applications transport of iodide by NIS, combined with the metabolic trapping of radioiodine into thyroid hormone, is the fundamental molecular basis for the use of radioactive iodine in treatment of thyroid diseases. ^{131}I-iodide has been used for thyroid therapy

since the 1940s and continues to be a stronghold therapeutic agent (Verburg et al., 2011). Additionally, targeted radioiodine therapy has been researched for the treatment of extra thyroidal tumours post-transcriptional NIS gene transfer (Klutz et al., 2009). However, high dose ^{131}I treatment has a number of limitations and disadvantages. In particular, the abundant high-energy gamma rays emitted at the same time as the beta emissions cause a large fraction of the total radiation dose. Therefore, many groups of researchers have been interested in using alternative radiotracers for NIS expressing tumours.

^{186}Re- and ^{188}Re-perrhenate are also substrates of NIS (but not of subsequent metabolic steps) which have been examined for therapeutic purposes of NIS-bearing tumours in preclinical research such as thyroid, breast or prostate cancer (Dadachova et al., 2005; Ferro-Flores and Arteaga de Murphy, 2008a). Nevertheless, further *in vivo* information is still required for clinical translation.

In addition, Astatine-211 (^{211}At) is a new therapeutic candidate for cancer which emits high energy alpha particles. The physical properties of ^{211}At are promising, however it is currently available at only a few centres worldwide.

The physical characteristics of available NIS radiotracers and production tabulate in following table.

Table 3-1 NIS radiopharmaceuticals with the physical characteristics

Radionuclides	Half-life	Main Emissions	Most Abundant Energy	Production
^{18}F (tetrafluoroborate)	109.8 min	Positron, Gamma	633.5 keV/511 keV	Cyclotron
^{99m}Tc (pertechnetate)	6.0 h	Gamma	140 keV	Mo-99/Tc-99m Generator
^{123}I (sodium iodide)	13.2 h	Gamma	159 keV	Cyclotron
^{124}I (sodium iodide)	4.2 d	Positron, Gamma	511 keV/819 keV	Cyclotron
^{131}I (sodium iodide)	8.0 d	Beta, Gamma	606 keV/364 keV	Nuclear Reactor
^{186}Re (perrhenate)	90.6 h	Beta, Gamma	1070 keV/59 keV	Nuclear Reactor, Cyclotron
^{188}Re (perrhenate)	16.9 h	Beta, Gamma	2120 keV/155 keV	W-188/Re-188 Generator
^{211}At (free astatine or astatide)	7.2 h	Alpha, X-ray	7500 keV/77-92 keV	Cyclotron

Non-invasive *in vivo* pre-clinical imaging is a useful tool to study the distribution and kinetics of radiotracers in biomedical research. While single time-point imaging in planar or tomographic (SPECT or PET) mode has been used to obtain static information (or “snapshot”) about tracer distribution at particular time after injection, dynamic *in vivo* imaging is more advantageous for tracer development as it enables accessing information about the organ kinetics, the metabolic pathways and the physiological processes while the animal is alive (albeit under general anaesthetic). For dosimetric studies, time-activity curves (TACs) derived from dynamic data are key to determine the cumulated activity, effective half-life, tracer residence time and dosimetry for therapeutic nuclear medicine. In diagnostic nuclear medicine applications, dynamic data can be used to find the optimal time to image the organ of interest (Franc et al., 2008; Johnström et al., 2012; Matthews et al.).

A key advantage of dynamic *in vivo* imaging is that it allows the acquisition of image data over a series of time-points to complete the dynamic sequence using a single animal. Quantitative imaging using a single animal reduces the variability when compared with *ex vivo* bio-distribution, which has several disadvantages. The recent work (2012) by Brandt et al. has used preclinical

imaging to image the thyroid and salivary glands in mouse, investigating variable parameters that affect the ^{99m}Tc-pertechnetate and ^{123}I-iodide image. The authors concluded that the potential advantages of whole-animal imaging can reduce inter-experimental variability of thyroid and salivary glands uptake in contrast to using a set of animals sacrificed at different time-points to derive tracer kinetics (Michael P. Brandt, 2012). *Ex vivo* bio-distribution requires sacrifice of many animals for each time-point. Also, the *ex vivo* measurement combines the radiation measurements from difference modalities (dose calibrator and gamma counter) which differ in measurement unit and counting efficiency. Also the self-absorption, geometry and dead-time difference between organs are also sources of errors in the gamma counter. Furthermore, the human errors such as dissection skill (excess/loss of tissue and body fluid e.g. blood during dissection), weighing error, and time synchronisations are also the main source of errors for ex vivo bio-distribution (Franc et al., 2008).

3.2 Aims

In this chapter, we aim to compare the *in vivo* behaviour of NIS radiotracers in normal healthy Scid/Beige mouse with different radiotracers available; ^{99m}Tc-pertechnetate ($^{99m}TcO_4^-$), ^{123}I-iodide (^{123}I-NaI), ^{131}I-iodide (^{131}I-NaI), ^{188}Re-perrhenate ($^{188}ReO_4^-$) and ^{18}F-tetrafluoroborate ($^{18}F\text{-}BF_4$). We also set out to examine the *in vivo* kinetics of NIS radiotracers in mice bearing NIS-expressing tumours in the murine xenograft adenocarcinoma model (MTLn3EΔ34CXCR4-hNIS). In tumour-xenografted mice, we evaluated the kinetics with ^{99m}Tc-pertechnetate, ^{123}I-NaI and ^{188}Re-perrhenate. So, iodide is expected to be different to others because it is metabolised and trapped in thyroid while the pertechnetate, perrhenate and tetrafluoroborate are not.

The distribution of the radiotracers in NIS-expressing organs/tissues and temporal change over time (Spatio-Temporal quantification) were quantitatively investigated in this chapter. In small animal imaging, the spatial resolution is an important concern due to the small size of organs/ tissues. It is therefore necessary to use appropriate imaging devices with high spatial and temporal resolution and high sensitivity. The dedicated small-animal nanoScan SPECT/CT (Mediso, Hungary) and nanoScan PET/CT (Mediso, Hungary) were used as the imaging systems for this study

3.3 Materials and Methods

3.3.1 Animal Experiments

All animal experiments were performed according to the licence requirements under the United Kingdom (UK) Home Office and the Animal (Scientific Procedure) Act 1986 (ASPA). The study protocol was approved by the local ethics committee. Age- and sex-matched female healthy Scid/Beige mice were purchased from Charles River Breeding Laboratory (London, UK). Animals with age between 4-8 weeks were used in this experiment. All mice were kept in standard BSU (Biological Service Unit) conditions with autoclaved water bottle and normal food at King's College London BSU unit, St Thomas Hospital (London, UK).

3.3.2 Healthy Model and Tumour Xenograft Model

Animals were randomly divided into 2 main groups; healthy and tumour xenograft. Healthy female mice (n=3 for each radiotracer) were used to serve as the control in this study. The mammary adenocarcinoma cell line (MTLn3E) was chosen to use in this study. MTLn3E was engineered to uniformly express human sodium iodide symporter (hNIS). This cell line was also engineered by overexpressing truncated CXCR4 to become highly metastatic; the cell line is known as MTLn3EΔ34CXCR4-hNIS (Fruhwirth et al., 2014). Mice were housed for one week before tumour initiation. 5×10^5 cells in sterile 0.9% saline were subcutaneously initiated at the lower left side flank of the mouse mammary fat pad. Tumour growth and mice health were closely monitored and recorded. Xenograft mice were imaged when the tumour could be palpable (usually between days 9 and 19 after the tumour initiation), with tumour diameter not exceeding 12 mm according to the Home Office project license and local ethic rules. The details for engineering of stable cell lines, cell culture, radionuclide *in vitro* uptake and specific information of this animal model were previously described and published by colleagues (Dr. G Fruhwirth and Dr. S Diocou) (Fruhwirth et al., 2014).

3.3.3 NIS Radiotracers

Clinical standard radiopharmaceuticals ^{99m}Tc-pertechnetate, ^{123}I-NaI and ^{131}I-NaI were kindly supplied by the Radiopharmaceutical Unit, Guy's Hospital (Guy's & St Thomas' Hospitals NHS Foundation Trust, London, UK). ^{99m}Tc-pertechnetate was eluted as per clinical routine at Guy's Hospital, ^{123}I-NaI was purchased from Mallinckrodt Pharmaceutical (Petten, Netherlands) and ^{131}I-NaI was purchased from GE Healthcare (Amersham, Buckinghamshire, UK). ^{188}Re-perrhenate was eluted from our on-site W-188/Re-188 generator (ITG-Isotope Technologies,

Germany) using sterile normal saline for injection (Baxter Healthcare, Newbury, UK). The radiochemical purity of ^{188}Re-perrhenate was tested by radio-TLC (Thin Layer Chromatography) using saline as a solvent and ITLC-SG (Agilent Tech, Berkshire, UK) as a stationary phase.

^{18}F-BF_4 was produced at the cyclotron in the Clinical PET Centre, St Thomas' Hospital (London, UK). The method of synthesis was published by colleagues with the specific activity of 10 GBq/mg (Jauregui-Osoro et al., 2010b). GMP (Good Manufacturing Practice) standard analysis and quality controls were performed before the product was released for use.

The radiotracers were intravenously injected at required levels of activity for each mouse with a volume of approximately 150 µl (Table 3-2). All injections were performed under anaesthesia with 2-3% isoflurane in O_2 in an induction box.

Table 3-2 Activity of radiotracer injected to the animal (mean ± SD)

Animal Model - Radiotracer	**Injected Activity (MBq)**
Healthy Mice (n=3 for each radiotracers)	
^{99m}Tc-Pertechnetate	199.53 ± 2.95
^{188}Re- Perrhenate	36.99 ± 3.47
^{131}I-Sodium iodide	37.34 ± 2.96
^{123}I- Sodium iodide	15.15 ± 0.29
^{18}F- Tetrafluoroborate	5.11 ± 0.14
Tumour Xenograft Mice (n=3 for each radiotracers)	
^{99m}Tc-Pertechnetate	20.27 ± 0.80
^{188}Re- Perrhenate	36.77 ± 0.40
^{123}I- Sodium iodide	15.00 ± 0.25
^{18}F- Tetrafluoroborate	4.98 ± 0.21

3.3.4 Imaging Protocols

3.3.4.1 Imaging Protocols for Healthy Group

After injection under anaesthesia, animals were immediately transferred to the scanner bed with anaesthesia maintained using 1.5 - 2% isoflurane gas in O_2 air. In all scans, anaesthetised animals were monitored for breathing signal and bed warming was operated to preserve body temperature. Whole body dynamic SPECT commenced about 3-5 minutes after tracer administration (depended on transferring process from induction box to scanner bed). The photopeak windows of *nanoScan SPECT/CT* were set at 20% window width (ww) centred over a 140 keV photopeak for ^{99m}Tc-pertechnetate, 20% ww centred over a 159 keV photopeak for ^{123}I-NaI, 20% ww centred over a 364 keV photopeak for ^{131}I-NaI and 20% ww centred over a 155 keV photopeak for ^{188}Re-perrhenate. SPECT projections were acquired using a low energy multi-pinhole collimator with pinhole aperture of 1 mm except for ^{131}I-iodide where a high energy collimator was used with aperture 1 mm. For dynamic imaging, the frame duration was set at 10-12 minute per frame (exact frame rate slightly varied with axial field extend) per time frame with continuous scanning for 4 hr. Then, static SPECT was performed again at 8 hr, 24 hr and 48 hr after tracer administration (latter for ^{131}I-iodide only). At the end of the scan, a whole-body CT scan (55 keV X-ray, exposure time 1000 ms and 180 projections and pitch 1) was performed for anatomical localisation. All SPECT tomographic data were processed by HISPECT™ iterative reconstruction software using “standard reconstruction” reconstruction parameters.

For PET acquisition, ^{18}F-tetrafluoroborate was injected intravenously under anaesthesia (as previously described). Then, the mouse was transferred to scanner bed were anaesthesia, bed warming and vital signs monitoring were maintained as described above. Dynamic PET was continuously acquired for 4 hr on the nanoScan PET/CT in list mode using 400-600 keV energy window and coincidence relation of 1:3 followed by CT (55 keV X-ray, exposure time 1000 ms and 360 projections and pitch 1) for anatomical localisation and attenuation correction. All PET projection data were processed with the 3D reconstruction Tera-tomo® software package (supplied with the system) with attenuation, scatter and dead-time corrections applied.

3.3.4.2 Imaging Protocols for Tumour Xenograft Mice

For ^{123}I-NaI, the data were collected using the same protocol as for healthy mice with dynamic scanning for 4 h after injection and static SPECT at 8 and 24 h after injection. In case of ^{99m}Tc-pertechnetate and ^{188}Re-perrhenate, the whole-body dynamic data were acquired only for 4 h with no additional SPECT at later time-point due to technical limitations (low count levels).

^{18}F-tetrafluoroborate for xenograft were scanned for 2 h. All data were reconstructed and managed as describe for the healthy mice experiments (Krisanat Chuamsaamarkkee, 2013a).

3.3.5 Image Quantification

The VivoQuant© (InviCro, Boston, USA) software was used to view and quantify the data. Volumes of interest (VOIs) were drawn on the tracer accumulating organs using the CT as a guide to resolve areas not clear on the radionuclide images. The VOIs (integral method by setting a threshold of 10% of the maximum count to exclude background) were drawn over the thyroid, salivary glands, stomach, bladder, left-ventricle (for blood), and muscle (for background) with additional VOI at tumour for the xenografts (figure 3-4). The whole body VOI was drawn on the initial whole body (WB) SPECT (first time frame, about 12-14 min post injection). This initial WB activity was considered to be equal to the injected activity and this was used instead of the radionuclide syringe dose-calibrator reading mainly to avoid any errors due to tissue activity in the animal tail or other remnant activity (injection needle and tubing). The percentage uptake per injected dose (%ID) in each organ was calculated as the activity in the VOI (in units of MBq) divided by the injected activity (units of MBq) from the whole-body VOI with decay correction (eq.3-1) (Krisanat Chuamsaamarkkee, 2013a, b). The conversion of image counts to radioactivity in units of MBq is based on a calibration process for a user-defined quantification factor in VivoQuant©. The method for obtaining these quantification factors is described in chapter 2.

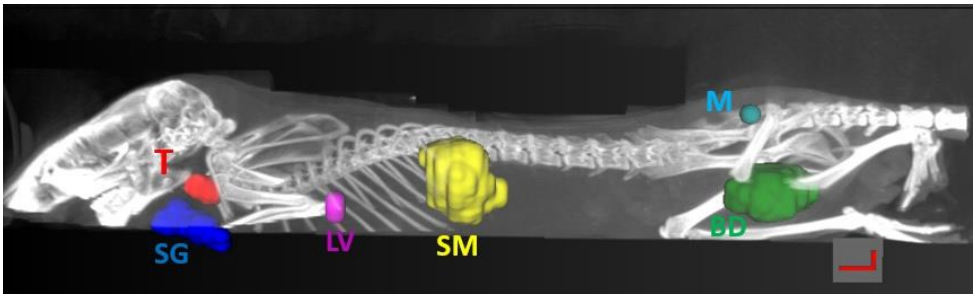

Figure 3-1 VOIs in lateral view of MIP image T-thyroid, SG-salivary glands, LV-left ventricle, SM-stomach, M-muscle and BD-bladder

The percentage uptake per organ weight (%ID/g) for all tracers (eq.3-2) were computed in 3 NIS-expressing organs; thyroid, salivary glands and stomach. For the healthy mice, we used the mean organ weight (n=14) to divide the percentage uptake. The mean organ weight was collected from the dissected organ of healthy mice after imaging session, these masses were not derived from whole group of mice due to technical problem. The average body weight (mean ± SD) of mice in this group was 22.71 ± 2.38 g. The average thyroid tissue (not including the

trachea) when dissected under microscope had mass of 0.0169 ± 0.0052 g. Dissecting mouse thyroid was very challenging due to their small size. So, the associated error in weighing is high. For this reason, the average group value is a good compromise in order to limit the inaccuracies. In addition, the average weights of salivary gland, stomach and urinary bladder from the same batch of animals were also used with mass of 0.1165 ± 0.0255 g, 0.2613 ± 0.0709 g and 0.0818 ± 0.0189 g respectively.

$$Percentage\ Injected\ Dose\ (\%ID) = \frac{Activity\ in\ the\ VOI\ (MBq)}{Activity\ in\ the\ initial\ WB\ (MBq)} \times 100 \qquad \text{Equation 3-1}$$

$$Percentage\ ID\ per\ Weight\ of\ Organ\ (\%ID/g) = \frac{Percentage\ Injected\ Dose\ (\%ID)}{Weight\ of\ Organ\ (g)} \qquad \text{Equation 3-2}$$

For the tumour xenograft mice, the mass of organs for individual mouse including actual dissected tumour mass were used to calculate the percentage uptake per weight of organ. The mass of tumours ranged from 0.348 to 0.548 g (average 0.452 ± 0.064 g for n = 9) (average 0.432 ± 0.046 g for n = 12), with the average weight of mice 23.91 ± 3.05 g (23.58 ± 2.95 g).

3.3.6 Statistical Analysis

A tracer uptake was presented as mean ± standard deviation (SD). The significance of changes in tracer uptake was determined by using a two-tail paired t-test for same animal and a two-tail unpaired t-test when compared to different animal. P-values of less than 0.05 were considered statistically significant.

3.4 Results

3.4.1 In *vivo* Spatio-Temporal Quantification in healthy mice

In this chapter, radiotracer distributions in NIS-expressing organs were identified, with clearly distinguished activity in thyroid and salivary glands as we also used anatomical information from CT to verify the tissue border between these organs. All images were displayed and analysed using VivoQuant© software. Decay-corrected time activity curves (TAC) based on VOIs over thyroid, salivary glands, stomach, urinary bladder, left ventricle (for blood pool) and muscle (for background) are illustrated in figure 3-6 and 3-7.

For SPECT radiotracers, the highest uptake was found in the stomach from initial time point with widely variable uptake values (high SD) from one animal to another and also varied across radiotracers. The stomach uptake reached its maximum at 4 hr for both iodine isotopes (^{123}I-iodide and ^{131}I-NaI), then continuously decreased over time and almost completely vanished at later time-points. On the other hand, stomach uptake of pertechnetate and perrhenate continuously increased and peaked at 8 hr after injection, then uptake gradually declined. By 24 hr after injection, stomach uptake of pertechnetate and perrhenate was found to be still high at 26.79 ± 3.03 %ID. Correspondingly at this time point, the pertechnetate excreted by saliva and gastric mucosa were transited and appeared in the gastrointestinal tract, As the activity in small and large bowel were seen at 24 hr time-point in representative mouse (matched coronal views of the representative mouse at various time-points are shown in figure 3.2 below.

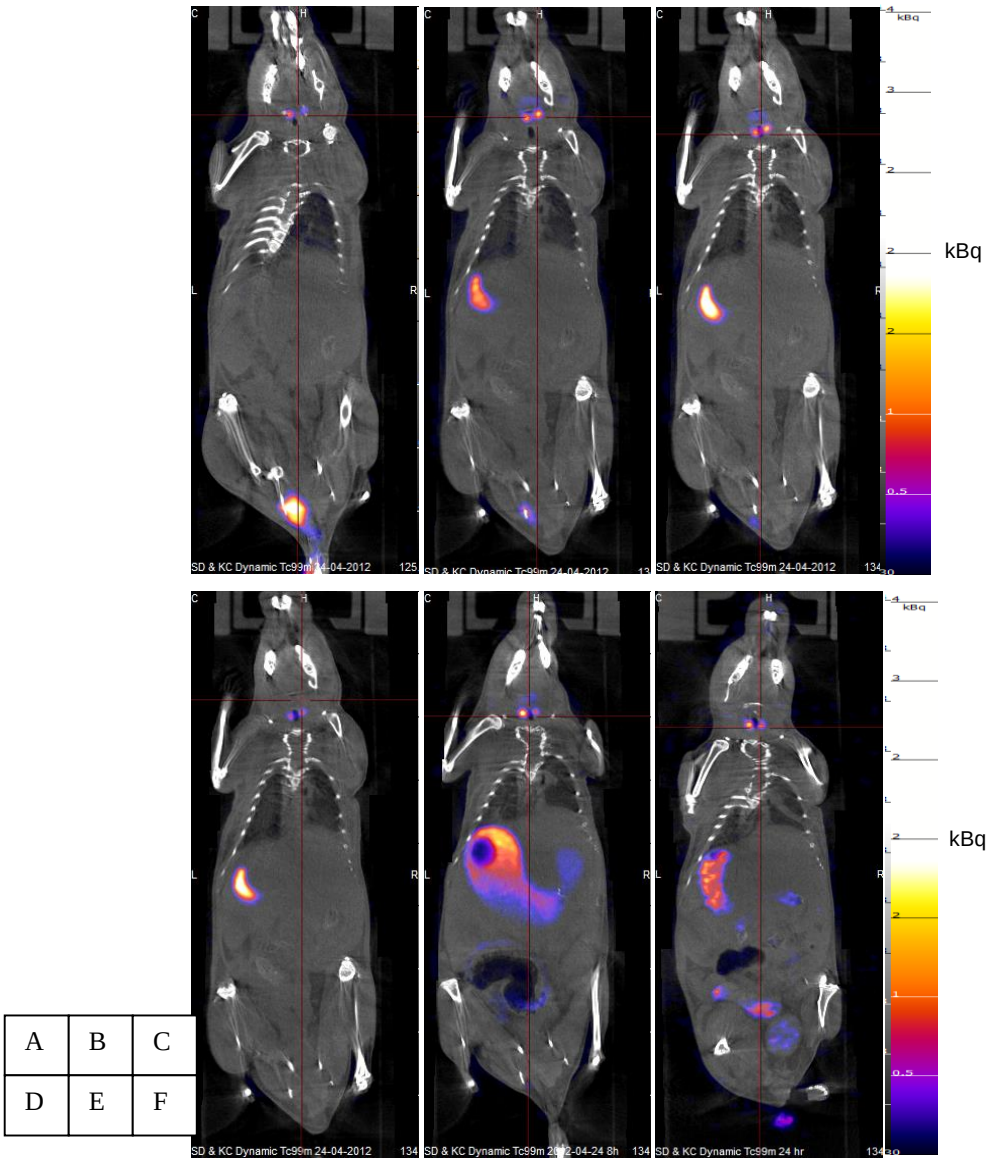

A	B	C
D	E	F

Figure 3-2 Matched coronal images of ^{99m}Tc-pertechnetate for each time points (A) 10 min (B) 45 min (C) 90 min (D) 4 hours (E) 8 hours and (F) 24 hours after injection

The uptake of non-metabolised radiotracer in thyroid increased gradually over time and peaked early at 1.22 hr (3.27 ± 0.29 % ID) for pertechnetate. The maximum uptake for perrhenate observed at about 3 hr after injection (1.39 ± 0.31 % ID). The different of peak times and uptake values of non-metabolised radiotracer could be resulted from imaging artefact which are discussed later in next part. In contrary for metabolised radiotracer iodine isotopes, peak activities for ^{123}I and ^{131}I were observed at 8 hr. The maximum uptake for iodine was comparatively high (14.80 ± 0.98 % ID and 11.04 ± 1.62 % ID for ^{123}I and ^{131}I respectively) when compared with non-organified tracers (pertechnetate and perrhenate). The iodine uptakes in thyroid slowly decreased but still remained fairly high when compared to uptake in other organs even at 24 h (for ^{123}I) and 48 h (for ^{131}I). This presumably resulted from iodine organification in thyroid hormones synthesis.

Thyroid uptake in non-organified tracers (pertechnetate and perrhenate) fell faster and almost completely washed out by 24 hr after administration.

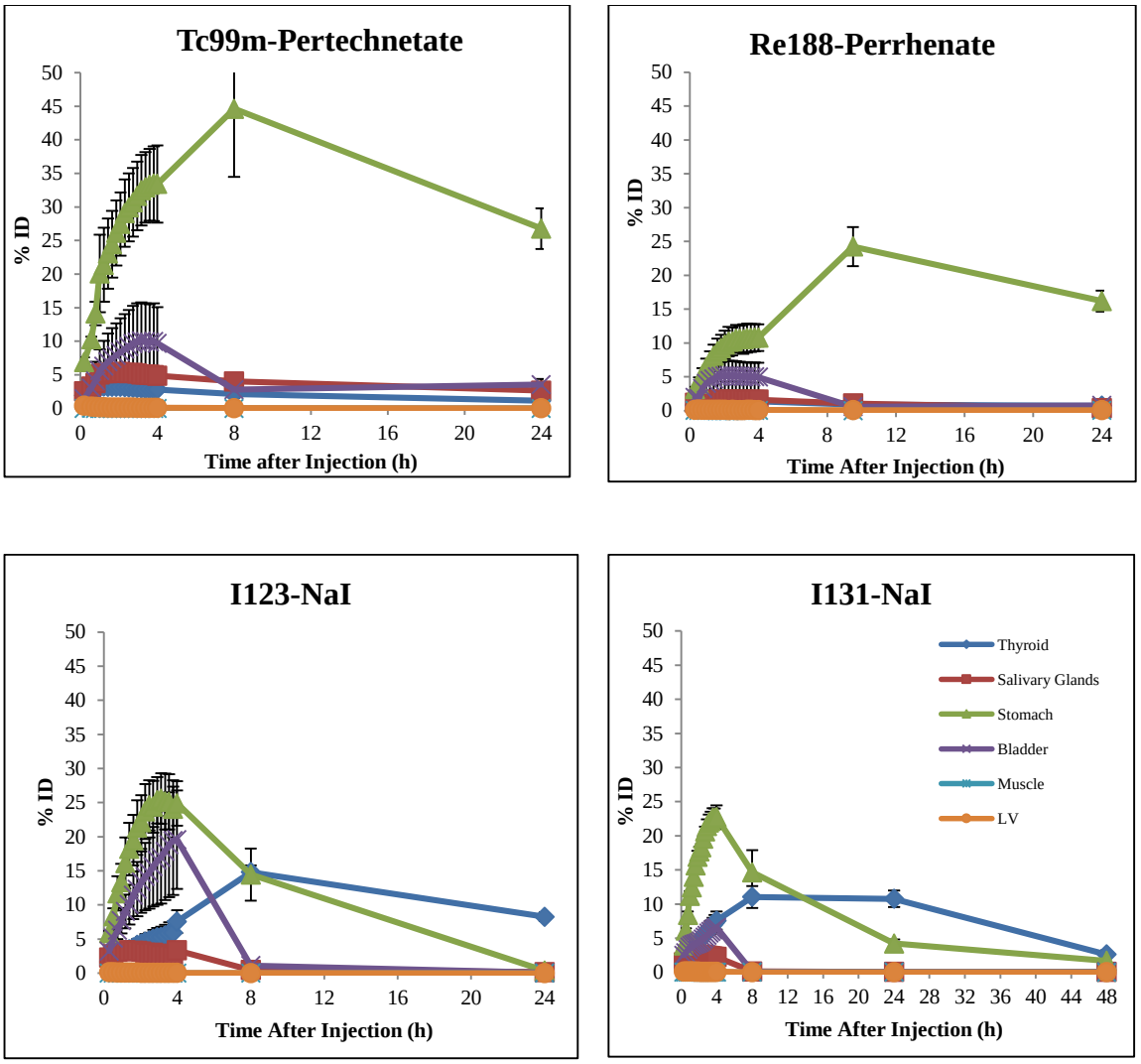

Figure 3-3 Time-Activity Curves demonstrate the uptake of NIS radiopharmaceuticals ^{99m}Tc-pertechnetate, ^{188}Re-perrhenate, ^{123}I- and ^{131}I-NaI in normal mouse (n=3). The data were analysed and presented as the mean of percentage injected dose (%ID) ± SD

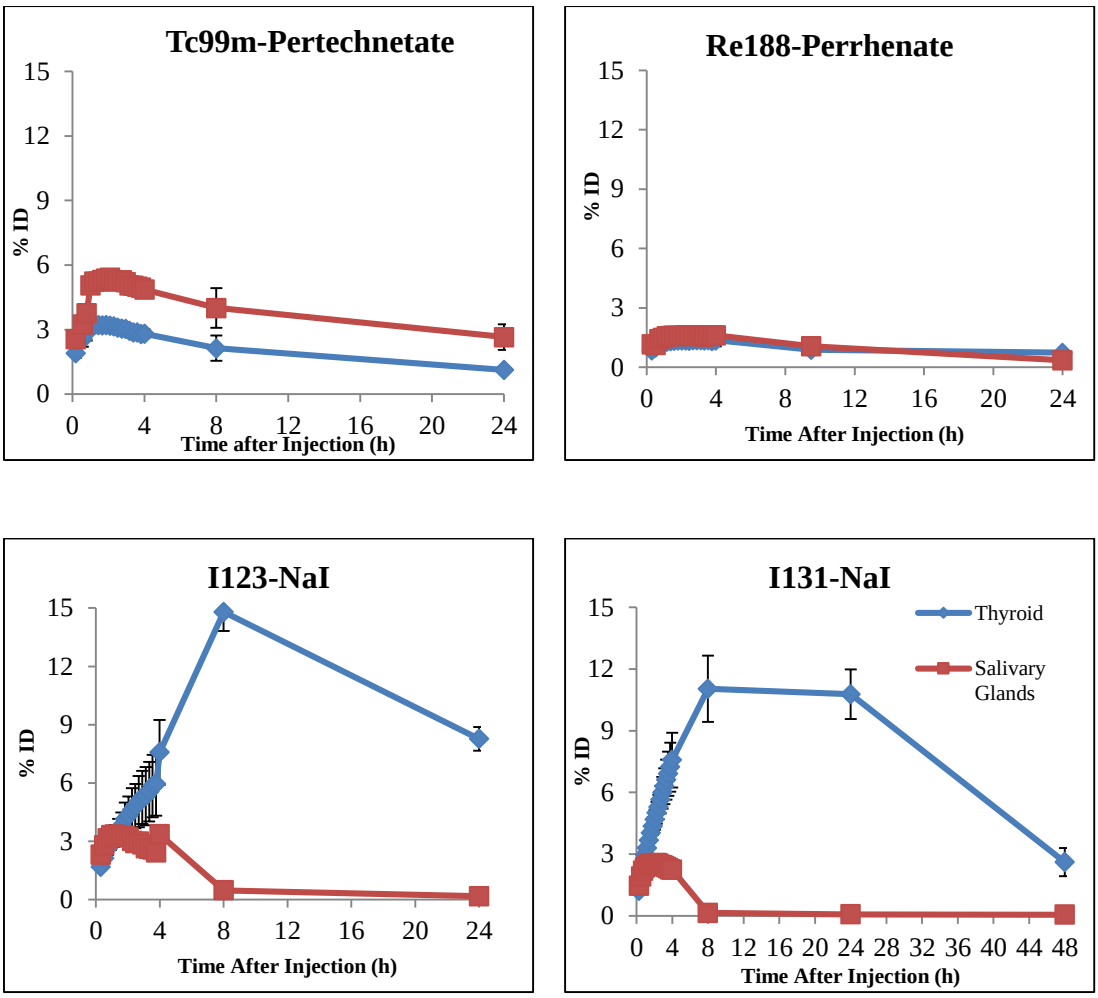

Figure 3-4 Time-Activity Curves (same data as figure 3-3 with expanding scale) demonstrate the uptake of NIS radiopharmaceuticals 99mTc-pertechnetate, 188Re-perrhenate,123I- and 131I-NaI in normal mouse (n=3) in thyroid and salivary glands. The data were analysed and presented as the mean of percentage injected dose (%ID) ± SD

In salivary glands, a similar pattern was seen for all radiotracers, in which the uptake increased slowly overtime followed by a plateau phase and gently washed out at later time-points. The activities in the urinary bladder indicated the excretion of radioisotopes via the genitourinary system. For the first 4 hr phase of the dynamic study, the bladder activities were characterised by a similar pattern for all radiotracers, in which bladder uptake increased gradually for 4 hr then animals were awakened from anaesthesia and urinated. Hence, this process caused the maximum activity mostly observed at 4 hr post injection and bladder activities were negligible at later time-points. Activity in tissues that do not express NIS (muscle) and the left ventricle (representing blood activity) were remarkably low and remained so over time for all tracers.

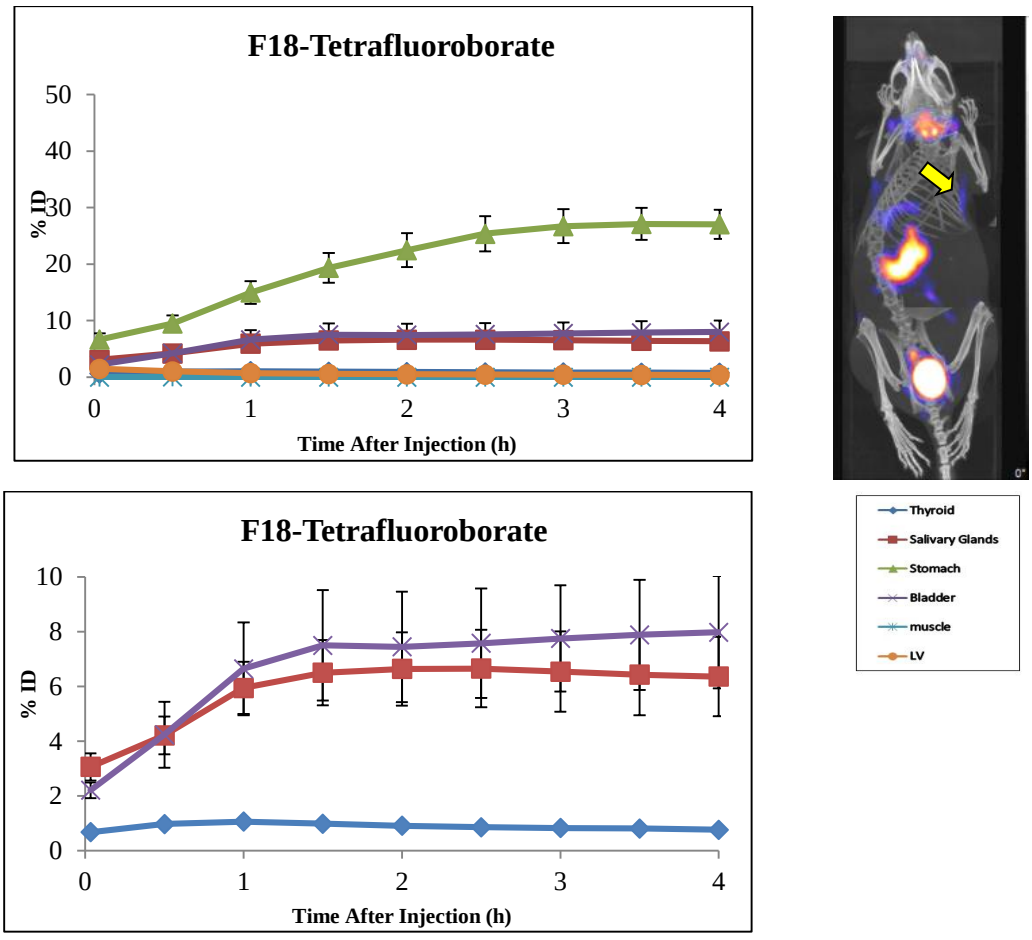

Figure 3-5 (A -Top Left) Time-Activity Curve shows the uptake of PET ^{18}F-BF4 in normal mouse (n=3). The data were analysed and presented as the mean of percentage injected dose (%ID) ± SD (B-Top Right) Maximum Intensifying Projection (MIP) of ^{18}F-BF4 accumulated in normal mouse. Tracer was accumulated in NIS-expressing organs (thyroid, salivary glands, stomach, urinary bladder) and also uptake in lateral part of chest (arrow) which might indicate mammary tissue (C – Bottom Left) Time-Activity Curve with expanding scale (similar data as presented in figure A) shows uptake pattern in thyroid, salivary glands and urinary bladder

For $^{18}F\text{-}BF_4$ (as illustrated in figure 3-5), whole body PET was dynamically acquired in list mode continuously for 4 hr after injection followed by CT for anatomical localisation and attenuation correction. Data were re-binned and reconstructed into a series of 30 min time frames. Based on the graph, it can be seen that the uptake pattern of $^{18}F\text{-}BF_4$ was similar to non-organified SPECT tracers ($^{99m}TcO_4^-$ and $^{188}ReO_4^-$). The uptake was highest in stomach and continued to increase for 4 hr post injection. TACs showed a fast accumulation of ^{18}F-BF4 in thyroid and salivary glands then the rate of uptakes slightly decreased. The activity in the salivary glands was higher than thyroid which is a pattern not seen in other tracers. The uptake in thyroid reached its maximum (1.06 ± 0.05 %ID) at 1 hr after injection while uptake in salivary glands approached its maximum (6.65 ± 1.42 %ID) at about 2.5 hr after injection. Interestingly, images showed tracer accumulation in lateral parts (not observed this in SPECT radiotracers) of the chest which might indicate uptake to mammary tissue (arrow in figure 3.5). The urinary

bladder activity represented renal excretion of radiotracer, the activity continue to increase to 4 hr due to the effect of anaesthesia as previously observed in other SPECT radiotracers. Activity in the left ventricle (representing blood pool) and muscle (representing background) remained low over time.

The percentage uptake per organ weight for all tracers is shown in the following figures (figure 3-6 and 3-7).

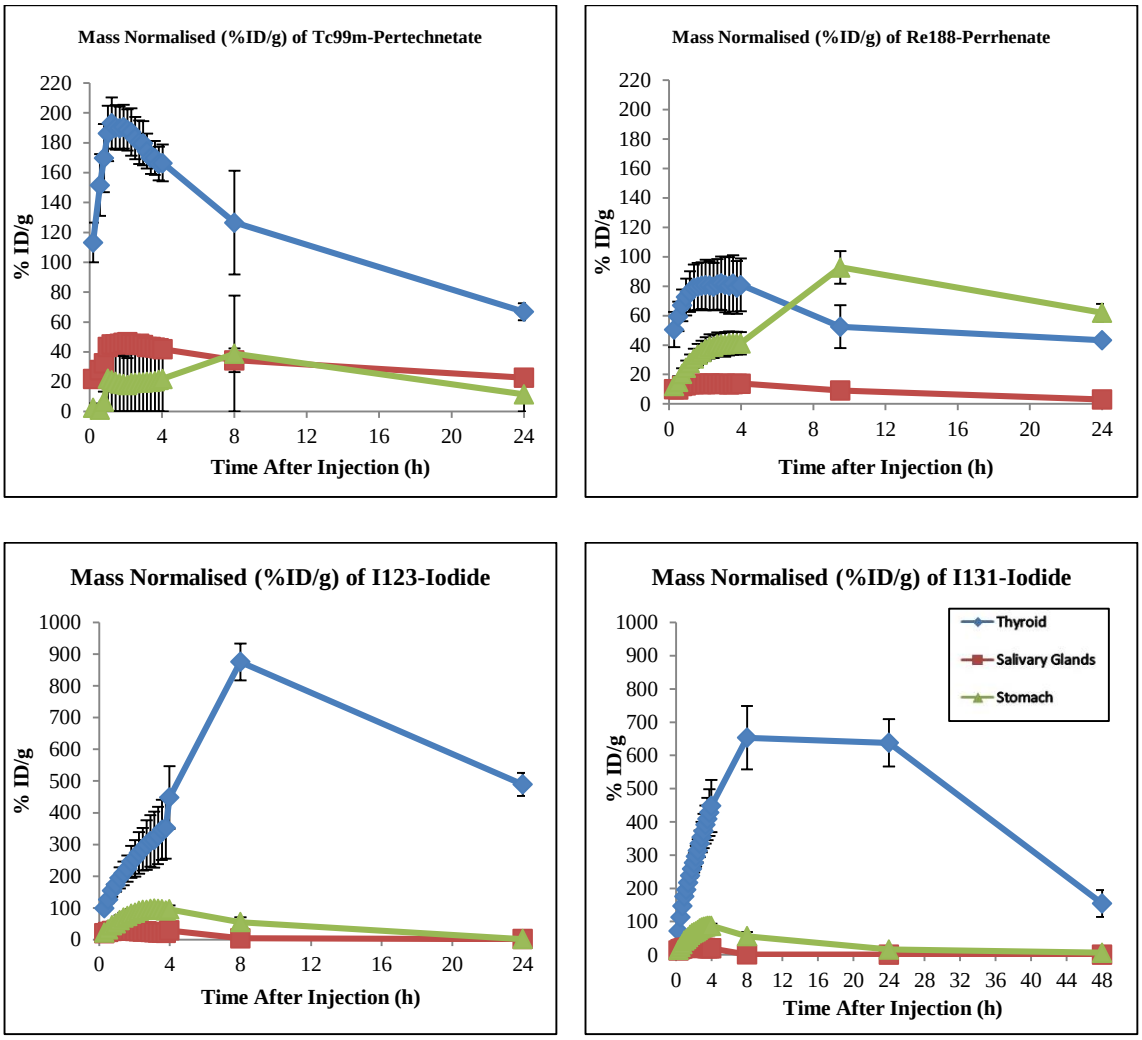

Figure 3-6 Time-Activity Curves demonstrate the uptake of SPECT NIS radiopharmaceuticals ^{99m}Tc-pertechnetate, ^{188}Re-perrhenate,^{123}I- and ^{131}I-NaI in normal mouse (n=3). The data were analysed and presented as the mass normalised of percentage injected dose (%ID/g)

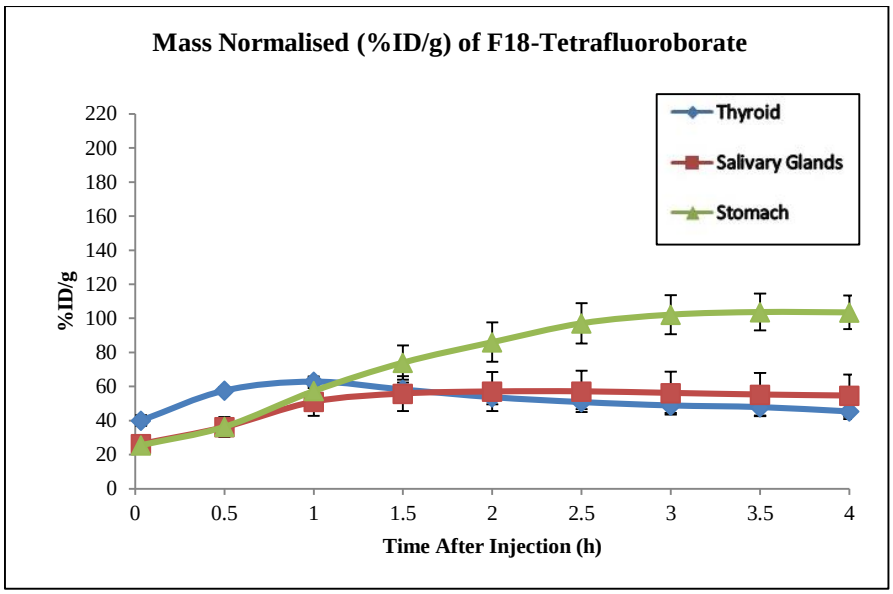

Figure 3-7 Time-Activity Curve shows the uptake of PET ^{18}F-BF4 in normal mouse (n=3). The data were analysed and presented as the mass normalised of percentage injected dose (%ID/g) ± SD

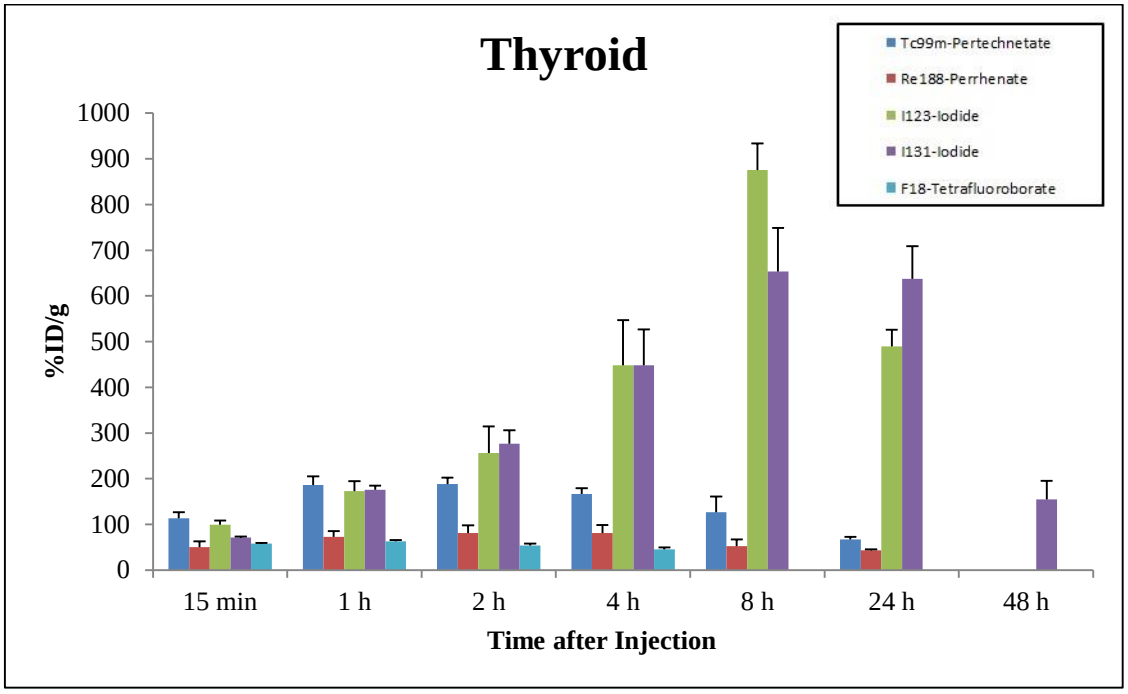

Figure 3-8 Bar graph of uptake per gram of tissue in thyroid (Mean ± SD) for all radiotracers

When comparing uptake in thyroid and salivary glands for non-metabolised tracers (pertechnetate, perrhenate and tetra-fluoroborate), the percentage uptake per injected activity was slightly higher in salivary glands. However when comparing the normalised activity per gram of tissue, thyroid showed higher values than salivary glands. This pattern was observed over time for ^{99m}Tc-pertechnetate and the initial phase of 1 and 4 hr for ^{18}F-BF4 and ^{188}Re-perrhenate

respectively. Thyroid uptake of $^{123}I^-$ and $^{131}I^-$ were much higher (about 20 folds at 8 hr after injection) than that observed in non-metabolised tracers and continued to increase through the 8 hr time-point then decreasing by 24 and 48 hr post injection (as illustrated in figure 3-8), presumably as a result of a hormone production process.

We additionally analysed the percentage injected dose per tissue mass ratio of uptake in thyroid divided by salivary glands for all radiotracers in the dynamic phase (first 4 hr after injection) (Figure 3-9). At 15 min post injection, the uptake ratios of all radiotracers were similar except for that of BF_4 which was lower than other tracers. Then, the uptake ratios of iodide radiotracers (^{123}I- and ^{131}I-NaI) were starting to increase while other decreased. The thyroid to salivary glands ratio of iodide was more distinct at 8 hr and 24 hr post injection.

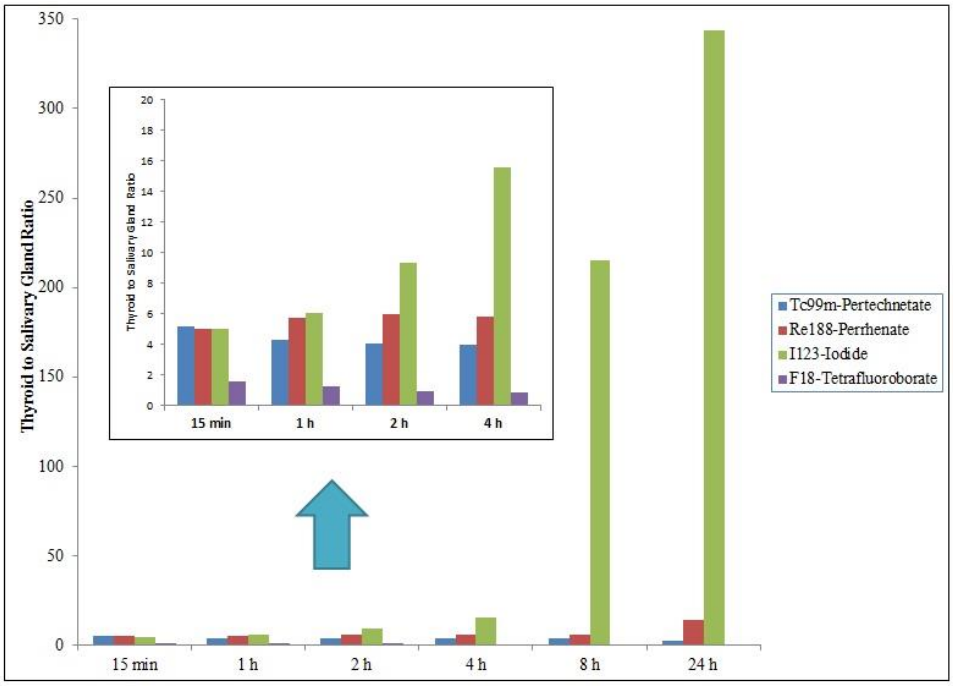

Figure 3-9 The percentage injected dose per tissue mass ratio of uptake in thyroid divided by salivary glands show clearly differences of uptake pattern for each radiotracers

3.4.2 In *vivo* Spatio-Temporal Quantification in Xenograft mice

Xenograft bearing breast adenocarcinoma cell line (MTLn3E) overexpressing truncated CXCR4 and human sodium iodide symporter (hNIS) was selected to examine the kinetics of radiotracers in this study. Time-activity curves of NIS radiotracers accumulated in xenograft are presented in figure 3-10. *In vivo* dynamic imaging showed similar pattern of NIS-expressing organs as seen in normal subjects. Interestingly, uptake in tumours was higher than thyroid and salivary glands in all tracers. For ^{123}I-NaI, activity in tumour was higher than stomach. The tumour uptake in ^{123}I-NaI elevated over time and peaked at 4 hr post injection (21.90 ± 0.98 % ID). However, the tumour uptake for ^{123}I was remained only about 0.6 % ID at 24 hr after injection. A similar pattern was found in pertechnetate with tumour activity higher than that observed in the stomach for the first 2.5 hr, before reaching its maximum at about 26 % ID at plateau and still remaining high at 4 hr after injection. For ^{188}Re-Perrhenate, the tumour uptake was remarkably low when compared with pertechnetate and iodide. Rhenium tumour uptake reached a maximum (5.64 ± 1.42 % ID) at approximately 3 hr and still accumulated in tumour about 5 % ID until 4 hr after injection. For ^{18}F-BF_4 PET radiotracer, tumour uptake was low when compared with SPECT radiotracer. At 2 h , the uptake of BF_4 was still not reached its peak yet, the data at this time-pint shown the uptake at 3.25 ± 1.98 % ID)

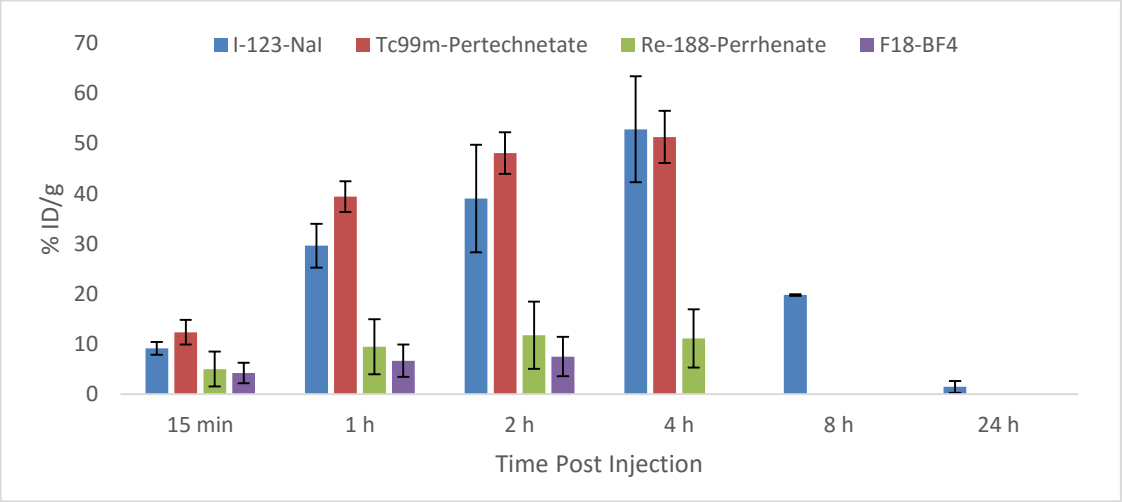

Figure 3-10 shows the tumour uptake in NIS-radiotracers per gram of tissue (% ID/g) in xenograft (n=3). Data are expressed as mean ± SD

After imaging all mice were dissected to obtain the tumour weight. Then, the percentage uptake per gram of tumour (% ID/g) was calculated as shown in figure 3-11, ^{18}F-tatrafluoroborate accumulated in tumour at about 4-8 % ID/g, compared with SPECT radiotracers approximately 5-12 % ID/g of ^{188}Re-perrhenate, 45-55 % ID/g of ^{99m}Tc-pertechnetate and 42-62 % ID/g of ^{123}I-NaI.

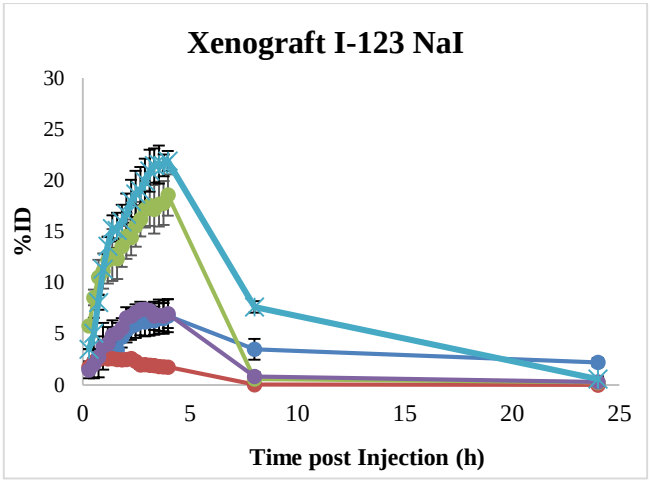

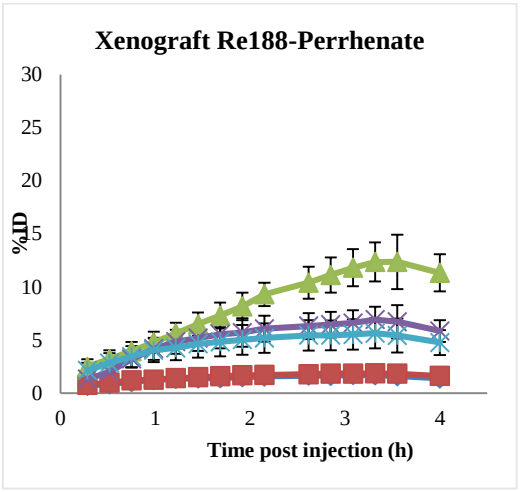

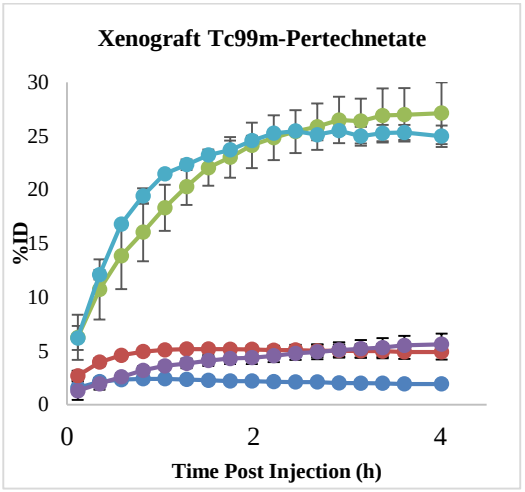

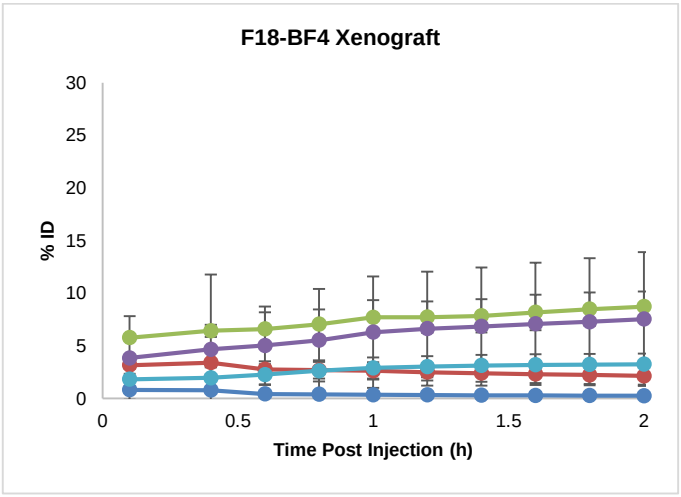

Figure 3-11 Time-Activity Curves demonstrate the uptake of NIS radiopharmaceuticals ^{99m}Tc-pertechnetate, ^{188}Re-perrhenate and ^{123}I-NaI in mouse bearing rat adenocarcinoma xenograft tumour expressing hNIS (n=3). The data are presented as the mean of percentage *injected dose (%ID)* ± *SD*

3.5 Discussion

In this chapter, *in vivo* spatio-temporal quantification of NIS radiotracers in normal healthy and tumour bearing xenograft mice was studied. TACs were graphically plotted in terms of percentage injected dose (%ID) over time after injection as well as normalised percentage injected dose per organ/tissue weight. This information afforded a side by side comparison of pharmacokinetics. ^{99m}Tc-pertechnetate and ^{123}I-NaI are well known SPECT imaging agents. ^{131}I-NaI has long been recognised as a therapy agent in the management of thyroid diseases. ^{188}Re-perrhenate is another NIS substrate whose physical properties appealed for therapeutic purposes but have not been assessed clinically. In addition, ^{18}F-Tetrafluoroborate is a forthcoming diagnostic PET imaging agent for thyroid disease (clinical trial currently underway) and NIS reporter gene imaging. All these NIS radiotracers have been examined and compared in this chapter.

The availability of preclinical imaging allows an assessment of radiotracer behaviour with high spatio-temporal resolution throughout the whole body of the animal which enables us to localise and quantify the uptake of radiotracer in small organs of laboratory animals. The sub millimetre resolution from multi-pinholes allows the high resolution imaging of thyroid with both its lobes clearly resolved and the ability to distinguish and quantify the radiotracer accumulated between thyroid and the salivary glands.

For pharmacokinetics in normal healthy mice, the thyroid, salivary glands and stomach were the main organs that accumulated the radiotracers. Uptake in urinary bladder showed the excretion of radiotracer via kidneys. The uptake in those organs was found to be varied across radiotracers. A large proportion of radiotracer was accumulated in the stomach when compared with other organs (thyroid, salivary glands, and urinary bladder) in all radiotracers for first 4 hours of the dynamic phase after injection. However, as the mass of the salivary glands and stomach are much greater than the mass of thyroid in this species, the normalized uptake (%ID/g) was highest in thyroid followed by salivary glands or stomach. However, this pattern was difference in ^{18}F-BF_4. Thyroid to salivary gland uptake ratios were 1.59 and 1.23 at 30 minutes and 1 h after injection, then decreased to 0.94 and 0.83 at 2 h and 4 h respectively. Our study found that normalized uptake of ^{18}F-BF_4 was highest in thyroid only for the first hour after injection then the stomach and salivary gland activity were greater than the activity accumulated in thyroid. However, there appeared to be some difficulty when comparing SPECT and PET data. As

nanoScan SPECT/CT has a spatial resolution better than that of nanoScan PET/CT (about 0.7 and 1.2 mm FWHM at CFOV for ^{99m}Tc with nanoScan SPECT/CT and ^{18}F with nanoScan PET/CT respectively), small organ quantification in PET may be subject to stronger influence by partial volume effects (PVE) than in SPECT.

Furthermore, in this study we have shown data for a potential for new therapeutic agent (^{188}Re-Perrhenate) for comparison with conventional ^{131}I-NaI. As mentioned above, the uptake patterns in thyroid can be categorised into metabolised (iodide) and non-metabolised (perrhenate, pertechnetate, tetrafluoroborate) group. For ^{188}Re-perrhenate, the maximum uptake in thyroid was about 2 hr after injection and subsequently decreased at later time points, where both iodide radiotracers continued to increase and reach maximum at 8 hr (for ^{123}I-NaI) and 24 hr (for ^{131}I-NaI) after injection. Interestingly, the thyroid uptake value of $^{123}I^-$ was higher than $^{131}I^-$ which could due to stunning effect. The stunning effect is defined as a temporary defeat of iodine and trapping function of the thyrocytes as a result of the radiation given off by the ^{131}I.

Based on the dynamic TACs in figure 3-6, it can be seen that the pharmacokinetics pattern of ^{188}Re-perrhenate and ^{99m}Tc-pertechnetate were very similar. However, the uptake values of NIS-expressing organs in ^{188}Re-perrhenate were quite low when compared to images obtained with ^{99m}Tc-pertechnetate. This might be influenced also by the elevated background counts observed in ^{188}Re images (as shown in figure 3-12) from a strong Bremsstrahlung component which has a boarding spectrum up to MeV (with the subject and the camera), septal penetration from high-energy lines (478 and 632 keV) and also a random noise from low-abundance of 155 keV gamma photons (about 15% gamma abundance). According to study by Manjunatha HC, the Bremsstrahlung radiation spectrum of ^{188}Re was estimated using Bethe and Heitler's analytical formula. Manjunatha HC showed that Bremsstrahlung spectrum of ^{188}Re interacted with bone and muscle has a continuous spectrum from 0.1 up to 2 MeV. Also, high-energy photons (0.487 MeV – 0.62 % abundance and 0.632 MeV – 1 % abundance) can penetrate collimator septa, then creating significant background elevated in the image (as observed in figure 3-12). The combination of all these effects may result in elevated background and hence high "whole body" activity in the denominator contributing to inaccuracies (underestimation) in quantification of ^{188}Re-perrhenate uptake in various organs.

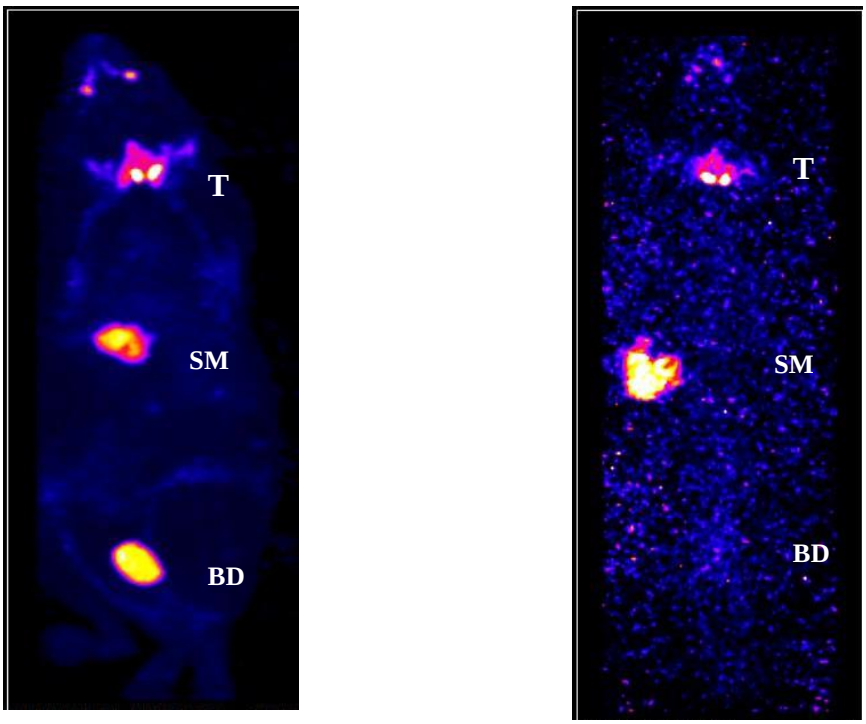

Figure 3-12 Maximum Intensity Projection (MIP) at 90 min post injection (Left) ^{99m}Tc-Pertechnetate and (Right) ^{188}Re-Perrhenate. These images demonstrate differences in background values (potentially due to Bremsstrahlung, septal penetration and a random noise from low-abundance of *gamma photon when acquiring ^{188}Re) (T-Thyroid, SM-Stomach and BD-Bladder)*

The kinetic comparison of NIS radiotracers (perrhenate, pertechnetate and iodide) in healthy CD mice also has been reported by Zuckier et al (Zuckier et al., 2004). However, the kinetic results from Zuckier et al were based on the *ex vivo* bio-distribution from a different sets of mice and at different time-points (20 min, 2 h and 19 h post injection). We consider that time-activity curves derived by ex-vivo bio-distribution (rather than single animal kinetics) are subject to strong influence by inter-animal variability and organ dissection errors. This variation confirmed by the study by Brandt et al in 2012. In this study, the inter- and intra-experimental viability of thyroid and salivary uptake of ^{99m}Tc-pertecnetate was evaluated. Brandt's study concluded that the magnitude of variability among different animals were greater than the inter-experimental variability in the same mouse (Brandt et al., 2012). Furthermore, Traditional *ex vivo* bio-distribution needs to sacrifice many animals. The substantial expense of animal lives, costs, and time are constrained the number of time-points of time-activity curve. In our study, *In vivo* imaging with preclinical SPECT/CT and PET/CT are offered series of imaging of live mice. The full time course of pharmacokinetics was measured on the same animals. This reduces biological variability over the time course of the radiotracers and avoids errors from *ex vivo* bio-distribution which may be quite large and difficult to address (Franc et al., 2008). However, there are still pitfalls for comparing *in vivo* data resulting from imaging instrument (previously described in detail

in Chapter 2) such as, calibration factor and different artefacts (e.g. scatter) from different isotopes, also different in physical properties (low abundance of gamma photons, positron range, bremsstrahlung).

To compare uptake in thyroid and salivary glands, Zuckier et al showed only the 2D planar quantification from representative mice. Interestingly, Zuckier et al reported that uptake pattern of iodide (^{125}I-NaI), pertechnetate (^{99m}Tc-pertechnetate) and perrhenate (^{188}Re-perrhenate) in mice salivary glands were similar in which remained elevated for initial 2 h PI and then washed out. For thyroid, Zuckier et al showed a similar bio-distribution pattern of ^{188}Re and ^{125}I for initial phase (20 min and 2 h post injection), then at later time-point (19 h PI), perrhenate uptake was decreased while iodide decreased by organification process. However, *in vivo* imaging from Zuckier's study was unable to show this because ROIs were drawn at the neck region where thyroid and salivary glands are indistinguishable in the planar views. A publication by Grewal RK et al stated that the salivary gland is the critical organ for using high dose ^{131}I-iodide treatment(Grewal et al., 2009). The understanding of dynamic accumulation of NIS radiotracers might lead to better clinical outcome in high dose radioiodine treatment.

Our study demonstrated the capability of preclinical tomographic imaging and specifically its superior ability to distinguish the thyroid from the salivary gland. Based on literature data, each lobe of the mouse thyroid is about 1 × 0.3 mm and it alights closely to the salivary glands, the approximately distance is around 2-5 mm from CT images (Franken et al., 2010). The images have shown the ability of emission tomography to identify each lobe of the thyroid clearly in the sagittal planes. Furthermore, the superimposition of CT images can additionally help to define the boundary of the salivary glands and thyroid.

In other work using 3D SPECT, Franken et al. published the SPECT dynamic assessment of ^{99m}Tc-pertechnetate using clinical SPECT equipped with pinhole collimator. Franken's work has shown dynamic data only over 2 hours after injection with the tomographic area limited only to the neck region. The additional whole body planar view was acquired separately for the stomach uptake(Franken et al., 2010). Franken's work showed that pertechnetate uptake reached its maximum in thyroid within 20-40 min whereas uptake in salivary glands still not reached its peak after 100 min. This was similar to our finding that thyroid reached its peak rapidly followed by the salivary glands (thyroid 75 min and salivary glands 120 min after injection) (Spitzweg et al., 1998). Franken's et al discussed that there were many complex factors related with the NIS uptake such as level of NIS (expression, transporting efficiency, number, size), organ (passive

diffusion, physiological influx, efflux and size of cell compartment of each organ - cell compartment of salivary glands are much larger than follicular cells in thyroid) and also the level of regulation and action of hormones that control NIS in among different animals (Franken et al., 2010; Michael P. Brandt, 2012).

The variation in uptake patterns of NIS radiotracers can be further explained by an assumption of anion selectivity however all published studies were performed *in vitro* (Eskandari et al., 1997b; Van Sande et al., 2003). Eskandari et al (1997) performed electrogenicity of Na^+/I^- symporter to evaluate the inward currents induced by various anions in *Xenopuslaevis* oocytes. From this study, the best transported substrate was iodide (I^-) which the relative I_{max} value equal to 1. The anion group of ClO_3^-, SCN^-, $SeCN^-$ and NO_3^- were intermediate high (I_{max} value between 0.5 to 1) while Br-, BF_4^- and IO_4^- were categorized in the intermediate low anion selectivity group. Interestingly, authors found perrhenate (ReO_4^-) to be an effective blocking agent for NIS (I_{max} value nearly approached zero), second only pertechnetate (ClO_4^-) which did not induce an appreciable inward current in their study (Eskandari et al., 1997b). Furthermore, another *in vitro* study by Van Sande et al (2003) reported different order of affinity in FRTL-5 in NIS-transfected COS cells. Authors concluded that the order of blocking affinity was $ClO_4^- > ReO_4^- > I^- \geq SCN^- > ClO_3^- > Br^-$ (Van Sande et al., 2003). In our study, the normalised uptake of thyroid at early phase (15 min after injection) was $^{99m}TcO_4^-$>^{123}I-iodide >^{131}I-iodide >^{18}F-BF_4^->$^{188}ReO_4^-$whereas for 4 h after injection the order was ^{123}I-iodide ≥^{131}I-iodide >$^{99m}TcO_4^-$>$^{188}ReO_4^-$>^{18}F-BF_4^-. However, the thyroid uptake of both iodide isotopes was not statistically different as described in previous section.

Considering of pharmacokinetics in xenografts, we performed the whole-body dynamic *in vivo* study in mice with rat adenocarcinoma (Δ34CXCR4-hNIS). All radiotracers detected the tumour with high target to background ratio. In our study, perrhenate uptake in tumour was significantly low when compared with pertechnetate or iodide. Our findings were similar to the *in vivo* study of ^{188}Re-perrhenate in a prostate cancer cell expressing NIS (Willhauck et al 2007) and study by Kang et al (2004) in a liver cancer xenograft transplant model. However, these data showed higher uptake of ^{188}Re-perrhenate when compared with published work by Dadachova et al. (2002) where the bio-distribution in xenografts with mammary adenocarcinoma showed only 3 – 4 % ID/g of ^{188}Re-perrhenate accumulated in tumour at 2 hr post injection. Also, this could be due to different expression levels of NIS, so, the mammary tumours were not transfected with

engineered NIS, only endogenously expressing at low level (Kang et al., 2004; Willhauck et al., 2007).

In addition, the tumour uptake can be increased by blocking or decreasing the NIS uptake in other NIS-expressing organs such as thyroid, salivary glands and stomach. This is also called the “sink” effect (Dadachova et al., 2002; Dadachova et al., 2005; Zuckier et al., 2004). The study by Dadachova et al. (2005) demonstrated that eliminating or blocking the uptake of radiotracer in thyroid by pre-treating them with T3 thyroid hormone which reduces the thyroid uptake, it can contribute to elevated uptake of rhenium in tumour. This can also reduce radiation damage to the thyroid (Dadachova et al., 2005).

Since the study by Eskandari et al. (as explained above) in rat thyroid NIS using electrophysiological measurement reported that ReO_4^- is a potent blocking agent for NIS and is inferior (for blocking) to only perchlorate ($KClO_4^-$) (Eskandari et al., 1997a). The significant finding from this study demonstrated that there may be a window for using perrhenate for the treatment of NIS-expressing tumours.

Also, it should be noted that our animal model is initiated with genetically engineered (hNIS) which is unlike the endogenous mouse sodium iodide symporter or mNIS that is expressed in thyroid, salivary glands and stomach. Therefore, this might partly explain the variation of tumour accumulation in xenograft model in our study (Penheiter et al., 2012).

3.6 Conclusion

In this chapter, we have used high resolution preclinical imaging to quantify the spatio-temporal distribution of the available NIS-radiotracers. In healthy model, this experiment has demonstrated distinct differences in uptake patterns between metabolised and non-metabolised tracers, and also subtle differences between the putatively non-metabolised tracers. The uptake of radiotracers in thyroid can be categorised into 2 assemblies: metabolised (^{123}I- and ^{131}I- sodium iodide) and non-metabolised tracers (^{18}F-tetrafluoroborate, ^{99m}Tc-prtechnetate and ^{188}Re-perrhnate). In salivary glands, similar patterns of uptake were observed for all tracers which uptake increased gradually over time then remained steady and slowly decreased. The activity in thyroid can be distinguished from salivary glands along with high spatial resolution imaging of other NIS-expressing organs. Stomach uptake was high compared with other organs, the uptake in stomach peaked at 4 h for metabolised radiotracers. In contrary, peak uptake in stomach found at 8 h for non-metabolised radiotracers, except with ^{18}F-BF_4 which showed peak values at around 3 h after injection (as we collected data only 4 h). Activity in muscle (not expressing-NIS) and left ventricle (representing blood activity) were low and remained so over time for all tracers.

In xenograft model, all radiotracers (^{18}F-tetrafluoroborate, ^{99m}Tc-prtechnetate, ^{123}I-sodium iodide and ^{188}Re-perrhnate) detected the tumour with high target to background ratio. This work demonstrated the capability of ^{188}Re-perrhenate with appealing therapeutic and imaging properties (high energetic beta and imaginable gamma emission). However, perrhenate uptake in tumour was significantly low when compared with pertechnetate or iodide the percentage uptake per gram of tumour about 5 - 12 %ID/g for ^{188}Re-perrhenate, 45-55 % ID/g for ^{99m}Tc-pertechnetate and 42-62 % ID/g for ^{123}I-NaI). This work also showed kinetic data of forthcoming PET radiotracer (^{18}F-BF_4) for imaging of NIS-expressing tumour, ^{18}F-tatrafluoroborate accumulated in tumour at about 4-8 % ID/g.

Regarding to imaging artefact of ^{188}Re, the images of ^{188}Re-perrhenate showed in this study had a problems from (1) a continuous spectrum of Bremsstrahlung radiations (energies 0.1 up to 2.0 MeV), (2) septal penetration cause by down scatter from the higher energy photons creating significant background in the image, (3) scattered photon corresponding to the 0.478 and 0.632 MeV and (4) a random noise from low-abundance of 155 keV gamma photons (about 15% gamma abundance). The combinations of all these effects are resulted in elevated background, contamination of counts in main photo-peak and hence contributing to inaccuracies in

quantification of ^{188}Re-perrhenate. As the complexity of multi-pinhole, we cannot employ the triple-windows correction to ^{188}Re data at this stage. These will be very important things to investigate further for future work.

In conclusion, the data showed the capability of pre-clinical imaging for spatio-temporal quantification. Such data can be used to determine optimal imaging times to maximise image quality in diagnostic studies and allowing accurate quantitative *in vivo* analysis for the dosimetry study in next chapter.

.

Chapter 4 Human-Equivalent Dosimetry of NIS Radiotracers in Healthy and Tumour Model Mice Based on Preclinical Spatio-Temporal Data

4.1 Introduction

4.1.1 Nuclear Medicine Dosimetry

In general, radiation dosimetry aims to estimate risks and benefits of using ionizing radiation. In nuclear medicine, radionuclides are administered for a variety of diagnostic and therapeutic applications. Specifically, nuclear medicine dosimetry deals with the energy deposited by internally emitted radionuclides into organs, tissues or the whole body. The energy absorbed per unit mass in terms of “absorbed dose” is used to indicate the effects of radiation on the tissue or organ. The direct measurement of absorbed dose for internalised emitting radionuclides is difficult to perform, hence in nuclear medicine this quantity is usually indirectly determined by calculation. The methodology and associated assumptions are discussed below.

4.1.1.1 Medical Internal Radiation Dose (MIRD)

Historically, the first formalism for dose calculations from internal deposited radionuclides was defined and published by Marineli et al (1948) and Quimby and Feitlberg (1963)(Stabin, 2006). After that in 1968, the Medical Internal Radiation Dose (MIRD) committee of the Society of Nuclear Medicine (SNM) was established. The MIRD committee contributes to defining the methods, equations and models for dosimetry calculation in nuclear medicine. MIRD has provided an extensive body of data for several radionuclides to assist in dose estimation. The estimation of absorbed dose is based on assumptions of biological distribution, clearance and the physical decay properties of the radiotracers. The cumulated activity $(\widetilde{A})_i$ is proportional to the total number of disintegrations that take place and can be calculated by integrating the time-activity curve for each organ (this also called the time-integrated activity in the MIRD primer) (see figure 4-1). Time-activity curve is decreased exponentially (in its simplest form) with an effective half-life (T_{eff}) which results from the combination of both physical decay of the radionuclide and bio-kinetic clearance. The cumulated activity can be obtained with a counting probe, quantitative imaging (planar imaging, SPECT, PET) or excretion sampling (urine, faces, blood) at different time points after tracer administration.

The mean absorbed dose, $\overline{D}$, within the k^{th} target from the i^{th} source is denoted in equation (4-1). The unit of absorbed dose is the Gray (Gy), which refers to absorbed energy of one Joule of ionising radiation in one kilogram (1 Gy = 1 J/kg).

$$\overline{D} = \widetilde{A}_i \sum \Delta_j \frac{\emptyset_j(k \leftarrow i)}{m_k} \qquad \text{Equation 4-1}$$

where $\widetilde{A}_i$ is the cumulated activity (μCi.h or MBq.s) in the i^{th} source, Δ_j is the mean energy emitted per nuclear transition from the j^{th} transition, $\emptyset_j$is the absorbed fraction representing the fraction of energy emitted from the i^{th} source which is absorbed by the k^{th} target, and m_k is the mass of the target (Howell et al., 1999).

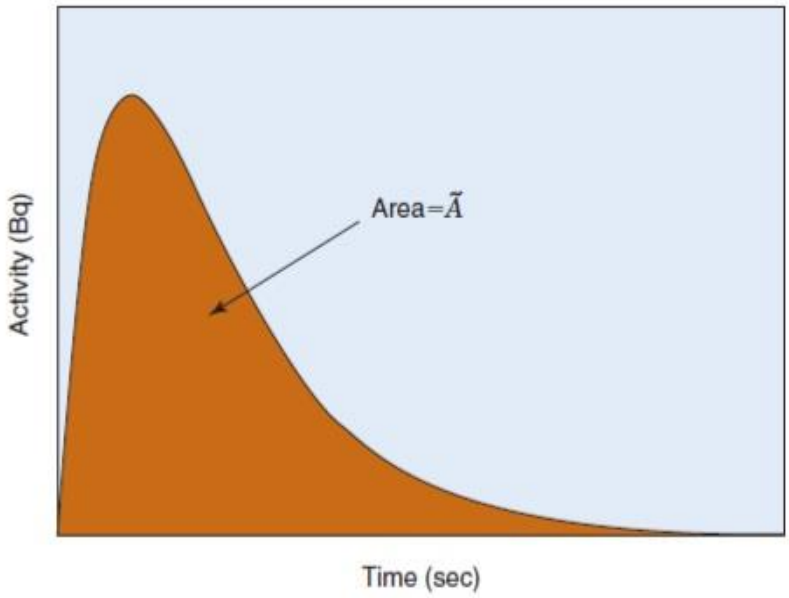

Figure4-1 Example time-activity curve for calculating the cumulated activity. From the graph, the cumulated activity is the area underneath or mathematical integration of the time-activity curve – Adapted from (Cherry et al., 2012)

The absorbed fraction term ($\emptyset_j$) depends on the emission type and energy and also the geometry of the source and target organ. Generally, this term is determined by Monte Carlo simulations. The photons (gamma rays and X-rays) take into account that some of the emitted energy will escape from the source organ due to their high penetration with variation due to the dimensions of tissue or organ. For therapeutic tracers (Auger electrons, beta and alpha particles), most energy is typically absorbed (non-penetrating emission), so the absorbed fraction from source to source organ ($\emptyset_{s \leftarrow s}$) is set to 1 and for source to target organ ($\emptyset_{t \leftarrow s}$) is set to 0. However, this assumption is only valid at macroscopic level when the size of organ is greater than the

particle track length (Stabin, 2006). The tissue absorbed fraction of photon versus electron or alpha particle is illustrated in figure below.

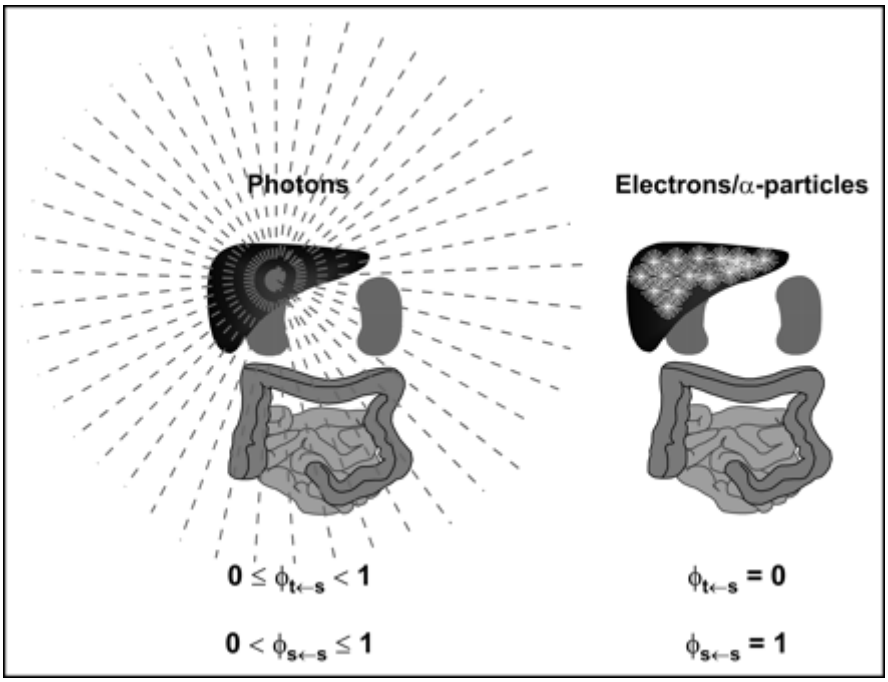

Figure 4-2 Gamma photons can irradiate distant organs while electrons/alpha particles will be absorbed within source tissue. However, it also depends on the energy, range and size of source organ – Adapted from (Roeske et al., 2008b)

The MIRD equation (eq. 4-1) can be simplified by defining the S-factor which is the mean absorbed dose per unit of cumulated activity. The S-values can be obtained by using analytical or computer (Monte Carlo) methods. The selection of method depends on the complexity of source-to-target geometry, and in some cases the S-value is not constant e.g. tumour dose with changing size during treatment.

In 1975, the MIRD committee published the S-values for 117 radionuclides with various pairs of source-target organs based on a mathematically defined adult anthropomorphic phantom. The reference phantom in MIRD pamphlet no. 5 was limited by data from planar imaging, with organ configurations based on geometric shapes (sphere, cylinder, cone etc.) as showed in figure 4-3. The S-values were computed by using data from the MIRD standard man phantom. The atomic composition and density were based on the report of ICRP reference man in 1975.

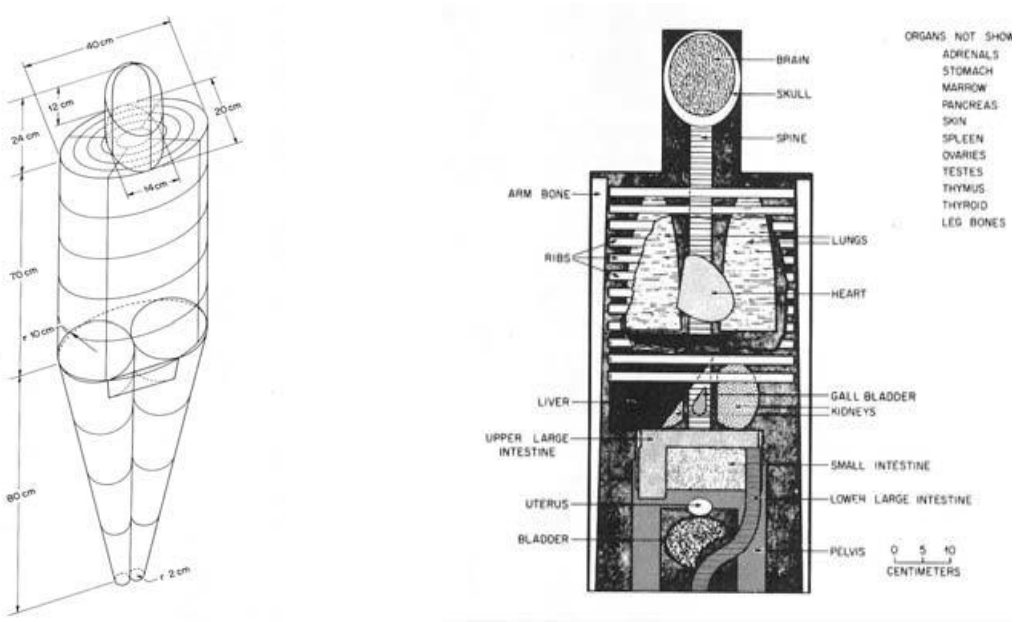

Figure 4-3 Reference Man Phantom from MIRD pamphlet no. 5 in 1975

The mathematical expression of the S-factor is described in the following equation.

$$S_{(k\leftarrow i)} = \frac{\sum \Delta_j \emptyset_j(k\leftarrow i)}{m_k} \qquad \text{Equation 4-2}$$

Where $\emptyset_j(k \leftarrow i)$ is the absorbed fraction for particular target organ (k) and source organ (i), m_k is mass of the target organ. Using the S-value, the equation (4-1) can be simplified as follows:

$$\overline{D} = \sum \widetilde{A}_i \, S(k \leftarrow i) \qquad \text{Equation 4-3}$$

4.1.1.2 Calculation Tools and Models

Many dosimetry programs have been developed from the MIRD formalism, for example MABDOSE (University of Colorado), INDOSE (Nuclear Energy Agency), MIRDOSE3 and OLINDA/EXM (Oak Ridge and RADAR) (Sgouros et al., 2010; Stabin, 2006). MIRDOSE is the most widely used software for medical internal dose calculations. MIRDOSE was first established in 1984 at Oak Ridge National Laboratory (ORNL). MIRDOSE 1 (Watson and Stabin 1984) was implemented in a Tektronix-PC.(2004; Stabin, 1996; Stabin and Siegel, 2003; Stabin et al., 1999). MIRDOSE 2 (Stabin 1987) migrated to DOS-PC. MIRDOSE 3 and 3.1 (Stabin 1996) run in the Windows PC (the software is not associated with the MIRD Committee of the SNM). The S-values in MIRDOSE 3.1 were calculated using the phantom series of Cristy and Eckerman. The six phantoms from this series allowed users to calculate dose estimates for children and adults of both genders. The pregnant female series by Stabin was also added to MIRDOSE 3.1. The table

of S-values for numerous radionuclides (>200 radionuclides) and about 25 source-target organs was made available in this software (Stabin, 1996). MIRDOSE was later replaced by the new generation software OLINDA/EXM (Organ Level Internal Dose Assessment/Exponential Modelling) in 2005 (Stabin et al., 2005). The OLINDA/EXM is written in the Java programming language and the Java Development Kit environment. There are several new features that have been developed from MIRDOSE software such as applications with alpha and beta emitters (over 800 radionuclides) and the programme (EXM part) consists of a multi-exponential curve fitting tool which allows the user to calculate the cumulated activities from measured bio-distribution data. OLINDA/EXM has incorporated new physical models such as the Stabin prostate gland model, the Watson & Stabin peritoneal cavity model, the Evans et al. spinal cord model, the MIRD head and brain model, the MIRD dynamic bladder and distribution of electrons in small spheres model. The dose agreement between MIRDOSE3.1 and OLINDA/EXM was within 1-2% for most cases. The OLINDA/EXM is the first computer dosimetry calculation software to receive US FDA approval (Stabin, 2007; Stabin et al., 2011; Stabin et al., 2005). In this chapter, the OLINDA/EXM was used to estimate absorbed doses, with details of calculations provided in the next sections.

4.1.2 Dosimetry for NIS Radiotracers

4.1.2.1 Effective Dose of NIS Radiotracers for Diagnostic Use

According to ICRP (International Commission on Radiological Protection), the effective dose is the summed radiation-risk weighted equivalent to organ and tissue (W_T), representing the potential risks from stochastic (mainly lethal cancer and serious hereditary disorder) from exposure to radiation. Primarily, this quantity was used for radiation protection of occupationally exposed persons. Nevertheless, the concept of effective dose is useful in nuclear medicine as this value can be used to compare the stochastic effects and relative risk from different examinations e.g. comparing dose to a patient injected with ^{123}I-NaI SPECT or ^{124}I-NaI PET imaging.(Charles, 2008; Johansson et al., 1984; Mattsson et al., 2011)

Radiation doses from diagnostic use of radiopharmaceuticals have been published in ICRP publication 53, 80 and 106. Basically, the ICRP report contains the absorbed doses to organs/tissues and the effective dose per unit of administered activity. Since ICRP 53 was published in 1988, the tissue/organ weighting factors have been revised twice and the quantity changed from “effective dose equivalent” to “effective dose”. The differences between the tissue

weighting factors of ICRP 60 and ICRP 103 are illustrated in the following table (Andersson et al., 2014; Charles, 2008; Mattsson et al., 2011).

Table 4-1compares weighting factors in ICRP publication 60 and 103

Tissue/Organ	Tissue/Organ Weighting Factor	
	ICRP 103 (2007)	**ICRP 60 (1991)**
Breast	0.12	0.05
Bone Marrow	0.12	0.12
Colon	0.12	0.12
Lung	0.12	0.12
Remainder	0.12[a]	0.05[b]
Stomach	0.12	0.12
Gonads	0.08	0.20
Bladder	0.04	0.05
Liver	0.04	0.05
Oesophagus	0.04	0.05
Thyroid	0.04	0.05
Bone Surfaces	0.01	0.01
Brain	0.01	-
Salivary Glands	0.01	-
Skin	0.01	0.01

a - Shared by remainder tissues (14 in total, 13 in each sex) adrenals, extrathoracic tissue, gall bladder, heart, kidneys, lymphatic nodes, muscle, oral mucosa, pancreas, prostate (male), small intestine, thymus, uterus/cervix (female)
b – Shared by the five most highly exposed

For NIS radiotracers, a range of isotopes has been used in nuclear medicine as mentioned in previous chapter. In 2011, a task group within ICRP published the effective dose in adults for commonly used radiopharmaceuticals (Mattsson et al., 2011). All doses have been calculated based on the MIRD formalism using published bio-kinetic data with the mathematical Cristy and Eckerman phantom. The S-values and tissue weighting factors were taken from MIRD pamphlet 11 and ICRP publication 60 respectively. The effective doses per unit administered activity (mSv/MBq) for adults with ICRP publication references for bio-kinetic models are illustrated in the following table.

Table 4-2 (Wrixon, 2008)Effective Dose per Administered Activity for Adults (Adapted from ICRP 2011)

Radiotracer	Effective Dose per Administered Activity (mSv/MBq)	ICRP no.
^{99m}Tc-pertechnetate without thyroid blocking	0.013	80
^{99m}Tc-pertechnetate with thyroid blocking	0.0042	80
^{123}I-iodide, 35% thyroid uptake	0.22	53/80
^{123}I-iodide, After ablation 1 % thyroid uptake	0.02	53
^{131}I-iodide, 35% thyroid uptake	24	53/80
^{131}I-iodide, After ablation 1 % thyroid uptake	0.5	53

More recently, the development of medical imaging techniques offered high resolution images (e.g. CT, MRI) together with the advanced nuclear medicine modalities and new generation of computer algorithms. In 2009, ICRP/ICRU published new adult reference voxel phantoms for male and female with more realistic details for organs size and shape. Recent work by Anderson M et al. (2014) published the effective dose using the new ICRP/ICRU phantom, updated radionuclide decay data (ICRP 107), the new human alimentary tract model and the latest tissue weighting factor from ICRP 103. Anderson M et al. also compared the results with the conventional data (Cristy & Eckerman Phantom with ICRP 60 tissue weighting factor-as displayed in table 4-3). The effective dose per unit administered activity from Anderson's work is shown in the table below.

Table 4-3 Effective dose from ICRP/ICRU phantom and tissue weighting factor ICRP 103 (Wrixon, 2008)

Radiotracer	Phantom-ICRP/ICRU W_T-ICRP 103 (mSv/MBq)	Comparison with previous data Phantom-MIRD W_T-ICRP 60 (%)
^{99m}Tc-pertechnetate without thyroid blocking	0.0159	22
^{99m}Tc-pertechnetate with thyroid blocking	0.00412	-2
^{123}I-iodide, 35% thyroid uptake	0.233	6
^{123}I-iodide, After ablation 1 % thyroid uptake	n/a	n/a
^{131}I-iodide, 35% thyroid uptake	22.2	-8
^{131}I-iodide, After ablation 1 % thyroid uptake	n/a	n/a

4.1.2.2 Dosimetry for NIS Radiotracers for Therapeutic Use

The administration of radioiodine (^{131}I-NaI) for therapeutic purposes has been commonly accepted for the treatment of benign and malignant disease of the thyroid gland since the 1940s (Lee et al., 2006).

The common indications of RAIT are classified in two types: benign nodular thyroid disease and thyroid malignancy according to EANM guidelines (Stokkel et al., 2010). RAIT is used for treatment of hyperthyroidism, and the effects of excessive action of thyroid hormone. Hyperthyroidism includes the following: (I) Grave's disease, (II) solitary hyper-functioning thyroid nodule, (III) Plummer's disease (toxic multi nodular goitre), (IV) silent and acute thyroiditis. Additionally, RAIT is also used to decrease the size of thyroid nodules and also for suppressing the function of the thyroid gland in non-toxic diffuse goitre and euthyroid multi-nodular goitre. In thyroid cancer, RAIT is used to ablate thyroid cancer and/or metastasis at local or systemic level after partial or complete thyroidectomy (Stokkel et al., 2010).

The fundamental molecular mechanism behind RAIT is the sodium iodide symporter (NIS) which is an intrinsic plasma membrane glycoprotein located at the baso-lateral plasma membrane of thyroid follicular cells. In normal thyroid, the thyroid follicle is formed from "colloid" surrounded by a single layer of follicular cells called "thyrocytes" (as shown in figure 4.4a and 4.4b). ^{131}I radioiodine (in the form of iodide ion) is trapped into follicular cells by NIS. This symporter co-accumulates both Na^+ and I^- into the cell with a 2:1 ratio of Na^+ to I^-. Then, iodide is moved apically into the colloid via the exporter protein pendrin and iodide is oxidised to iodine and then incorporated into tyrosyl residues in thyroglobulin. It then remains in the colloid until exported (fig 4.4c) (Champion et al., 2007a; Chung, 2002).

RAIT has a number of limitations and disadvantages. The ^{131}I radioiodine has a long physical half-life of 8 days and the abundant high-energy gamma rays (0.36 MeV, abundance 81.7%) cause a large fraction of the whole body radiation dose. These also irradiate other individuals especially medical staff, family and members of the public. Consequently, the treated patient needs isolation in a specially designed shielded ward for several days, and lifestyle restrictions for a further several weeks, causing great cost to health services and disruption of family life. Furthermore, the beta-particles emitted by ^{131}I-NaI are of relatively low energy (E_{mean} = 0.18 MeV) with a mean range in soft tissue of only 0.39 mm (Lee et al., 2006; Verburg et al., 2011).

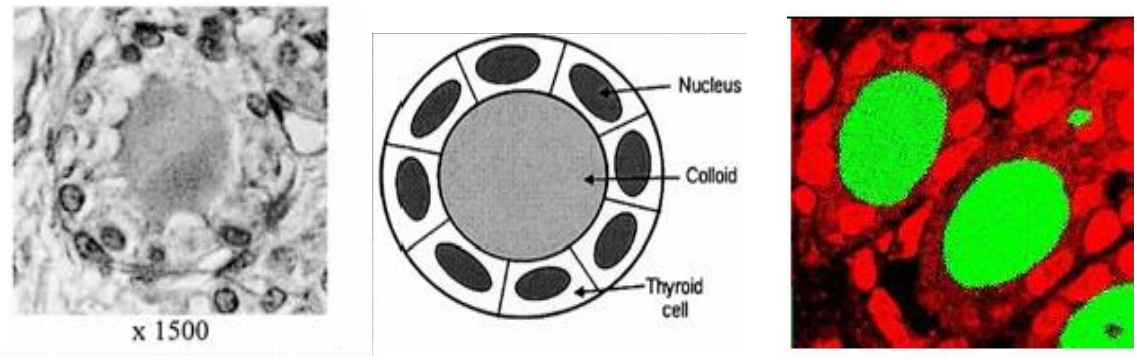

(a) **(b)** **(c)**

Figure 4-4 (a) Follicle of normal thyroid imaged by SIMS (secondary ion mass spectroscopy) (b) geometrical model, the thyroid follicles are formed from "colloid" surround by a shell of thyrocyte (c) digitised image with phosphorus (red) and iodine (green), Image shows that iodine is almost entirely located in the colloid and not thyrocytes. No corresponding micro-distribution data for perrhenate (ReO_4^-) are available but it is expected to localise in thyrocytes. Images were taken from Champion et al (Champion et al., 2007a)

In this study, we propose to evaluate a novel radionuclide therapy agent using rhenium radioisotopes (^{186}Re- and ^{188}Re-perrhenate). Perrhenate is also a substrate of NIS but not metabolised in processes of thyroid hormone production and hence once trapped in thyrocytes can slowly leak out rather than being semi-permanently trapped in the colloid. This means that whilst remaining in the thyroid, the perrhenate remains within thyrocytes rather than extracellular (in colloid). The radiobiological consequences of the different emission properties and the different location and shorter residence time would be interesting to ascertain; it is not obvious whether the effectiveness per emission would be greater or less than that of ^{131}I as a result. Several studies have reported the therapeutic application of other rhenium labelled compounds in systems that do not involved iodine metabolism, for example palliation of skeletal bone pain (using labelled HEDP), hepatic tumour (using labelled lipiodol) and neuroendocrine tumour (using labelled peptides) (Ferro-Flores and de Murphy, 2008; Jeong et al., 2001; Li et al., 2001). However, after the cloning of NIS followed by the development of the NIS gene transfer technique into various cancer cells, rhenium has become appealing for treatment of NIS-expressing tumours of non-thyroidal origin such as breast, prostate, liver and colon cancer (Dadachova, 2010; Dadachova et al., 2002; Dadachova et al., 2005; Willhauck et al., 2007).

^{188}Re-perrhenate is easily eluted from tungsten-188/rhenium-188 (^{188}W/^{188}Re) generators, which have a high elution yield (75 to 80% of the available ^{188}Re) and long shelf-life (more than 6 months for generator size of 7.4 GBq). The long shelf-life of generators may contribute to cost effectiveness for treatment in areas where ^{131}I is not available. The ^{188}W/^{188}Re generator can reach a 62% of equilibrium activity at 24 h after previous elution. Therefore, the

generator can be eluted every day with the breakthrough of W-188 kept generally very small within ($<10^{-3}$ %) over an extended shelf-life with further elimination by simple removal using an alumina column (Argyrou et al., 2013; Jeong and Knapp Jr, 2008a; Jeong and Knapp Jr, 2008b). Regarding the physical properties, ^{188}Re has a physical half-life of 16.7 h (compared to 192 h for ^{131}I) which is a good match to its biological half-life in non-organifying tumours. The long half-life of ^{131}I radioiodine results in increases radiation dose to organs and whole body as well as thyroid tissue. Also, Re-188 emits more energetic beta-particles (E_{mean} = 0.764 MeV) when compared with I-131 (E_{mean} = 0.182 MeV). The higher beta energy of ^{188}Re may offer improved radio-biological effectiveness when treating larger benign disease or tumours as the mean beta-particle range in soft tissue of ^{188}Re is 3.10 mm when compared with ^{131}I-NaI is 0.39 mm. The gamma photons of 0.15 MeV (15% abundance) emitted by ^{188}Re offer a more gentle profile for imaging than the 0.36 MeV (82% abundance) emitted by ^{131}I-NaI (Argyrou et al., 2013; Ferro-Flores and Arteaga de Murphy, 2008b). Also attractive is the dosimetric profile of another rhenium isotope, ^{186}Re which has a half-life of 90.6 hours, medium energy beta particles (E_{mean} 0.346 MeV and E_{max}1.070 MeV), and photon emissions suitable for gamma camera imaging (0.137 Mev with 9.4 % abundance). ^{186}Re is produced by nuclear processing using thermal reactor or cyclotron. The physical properties of ^{186}Re appear to be intermediate between ^{131}I and ^{188}Re, therefore it can be a therapeutic radionuclide of choice for benign thyroid disease or NIS-expressing tumours (Moustapha et al., 2006).

Regarding radiation protection, the dose contribution from gamma radiation emitted promptly with high energetic beta particles from both rhenium isotopes is of considerably lower energy and lower abundance than that form ^{131}I. Rhenium gamma photons are still detectable by a gamma camera for planar or SPECT (Single Photon Emission Tomography) imaging but imparts less whole body radiation dose when compared to conventional radioiodine. Consequently, the cost of radiation protection will be reduced due to lower demand on shielding and radioactive waste management provision. Furthermore, this may alleviate the need for isolation and hospitalisation of patients in specialised shielded rooms after treatment unlike patients treated with ^{131}I-NaI. Therefore, this will be a substantial cost saving for the healthcare system and shorter restrictions period for the patient's lifestyle and their families.

Table 4-4 Comparison Physical Characteristics of ^{131}I, ^{188}Re and ^{186}Re

Radionuclide	Half-life (h)	Energy of the main gamma (MeV) [Abundance (%)]	Mean energy of β^- emitted (MeV)	Maximum energy of β^- emitted (MeV)	Mean range in soft tissue (mm)	Maximum range in soft tissue (mm)
^{131}I	192	0.364 [82]	0.182	0.610	0.39	2.30
^{188}Re	16.9	0.155 [15]	0.764	2.120	3.10	11.00
^{186}Re	90.6	0.137 [9]	0.346	1.070	1.10	4.50

Owing to these potential advantages, rhenium is an excellence candidate for internal radionuclide therapy and we hypothesised that ^{188}Re- and ^{186}Re-perrhenate may offer several benefits over ^{131}I-NaI for radionuclide therapy of benign nodular thyroid disease and NIS-expressing tumours with better patient quality of life and treatment cost effectiveness in term of isotope production, healthcare and waste management.

4.2 Chapter Aims

The aims of this chapter are three-fold. The first part of this chapter aims to estimate and compare the human-equivalent effective dose of NIS radiotracers (^{99m}Tc-pertechnetate, ^{123}I-iodide ^{131}I-iodide and ^{188}Re-perrhenate and ^{18}F-BF4) for diagnostic use based on preclinical spatio-temporal data from mice presented in the previous chapter. The dose comparison studies were conducted on the same strain, sex- and age-matched animals to allow for dosimetric comparison to approximate radiation dose for diagnostic clinical use of these tracers.

Secondly, this chapter aims to evaluate the potential of rhenium (^{186}Re- and ^{188}Re-) in the form of perrhenate (ReO_4^-) as alternative therapeutic agent compared with conventional ($^{131}I^-$) radioiodine, with the primary intention to examine the dosimetric feasibility in the treatment of benign nodular thyroid diseases and NIS-expressing tumours based on mouse model bio-kinetic data. The absorbed doses in critical organs together with whole-body and effective doses were computed on the basis of extrapolated animal data from the previous chapter using the OLINDA dosimetry software package.

Thirdly, this chapter aims to examine the impact of the partial volume effect (PVE) on dosimetry calculation from preclinical imaging data. The recovery coefficient obtained earlier from the multi-hollow sphere phantom in Chapter 2 will be applied to the *in vivo* kinetic data in Chapter 3. This correction would allow us to investigate the impact on the dosimetric error of small-objects/organs in preclinical research.

4.3 Materials and Methods

The details of animal experiments, radiotracers, image acquisition, and data analysis for spatio-temporal quantification were described in chapter 3. In our study, we used the healthy animal data without a thyroid-blocking agent or exogenous thyroid hormone to represent the uptake of benign nodular thyroid disease. For NIS expressing tumours, the data from xenografted mice bearing breast adenocarcinoma cell line (MTLn3E) overexpressing truncated CXCR4 and human sodium iodide symporter (hNIS) discussed in previous sections were used to calculate dosimetry in this chapter.

4.3.1 Dosimetry Calculations

To extrapolate the human dose from the preclinical data, the linear mass scaling by Kirschner originally published in 1973 was applied to account for uptake differences between animal and human (Kirschner et al., 1973). In this work, equation 4-4 was used to convert percentage uptake per gram of organ (%ID/g) in mice to percentage uptake in organ (%ID) in human (Chang et al., 2012; Chung et al., 2010b).

$$(\%ID)_{human} = \left[\left(\frac{\%ID}{g_{organ}}\right)_{animal} \times g_{WB\ animal}\right] \times \left(\frac{g_{organ}}{g_{WB}}\right)_{human} \quad \text{Equation 4-4}$$

All measured pre-clinical mouse values were extrapolated to human values using the above equation. Effectively, this model assumes preservation of standard uptake values (SUV) across species. The human organ weights were extracted from the Cristy-Eckerman and Stabin-Siegal standard phantom series for the total body mass of a reference adult male (73700 g) and female non-pregnant (56912 g) which were implemented and used in the OLINDA/EXM human dosimetry software version 1.1 (Vanderbilt University, Nashville, TN, USA). Animal organ masses in this study were taken from age- and sex-matched groups as discussed in the previous chapter. The values for selected mouse organs and standard human masses are illustrated in the following table:

Table 4-5 Size of selected relevant organs in mouse and standard phantom

Organ	Mice (n=14)		Standard Phantom in OLINDA	
	Weight (g)	SD	Male (g)	Female (g)
Thyroid (dissected under microscope)	0.0169	0.0052	20.7	17
Salivary Glands	0.1165	0.0255	n/a	n/a
Stomach	0.2613	0.0709	158	140
Urinary Bladder	0.818	0.0189	47.6	35.9
Whole-Body	22.71	2.38	73700	56912

The human extrapolated time-activity curves (TACs) were generated as the function of time post injection (h) and non-decay-corrected human data (%ID). The source organ cumulated activity ($\tilde{A}$) was estimated by integrating TACs using MATLAB software version R2011b (MathWorks Inc., USA). The area under the curve beyond the last measured point was extrapolated to infinity using a single exponential based on the effective half-life from the last 2 or 3 measured points (Behr et al., 1997). Consequently, the total accumulated activity (A) in each source organ was defined as:

$$\tilde{A} = \int_0^\infty A(t)dt \qquad \text{Equation 4-5}$$

From the cumulated activity, the residence times for each source organ, which can be called “normalised cumulated activity”, were obtained and input into the OLINDA/EXM software version 1.1. The MIRD principal equation (equation 4-3) was simplified as follows:

$$\mathrm{D} = \mathrm{N} \times \mathrm{DF} \qquad \text{Equation 4-6}$$

Where N is the number of disintegrations that occur in the source organ and DF is mathematically the same as S-factor which is defined by the MIRD committee (Stabin et al., 2005).

The outputs of OLINDA/EXM are the organ absorbed dose (mGy) per administered activity for source and target organs and the effective dose (mSv) based on the tissue weighting factor from ICRP publication 60. In this study, we also introduced the therapeutic dose ratio , i.e. thyroid absorbed dose to effective dose ratio (mGy/mSv), a tumour absorbed dose to effective dose ratio (mGy/mSv) and a tumour absorbed dose to thyroid absorbed dose ratio in order to compare therapeutic efficiency. The details are described in the following section.

4.3.1.1 Source Organ

In this study, thyroid, salivary glands, stomach, urinary bladder and the remainder of the body were designated as the source organs. The uptake for the remainder of body was calculated as the whole-body uptake after subtracting all other evaluated organs. Also, it is important to note that the radioactivity was assumed to be uniformly distributed in all source organs and throughout the remainder of the body. Also, OLINDA/EXM provided the ICRP 30 GI (gastro-intestinal) and urinary voiding model to estimate the dosimetry in the excretory organ but we did not include these models in our calculation after considering the variation from anaesthetised mice to awake human physiology in these systems.

4.3.1.2 S-values for Salivary Gland and Tumour

As the current version of OLINDA/EXM software has not included the salivary glands which appears to be a major uptake organ for NIS radiotracers in humans and also in laboratory animals, the radiation absorbed doses to salivary glands were estimated by using a spherical S-value typically used for interpolating self-dose for tumour in OLINDA. The mass of the human salivary gland was assumed to be 77 g for both male and female (Chin et al., 2014; Coleman et al., 2009).

The tumour S-values were computed based on considering tumour to be a sphere. The OLINDA sphere-model was assumed with uniformly distributed activity. For calculation of tumour dosimetry, the standard human phantom was assumed to be bearing a 2 g tumour. Therefore, the actual dissected tumour mass from each xenograft mouse was extrapolated to a 2 g tumour so that a TAC was generated for use in dosimetry based on the method described for other organs. It is important to note that, the dosimetric calculations were performed without accounting for changes in tumour size (Coleman et al., 2009; Stabin et al., 2005) or taking into account differences of levels of NIS expressed in tumours across species.

4.3.2 Statistical Analysis

For the statistical analysis, every dynamic TAC was considered separately and the residence time from each mouse was individually input to the OLINDA software. The mean and standard deviation (SD) were considered across all time-points in the scan. All of %ID, %ID/g, organ absorbed dose, tumour absorbed dose, effective dose and all therapeutic index were expressed as mean ± SD.

4.4 Results

4.4.1 Effective Dose of NIS Radiotracers for Diagnostic Use

To estimate the effective dose, the spatio-temporal data from healthy mice from the previous chapter were used for human dosimetry calculation in this chapter. The animal data were extrapolated to human by the commonly used Krischer's linear mass scaling equation in order to predict the human-equivalent bio-distribution. The extrapolated human-equivalent uptakes derived from preclinical data are shown in the following figures 4.6. In this study, the human-equivalent of standard male and female were computed from female mouse data, assuming that the percentage injected dose multiplied by the body weight is constant across species.

Figures 4-5 below illustrates extrapolated human-equivalent percent injected dose in 4 source organs; thyroid, salivary glands, stomach and urinary bladder. The values in each graph are averages across 3 mice at 15 min, 1 hr, 4 hr, 8 hr and 24 hr post injection.

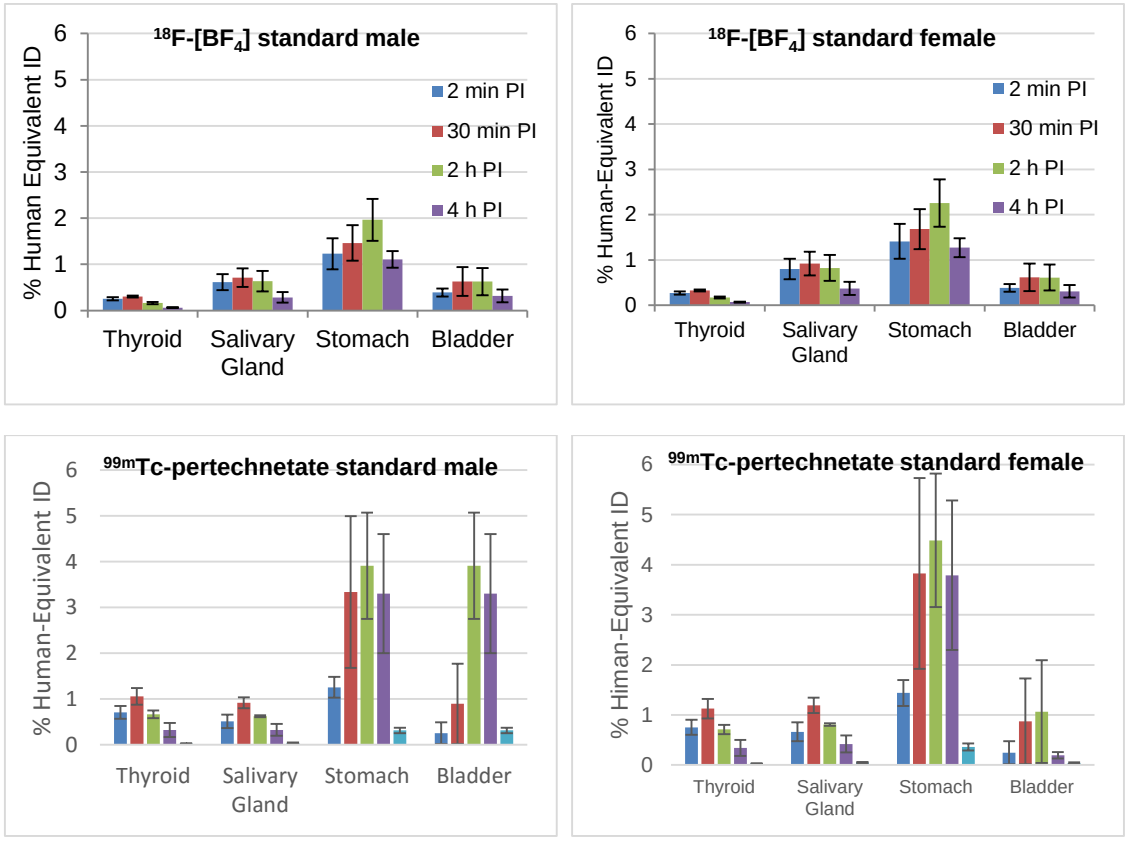

Figure 4-5 Extrapolated human-equivalent percentage uptake using Krischer's mass scaling method, data were expressed as mean and standard deviation (Top Left) ^{18}F-[BF$_4$] standard male, (Top Left) ^{18}F-[BF$_4$] standard female, (Bottom Left) ^{99m}Tc-pertechnetate standard male and (Bottom Right) ^{99m}Tc-pertechnetate female

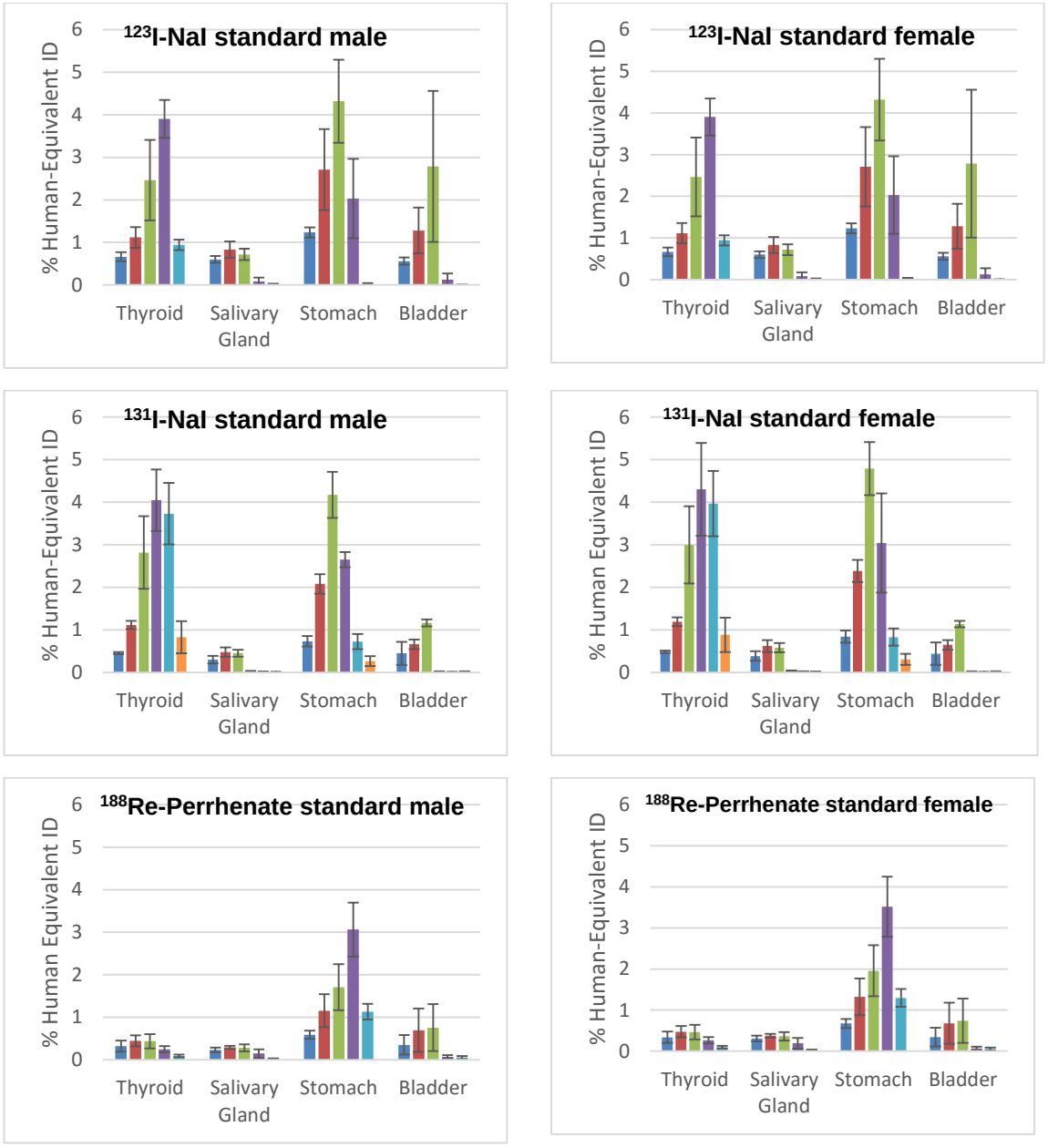

Figure 4-6 Extrapolated human-equivalent percentage uptake using Krischer's mass scaling method (A and B) ^{123}I-NaI standard male and female (C and D) ^{131}I-NaI standard male and female (E and F) ^{188}Re-Perrhenate standard male and female (n=3 for each radiotracer)

Based on the human-equivalent uptake, the time-activity curves were constructed then the tracer residence times for humans in 4 source organs (thyroid, salivary glands, stomach and bladder) and remainder of the body were calculated. The area under the TAC from initial time-point (t=0) to infinity is equivalent to residence time (also called "time-integrated activity coefficient" by MIRD pamphlet 21) and these values were input to OLINDA in order to estimate the human-equivalent doses. The mean tracer residence times and standard deviations are presented in the following table.

Table 4-6 Human equivalent residence times (mean ± SD, in Becquerel-hour per Becquerel administered) of NIS radiotracers (n=3 for each radiotracer)

Radiotracers – Source Organs	**Human Equivalent Residence Times** (Bq-hr/Bq)	
	Male	**Female**
^{18}F-[BF_4]		
Thyroid	0.008 ± 0.001	0.009 ± 0.001
Salivary Glands	0.030 ± 0.010	0.039 ± 0.013
Stomach	0.097 ± 0.017	0.111 ± 0.019
Bladder	0.035 ± 0.012	0.034 ± 0.011
Remnant of the Body	3.150 ± 0.580	3.127 ± 0.580
^{99m}Tc-pertechnetate		
Thyroid	0.083 ± 0.022	0.089 ± 0.024
Salivary Glands	0.079 ± 0.014	0.103 ± 0.018
Stomach	0.596 ± 0.169	0.683 ± 0.194
Bladder	0.087 ± 0.057	0.085 ± 0.056
Remnant of the Body	7.178 ± 0.733	7.064 ± 0.739
^{123}I-NaI		
Thyroid	0.722 ± 0.011	0.767 ± 0.012
Salivary Glands	0.039 ± 0.009	0.050 ± 0.012
Stomach	0.378 ± 0.073	0.433 ± 0.084
Bladder	0.146 ± 0.090	0.143 ± 0.088
Remnant of the Body	8.875 ± 0.914	8.766 ± 0.908
^{131}I-NaI		
Thyroid	1.649 ± 0.099	1.779 ± 0.066
Salivary Glands	0.039 ± 0.008	0.050 ± 0.010
Stomach	0.694 ± 0.056	0.797 ± 0.064
Bladder	0.067 ± 0.008	0.066 ± 0.008
Remnant of the Body	18.916 ± 0.626	18.675 ± 0.595
^{188}Re-perrhenate		
Thyroid	0.072 ± 0.022	0.077 ± 0.024
Salivary Glands	0.037 ± 0.014	0.048 ± 0.018
Stomach	0.751 ± 0.098	0.861 ± 0.112
Bladder	0.069 ± 0.020	0.067 ± 0.020
Remnant of the Body	9.133 ± 0.167	9.008 ± 0.176

In our dosimetric calculations, the residence times from each mouse were input separately into OLINDA. Therefore, the variation in mean effective doses resulted from the dose variation stemming from bio-kinetic variation across animals. The effective dose comparison shown below was conducted from the same strain-, sex- and age-matched animals to allow proper dosimetric comparison. The organ weighing factors used in the calculations were based on ICRP 60.

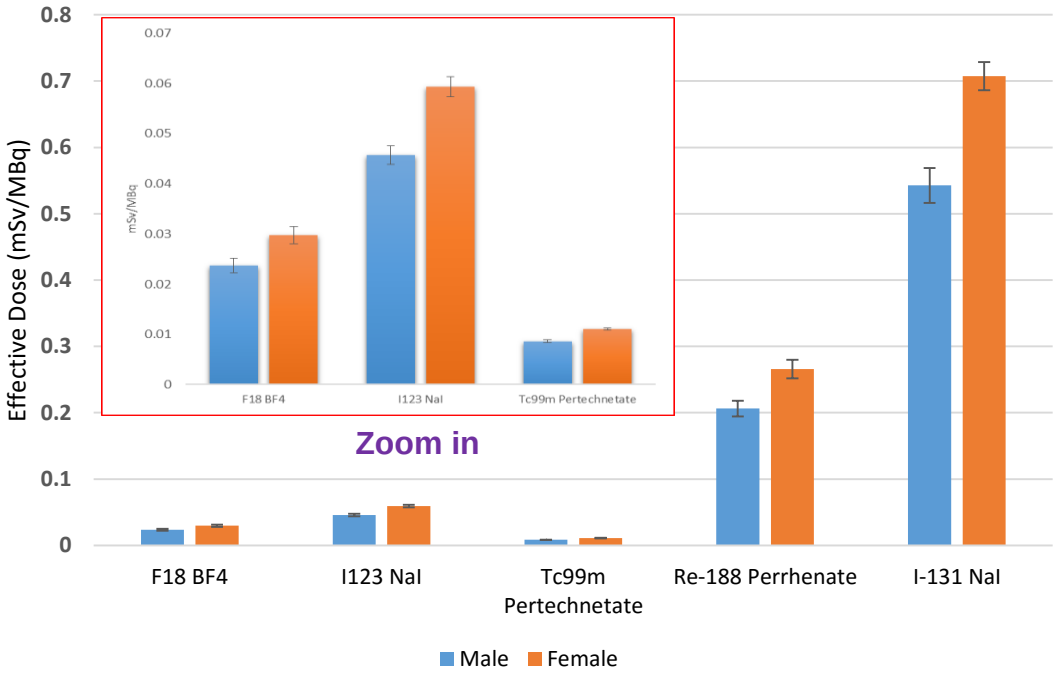

Figure 4-7 Mean human-extrapolated effective dose per unit administered activity (mean ± SD) in units of mSv/MBq (n=3 for each radiotracer); data comparison for 5 NIS-radiotracers based on weighting factors from ICRP 60

The mean of human-equivalent effective dose from the PET radiotracer $^{18}F\text{-}BF_4$ was 0.024 ± 0.001mSv/MBq for the standard adult male model and 0.030 ± 0.002mSv/MBq for the standard adult female model. The mean effective doses for established SPECT radiotracers were: for ^{123}I-iodide 0.046 ± 0.002mSv/MBq and 0.059± 0.002mSv/MBq for male and female model, and for ^{99m}Tc-pertechnetate 0.009 ± 0.001mSv/MBq and 0.011 ± 0.001mSv/MBq for male and female model respectively. The effective doses from therapeutic agents were higher as expected for ^{131}I-iodide: 0.543 ± 0.026mSv/MBq and 0.707 ± 0.021 mSv/MBq for male and female model, and for ^{188}Re-perrhenate 0.206 ± 0.012mSv/MBq and 0.266 ± 0.021mSv/MBq for male and female respectively.

As mentioned earlier, the effective dose calculated by OLINDA software version 1.0 (as shown in figure 4-7) was based on tissue-weighting factors from ICRP 60 (1990). However, the

latest tissue weighting factors from ICRP (103) were announced by ICRP in 2007. In this study, we also calculated the effective dose based on the new ICRP guideline from the output of OLINDA. Furthermore, we included the dose from the salivary gland into the effective dose using the S-value from sphere as described above. Therefore, the sum of tissue-weighting factors for these calculations was 0.93, instead of 1 because some organs contributing to effective dose were not listed in OLINDA. For comparison, the effective dose calculations were performed for each NIS radiotracer in 3 different ways (a) original OLINDA (W_T-ICRP 60, salivary gland included in remainder of the body), (b) W_T-ICRP 60 with salivary glands excluded from remainder of the body and assuming S-value of salivary glands from the sphere model and (c) ICRP 103 weighting factors excluding salivary glands from remainder of the body and assuming S-value of salivary glands from sphere model. The effective doses from 3 different methods are given in the table below.

Table 4-7 Mean human-equivalent effective doses from NIS radiotracers determined using 3 different methods, the effective dose shown as the mean effective dose per unit administered activity (mSv/MBq) with n=3 for each radiotracer

Radiotracers	**Mean Effective Dose Male (mSv/MBq)**				
	Original OLINDA (a)	ICRP 60 and SG Sphere (b)	%difference from original (%)	ICRP 103 and SG Sphere (c)	%difference from original (%)
^{18}*F-BF$_4$*	2.37E-02	2.35 E-02	-0.56	2.40 E-02	1.51
^{99m}*Tc-Pertechnetate*	8.63E-03	8.59E-03	-0.46	8.52E-03	-1.29
^{123}*I-NaI*	4.57E-02	4.65 E-02	1.75	4.16 E-02	-9.06
^{131}*I-NaI*	5.43E-01	5.42E-01	-0.06	4.79E-01	-11.80
^{188}*Re-Perrhenate*	2.06E-01	2.06E-01	-0.16	2.05E-01	-0.54
	Mean Effective Dose Female (mSv/MBq)				
^{18}*F-BF$_4$*	2.98 E-02	2.96 E-02	-0.67	2.96 E-02	-0.70
^{99m}*Tc-Pertechnetate*	1.11 E-02	1.10 E-02	-0.90	1.07 E-02	-2.94
^{123}*I-NaI*	5.93 E-02	5.93 E-02	0.00	5.28 E-02	-11.09
^{131}*I-NaI*	7.07 E-01	7.07 E-01	0.00	6.21 E-01	-12.25
^{188}*Re-Perrhenate*	2.66E-01	2.66 E-01	0.00	2.61 E-01	-1.60

The effective doses were slightly changed (approximately in the range of ± 1%) when excluding the salivary glands from the remnant of the body and assuming a specific S-value of salivary glands from the sphere model. Interestingly, the effective doses were decreased by about 10% for iodide isotopes (^{123}I- and ^{131}I-NaI), whereas, the estimated effective doses were a little bit lower when calculated with the most recent tissue weighting factors (ICRP 103),

4.4.2 Dosimetry and Potential Use of ^{188}Re and ^{186}Re-perrhenate in benign nodular thyroid diseases and NIS-expressing xenograft model

The second part of this chapter was intended to examine the dosimetric possibility of using ^{186}Re- and ^{188}Re-perrhenate in treatment of benign nodular thyroid disease and breast adenocarcinoma expressing NIS tumour by using preclinical data for comparison with ^{131}I-NaI.

4.4.2.1 Benign Nodular Thyroid Disease

In our study, we used the healthy animal data without a thyroid-blocking agent and exogenous thyroid hormone to represent the uptake of benign nodular thyroid disease. As mentioned in the discussion part of chapter 3, the pharmacokinetics of ^{188}Re-perrhenate and ^{99m}Tc-pertechnetate were characterised as very similar but the uptake values of ^{188}Re were fairly low when compared to ^{99m}Tc. These might be influenced by the elevated background counts from septal penetration and a strong Bremsstrahlung component which has a broad spectrum and by random noise from low-abundance of gamma photon of ^{188}Re. Hence, all these effects contributed to high background counts in the image with consequent effects in image quantification. In a clinical setting, the correction of this effect could be performed using scatter correction techniques such as triple energy window (TEW) together with a medium energy collimator to limit septal penetration, or a reconstruction based method that includes a model for such background photons. However, this is still problematic for a multi-pinhole acquisitions with the nanoScan SPECT/CT because at this stage, the system does not allow users to re-import raw projection data after processing (e.g. subtraction of energy windows) or intervene with the image reconstruction in the HISPECT reconstruction software.

The estimated organ absorbed doses to thyroid, salivary glands, stomach, red marrow, urinary bladder and total body (mGy), as well as effective dose (mSv) based on ICRP 60 for the standard male and female, are listed in table 4-8. The table shows the human-equivalent dosimetry calculated based on the ^{188}Re-perrenate.

Furthermore, since our study indicated that pharmacokinetics of perrhenate and pertechnetate were characterised as similar but the relative uptake of ^{188}Re was relatively low, possibly due to systemic error explained earlier, we therefore attempted to recalculate using pertechnetate kinetic data with applied ^{188}Re physical half-life to perform the human-equivalent dosimetry. The key assumption here was that changing isotope does not alter the bio-distribution or pharmacokinetics.

Table 4-8 Estimated human equivalent dose (mGy/MBq), effective dose (mSv/MBq) and thyroid to effective dose ratio from ^{188}Re-Perrhenate, ^{188}Re-Perrhenate (based on ^{99m}Tc-pertechnetate kinetic) and ^{131}I-NaI in reference adult male and female. Values are expressed as mean ± SD (n=3 for each radiotracer)

Organ Absorbed Dose (mGy/MBq)	Male		
	Re-188	Re-188 (based on $^{99m}TcO_4^-$ kinetics)	I-131
Thyroid	1.512 ± 0.465	3.087 ± 0.716	9.453 ± 0.564
Salivary Glands	0.212 ± 0.079	0.892 ± 0.249	0.063 ± 0.013
Stomach Wall	0.697 ± 0.082	1.253 ± 0.276	0.227 ± 0.016
Urinary Bladder Wall	0.131 ± 0.021	0.241 ± 0.073	0.074 ± 0.004
Red Marrow	0.077 ± 0.062	0.023 ± 0.003	0.045 ± 0.001
Whole-body Dose	0.059 ± 0.001	0.035 ± 0.004	0.054 ± 0.002
Effective Dose (mSv/MBq) ICRP 60 W_T	0.206 ± 0.014	0.339 ± 0.030	0.543 ± 0.026
Thyroid to Effective Dose Ratio	7.340	9.106	17.410
Thyroid to Whole-body Dose Ratio	25.627	88.200	175.056
	Female		
	Re-188	Re-188 (based on $^{99m}TcO_4^-$ kinetics)	I-131
Thyroid	1.950 ± 0.601	3.980 ± 0.923	12.367 ± 0.451
Salivary Glands	0.275 ± 0.103	1.155 ± 0.322	0.081 ± 0.016
Stomach Wall	0.905 ± 0.109	1.623 ± 0.355	0.295 ± 0.020
Urinary Bladder Wall	0.168 ± 0.027	0.305 ± 0.092	0.088 ± 0.005
Red Marrow	0.049 ± 0.001	0.026 ± 0.004	0.055 ± 0.002
Whole-body Dose	0.076 ± 0.001	0.045 ± 0.006	0.068 ± 0.002
Effective Dose (mSv/MBq)	0.266 ± 0.018	0.437 ± 0.038	0.707 ± 0.021
Thyroid to Effective Dose Ratio	7.331	9.108	17.492
Thyroid to Whole-body Dose Ratio	25.658	88.444	181.868

The estimated doses were higher in female than in male subjects as expected. The largest mean absorbed dose was received by thyroid which is our target treatment organ for both radiotracers. By using actual ^{188}Re kinetics, the thyroid absorbed doses were calculated to be 1.512 ± 0.465 mGy/MBq for adult male and 1.950 ± 0.601 mGy/MBq for adult female. The estimated thyroid absorbed doses from ^{188}Re (based on ^{99m}Tc-pertechnetate kinetics) were 3.087 ± 0.716 and 3.980 ± 0.923 mGy/MBq for male and female respectively while for I-131, the thyroid absorbed doses were 9.453 ± 0.564 mGy/MBq for male and 12.367 ± 0.451 mGy/MBq for female. The thyroid to effective dose ratio for conventional radioiodine (^{131}I) was still found to be greater than ^{188}Re-perrhenate (about 7.34 for actual ^{188}Re, 9.10 mGy/mSv for ^{188}Re based on ^{99m}Tc kinetic and 17.45 mGy/mSv for ^{131}I). In the same manner, the thyroid to whole-body dose ratio for 131I-NaI was also higher than ^{186}Re- and ^{188}Re-perrhenate.

Based on the dynamic animal data as described in chapter 3, the uptake in stomach and urinary bladder were very variable across animals and these factors strongly influenced uptake in other NIS expressing organs. The biological factors affecting tracer uptake (such as diet, fluid intake, voiding of bladder and anaesthesia) are very difficult to control in animal studies whereas for clinical application such factors may be possible to control. For example for urinary bladder, patients can be encouraged to have high fluid intake and to frequently void, also administration of diuretic drug is possible in order to accelerating renal clearance (Seabold et al., 1993). Thus, we also analysed the data by eliminating/removing the activity in the urinary bladder. As explained earlier about image noises and artefacts with ^{188}Re, these dosimetric results for rhenium isotopes (^{186}Re- and ^{188}Re-perrhnate) were calculated using pertechnetate kinetics whereas actual ^{131}I-NaI kinetics were used for conventional radioiodine.

Table 4-9 Human equivalent organ absorbed dose (mGy/MBq) and effective dose (mSv/MBq) from ^{131}I-NaI versus ^{188}Re-, ^{186}Re-Perrhenate based on ^{99m}Tc-pertechnetate kinetic in adult male and female. These data were modified from previous table by eliminating the urinary bladder. Dosimetric data were extrapolated from normal mouse without hormone supply and thyroid blocking agent representing conditions relevant to the thyroid nodular goitre. Values are expressed as mean ± SD (n=3 for each radiotracer)

Organ Absorbed Dose (mGy/MBq)	Male			Female		
	I-131	Re-186 (based on $^{99m}TcO_4^-$ kinetics)	Re-188 (based on $^{99m}TcO_4^-$ kinetics)	I-131	Re-186 (based on $^{99m}TcO_4^-$ kinetics)	Re-188 (based on $^{99m}TcO_4^-$ kinetics)
Thyroid	9.140 (± 0.599)	2.087 (± 0.368)	3.247 (± 0.781)	11.833 (± 0.764)	2.953 (± 0.488)	4.220 (± 0.958)
Salivary Glands	0.065 (± 0.013)	0.776 (± 0.321)	0.925 (± 0.262)	0.084 (± 0.016)	1.003 (± 0.412)	1.198 (± 0.340)
Stomach Wall	0.177 (± 0.107)	1.130 (± 0.182)	1.262 (± 0.240)	0.300 (± 0.021)	1.360 (± 0.061)	1.630 (± 0.306)
Urinary Bladder Wall	0.056 (± 0.001)	0.011 (± 0.003)	0.032 (± 0.004)	0.064 (± 0.002)	0.014 (± 0.003)	0.039 (± 0.006)
Red Marrow	0.045 (± 0.001)	0.008 (± 0.002)	0.023 (± 0.003)	0.055 (± 0.002)	0.009 (± 0.002)	0.026 (± 0.004)
Whole-body Dose	0.055 (± 0.001)	0.015 (± 0.003)	0.035 (± 0.004)	0.068 (± 0.002)	0.018 (± 0.003)	0.044 (± 0.005)
Effective Dose (mSv/MBq)	0.521 (± 0.023)	0.248 (± 0.020)	0.338 (± 0.028)	0.678 (± 0.0037)	0.322 (± 0.027)	0.436 (± 0.034)
Thyroid to Effective Dose Ratio	**17.543**	**8.415**	**9.607**	**17.453**	**9.171**	**9.679**
Thyroid to Whole-body Dose Ratio	**166.182**	**139.133**	**92.771**	**174.015**	**164.056**	**95.909**

By removing urinary bladder, the conventional radioiodine also showed superior ratio (thyroid to effective dose ratio) over ^{186}Re- and ^{188}Re-perrhenate. In addition, EANM guideline suggested that medication such as H-2 blocker and liberal oral hydration can be used to decrease stomach activity (Luster et al., 2008). Furthermore, invasive methods such as gastric lavage have also been reported in a US patent by Dadachova (Dadachova, 2010). Hence, we analysed the data again by eliminating and removing the activity in both stomach and urinary bladder to anticipate such clinically controlled conditions. The data were shown in table 4-10. The dosimetric estimation of rhenium isotopes were still based on ^{99m}Tc-pertechnetate kinetic as explained earlier.

Table 4-10 Human equivalent organ absorbed dose (mGy/MBq) and effective dose (mSv/MBq) from ^{131}I-NaI ^{188}Re-Perrhenate and ^{186}Re-Perrhenate in reference adult male and female. These data set were modified from previous table by eliminating the stomach and urinary bladder Data were extrapolated from normal mouse without hormone supply and thyroid blocking agent representing conditions relevant to the thyroid nodular goitre. Values are expressed as mean ± SD (n=3 for each radiotracer)

Organ Absorbed Dose (mGy/MBq)	Male			Female		
	I-131	Re-186 (based on $^{99m}TcO_4^-$ kinetics)	Re-188 (based on $^{99m}TcO_4^-$ kinetics)	I-131	Re-186 (based on $^{99m}TcO_4^-$ kinetics)	Re-188 (based on $^{99m}TcO_4^-$ kinetics)
Thyroid	10.233 (± 0.153)	3.387 (± 0.458)	5.043 (± 0.576)	13.200 (± 0.200)	4.383 (± 0.589)	6.510 (± 0.747)
Salivary Glands	0.063 (± 0.013)	1.145 (± 0.432)	1.451 (± 0.264)	0.081 (± 0.016)	1.481 (± 0.559)	1.881 (± 0.344)
Stomach Wall	0.056 (± 0.002)	0.020 (± 0.002)	0.041 (± 0.003)	0.070 (± 0.002)	0.026 (± 0.002)	0.053 (± 0.004)
Urinary Bladder Wall	0.057 (± 0.002)	0.020 (± 0.002)	0.041 (± 0.003)	0.066 (± 0.002)	0.026 (± 0.002)	0.053 (± 0.004)
Red Marrow	0.046 (± 0.001)	0.014 (± 0.001)	0.029 (± 0.002)	0.056 (± 0.002)	0.018 (± 0.002)	0.035 (± 0.002)
Whole-body Dose	0.055 (± 0.002)	0.021 (± 0.002)	0.043 (± 0.003)	0.069 (± 0.002)	0.027 (± 0.002)	0.055 (± 0.004)
Effective Dose (mSv/MBq)	0.562 (± 0.006)	0.187 (± 0.022)	0.288 (± 0.029)	0.723 (± 0.008)	0.242 (± 0.029)	0.371 (± 0.038)
Thyroid to Effective Dose Ratio	**18.208**	**18.112**	**17.510**	**18.257**	**18.112**	**17.547**
Thyroid to Whole-body Dose Ratio	**186.055**	**161.286**	**117.279**	**191.304**	**162.333**	**118.364**

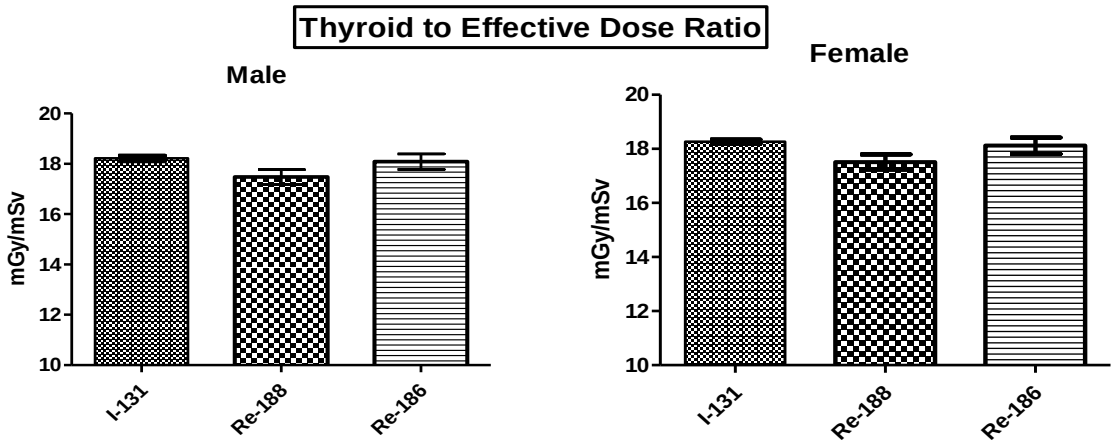

Figure 4-8 Thyroid to Effective Dose Ratio calculated from normal mouse of ^{131}I-NaI and ^{188}Re-Perrhenate and ^{186}Re-Perrhenate (based on 99mTc-pertechnetate kinetic) after eliminating the stomach and urinary bladder activity

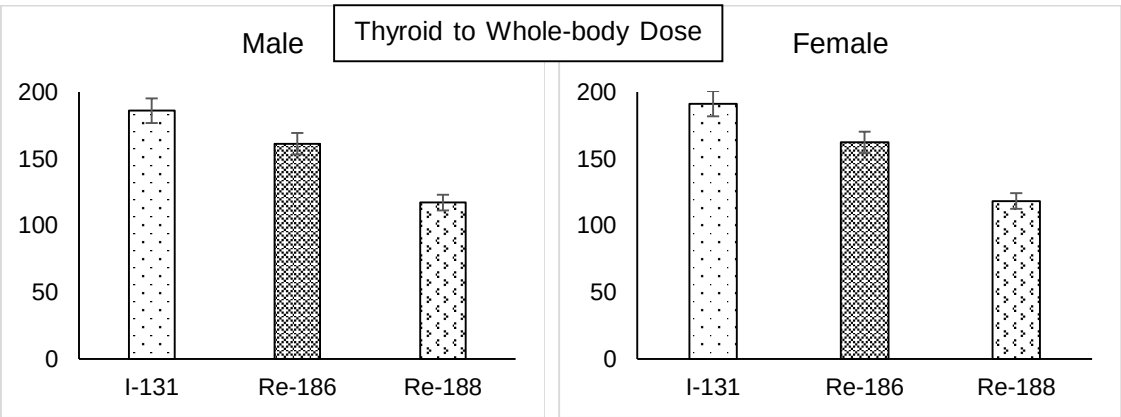

Figure 4-9 Thyroid to Whole-body Dose Ratio calculated from normal mouse of ^{131}I-NaI and ^{188}Re-Perrhenate and ^{186}Re-Perrhenate (based on ^{99m}Tc-pertechnetate kinetic) after eliminating the stomach and urinary bladder activity

By eliminating the stomach and urinary bladder activity, the thyroid to effective dose ratios for rhenium (as illustrated in figure 4.8) were found identical to iodine demonstrating that the same thyroid absorbed dose from rhenium results in equal effective dose (based on ICRP 60). Furthermore, the red marrow, stomach, whole-body and bladder absorbed doses from rhenium were less than that produced by conventional radioiodine. However, the thyroid to whole-body dose ratio for conventional radioiodine (^{131}I) was still found to be greater than ^{186}Re- and ^{188}Re-perrhenate.

In addition, we also calculated the thyroid to effective dose ratio using the current tissue weighting factors from ICRP publication 103 (2007) with and without thyroid listed on the radiation weighted dose quantity (showed in table 4-11). As in this study, thyroid is the main treatment target. According to ICRP publication 103, the radiation weighted dose quantity for thyroid is 0.04 (4%) whereas in ICRP 60 (1991), thyroid is contributed 0.05 (5%) from tissue lists.

Table 4-11 Thyroid to effective dose ratio based on effective dose calculated with ICRP 60 and ICRP 103 (with and without thyroid included in tissue weighing factor)

Effective Dose Calculation Method	Thyroid to Effective Dose Ratio					
	Male			Female		
	I-131	Re-186 (based on ^{99m}Tc-TcO_4^- kinetics)	Re-188 (based on ^{99m}Tc-TcO_4^- kinetics)	I-131	Re-186 (based on ^{99m}Tc-TcO_4^- kinetics)	Re-188 (based on ^{99m}Tc-TcO_4^- kinetics)
ICRP 60 (original OLINDA)	18.208	18.112	17.510	18.257	18.112	17.547
ICRP 103	20.885	20.648	18.704	21.037	19.355	18.835
ICRP 103 (removed thyroid from W_T)	192.393	105.800	89.652	206.650	109.268	93.931

Thyroid to effective dose ratios were increased when the effective dose were calculated based on tissue weighting factors from ICRP 103. As from this ICRP publication, the calculated effective doses gave lower values than that computed using weighting quantity from ICRP 60. With ICRP 103 weighting factors, the ratios for ^{186}Re were still equalled to ^{131}I, whereas ^{188}Re ratios were presented a little bit lower. Additionally, the ratios of ^{131}I-NaI were much higher than both rhenium isotopes when not including thyroid in tissue weighing factors.

4.4.2.2 Xenografts Mice and NIS-bearing Tumour

Rat adenocarcinoma (Δ34CXCR4-hNIS) tumour was selected to graft to scid/beige mice. The pharmacokinetics of NIS radiotracers (^{123}I-NaI, ^{99m}Tc-pertechnetate and ^{188}Re-perrhenate) and tumour uptakes were explored in chapter 3. Again, the tumour pharmacokinetic pattern of ^{188}Re-perrhenate and ^{99m}Tc-pertechnetate were similar but the uptake fraction of ^{188}Re-perrhenate was significantly lower when compared with pertechnetate. The potential role of partial volume effects, image noises and scatter were discussed in the previous section. Hence the pertechnetate kinetics were used instead of perrhenate for dosimetry calculation. For iodine isotopes, the kinetics of ^{123}I-NaI were used and then adapted to the physical half-life of ^{131}I (i.e. TACs were decay corrected for ^{123}I and then decayed for the half-life of ^{131}I) to estimate the tumour dosimetry of conventional radioiodine. The dosimetry for xenografts was calculated without stomach and bladder elimination.

Table 4-12 lists human-equivalent tumour absorbed doses, organ absorbed doses and effective doses estimated from mouse xenografts bearing adenocarcinoma tumour. The calculation of tumour absorbed dose was performed using a sphere S-value with the assumption that tumour mass in human is 2 g for both standard male and female and that the standard uptake values (SUV) [normalised by tumour weight] is maintained across species.

Table 4-12 Human-equivalent tumour, organ absorbed dose (mGy/MBq) and effective dose (mSv/MBq) from ^{131}I-NaI, ^{188}Re-Perrhenate and ^{186}Re-Perrhenate in reference adult male and female. Data were extrapolated from mouse bearing xenografted rat adenocarcinoma (Δ34CXCR4tumour. Values were expressed as mean ± SD (n=3 for each radiotracer)

Organ Absorbed Dose (mGy/MBq)	Male				Female	
	I-131	Re-186	Re-188	I-131	Re-186	Re-188
Tumour (2 g)	0.184 (± 0.055)	1.164 (± 0.692)	1.597 (± 0.361)	0.238 (± 0.071)	1.512 (± 0.902)	2.080 (± 0.453)
Salivary Glands	0.074 (± 0.037)	0.440 (± 0.227)	0.965 (± 0.963)	0.096 (± 0.048)	0.570 (± 0.293)	1.255 (± 1.240)
Stomach	0.095 (± 0.050)	0.758 (± 0.937)	0.406 (± 0.098)	0.123 (± 0.066)	0.266 (± 0.030)	0.531 (± 0.136)
Red Marrow	0.035 (± 0.002)	0.010 (± 0.001)	0.017 (± 0.002)	0.043 (± 0.003)	0.012 (± 0.002)	0.020 (± 0.002)
Thyroid	2.927 (± 0.548)	2.240 (± 1.845)	3.717 (± 1.835)	3.783 (± 0.709)	2.900 (± 2.391)	4.830 (± 2.310)
Urinary Bladder Wall	0.123 (± 0.021)	0.161 (± 0.043)	0.393 (± 0.099)	0.156 (± 0.028)	0.207 (± 0.055)	0.512 (± 0.134)
Whole-body Dose	0.041 (± 0.003)	0.015 (± 0.002)	0.027 (± 0.003)	0.051 (± 0.004)	0.018 (± 0.002)	0.033 (± 0.004)
Effective Dose (mSv/MBq)	0.195 (± 0.035)	0.154 (± 0.091)	0.272 (± 0.081)	0.250 (± 0.045)	0.199 (± 0.118)	0.352 (± 0.101)

The tumour absorbed doses from ^{188}Re were 1.597 ± 0.361 mGy/MBq and 2.080 ± 0.453 mGy/MBq for male and female respectively, while for ^{186}Re the tumour absorbed doses were a bit lower with 1.164 ± 0.962 mGy/MBq for male and 1.512 ± 0.902 mGy/MBq for female. The tumour absorbed doses from radioiodine (^{131}I-NaI) were found to be 0.184 ± 0.055 mGy/mSv and 0.238 ± 0.071 for male and female due to the combination of similar transit times to Re isotopes (unlike the thyroid where iodine is organified) and physical characteristics of the particle emissions (lower energy betas). The tumour absorbed dose from rhenium isotopes (^{186}Re- and ^{188}Re-perrhenate) were about 6-8 folds higher than conventional radioiodine (^{131}I-NaI). In addition, the highest organ absorbed dose was received by the thyroid gland with ^{131}I inducing 2.927 ± 0.548

and 3.783 ± 0.709 mGy/MBq for male and female, ^{186}Re inducing 2.240 ± 1.845 mGy/MBq for male and 2.900 ± 2.391 mGy/MBq for female with ^{188}Re thyroid absorbed dose of 3.717 ± 1.835 and 4.830 ± 2.310 mGy/MBq for male and female respectively. In contrast, the red marrow absorbed dose delivered by rhenium isotopes were lower than radioiodine (~ 0.27 times for ^{186}Re and 0.5 times for ^{188}Re). The mean whole-body absorbed doses delivered by rhenium isotopes and iodide (^{131}I-NaI) are also illustrated in table 4-12 with highest values for radioiodine (0.041 ± 0.003 and 0.051 ± 0.004 mGy/MBq for male and female), followed by ^{188}Re (0.027 ± 0.003 and 0.033 ± 0.004 mGy/MBq for male and female) and ^{186}Re (0.015 ± 0.002 and 0.018 ± 0.002 mGy/MBq for male and female).

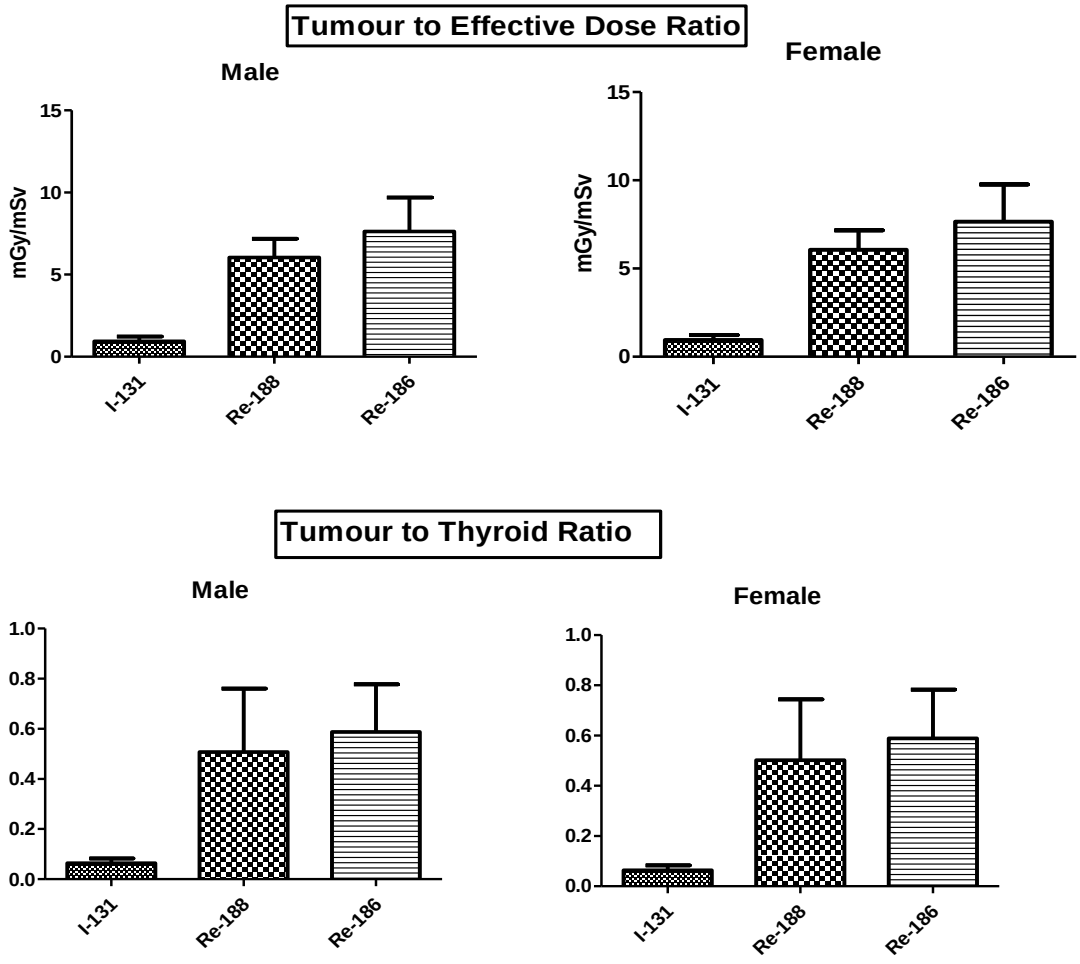

Figure 4-10 **(Top)** tumour to effective dose ratio (mGy/mSv) calculated from mouse xenografts. Ratios were shown as mean ± SD (n=3). **(Bottom)** tumour to thyroid ratio as mean ± SD (n=3)

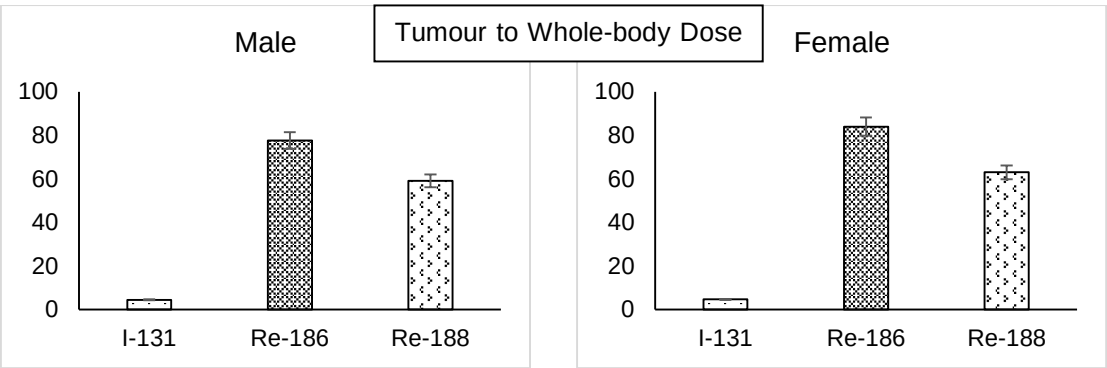

Figure 4-11 Tumour to whole-body dose ratio calculated from mouse xenografts. Ratios were shown as mean ± SD (n=3)

The therapeutic ratios in 3 radiotracers are shown in figure 4-10 and 4-11. Tumour to effective dose ratios were shown as mean ± SD (n=3). For ^{131}I, ratios were 0.949 ± 0.279 and 0.956 ± 0.279 mGy/mSv for male and female. ^{188}Re were 6.048 ± 1.146 mGy/mSv for male and 6.064 ± 1.106 mGy/mSv for female. ^{186}Re were 7.634 ± 2.061 mGy/mSv for male and 7.660 ± 2.107 mGy/mSv for female. The tumour to effective dose ratio of both rhenium isotopes were greater when compared with conventional radioiodine so for the same effective dose to the whole-body, rhenium can deliver more dose to the tumour. Tumour to thyroid ratios were 0.063 ± 0.019 and 0.062 ± 0.029 mGy/mSv for male and female for ^{131}I-NaI, 0.507 ± 0.252 and 0.502 ± 0.241 mGy/mSv for male and female for ^{188}Re-Perrhenate and 0.587 ± 0.190 and 0.589 ± 0.194 mGy/mSv for male and female for ^{186}Re-Perrhenate. In the same manner, the tumour to whole-body dose ratio of both rhenium isotopes were greater when compared with conventional radioiodine (^{131}I-NaI) so for the same whole-body dose, rhenium can deliver more dose to the tumour. Hence, these data are indicate that rhenium produced a lower fraction of dose to the thyroid when treating the NIS-expressing tumour compared with ^{131}I.

4.4.3 Impact of Partial Volume Effects in Preclinical Dosimetric Calculation

As mentioned earlier in this chapter, the main purpose of this work was to study the feasibility of new therapeutic NIS radiopharmaceuticals for thyroid disease (benign and malignant) and other NIS-expressing tumours. We used pre-clinical tracer kinetics scaled by Krischer's equation to estimate human dosimetry. Hence, a critical challenge in this process was the accuracy of quantification of the radiotracer uptake in small-organs (e.g. thyroid and salivary glands) with preclinical SPECT and PET. It is well known that tracer quantification in organs of this scale is hampered by the partial volume effect. In chapter 2, we evaluated the quantification

accuracy and the influence of PVE using the MHS phantom with the nanoScan SPECT/CT. Based on the phantom study, we examined the relation between percentage quantification accuracy versus volume of sphere in 3 SPECT radiotracers; ^{99m}Tc, ^{123}I and ^{188}Re. We defined VOI using integral method by setting a threshold of 10% of the maximum count to exclude background. The image quantification was performed in InVivoQuant software. Then, we fitted these curves with the second order polynomial equations. The equations and polynomial regressions are displayed in the figure below.

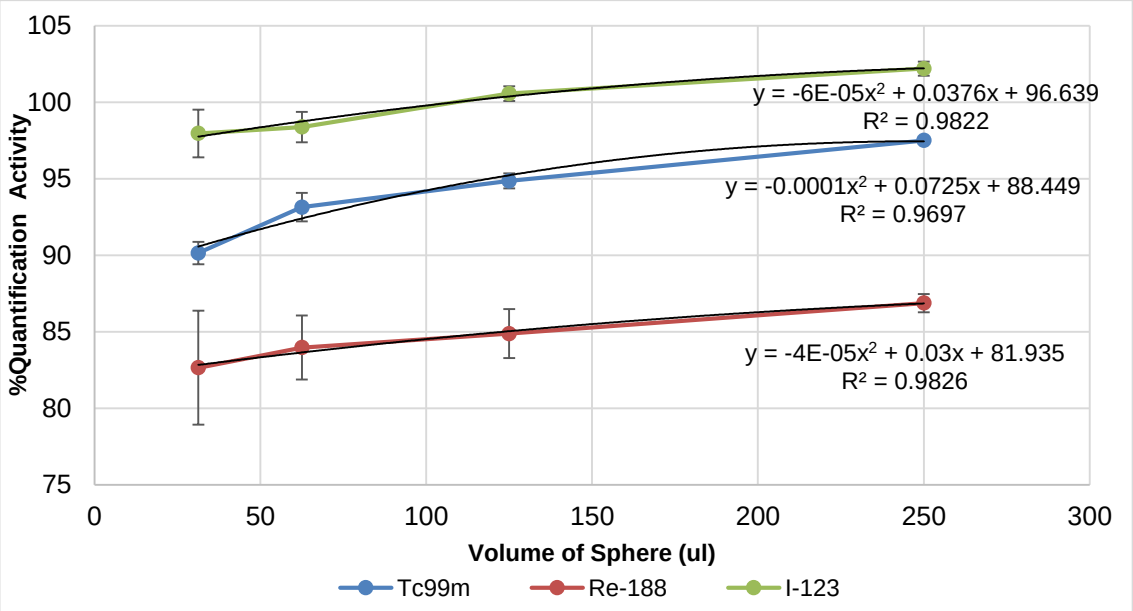

Figure 4-12 MHS phantom acquired with 20 second per projection and standard reconstruction with second order polynomial curve fitting

The second-order polynomial function used to fit the data and polynomial coefficients are shown in the following table;

$$Y = ax^2 + bx + c \qquad \text{Equation 4-7}$$

Table 4-13 Polynomial regression and polynomial coefficient from second-order fitting

	Polynomial Regression	a	b	c
^{99m}Tc	0.9697	-1.00E-04	7.25E-02	8.84E01
^{123}I	0.9822	-6.00E-05	3.76 E-02	9.67E01
^{188}Re	0.9826	-4.00E-05	3.00 E-02	8.19E01

The polynomial regressions showed a good correlation between the volume of sphere and quantification accuracy (R^2 = 0.9697, 0.9822 and 0.9826 for ^{99m}Tc, ^{123}I and ^{188}Re respectively). These equations were used to calculate volume-specific correction factors in order

to correct our original *in vivo* data. The organ volumes were obtained from VOI analysis based on the high resolution CT images (n = 15) of the same strain as in the kinetic experiments. The mean volume of the organs with SDs and the correction factors derived from MHS phantom and equation 4-7 are tabulated below.

Table 4-14 Organ volumes from CT images (n=15) and correction factors (CFs) derived from MHS phantom

Organ	Volume from CT (µl)		Tc99m	I-123	Re-188
	Mean	SD			
Thyroid	22.07	3.99	1.099	1.022	1.207
Salivary Gland	95.71	8.36	1.072	1.006	1.188
Stomach	348.57	62.08	1.021	0.976	1.150
Bladder	197.50	26.55	1.037	0.986	1.162

Based on our results, the volume of the mouse thyroid was approximately about 22.07 ± 3.99 µl. The VOI for thyroid was drawn together as one VOI for both lobes with included the isthmus. This volume was smaller than the volume of the smallest sphere (31.3 µl) of the MHS phantom which is smallest possible compartment among the commercially available phantoms. The mean volumes of stomach and urinary bladder were based on the CT images at the end of the dynamic phase (approximately 4 hours after injection). Hence, these volumes showed large variations due to the different contents in stomach and bladder across animals. Organ volumes of the particular mouse strain (female scib/beige, 4-8 weeks old) were not found to be reported elsewhere. Hence, it was difficult to compare our volumes with other published data.

4.4.3.1 Influence of Volume-specific PVE Correction Factor to *in vivo* Kinetic Data

The volume-specific PVE correction factors were applied to the *in vivo* kinetic data described in chapter 3 for ^{99m}Tc, ^{123}I and ^{188}Re. To analyse the impact on dosimetric calculation, the corrected *in vivo* kinetics were used to calculate the tracer residence time using equation 4-5. According to the mathematical integral property, the tracer residence times were changed by the same factor as we applied to *in vivo* kinetic. In this study, we calculated the percentage difference from the healthy animal data, the mean percentage difference (mean ± SD) in thyroid, salivary glands, bladder, red marrow and whole-body effective dose (based on ICRP 60) are illustrated in the following table. (The percentage difference calculated using the original non PVE-corrected dose as reference values)

Table 4-15 Percentage difference (Mean ± SD) of PVE-corrected absorbed doses for each organ with respect to original dose prior to PVE correction

Organ	Male (%)			Female (%)		
	Tc99m	**I-123**	**Re-188**	**Tc99m**	**I-123**	**Re-188**
Thyroid	9.24 (± 0.20)	2.16 (± 0.06)	20.61 (± 0.26)	9.44 (± 0.03)	2.20 (± 0.03)	20.78 (± 0.47)
Salivary Gland	7.07 (± 0.34)	0.64 (± 0.45)	18.80 (± 0.27)	7.19 (± 0.42)	0.61 (± 0.13)	18.74 (± 0.08)
Stomach	1.64 (± 0.14)	-1.95 (± 0.32)	13.60 (± 0.26)	1.72 (± 0.16)	-1.87 (± 0.21)	13.60 (± 0.03)
Urinary Bladder	1.45 (± 0.61)	-0.91 (± 0.17)	8.52 (± 1.02)	1.81 (± 1.06)	-0.94 (± 0.29)	8.14 (± 1.51)
Red Marrow	-0.19 (± 0.16)	0.00 (± 0.00)	-1.47 (± 0.03)	-0.23 (± 0.02)	-0.07 (± 0.12)	-1.70 (± 0.16)
Effective Dose (ICRP60)	3.12 (± 0.50)	1.51 (± 0.08)	13.05 (± 0.93)	3.00 (± 0.39)	1.63 (± 0.13)	13.00 (± 0.74)

After application of PVE CFs and re-calculation of the dose, the thyroid absorbed doses showed the highest impact, with doses increasing by approximately 20% for ^{188}Re, 10% for ^{99m}Tc and 2% for ^{123}I. Similarly, the salivary gland absorbed doses were raised by a similar magnitude. For the absorbed dose to the stomach, the absorbed doses were increased by 13.6 % for ^{188}Re, 1.7% for ^{99m}Tc whereas decreased by approximately 2% for ^{123}I. Similar findings were observed for the bladder with absorbed dose most effected for ^{188}Re (increased by approximately 8%), with minimal effect for ^{99m}Tc (increased about 1.5%) and ^{123}I (decreased about 1%). Red marrow absorbed dose was not much affected for ^{99m}Tc and ^{123}I, while for ^{188}Re dose increased by about 2% (indirect effect from other ROIs). For effective dose (based on ICRP 60), overall values were raised by approximately 13%, 3% and 1.5% for ^{188}Re, ^{99m}Tc and ^{123}I respectively.

4.5 Discussion

In the first part of this chapter, we estimated the effective dose of NIS radiotracers (^{18}F, BF_4, ^{99m}Tc-pertechnetate, ^{123}I-NaI, ^{131}I-NaI,^{188}Re-perrhenate) for diagnostic use. In the second part, the feasibility of using rhenium isotopes (^{186}Re and ^{188}Re-perrhenate) for therapeutic applications in benign thyroid diseases and NIS-expressing tumours was examined for comparison with conventional radioiodine (^{131}I-NaI). In the third part, we used the quantification accuracy results from the phantom study in chapter 2 to correct the *in vivo* kinetic data to investigate the impact of volume-specific PVE correction on the dosimetric calculations.

In our study, murine organ uptakes were extrapolated to human using the Krischer's linear mass scaling equation which assumes that SUVs remain constant across species. Then, the human-equivalent dosimetry was performed using the OLINDA/EXM internal dosimetry software package. This software was intended to estimate the internal dosimetry for standard human models. Criticism has previously been raised over the mass scaling method, the size and mass of organs as well as the extent of physiological differences between two species (Stabin, 2008). However, as Stabin proposed, *"Extrapolation to human values of uptake and clearance is far from certain, but these preliminary data provide a basis for going forward with clinical trials if the results are generally favourable"* (Stabin, 2003).

4.5.1 Effective Dose of NIS Radiotracers for Diagnostic Use

In the ICRP publications (ICRP 53, 80 and 106), the effective dose values were calculated based on the published bio-kinetic data. However, as was discussed in ICRP 106 there were several problems in finding and selecting good bio-kinetic data for dosimetry. Published kinetic data in literature are often reported by workers interested only in the initial phase of the tracer distribution, are often restricted to imaging a particular section rather than providing whole-body data and lack information about tracer retention at later time-points which can strongly influence dosimetry calculation (ICRP, 2008).In some cases, kinetic data acquisition was largely simplified due to limitations of the imaging technology at that time and no recent data have been revisited. For instance, the iodine model from ICRP 53 is mono-exponential developed from the Berman's early compartmental model in 1972 (Berman et al., 1975; Johansson et al., 2003).

In terms of comparison of data, it is also difficult to compare dosimetric results calculated from studies referring to different size, age, strain and gender (Pradhan et al., 2012). In our study,

the estimation of effective dose was based on a side-by-side comparison of available NIS-radiotracers from *in vivo* studies of the same strain, sex and age-matched animals.

To compare our effective dose calculations, the table below showed the comparison of our estimated values with the dose published by ICRP. For effective dose of iodine isotopes published in ICRP 53 & 60, the effective doses per unit administered activity were proposed on the maximal uptakes of thyroid at 0%, 5%, 15%, 25%, 35%, 45% and 55% (Andersson et al., 2014; Mattsson et al., 2011). Consequently, we fitted a linear function from these ICRP data and then the effective dose according to our maximal human-equivalent uptake value was calculated from the graph. For ^{99m}Tc-pertechnetate effective dose, the values were calculated based on the intravenous administion of radiotracer and no thyroid blocking agent given.

Table 4-16 Comparison of effective dose (male model) from our estimation (human-equivalent derived from preclinical data) and effective dose published in ICRP 53/80

Radiopharmaceutical	Effective Dose (mSv/MBq)		% Our Study Difference from ICRP	Note
	Our Study	ICRP 53/80		
^{123}I - NaI (3.67% thyroid uptake)	4.57E-02	3.86E-02	18.54	Maximum uptake at 8 h
^{99m}Tc - Technetium pertechnetate	8.63E-03	1.30E-02	-33.62	Intravenous, no blocking agent
^{131}I- NaI (4.05% thyroid uptake)	5.43E-01	2.97E+00	-81.71	Maximum uptake at 8 h

Estimation of effective doses from our study varied from the ICRP and this can be attributed mainly to the bio-kinetic models used as a basis for the calculations. Also, the urinary voiding and GI tract model were not included in our dosimetric calculation. It should also be noted that the values for effective dose in the various publications vary from each other and really depend on their selected method and kinetic model. For instance, the recent work by Andersson et al (2014) recalculated and compared the effective dose using conventional ICRP bio-kinetic data but Anderson used the new ICRP/ICRU computational reference phantoms (instead of the MIRD phantom published in ICRP 53/80/106). The recalculated value for ^{99m}Tc-pertecnnetate (IV administration, no thyroid blocking) changed from 1.30E-02 to 1.55E-02 mSv/MBq (+19 %) and when applying the new phantom combined with new ICRP weighting factors (ICRP 103, 2007), the effective value increased by approximately 22% when compared with the original value (Andersson et al., 2014). In this study, we demonstrated the difference when applying the new

ICRP 103 weighting factors and excluding the salivary glands from the remainder of the body applying an S-value of salivary glands from a 77 g sphere model. The OLINDA version 1.1 effective dose calculations are based on ICRP 60 with the salivary gland not listed in the Cristy-Eckerman's phantom series. Two main differences in this revised W_T weighting factors that may influence our study are the inclusion of tissues not previously listed (brain, salivary glands) and also the thyroid W_T slight decrease from 0.05 to 0.04. Hence, it can be seen from table 4-7 that our recalculated values (with ICRP 103) decreased by about 10 % for metabolised tracers (^{123}I and ^{131}I-NaI) while these modifications of W_T did not substantially affect non-metabolised tracers (^{18}F-BF_4, ^{99m}Tc-pertechnetate, ^{188}Re-perrhenate).

With the above points in mind, these values can still be practically useful for initial estimates and dosimetric comparison in the development of new radiotracers. For example, this study estimated the effective dose for ^{18}F-BF_4 as an initial approach with a forthcoming clinical trial for this PET radiotracer for clinical use in thyroid cancer due to start in 2015, with the ability to verify dosimetry based on the updated patient-derived kinetics. Based on the preclinical results, the effective dose from this new PET tracer was lower than conventional imaging agents (^{123}I-iodide and^{131}I-iodide). However, the ^{18}F-BF_4 estimated dose was still higher when compared with^{99m}Tc-pertechnetate, a long-established single photon tracer (Krisanat Chuamsaamarkkee, 2014). Obviously, such pilot data cannot easily be achieved directly from injecting the tracer to humans at early stages of research, hence this human-equivalent dosimetry and data evaluation is still very important and practically useful as a guiding tool for clinical translation.

4.5.2 Dosimetry and Potential Therapeutic Use of ^{186}Re- and ^{188}Re-perrhenate in benign nodular thyroid disease and NIS-expressing xenografts model

In this work, we investigated the feasibility of using rhenium isotopes (^{186}Re- and ^{188}Re-perrhenate) in treatment of benign nodular thyroid disease and NIS-expressing tumour using preclinical data for comparison with conventional ^{131}I-NaI.

For benign nodular thyroid disease, the normal healthy mouse without thyroid blocking was used to estimate the dose. As mentioned earlier, the kinetics of ^{99m}Tc-pertechnetate was used to estimate the dose of rhenium isotopes for this calculation. The dosimetry estimation in table 4-8 demonstrated that ^{131}I-NaI produced the highest dose per unit administered activity to thyroid among all tracers at about 3 times that of ^{188}Re, and a thyroid to effective dose ratio nearly 2 times higher for ^{131}I-NaI compared to ^{188}Re-perrhenate. After modification of the uptake by

eliminating urinary bladder, the treatment efficiency of ^{131}I-NaI (thyroid absorbed dose, thyroid to effective dose ratio) were still higher than rhenium isotopes. However, we have also recalculated the thyroid dose by eliminating the activity in the stomach and urinary bladder as uptake in these organs fluctuated widely across the mice while this can be potentially controlled in a clinical setting. After updating dosimetry calculations, the thyroid to effective dose ratios were almost identical for ^{131}I-NaI, ^{186}Re- and ^{188}Re-perrhenate while the absorbed dose to stomach, urinary bladder, red marrow, whole-body and effective dose from both rhenium isotopes were considered lower than conventional ^{131}I. Even therapeutic equivalence of ^{186}Re, ^{188}Re and ^{131}I are demonstrated in this study, however, the logistic and cost benefits and reduced adverse impact on quality of life would justify for further scientific evaluation of ^{188}Re.

In this work, we used the mean weight of each organ to calculate the percentage injected dose per gram for dosimetric calculations. The mean organ masses were obtained from dissection of animal after *in vivo* imaging. The thyroid was dissected under a microscope to isolate the thyroid gland without the trachea. The average mass of thyroid from our study was 0.0169 ± 0.0052 gram. However, the mass of thyroid (without trachea) from similar strain or same sex- or age-matched animals has not previously been reported in literature. As the organ was very small and the mass value was important in dosimetry calculations, this could be a potential source of error in this study.

Further investigation ideally with human-derived kinetics and the influence of thyroid hormones (e.g. recombinant thyroid stimulating hormone – rhTSH) would be of interest in order to examine potential methods to achieve a high therapeutic ratio such as by prolonging the retention of rhenium in thyroid or benign lesion.

Radiation damage to the salivary glands is one of the most frequently complications of radioactive iodine treatment. Salivary gland dysfunction has been reported with symptoms such as pain, swelling and xerostomia (dry mouth) (Liu et al., 2011). Therefore, it is important to estimate the absorbed dose to salivary glands in this therapeutic perspective. However, OLINDA excludes salivary glands. In this study, a single sphere was used to estimate the absorbed dose to the salivary gland with the approximation of a sphere with mass of 77 g for both male and female. Therefore, the salivary gland absorbed dose reported here was only based on self-absorption. The validity of the assumption is supported by the human study of salivary gland absorbed dose by Liu et al (2011) which reported that the cross-photon radiation from brain or thyroid to the submandibular and parotid salivary gland were only 3.6 and 5.5 % respectively (Liu

et al., 2011). Therefore, this contribution should be smaller for rhenium as the gamma photons from both rhenium radioisotopes are gentler than ^{131}I. Nevertheless, our results as shown in table 4-9, indicate that the salivary glands absorbed dose from rhenium are higher than from ^{131}I. Subsequently, this could be a limitation of using high activity of rhenium for therapy. However, numerous clinical studies have been published referring to methods such as using sour fruit or lemon juice for inducing the secretion of saliva and hastening the wash-out of the radionuclide from the salivary gland (Jentzen et al., 2010; Liu et al., 2011). Currently, there is still lack of data for radionuclide kinetics in the salivary glands, the resulting radiation exposure and cumulated absorbed dose from radiopharmaceuticals. Also, no data on dose limits and tolerance dose from ^{131}I-NaI therapy have been reported yet. To the best of our knowledge the only data available are from external beam radiotherapy (EBRT) where the dose limit to the parotid gland is reported to be 23 Gy and a complication can occur at doses of 26-30 Gy whereas doses of 45-60 Gy can severely damage the glands (Liu et al., 2011). Therefore, the total salivary glands absorbed dose should be taken into account to prevent such complications and future clinical translation of therapy agents should be mindful of these issues.

With regard to dosimetry in xenografts, our study calculated absorbed doses from ^{188}Re-perrhenate and ^{186}Re-perrhenate based on^{99m}Tc-pertechnetate kinetics, since the pharmacokinetic properties of perrhenate were similar to pertechnetate while image quantification seems less problematic with ^{99m}Tc as mentioned in previous chapter. Besides, we used ^{123}I-NaI kinetics for estimating dosimetric data of conventional ^{131}I-NaI due to issues with ^{131}I quantification (likely from septal penetration, uniformity map discrepancies and lack of optimisation of image reconstruction for high energy photons) as described in chapter 2. The human-equivalent dosimetric data (as shown in table 4-10) were estimated from the animal data with scaling to a reference standard adult male and female bearing a 2 g tumour. It is important to note that the NIS expression in these xenografts is unrealistically high as this model was genetically engineered with hNIS, but the comparisons between tracers are still valid. Also, the thyroid, salivary glands, stomach express endogenous mouse NIS (mNIS). Hence, this could have different substrate affinities from hNIS and this might explained the variation of uptake across organs and tumours in this xenograft model. Our results demonstrated that both rhenium isotopes delivered higher absorbed dose (per MBq administered) to tumour (6.33 and 8.68 times higher for ^{186}Re and ^{188}Re) compared to^{131}I-NaI. Tumour to effective dose ratio for ^{186}Re and ^{188}Re were about 6.5 fold higher than ^{131}I. Notably, the lower estimated effective doses from rhenium result

from the lower energy and lower abundance of gamma photons. Also, the perrhenate is not organified in, and hence does not give high dose to thyroid. These properties of rhenium isotopes make it a worthy candidate to investigate for treatment of non-thyroidal NIS expressing tumours.

Several research groups have published data showing *in vivo* uptake of ^{188}Re- and ^{186}Re-perrhenate with NIS gene therapy in extra-thyroidal tumours but only one included dosimetric data (Riesco-Eizaguirre and Santisteban, 2006). In support of our findings, results from our study agreed well with Dadachova et al (2005) which showed that ^{188}Re-perrhenate delivers 4.5 times higher dose to a 2 g tumour in a human than ^{131}I-NaI in a study of NIS-expressing mammary tumour mice (Dadachova et al., 2005). Another study by Shen et al. reported on the kinetics and dosimetry of NIS targeted therapy in a glioma-bearing rat model (F98 hNIS-transduced RG2 gliomas). The study showed similar results to our kinetics and in particular that iodine isotope had a higher tumour uptake and cumulated activity when compared with $^{188}ReO_4$ (authors co-injected dual isotopes of ^{125}I-NaI and $^{188}ReO_4$ in their study then applied physical decay factor of ^{188}Re and ^{131}I for dosimetric calculation). However, ^{188}Re was more efficient than ^{131}I in terms of dose delivery and prolonging the survival of rats bearing glioma (Shen et al., 2004). In addition, our dosimetry results also agree with human equivalent dosimetric estimations by Willhauck et al. using ^{188}Re-perrhenate in nude mice transfected with NIS-expressing prostate cancer model (NIS-transfected LNCaP cells) (Willhauck et al., 2007). Authors reported the concentration of $^{188}ReO_4$ in tumours (% ID/g) was two times lower when compare with ^{131}I. To compare dose and effectiveness of therapy, this study separated mice into 2 groups; small (tumour volume < 200 mm^3) and large tumour volume. In small tumours, ^{188}Re showed similar therapeutic efficiency (in terms of tumour reduction) as conventional radioiodine. However, ^{188}Re demonstrated a superior therapeutic effect in the larger tumour group due to their physical properties with greater range, higher energetic beta and “cross-fire” effect. (β $E_{average}$ of 0.346, 0.764 and 0.182 MeV for ^{186}Re, ^{188}Re and ^{131}I respectively)

Generally, thyroid acts as a sink during treatment with NIS-targeting radionuclide (also called “thyroid sink effect”), which refers to circumstances that most of the radionuclide is taken up in thyroid. In chapter 3, kinetic data illustrated that tumour uptakes were higher than thyroid. However, this might result from different affinity of endogenous and engineered NIS of this model. In addition, the dosimetric estimation in this chapter also showed that the tumour to thyroid ratio (figure 4-9) of rhenium isotopes was much higher than ^{131}I. Hence, it demonstrated that rhenium produced less radiation damage to thyroid when treating non-thyroidal NIS tumour.

One of the limitations of this study is that we followed the kinetics of ^{99m}Tc and ^{188}Re only up to 4 hours after injection due to technical limitations related to equipment sensitivity and radiotracer effective half-life. The extrapolation from the last imaging time point to infinity can introduce numerical errors in the estimation of accumulated activity. In addition, the limited number of animals was not adequate to fully understand sources of variability and to apply detailed statistics. Therefore, we have reported data in terms of average ± SD.

In summary, this study indicates the potential for improved therapeutic effectiveness of rhenium isotopes compared to ^{131}I in hNIS expressing tumours. The physical properties of ^{188}Re and ^{186}Re include emission of high energetic beta particles (E_{mean} 0.764 MeV with $\beta_{mean\text{-}range}$ 3.10 mm for ^{188}Re, E_{mean} 0.346 MeV with $\beta_{mean\text{-}range}$ 1.10 mm for ^{186}Re compared to E_{mean} 0.182 MeV with $\beta_{mean\text{-}range}$ 0.39 mm for ^{131}I). Therefore with greater range, these rhenium isotopes may improve treatment efficacy when treating larger benign disease, tumours or extensive metastatic disease allowing a greater fraction of cells in large lesions which are not directly targeted to be irradiated by the “crossfire” effect of rhenium betas.

Considering radiation protection and radiation safety, the shorter half-life of ^{188}Re (17 h compared to 8 days for ^{131}I) is a better match to its biological half-life in non-organifying tumours. The long half-life of ^{131}I is ‘wasted’ in such tumours (unlike in thyroid tissue) and serves only to increase radiation dose to normal thyroid and whole body. Moreover, both rhenium isotopes may potentially be more cost effective due to reduced concerns about shielding and waste management for shorter lived isotopes. Additionally, the gamma photons from both rhenium isotopes have lower abundance and a more gentle profile (155 keV with 15 % abundance for ^{188}Re, 137 keV with 9 % abundance for ^{186}Re compared to 364 keV with 82 % abundance for ^{131}I). We have previously discussed that the gamma photons of ^{188}Re emitted can be imaged quantitatively in clinical setting to provide data for dosimetry and therapy verification (Blower et al., 2000). Similarly, published data by other groups showed that ^{186}Re is possible for imaging (Eary et al., 1990).

In addition, the relative low gamma energy and short half-life (for ^{188}Re) allow for outpatient treatment. This may alleviate the need for isolation and hospitalisation after treatment with substantial cost savings and more economical treatment for the healthcare system. Likewise, the shorter restriction period would allow patients to return to their lifestyle, and alleviate the negative impact of radionuclide treatment upon patients and their families.

Considering isotope production, ^{131}I is produced from nuclear reactors, while ^{186}Re can be produced by either cyclotron or reactor (Moustapha et al., 2006). In contrary, ^{188}Re can be economically available daily from a generator that has a shelf life of 6 months. A single generator can provide treatments for many patients in a specialist centre at low cost. Availability from a generator also makes administration of fractionated doses practically feasible (Argyrou et al., 2013). However, it is important to note that, the radiation activity required by ^{188}Re is about 2 times higher than ^{131}I to yield similar thyroid absorbed dose (based on our thyroid ablation calculated with eliminating activity in the stomach and urinary bladder).

4.5.3 Impact of Partial Volume Effects in Preclinical Dosimetric Calculation

In chapter 2, the quantification accuracy and the effects of PVE in preclinical imaging of small organs were evaluated using the micro hollow sphere phantom. Thus, the volume-specific correction factors determined could be used to correct our *in vivo* kinetic data in chapter 3. In this chapter, we examined the impact of quantification accuracy and PVE on dosimetry calculation in preclinical research based on defining VOI with integral method.

As mentioned earlier, the mass of thyroid from dissection under the microscope was 0.0169 ± 0.0052 g. Therefore, the volume of thyroid converted by using the thyroid tissue density (1.05 g/cm^3) published in ICRU report no. 44, should be 16.10 ± 4.95 µl. However, the volume of thyroid obtained from CT images from our study was 22.07 ± 3.99 µl. Similarity with salivary glands, the volume converted from weight (density 1 g/cm^3) is 116.50 ± 25.50 µl whereas the volume obtained from CT was 95.71 ± 8.36 µl. These volumes were inconsistent between 2 methods and it was difficult to compare with other work as the organ volume and mass from this strain were not found published. We have listed the potential sources of error of these 2 approaches: dissection-based and CT image-based in the following table.

In addition, the CT based volume of stomach and urinary bladder had a large standard deviation due to different amounts of stomach contents and urine across the animals. As discussed in chapter 2, the quantification of ^{123}I was overestimated in large objects (over 125 µl), thus, this made correction factors for stomach and urinary bladder less than 1. We believe that a possible explanation might be that the nanoSPECT/CT only used ^{99m}Tc PSF (rather than isotope-specific) modelling in image reconstruction. This will be addressed for further investigation in the future.

Table 4-17 Summary of errors for obtaining the volume of organ from 2 methods

Method to Obtain Volume of Organ	Potential Error
Weight (convert to volume) from organ dissection	Human error - dissection skill Instrumental - weighing error Loss/Excess of body fluid during dissection (e.g. blood, urine, food in stomach) Tissue remaining in the body (e.g. isthmus)
CT Image based VOI from *in vivo* imaging	Human error – drawn ROI Instrumental - Limited resolution of CT Acquisition and reconstruction parameters Time dependency - drawn single snapshot at last time-point of dynamic phase(~4 h PI) e.g. for fluid-filling organs

In order to improve the accuracy of image-based VOI, alternative imaging techniques such as SPECT/MR or PET/MR should be investigated since those techniques can provide an improved soft tissue contrast which should make it easier to identify and distinguish the boundaries of small organs (e.g. thyroid, salivary glands) on the MRI images.

4.6 Conclusion

In summary, preclinical spatio-temporal data were used to provide initial estimates and dosimetric comparison of the human-equivalent effective dose for diagnostic and therapeutic use of NIS radiotracers; ^{18}F-tetrafluroborate, ^{99m}Tc-pertechnetate, ^{123}I-iodide, ^{131}I-iodide and ^{186}Re- and ^{188}Re-perrhenate. The dose comparison studies were conducted on the same strain sex- and age-matched animals to allow approximate comparison of radiation dose for tracer development.

Our results indicate that radionuclide therapy of thyroid benign disease with rhenium isotopes (^{186}Re- and ^{188}Re-perrhenate) appears promising in some circomestances and worthy for further investigation in human. This study is the first *in vivo* kinetic study that provided dosimetry estimation and compared the therapeutic efficiency in treating thyroid benign disease. The preclinical dosimetric estimation demonstrated that rhenium isotopes were equally effective when excluding uptake in stomach and urinary bladder (due to large variations affected by subject conditions). The higher beta energies and longer ranges of rhenium isotopes may improve treatment efficacy when treating larger benign disease in which radioiodine therapy is less effective due to its shorter range. The less abundant of gamma photons emitted by ^{186}Re and ^{188}Re are more favourable than those produced by ^{131}I, reducing radiation dose to the whole body and to other people and thus reducing or eliminating the need for isolation. Based on our study, effective dose per administered activity from ^{186}Re and ^{188}Re was lower than conventional radioiodine. Also red marrow absorbed dose was about 1.5 and 3 times (for ^{186}Re and ^{188}Re respectively) lower than that produced by radioiodine. Furthermore, treatments could therefore be offered on outpatient basis at great cost saving, and patients can return to normal lifestyle earlier. These factors make ^{186}Re- and ^{188}Re-perrhenate promising therapeutic radiopharmaceuticals for thyroid disease.

In xenograft bearing NIS adenocarcinoma tumours, our data indicated that both rhenium isotopes delivered higher absorbed dose to the tumour (6.33 and 8.68 times higher for ^{186}Re and ^{188}Re) compared to ^{131}I-NaI. Additionally, the therapy indexes (tumour to effective dose and tumour to thyroid ratio) for both rhenium isotopes were greater than that for ^{131}I-NaI. Tumour to effective dose ratios for rhenium isotopes were about 5 - 7 times higher whereas tumour to thyroid ratio of both rhenium isotopes were about 7 – 9 time higher than for ^{131}I-NaI . Furthermore, the red-marrow absorbed doses produced by rhenium were lower than radioiodine (~ 0.27 times for

^{186}Re and 0.50 times for ^{188}Re) so for the same effective dose to the whole-body, rhenium can deliver more dose to the tumour.

Although it is difficult to estimate the human dosimetry by scaling from animal data this preclinical dosimetric study is an important phase for initial estimation of the therapeutic potential and application of these radiotracers clinically and it supports the idea of performing dosimetry imaging studies with Tc and Re in humans.

It was demonstrated in this chapter that the quantification accuracy and partial volume effect in preclinical research can be evaluated and corrected for by using standard geometrical phantom data. Subsequently, data presented in this chapter shows the impact of these effects on dosimetry calculations in small organs (e.g. thyroid, salivary glands) and also influence on the whole-body effective dose.

Chapter 5 Tracer Localisation at Cellular Level and Small-Scale Dosimetry

5.1 Introduction

Organ-level macroscopic dosimetry has been extensively discussed in Chapter 4. However, in some cases there may be potential limitations from macroscopic dosimetry that may interfere with prediction of biological effects and treatment outcomes. Such limitations of macroscopic dosimetry are associated with several factors. One significant limitation is the assumption that the radionuclide distribution is homogeneous across an entire organ. Many studies showed that radionuclides may be inhomogeneously distributed in an organ (see next section). In addition, the radiation sensitivity for individual cells can be different and may depend on many factors (different cell types and cell cycle phases) (Goodhead, 1982).

Moreover, the assumptions used in macroscopic dosimetry are invalid in some cases. For instance, macroscopic dosimetry schemes often assume that beta and alpha particles are non-penetrating radionuclides. So, the absorbed fraction from source to target organ ($\emptyset_{t\leftarrow s}$) is set to zero for all beta and alpha emissions. However, this assumption is only valid when the size of organ is much greater than particle track ranges and can be incorrect when high energetic betas deposit their energy in small organs.

Also at macroscopic level, the effects of secondary Auger electrons are taken into account but it are attributed to the whole organ so high LET (linear energy transfer) of the Auger electrons loses its significance. These high LET electrons have low energy but are deposited in very short range hence the localised effects might be strong. So, they can cause genetic damage if the energy deposition occurs at close proximity to the critical target (e.g. cell nuclei). Although macroscopic dosimetry only considers deterministic effects of radiation, small-scale dosimetry take into account the stochastic effects in the micro-volume as well.

The determination of deposited energy by a small-scale dosimetry approach may provide a more accurate link to biological effects of radiation interactions which occur at the cell or organelle level. These may contribute towards predicting treatment outcome at organ or whole body level.

5.1.1 Tracer Localisation

Tracer localisation is key to understanding the micro-dosimetric profile of radiotracers at cellular level. In general, macro-dosimetry (based on MIRD formalism) usually assumes a uniform distribution of the tracer over the whole organ and also that radioactivity is uniformly distributed throughout the tissue and cell compartments in that particular organ. However, this assumption is not always correct as some cell populations in the organ may contain very different amounts of radioactivity, and even some cells may not show uptake of the radiopharmaceutical. Furthermore at cellular level, radionuclides may get incorporated into intracellular structures and subsequently the toxicity of radiation may depend on the precise location of the radioactive decay within the cell (Farragi et al., 1994; Humm et al., 1993a).

Various publications have reported that dose delivered to the cell is strongly dependent on sub-cellular distribution of radiotracers. For example, a study by Konijnenberg M et al. reported that *ex vivo* autoradiographs of the kidneys from patients who received ^{111}In-DTPA-Octreotide showed very heterogeneous distribution of the radiotracer. Furthermore, the authors also calculated the iso-dose curves with dose-volume histograms (DVH) using MCNP simulations based on the autoradiography data in order to illustrate the impact of tracer distribution with different radionuclides; ^{90}Y (β -emitter), ^{111}In (Auger electron and ɣ-emitter) and ^{177}Lu (β – and ɣ-emitter) (Konijnenberg et al., 2007).

Results (from Konijinberg et al) indicated that ^{111}In-DTPA-Octreotide was inhomogeneously distributed in kidneys showing different patterns in the cortex and medullar areas. The DVH demonstrated that the inhomogeneous tracer distribution generated inhomogeneous dose distributions especially with low energy particle-emitters (^{177}Lu and ^{111}In) where dose distribution reflected closely the spatial distribution of activity.

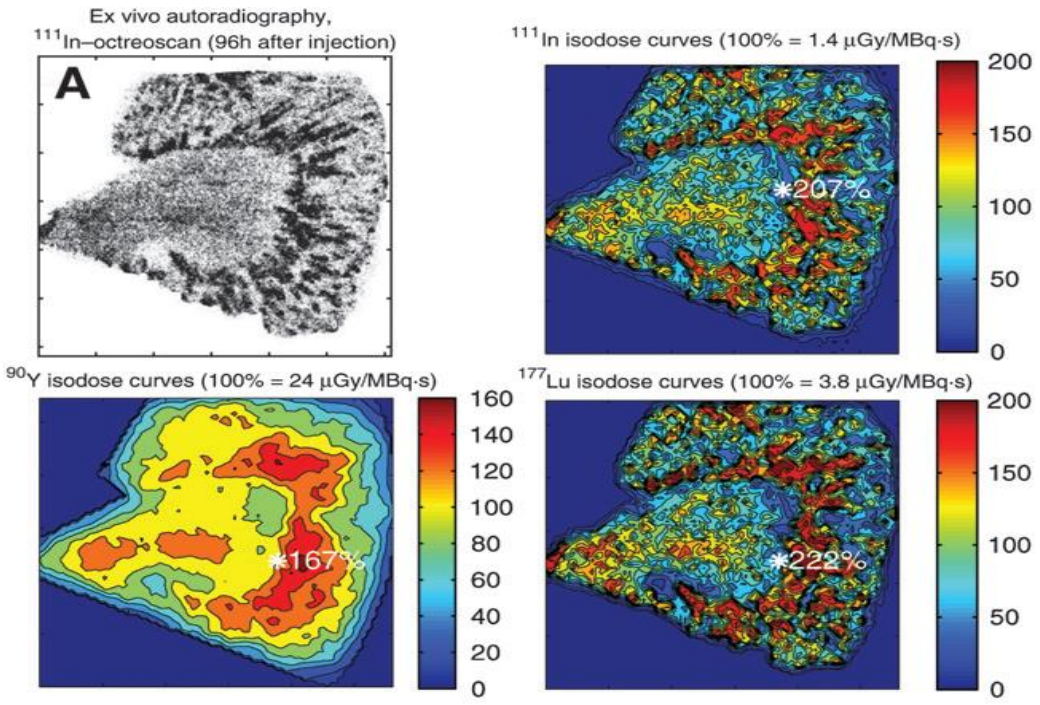

Figure 5-1 *Ex vivo* autoradiography of kidney section (section size of 0.37×0.37×10 mm^3) showing inhomogeneous distribution of radiotracer. MCNP was used to generate the dose distributions based on autoradiograph for ^{90}Y, ^{111}In and ^{177}Lu (modified from (Konijnenberg et al., 2007))

In the case of thyroid, iodide [I^-] has been used widely in thyroid imaging and therapy (^{123}I, ^{124}I, ^{125}I and ^{131}I-NaI). In normal thyroid, the thyroid follicular cells are formed from "colloid" surrounded by a single layer of thyrocytes (as shown in figure 5-2 *a* and *b*). Iodide is taken up into follicular cells by NIS-mediated active transport on the baso-lateral membrane. Iodide is driven into the apical membrane by an ion gradient and exported into the colloid via the exporter protein "pendrin". Then, iodide is oxidized and organified to thyroid hormones which are stored in the colloid until exported (Champion et al., 2007a; Zuckier et al., 2004). Champion et al. have demonstrated that iodine distribution is heterogeneous in the follicular cells, with most of iodine located in the colloid rather than in thyrocytes (figure 5-2 *c*).

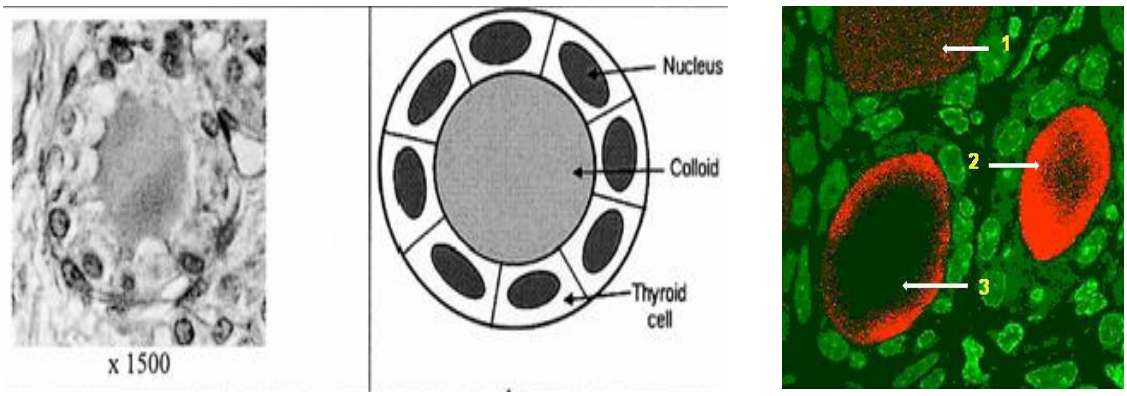

(a) (b) (c)

Figure 5-2 (a) follicular cell of normal thyroid by SIMS (secondary ion mass spectroscopy) (b) geometrical model, the thyroid follicular cells are formed from "colloid" surround by a shell of thyrocytes (c) digitized image with phosphorus (green) and iodine *(red). The arrows show the different patterns of distribution (1) homogeneous with (2) and (3) inhomogeneous [Images modified from Champion et al] (Champion et al., 2007b; Elbast et al., 2008a)*

Perrhenate ion [ReO_4^-] is also a substarte of NIS but is not metabolised to produce thyroid hormones. Also, perrhenate is chemically and biologically analogous to pertechnetate [TcO_4^-], which is a well known single-photon imaging radiotracer (in the form of $^{99m}TcO_4^-$) for studying the 'trapping' function of the thyroid glands. Therefore, we expect the perrhenate/pertechnetate to be located in the thyrocyte. However, no sub-cellular tracer distribution studies are available for perrhenate or pertechnetate (Puncher and Blower, 1994b).

Hence, this study aims to evaluate the perrhenate/pertechnetate ion distribution in normal rodents (mouse/rat) thyroid cells by using transmission electron microscopy (TEM) and micro-autoradiography techniques. Consequently, data on tracer distribution at the cellular level should lead to a realistic small-scale dosimetric assessment which can be used to evaluate and predict biological effects of the radiopharmaceuticals.

5.1.2 Transmission Electron Microscopy (TEM) imaging for tracer localisation

Transmission electron microscopy is an imaging technique to probe the small-scale structure of materials. The basic principle of TEM is same as the light microscope but TEM uses electrons instead of light. The electrons have much lower wavelength than light (wavelength is 6 pm for electrons and about 400-700 nm for visible light). This makes it possible to get much higher resolution when compared with the light microscope. TEM has the capabilities to investigate crystal structures, specimen orientations and also chemical composition and distribution of elements using the principles of diffraction pattern and/or X-ray/electron-energy analysis (Kazy et al., 2009).

The detection in TEM is not related to radioactivity but rather uses the principle of interaction of an electron beam with the electronic structure of the sample. Thus, the non-radioactive perrhenate compound (cold perrhenate) can be used instead of radioactive rhenium. A schematic diagram of the main components of TEM is illustrated in figure 5-3.

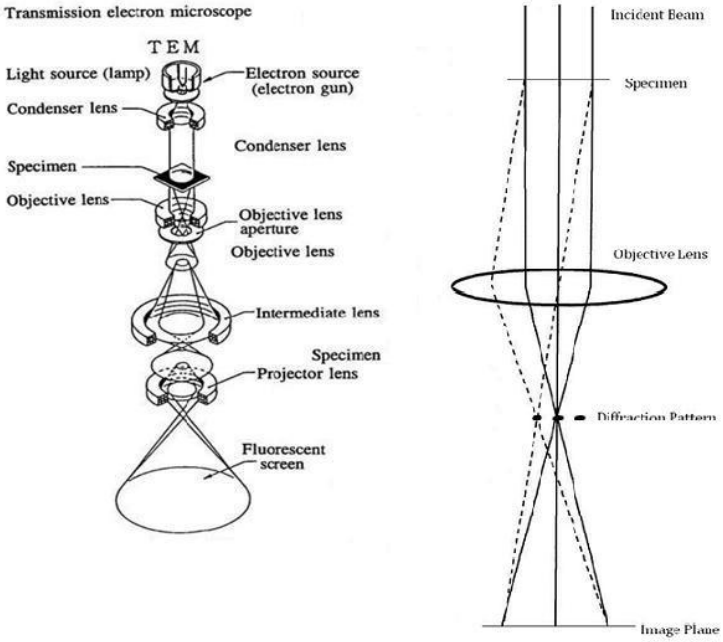

Figure 5-3 Schematic diagram of TEM (modified from JFOL 2000FX Handbook)

The electron source (‘electron gun’) emits electrons which travel through a vacuum column. The electro-magnetic lens is used to focus the electrons into a very thin beam to travel through the specimen (as the term ‘transmission’ suggests). For imaging purposes, the sample can stop or deflect electrons on their path as they pass through the sample. Then, the deflected electrons are detected by means of the bright dots generated on the screen below the sample, on the other hand, dark areas result from regions where electrons stop in the sample. Hence, a

wide range of grey scale values can be formed on the screen which refer to the different modes of interaction of the electrons with the sample e.g. deflection, scatter, transmission and stopping by the sample. There are many electron microscopy (EM) techniques that can be used to identify the elemental composition or localisation of the chemical map and/or chemical concentration in the sample. In our study, we used 2 techniques; STEM/HAADF (Scanning Transmission Electron Microscopy/High Angle Annular Dark Field) and EDX (Energy Dispersive X-ray Spectroscopy) (Nerl et al., 2011). For STEM/HAADF, the small-spot electron beams scan across the sample and then the HAADF images are formulated by gathering high-angle scattered electrons using an annular dark-field detector to collect those scattered electrons. The image contrast of HAADF images is strongly depended on the atomic number, hence, brighter spots in the image refer to areas composed of higher atomic numbers in the sample.

The fundamental principle of the EDX technique (also called EDS – Energy Dispersive Spectroscopy) uses a focussed electron beam bombarding the sample. The interactions cause characteristic X-rays which can be detected and measured by an energy-dispersive spectrometer. The spectra of characteristic X-rays refer to the energy difference between the two shells of the atomic structure of the sample. This spectrum is a unique characteristic for each element and this allows the qualitative and quantitative elemental analysis of materials (Kazy et al., 2009; Utsunomiya et al., 2011).

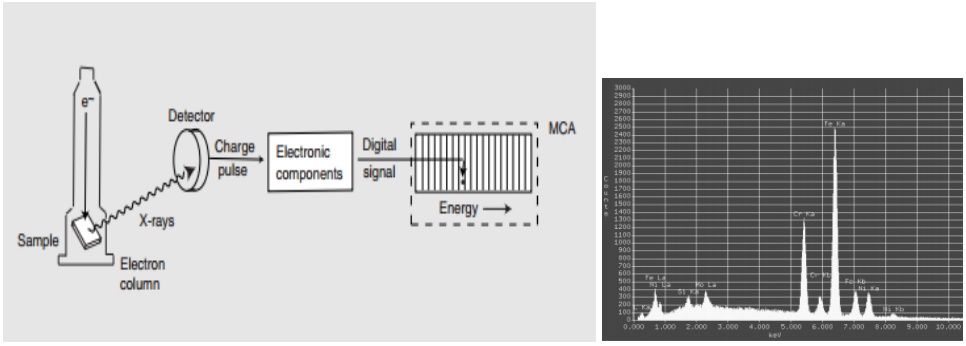

Figure 5-4 Schematic diagram of EDX Technique. A solid sample is bombarded with electrons then it emits characteristic X-ray which result from the loss of electron from various energy shells (usually the K, L, M shells are primary interest) and we can analyse this as spectroscopy for elemental analysis (modified from (Goldstein et al., 2012)

5.1.3 Small-Scale Dosimetry

Small-scale dosimetry most generally means measuring the energy deposited on a microscopic scale or a scale below the resolution of the scanner. More specifically, small-scale dosimetry studies the spatial-, temporal- and energy-dependency of radioactivity imparted in cellular and sub-cellular structures (Attix, 2007; Rossi and Zaider, 1991). Furthermore, small-scale dosimetry takes into account the stochastic fluctuations in the micro volume. This contrasts with macrodosimetry, where the radiation absorbed dose is obtained by dividing the total energy deposited by the mass of that particular volume. The macrodosimetry calculation does not include the stochastic effects because of the large target volume of interest.

To illustrate the importance of stochastic fluctuation, Humm et al. provided a schematic diagram of cells irradiated by alpha particle emitters. As shown in figure 5-5, some cells received multiple hits, while other might have received none at all (Humm et al., 1993b).

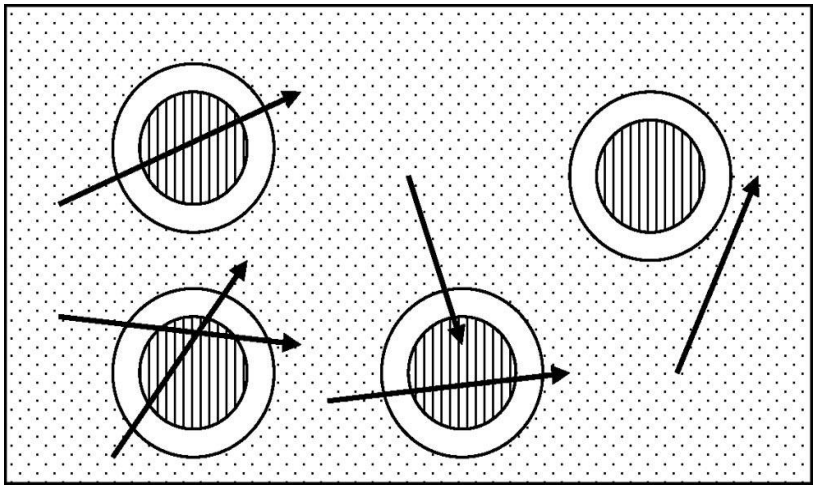

Figure 5-5 Schematic diagram of cells irradiated by alpha emitters (arrows are individual alpha particle emission), some cells received multiple hits, while other receive none at all (modified from *(Humm et al., 1993b; Roeske et al., 2008a))*

Small-scale dosimetry in nuclear medicine is increasingly of interest because of the clinical application of high LET (LET ≥ 10-30 keV/µm) alpha emitting radionuclides e.g. ^{211}At, ^{213}Bi and ^{223}Ra. Alpha particles have high energy but penetrate only less than 100 µm in tissue. Macro-dosimetry does not describe the association between the range of the particle and target size (volume) (Rossi and Zaider, 1991). The definition of LET in conventional dosimetry is only based on the mean (linear average) of a fluctuating energy loss. However for alpha emitting radionuclides, LET might vary along the path so it is not sufficient to use average LET. Also the stochastic nature of the energy deposition for high LET has to be taken into account (Loncol et al., 1994).

In addition, macro-scale dosimetry does not address the effects of delta rays. Delta rays refer to energetic electrons with sufficient kinetic energy to produce secondary ionisation. Delta rays occur when a charged particle (e.g. electrons, protons and alpha particles) penetrates matter and it loses energy by interaction with orbital electrons. The result of their interaction can be high enough for knocking orbiting electrons out of the atoms and the kinetic energy of those ejected electrons can be very high to cause further ionisation events, such energetic electrons are called “delta rays” (Attix, 2007; Cucinotta et al., 1998).

For Auger electrons, there are emitted when an inner shell electron vacancy is created. The processes of vacancy are induced after electron capture and/or internal conversion. The spectra of electrons emitted are very multifaceted and include high LET particles with sub-cellular ranges (Stepanek et al., 1996). Therefore, these delta rays and Auger electrons are also attractive reasons for studying small-scale dosimetry (Makrigiorgos et al., 1990; Puncher and Blower, 1994a).

As there are many diagnostic radionuclides which emit Auger electrons, such as ^{51}Cr, ^{64}Cu, ^{67}Ga, ^{99m}Tc, ^{111}In, ^{123}I, ^{125}I and ^{201}Tl (Chen, 2008; Makrigiorgos et al., 1990). The understanding of small-scale dosimetry is also important for diagnostic nuclear medicine (Humm et al., 1993b; Roeske et al., 2008a). Makrigiorgos et al. (1989) compared the estimated dose at the cellular level with the conventional organ-level dosimetry. Authors expressed their concern that conventional dosimetry may underestimate radiation effects by 2 to 25-fold for radionuclides that emit Auger electrons (Makrigiorgos et al., 1989).

For illustration, another recently published study by Kassis et al. (2011) (Kassis, 2011) confirmed that high LET and Auger electron emitting radionuclides caused severe damage to sub-cellular structures. Kassis’s study also reported that the biological effect could be 10–100 fold higher than for electrons from conventional radioactive iodine, especially with the ionisations clustered within nanometre range from the decay site (as shown in figure 5-6). As a consequence of this, small-scale dosimetry is necessary for detailed studies of radionuclide therapy in nuclear medicine.

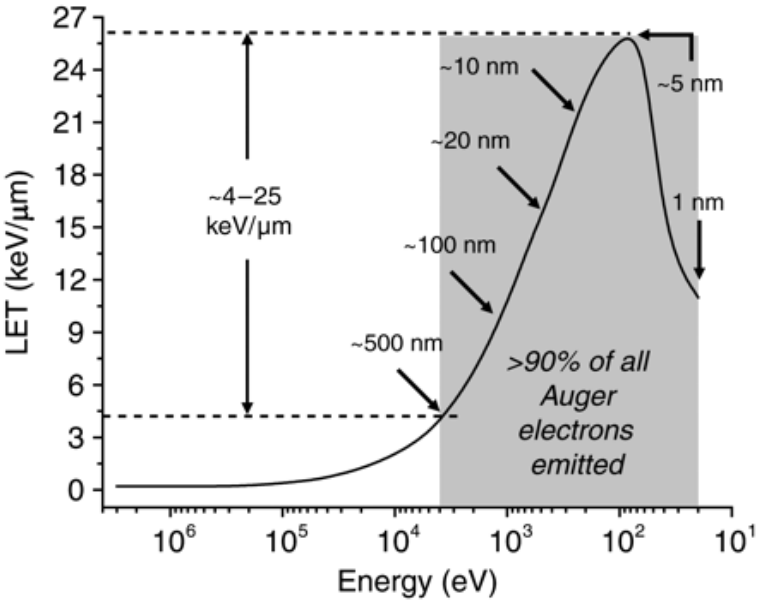

Figure 5-6. LETs of Auger electrons as function of their energy. Arrows indicate their range. It can be seen that LET might vary along the path (modified from (Kassis, 2010))

There are two main methods for calculating the energy deposited on the cell nucleus. It is commonly accepted that the main cell compartment for radiation-induced cell killing is the cell nucleus. The S-value for calculating the average dose was firstly published in 1994 by Goddu et al. using analytical and experimental range-energy methods (Goddu et al., 1994). Goddu and his co-workers developed the model for calculating cellular dosimetry with cell radius ranging from 3 to 10 µm and nuclei radius ranging from 1 to 9 µm. Goddu et al. proposed many source-target pairs for electron and mono-energetic alpha particle at cellular level for example cell to cell, cell to cell surface, nucleus to nucleus, cytoplasm to nucleus and cell surface to nucleus (Goddu et al., 1994; S. Murty Goddu, 1994).

In 1997, the MIRD schema was extended to publish S-values for calculating cellular dose at the cellular level and also to provide a simple cellular model (Thierens et al., 2001). The model comprised two concentric homogeneous compartments representing cell and cell nucleus (as shown in figure 5-7). The cell radius (R_C) and the cell nucleus radius (R_N) ranged from 6 to 20 µm and 4 to 18 µm respectively (Bolch et al., 1999). The distribution of radionuclide activity was assumed to be uniform for the cellular compartment (e.g. uniform in whole-cell, nucleus or cytoplasm). The source regions in these models included the whole cell (C), cell surface (Cs), cell cytoplasm (Cy) and nucleus (N)(Roeske et al., 2008a). The example of cellular S-value for ^{90}Y for different cell diameters is illustrated in the following table (table 5-1).

Table 5-1 Cellular S-values for ^{90}Y, R_c and R_n are radius of cell and nucleus, C, Cs, N, Cy are whole-cell, cell surface, nucleus and cytoplasm respectively (modified from (Roeske et al., 2008a)

Rc (µm)	Rn (µm)	S-value (C←C) (Gy/Bq-s)	S-value (C←Cs) (Gy/Bq-s)	S-value (N←N) (Gy/Bq-s)	S-value (N←Cy) (Gy/Bq-s)	S-value (N←Cs) (Gy/Bq-s)
7	3	1.23E-04	8.19E-05	6.79E-04	1.14E-05	5.63E-05
8	7	9.41E-05	6.25E-05	1.23E-04	6.32E-05	5.19E-05
8	6	9.41E-05	6.25E-05	1.68E-04	6.78E-05	4.78E-05

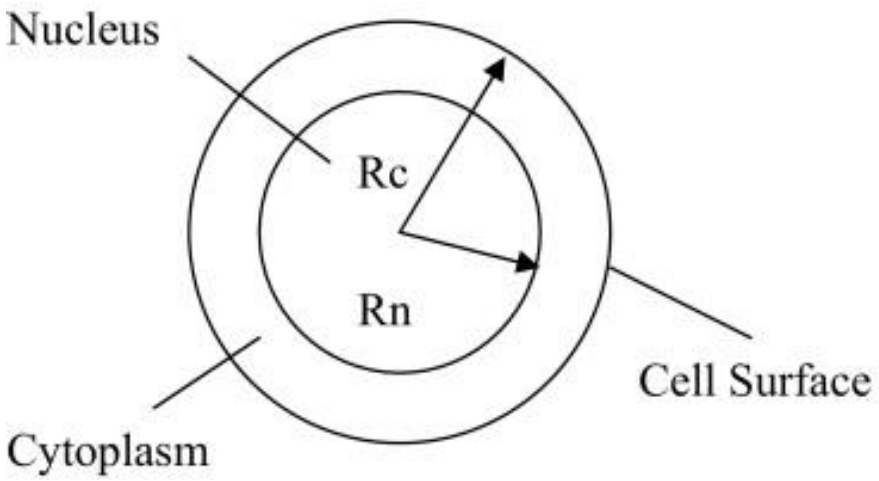

Figure 5-7 MIRD cell model, the model composes with nucleus, cytoplasm and cell surface (modified from (Goddu and Budinger, 2003))

Extensive tables of cellular S-value have been published for several radionuclides such as ^{32}P, ^{35}S, ^{86}Rb, ^{89}Sr, ^{90}Y, ^{91}Y, ^{114m}In, ^{131}I including Auger electron-emitters ^{51}Cr, ^{64}Cu, ^{67}Ga, ^{99m}Tc, ^{111}In, ^{123}I, ^{125}I ,^{201}Tl and the alpha emitter ^{210}Po and ^{211}At for a range of sizes of cell, cell nuclei and a variety of source compartment (S. Murty Goddu, 1994; Stinchcomb and Roeske, 1992). However, there are many restrictions and limitations with the cellular S-values and the MIRD cell model. The cellular S-value is only the self-absorbed dose; the cross-fire and bystander effect are not taken into account (Amin I, 2008). Additionally, the assumption of uniform tracer distribution in the source compartment is not a realistic assumption (Bardies and Pihet, 2000; Puncher and Blower, 1994a).

The second method for calculating small-scale dosimetry is analytical- or computational-based methods. Typically, the micro-dosimetric spectra are given in terms of stochastic quantities and can be calculated by using analytical methods or Monte Carlo (Berger, 1970).

For the analytical method, this calculation technique usually employs dose point kernel (DPK) convolutions of the single event spectrum to calculate multi-event distributions. Kellerer developed initial patterns of specific energy deposition for a single hit to determine the spectra of multiple hits via Fourier transform (Kellerer, 1981; Kellerer and Chmelevsky, 1975). In 1995, Giap et al. used this method with 3D voxel dose distribution and compared results with absorbed dose calculation by MIRD. They found a good agreement between the two methods (Giap et al., 1995). However, the computation time and limited source-target geometry often restrict this method (Gardin et al., 1995).

With computational-based methods, Monte Carlo (MC) is a powerful computational technique to assess the dose at small-scale. The MC track structure randomly considers all generated particles event by event, incorporating the stochastic nature of radiation (Bardies and Pihet, 2000; Bousis et al., 2009). MC also provides more flexibility in inhomogeneous medium distributions while conventional analytic methods (such as dose point kernel-DPK) can be computed only in an infinite homogenous medium (usually water). The use of MC to evaluate charged particle interactions has been of interest and several codes have been published based on MC platforms for assessing small-scale dosimetry. The code was established in the 1960s by Berger and Seltzer (Berger and Seltzer, 1973). This code was used to calculate beta-particle dosimetry of 6 radionuclides in RIT (radio-immunotherapy). ETRAN improved dosimetry calculations from DPK in various processes such as in overcoming CSDA (continuously slowing down approximation) and also including electron stopping power and Bremsstrahlung cross-section.

In addition, small-scale dosimetry with MC simulations has been developed by many research groups. For example, full MC simulation of energy deposition at cellular level include the stochastic variation of astatine-211 (^{211}As) (alpha emitter) published by Humm et al. (1987) (J.L, 1987). Larson et al. conducted in vitro studies of the cytotoxicity to human glioma and melanoma cells from At-211 labelled chimeric monoclonal antibodies (Larsen et al., 1998). The authors also provided the micro-dosimetric analysis using MC and determined cell sensitivity response based on micro-dosimetric quantities. Akabani and Zalutsky used the digitised histological images to determine chord-length distribution of At-211 (Akabani and Zalutsky, 1997). A chord-length is

defined by the intersection of particle track within a sphere. In micro-dosimetry, it is an important parameter to obtain the distribution of particle energy within the medium. Also this parameter can be used to demonstrate the influence of cell conglomeration and activity distribution. Another example of MC-based estimation for small-scale dosimetry is the CELLDOSE software by Champion et al. (2008). CELLDOSE is Monte Carlo-based software for calculating cellular S-values for I-131 in spheres of various sizes. Authors concluded that their S-values agreed well with published analytic methods (Champion et al., 2008).

Small-scale dosimetry can also be calculated by the GEANT4 toolkit which is a C++ class library (Archambault et al., 2003). Initially, GEANT4 was developed for applications in high-energy physics but also provides low energy packages. An example of using this code is the work by Freudenberg and co-workers (Freudenberg and Kotzerke, 2010). The S-values of four radionuclides (^{131}I, ^{188}Re, ^{90}Y and ^{99m}Tc) were computed for various activity distributions at cellular level. The authors also provided biological measurements of cellular survival curves by GEANT4 (Freudenberg and Kotzerke, 2010). Subsequently, many groups used GEANT4 as a standard tool for small scale dosimetry in RIT. For example, Chouin et al. used GEANT4 to calculate microdosimetry for alpha emitting radionuclides (Chouin et al., 2009) and Chauvie et al. developed the GEANT4 codes for nano-scale DNA dosimetry; this GEANT4 package is called “Geant4 DNA project” (Chauvie et al., 2007).

Along with the use of Monte Carlo in small-scale dosimetry, improvements were also developed in cellular geometrical modelling. A model published by Larsson used MC to study a realistic anatomical structure of testes including seminiferous lobules with interstitial tissue between them (Larsson et al., 2012). The model consists of an ellipsoid with mosaic pattern and hexagonal cylinders to characterize the complex structure of testicular lobule and seminiferous tubule patterns respectively (as illustrated in figure 5-8) (Larsson et al., 2012).

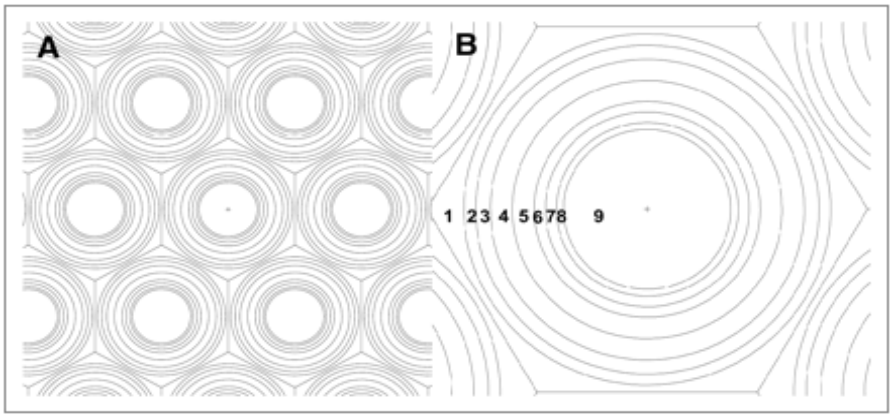

Figure 5-8. Cross-section of testicular cell geometrical model, simulated using MC code (modified from (Larsson et al., 2012))

The understanding of radiation biological effects is the goal for studying radiation dosimetry. However, currently there is limited link between dosimetry and biological effects. The link is rather unclear and perhaps limited because it is only based on external gamma/X-ray exposure and atomic bomb survival data. At the macroscopic scale, the radiation toxicity relies only on whole-tumour/whole-organ absorbed dose, which might not be a trustworthy predictor of the biological effects of internalised radionuclides. Also, the assumptions that activity and energy deposition distributed uniformly are not generally valid. Hence, the actual biological effects among cells in the same tumour/organ may be varied and dependent on spatial distribution of radioactivity at the multi-cellular, cellular or sub-cellular levels.

For small-scale dosimetry, the microscopic dose, energy deposition and stochastic nature of radiation can be considered. Goodhead (1982) stated that the micro-dosimetric properties are important factors in determining the biological effectiveness of radiation (Zaider and Brenner, 1985). True absorbed dose (or specific energy distribution) can be calculated from the area under micro-dosimetric spectra curves, and this can be linked to other radiobiological parameters, for example relative biological effectiveness (RBE), tumour control probability (TCP), cell mutagenesis and cell survival curves (Alan, 1996; Roeske and Stinchcomb, 1996; Stinchcomb and Roeske, 1992).

RBE can be used to compare the qualities of new radionuclides relative to reference radiation (in terms of producing similar biological damage). In nuclear medicine, several reference radiation emissions are used to compare the efficacy of radionuclide treatments with different biological end-points. The table below is an example of using RBE to compare the efficacy of *in vivo* alpha radio immunotherapy.

Table 5-2. *RBE values for different alpha radio immunotherapy studies, in vivo (Sgouros et al., 2010)*

Radionuclide	Biological end-point	Reference radiation	RBE
^{213}Bi-(Fab´)	marrow	^{90}Y- (Fab´)	~ 1
^{213}Bi-(Fab´)	tumour growth delay	^{90}Y- (Fab´)	2 - 14
^{211}At- (IgG)	WBC reduction	Whole body Co-60	5.0 ± 0.9
^{211}At- (IgG)	WBC reduction	^{99m} Tc- (F(ab´)$_2$)	3.4 ± 0.6
^{211} At- (F(ab´)$_2$)	tumour growth delay	Whole body Co-60	4.8 ± 0.7
^{213}Bi- (IgG)	leukaemia reduction	^{90}Y- (IgG)	~ 1

Cell survival curves and the tumour control probability provide additional ways to predict the biological response of cells to radiation. The cell survival curve is a mathematical curve used to describe the survival of a population of irradiated cells. Generally, the cell surviving fraction is plotted in logarithmic scale on the y-axis against the dose on the x-axis. Several published papers have used microdosimetry to analyse cell survival curves (Roeske and Stinchcomb, 1996, 2000). Aurlien et al. used microdosimetry to analyse cell survival curves of human osteosarcoma and bone marrow cells in vitro (Aurlien, 2000). The experiments were performed to simulate the effects of alpha therapy, evaluated by Monte Carlo microdosimetry and clonogenic cell survival. The cumulated activity and absorbed dose were calculated from microdosimetric parameters of average specific energy by single event, number of hits and single-event frequency distribution. The survival fractions were estimated experimentally for each cell line. Thus, the cell survival can be plotted and can be used to predict the outcome of the therapeutic radiotracer for clinical study. The cell survival curves of two types of cell lines (OHS - human osteosarcoma and BM - mononuclear bone marrow) from Aurlien et al. are shown in figure 5-9 (Aurlien, 2000).

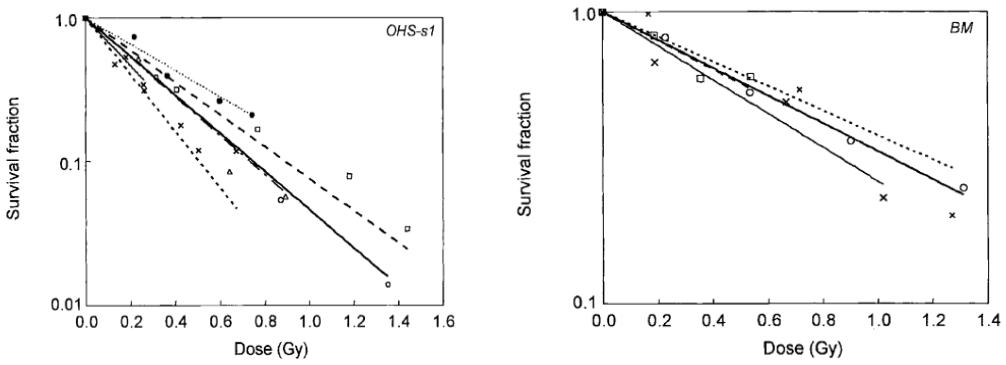

Figure 5-9 Cell survival fraction as a function of absorbed dose for OHS-s1 and BM cells –modifed from (Aurlien, 2000)

In light of the above arguments, this chapter aims to study the cellular distribution of radiotracer in a thyroid model. In the first part of this chapter, we aim to use EM and MAR to study the cellular distribution of non-metabolised tracers (pertechnetate/perrhenate) in rodent (rat and mouse) thyroid. In the second part of this chapter, we aim to apply small-scale dosimetry to consider the absorbed dose distribution when radionuclides were distributed in different locations within or outside the cell. The thyroid geometrical model and tracer distribution from MAR were used as input information for small-scale dosimetry calculation using the MCNPx platform.

5.2 Materials and Methods

5.2.1 Tracer localisation

There were 2 methods that performed in this study; (1) Electron microscope and (2) micro-autoradiography

5.2.1.1 Electron Microscope

5.2.1.1.1 Animal samples

Animal experiments were performed according to the licence under the United Kingdom (UK) Government Home Office and protocols were approved by the local ethic committee. TEM tracer localisations were initially performed using healthy *BALB/c* mouse (female, 4-8 weeks old, weight ~ 25 g.). Due to small size and difficulty in dissection of the mouse thyroid, we re-designed the study to use the larger rodent species. Hence, the *Wistar* rat (female, weight ~ 250 g.) was chosen to use in this study.

5.2.1.1.2 Perrhenate Compound

The detection principle of TEM is not related to radiation but uses the interaction of an electrons beam with the electronic structure of the sample. Hence in this experiment, the non-radioactive compound (cold perrhenate [ReO_4^-]) was used instead of radioactive perrhenate ($^{188}ReO_4^-$).

Cold perrhenate (ReO_4^-) compound in form of sodium perrhenate ($NaReO_4$) was purchased from Sigma-Aldrich (Gillingham, UK). There are no data in the literature about the concentration levels of perrhenate (or rhenium) that cause toxicity to the cell/animal. We have calculated that the amount of rhenium based on the activity of 100 MBq of $^{188}ReO_4^-$ to be approximately 0.015 nM of rhenium. Then, we increased this concentration 100 times. Therefore, the compound was prepared in a phosphate buffer saline (PBS) with final rhenium concentration of 1 nM (186.21 pg/ml) and 10 nM (1862.10 pg/ml) for injecting to mouse and rat respectively.

5.2.1.1.3 Experimental Protocol

Cold perrhenate compound was injected into the animal via the lateral tail vein with volume of approximately 150 µl. Animals were terminated by exposure to carbon dioxide (CO_2) (schedule 1-appropriate methods of humane killing) 1 hr after injection. This time-point was

determined based on spatio-temporal quantification in scid/beige mice with ^{99m}Tc-pertechnetate in Chapter 3, in which pertechnetate reached its peak (3.27 %ID) at 1.22 hr after injection, however due to limitations of time, we used 1 hr time-point as this point the uptake determined by imaging was just slightly lower than maximum uptake (uptake at 1 h PI was about 3.15 %ID compared to 3.27 %ID at 1.22 h PI) but more convenience for experimental management.

5.2.1.1.4 Sample Preparation and TEM Imaging

After the termination process, the thyroid gland was immediately dissected under a microscope due to its small size (diameter about 1 mm with about 3 mm long). Then, the sample was quickly clamped using the copper clad pliers cooled to liquid nitrogen temperature. This selected method can fix the element in the cell and can protect the sample from ice crystals. Frozen samples were stored in liquid nitrogen until they were cryosectioned. Samples were sent to analyse at the Centre for Ultrastructural Imaging, King's College London, Guy's Campus (London, UK).

5.2.1.2 Micro autoradiography

5.2.1.2.1 Animal samples

Animal experiments were performed according to the licence under United Kingdom (UK) Government Home Office and protocols were approved by the local ethics committee. Female healthy Wistar rats (weight ~ 151-200 g) were selected to use in this study. Animals were housed in standard BSU conditions at BSU Unit (St Thomas Hospital, London, UK) with autoclaved water bottle and normal food (already irradiated).

5.2.1.2.2 Radionuclide

Clinical standard radiopharmaceutical ^{99m}Tc-pertechnetate was eluted as per clinical routine and dispensed from the Radiopharmaceutical Unit, Nuclear Medicine, Guy's Hospital (Guy's & St Thomas' Hospitals NHS Foundation Trust, London, UK). ^{188}Re-perrhenate was eluted from our on-site W-188/Re-188 generator (ITG-Isotope Technologies, Germany) using sterile normal saline for injection (Baxter Healthcare, Newbury, UK). The radiochemical purity of ^{188}Re-perrhenate was tested prior to inject into animal as described in chapter 3.

5.2.1.2.3 *In vivo* MAR protocol

Activity of 100 MBq of ^{99m}Tc-pertechnetate diluted in normal saline with volume less than 200 µl was injected into the rat via the lateral tail vein. For ^{188}Re-perrhenate, activity of 100 MBq (volume less than 200 µl) was intravenously injected into the lateral tail vein.

After injection under anaesthesia, the rats were sacrificed by schedule 1 (neck dislocation) at 1 hr after injection. This terminal time-point was based on spatio-temporal quantification of scid/beige mouse in Chapter 3, as discussed previously, taking into account practical limitations of time; Thus we chose the 1 hr time-point for our experiment (uptake about 3.15 %ID and about 1.25 %ID at 1 hr PI for ^{99m}Tc-pertechnetate and ^{188}Re-perrhenate respectively).

5.2.1.2.4 Sample Preparation

We tested our emulsion by preparing (A) positive control with ^{99m}Tc (B) negative control of cold ^{99m}Tc (10 half-lifes) and (C) negative control of PBS. Each tested sample was prepared by suspended (positive ^{99m}Tc or negative control of cold ^{99m}Tc or PBS) in 1 % agar, then snapped frozen with OCT (Optimal Cutting Temperature) tissue freezing medium at -170 C^{o} in liquid nitrogen-cooled iso-pentane. Sectioning was performed in a cryostat (Bright Instrument Company Ltd, UK) with specimen and chamber temperature of -20 and -40 C^{o} respectively. The sections were mounted on the emulsion coated slide for 24 hours then developed.

For *in vivo* sample, thyroid with trachea was dissected immediately after animal termination, then the thyroid was separated from the trachea under microscope due to its small size. The sample was snapped and sectioned as explained above. Thyroid sample was cut in sagittal section with thickness of 10 µm for ^{99m}Tc-pertechnetate and 7 µm for ^{188}Re-perrhenate then placed on the slide (whether before or after emulsion coated – see next part).

5.2.1.2.5 Emulsion

Ilford emulsion (Agar Scientific, UK) was used in this study. The K-5 emulsion with crystal diameter of 0.2 µm was obtained in gel form. This product is offered for shorter exposure time and the K-series is better suited for light microscopy. The Ilford nuclear emulsions have highly uniform particle size, low background, long time stability, and consistent grain size. Typically, the emulsion (gel form) must be stored at 4 C^{o} avoiding ambient exposure of background radioactivity.

In this study, we have performed experiments with 2 settings (a) Mounting section directly onto emulsion-coated slide and (b) Mounting section on plain slide then coat with emulsion.

(a) Mount sample section directly onto emulsion-coated slide

With this setting, the cryostat sectioning was performed in a dark room and the emulsion-coated slide was prepared prior the experiment with these following steps:

I. Microscope slides (Thermo Scientific Ltd., UK) were washed in chromic acid solution (10% $K_2Cr_2O_7$, 10% H_2SO_4) for 2 hours, rinsed for 2 hours in running tap water then rinsed overnight in distilled water on the laboratory shaker.

(Steps II to VI were performed in dark room with safelight while minimising other background radioactivity)

II. K5 nuclear emulsion (in gel form) was melted in a pre-warmed measuring cylinder in a water bath at 40°C. The emulsion was diluted with deionised water (dH_2O) for example 3 parts of emulsion and 5 parts of dH_2O. Glycerol was also added to a final concentration of 0.01 %.

III. Microscope slides were subbed in diluted emulsion (from step II) removing any excess emulsion from the other side that would not be used. Then, the emulsion coated slides were transferred onto a chilled aluminium plate for 15 minutes and then dried on a flat level surface with cool air for 1 hour. Generally, this dipping procedure provides about 1-2 µm thick of emulsion after drying.

IV. Emulsion-coated slides were stored over desiccant at 4 °C until use.

V. Frozen sample sections (10 µm thick) were mounted directly onto emulsion-coated slide and exposed for 24 h at 4 °C in the dark box while minimising ambient light and local radioactive background.

VI. The mounted sample section on the plain slide was then coated with emulsion

With the above method (mounting the sample section directly onto emulsion-coated slide), the major problem was the difficulty in sectioning tissue in the dark room. To solve this, the sample section was mounted on a plain microscope slide and then the slide was later coated with emulsion in the dark room. As there were many steps in the process for emulsion-coated slide, there was the risk that the tissue might be detached from the slide surface. Therefore, we used the adhesive charged slide (Super-Frost Plus™, Thermo Scientific, UK) in order to adhesively bind the sample onto the slide surface. The processes for this method are listed below. Tissue section was placed onto positively charge slide

Slides were transferred to the dark room. Then, steps II – VI from previous method were repeated in dark room with safe-light

The samples were exposed for 24 h at 4 °C in the dark box while eliminating ambient light and local radioactive background.

5.2.1.2.6 MAR Processing

After 24 hours, the slides were transferred to dark room. Then, the exposed MARs were developed in 16% Kodak D19 (Eastman Kodak Ltd, USA) for 5 min. This developing agent was made on the day of use. Additionally, the solution was protected from light as the latter would increase the chance of fogging artefact. The slides were placed in 1 % acetic acid (CH_3COOH) for 5 minutes (to stop the developing process) and dipped in 0.5 % gelatine before being air dried for 30 minutes. Once dry, slides were fixed in 30% sodium thiosulphate ($Na_2S_2O_3$) for 5 minutes and washed in running tap water for 10 minutes with final wash in distilled water. The slides were left until dry.

5.2.1.2.7 DAPI Staining

In this study, we stained MAR tissue with DAPI fluorescence staining agent after MAR developing process. DAPI can pass a cell membrane and bind to A-T rich regions in double-stranded DNA. Hence, this allows to visualise the cell nucleus. DAPI can emit blue light (~ 460 nm) using the ultraviolet light (UV) as excited source and a blue/cyan filter.

5.2.1.2.8 Haematoxylin and Eosin (H&E) Staining

We also stained thyroid tissue with H&E using following steps;

I. After developing micro-autoradiograph slides
II. Dehydrate (15 seconds for each step)
    a. 100% Ethanol alcohol
    b. 95% Ethanol alcohol
    c. 75% Ethanol alcohol
    d. dH_2O (deionised H_2O)
III. Dipped slide in Haematoxylin for 10 minutes
IV. Running in tap water for 15 minutes, then washed in dH_2O
V. Dipped slide in Eosin for 5 minutes

VI. Dipped in 100% ethanol (in separate container for avoid contamination of Eosin)

VII. Dipped slide in 100% Histoclear® (Agar Scientific, Essex, UK) for 15 seconds

VIII. Fixed and mounted slides with a synthetic resin using DPX (Sigma-Aldrich, Gillingham, UK)

5.2.1.2.9 Silver Grain Cell Imaging and Post Processing Imaging Technique

The tissue and emulsion were viewed under fluorescence microscope (EVOS® XL, Life Technology, UK). Silver grain and emulsion were on different layers, so, focus adjustment for each plane was necessary for interpretation of results. Silver grains were examined under bright field. Post processing technique was used to enhance silver grain by adjusting brightness, contrast and thresholding of image using the AMIDE (AMIDE is a Medical Image Data Examiner) software (version 1.0.4, http://amide.sourceforge.net). For tissue stained with DAPI, the slides were viewed in fluorescence mode with UV excited.

5.2.2 Small-scale dosimetry

5.2.2.1 Input data (models and assumptions)

The fused image of MAR and DAPI (figure 5-10) was used as an input for simulation. The original dimension of this image was 110.67 µm (horizontally) × 76.67 µm (vertically) with 498 × 345 pixels. The fused image was manually segmented using the ImageJ software version 1.48v (National Institutes of Health, USA). Pseudo orange areas refer to colloid and we assume rest of the images are follicular cell.

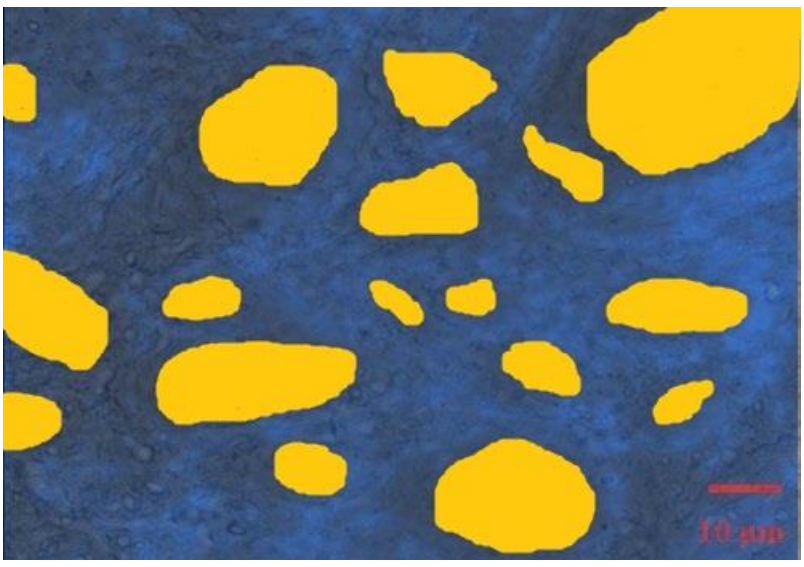

Figure 5-10 Segmentation of fused image (MAR, and DAPI), the orange areas indicate the colloid. We assume rest of the images are follicular cell.

The segmented image was digitised using MATLAB software version R2011b (MathWorks Inc., USA). We used a digitised number (0 and 1) to represent the location of radionuclide, “0” (white) means pixel element without radioactivity and “1” (dark) means pixel element with radioactivity.

Figure 5-11 Digitised images (“0” represents pixel element without radioactivity and “1” represents pixel element with radioactivity). There are 2 main conditions; (left) radioactive uniformly distributed in colloid and (right) radioactive uniformly distributed in follicle.

Ranges of electrons for both ^{188}Re and ^{131}I are far beyond the dimension of the original image. So, we propagated this image 5 times in both the X- and Y-axis, and also made the simulation 3D by overlapping 5 images in the Z-direction. The images below were propagated 5 times in 3 dimensions and resized to an integer matrix of 128 × 128 × 5 voxel (volume element dimension 1.6 × 1.6 × 1.6 μm^3). For interpolation, the “nearest neighbour” option was chosen to estimate an element value at a location in between original image voxel. With the “Nearest-neighbour interpolation”, the output element was assigned the value of the voxel that the point falls within, no other voxels are considered.

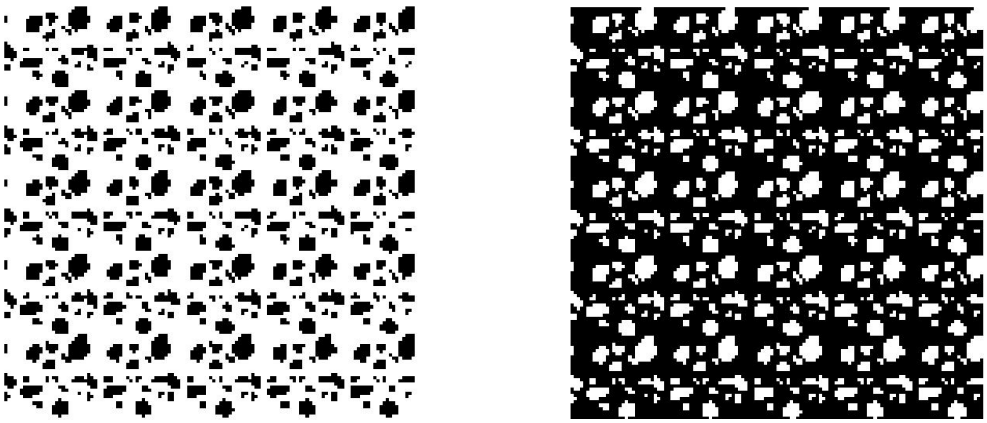

Figure 5-12 Simulation images after 5 times propagation in X-, Y- and Z-dimension. After resizing, the nearest option was used to interpolate the output element in between original image voxel

For micro-distribution of radiotracer, we initially set only 2 conditions (radionuclide in follicular cell or colloid, as shown in figure 5-12) with uniform distribution of the two radionuclides (^{131}I and ^{188}Re). Hence, we examined four scenario of tracer distribution for simulation.

(A) ^{131}I uniformly distributed in colloids, no radioactivity in other areas

(B) ^{131}I uniformly distributed in follicular cells, no radioactivity in other areas

(C) ^{188}Re uniformly distributed in colloids, no radioactivity in other areas

(D) ^{188}Re uniformly distributed in follicular cells, no radioactivity in other areas

The scenario of radiotracer distribution was assumed based on our data from previous part and also published data of thyroid distribution in new-born mouse accessed using SIMS (Elbast et al., 2008b). The simulation was assumed to be reflect only 2 tissue types; thyroid and soft tissue. Material compositions were taken from the ICRU report 44 (International Commission on Radiation Unit and Measurement, 1989) (Units and Measurements, 1989). Follicular cells were assumed to be of thyroid tissue composition whereas colloid was assigned to be of soft tissue composition from the available specifications of the ICRU report 44. The density of thyroid is 1.05 g/cm^3 and compositions in % of: hydrogen (H) 4, carbon (C) 11.9, nitrogen (N) 2.4, oxygen (O) 74.5, sodium (Na) 0.2, phosphorus (P) 0.1, sulphur (S) 0.1, chlorine (Cl) 0.2, potassium (K) 0.1 and iodine (I) 0.1. The density of soft tissue is 1.06 g/cm^3 with compositions in % of: H 10.2, C 14.3, N 3.4, O 70.8, Na 0.2, P 0.3, S 0.3, Cl 0.2, and K 0.3 (Ghorbani et al., 2014; Kramer et al., 1997; Units and Measurements, 1989)

5.2.2.2 Simulation

The overview process of the simulation is shown in the figure below. The first step was the preparation of input files (segmented MAR, tissue composition, and tracer distribution map) as previously described. OEDIPE (French acronym means Tool for the Evolution of Personalised Internal Dose) is a user friendly graphical interface developed in IDL® Interactive Data Language (ITT Visual Information Solution, Colorado, USA). OEDIPE was used to design and create the Monte Carlo input file. For the simulation, the MCNPX version 2.5.0 was used to calculate small-scale dosimetry in this study. In MCNPX, the electron and photon (Franck et al., 2007) cut-offs were set to 1 keV, the number of histories was set to 2 million to keep the statistical errors below 10 %.

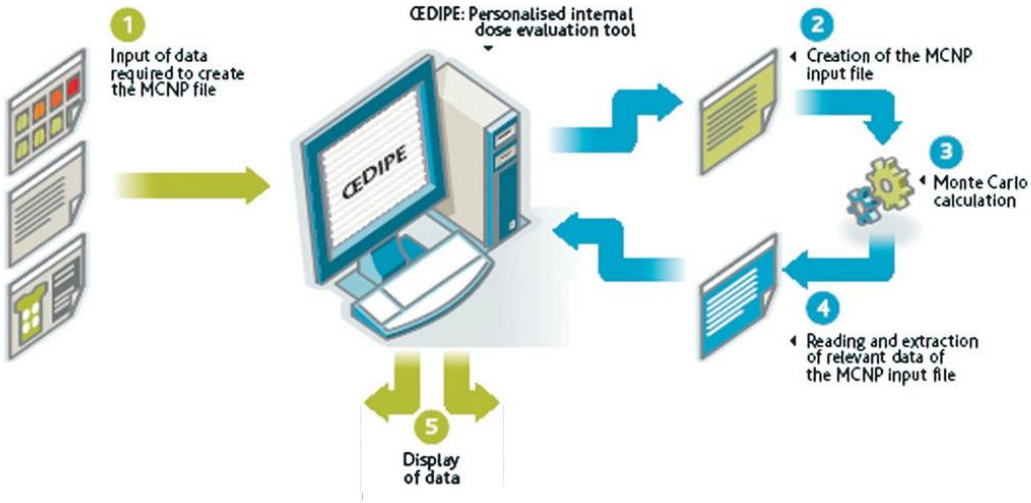

Figure 5-13 Schematic diagram of simulation in this study with OEDIPE and MCNPx (modified from (Franck et al., 2007))

Once the simulation of the predefined event population is complete, OEDIPE was used to export the results. The dose calculations and absorbed dose distribution histograms were analysed with IDL.

5.3 Results and Discussion

5.3.1 Tracer localisation

5.3.1.1 Electron Microscope

5.3.1.2 Electron Microscope with Balb/C Mouse

The mouse was injected with cold perrhenate compound and then culled at 1 hr after injection according to protocol stated above. The TEM, STEM/HAADF and EDX spectrum images acquired are shown in figure 5-14

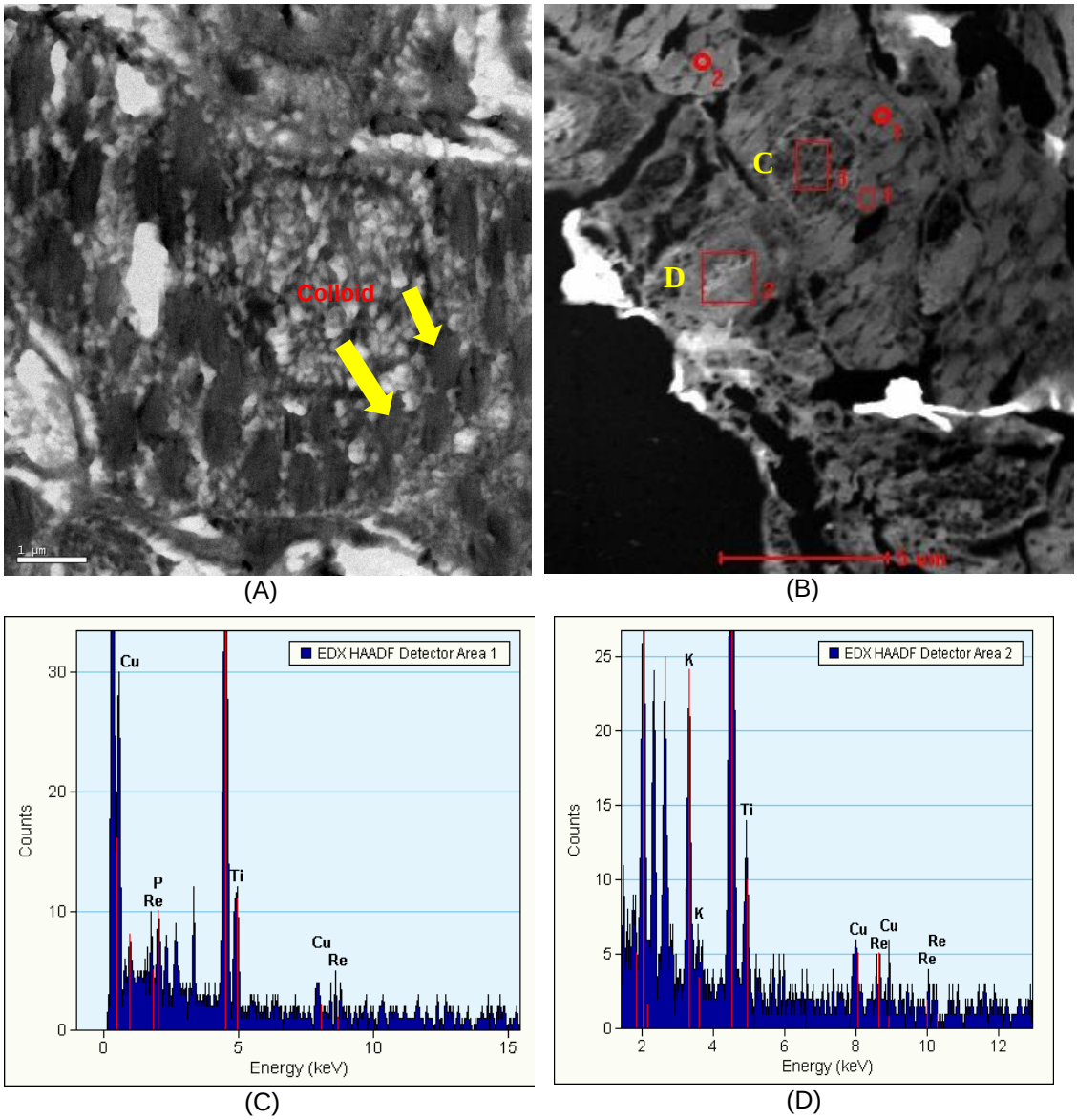

Figure 5-14 (A) Conventional TEM images, the dense area (arrow) represents colloid (B) HAADF (High Angle Annular Dark Field) technique. Spectra in figure (C) and (D) are correspond to the rectangular ROI in image (B). These spectra are used for elemental analysis

The figure 5-14 A was taken with conventional TEM imaging, where the dense areas (arrow) are colloid. The figure 5-14B was imaged using the HAADF technique. As explained earlier, the contrast of HAADF represents the average atomic number in that particular area. For

elemental localisation with EDX, the ROIs were drawn on the dense blobs (rectangular area in figure 5-5B). The spectra show peaks of copper (Cu), rhenium (Re), phosphorus (P), potassium (K) and Titanium (Ti). The Cu, P and K were suggested to be natural endogenous elements in thyroid gland (Błażewicz et al., 2010). The sample holder was made from titanium, so, the titanium spectrum was observed as well. The weak signals of rhenium were observed in both areas but it just a few counts above the background. Also, the position of spectrum (characteristic X-ray) was very close to endogenous copper and phosphorus which complicate accurate detection of the characteristic rhenium peak.

We have compared the size of thyroid from our images with the published work by Champion et al. The imaging study of newborn rat thyroid (Wistar, 7 day old) by Champion et al reported the size of colloid as 12 µm in diameter and for cellular shell (colloid + follicle cells) as 20 µm in diameter using SIM (secondary ion mass spectroscopy). However, our colloid was approximately 1 µm which it quite small when compared with those published data.

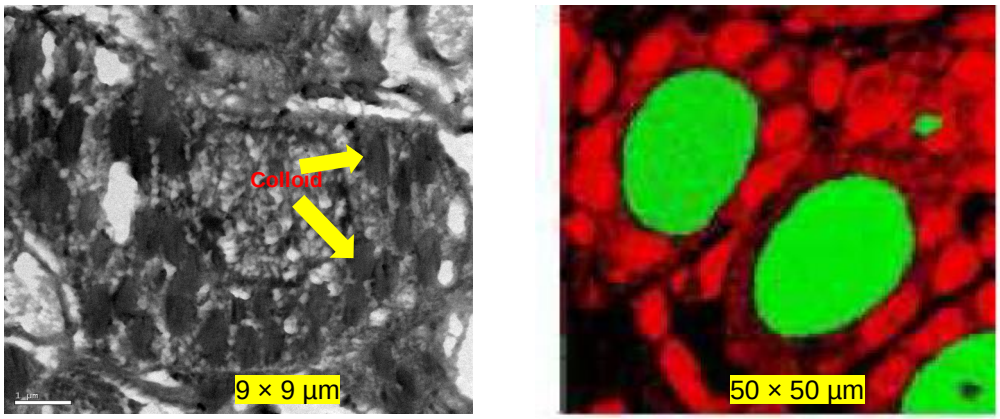

Figure 5-15 (Left) TEM image from the Balb/C mouse experiment (Right) new-born rat thyroid with SIM technique (image taken from Champion et al) (Champion et al., 2007a). According to Champion et al, the size of new born rat colloid was about 20 µm in diameter while in our Balb/C images the colloid diameter was just about 1-2 µm.

Hence, this observation limited our confidence in accurately sampling the required area with TEM imaging. Therefore, it was decided to repeat this experiment with larger species (easier to dissect the thyroid free from surrounding tissue) and to increase the concentration of cold perrhenate compound from 1 to 10 nM.

5.3.1.2.1 Electron Microscope with *Wistar* rat

As mentioned in previous part, we changed to larger species of rodent (from 25 g Balb/C mouse to 250 g Wistar rat). The concentration of cold perrhenate compound was increased 10 times (increased amount of cold perrhenate from 1 nm to 10 nm). All other protocol parameters remained as discussed in the previous section. The following figures demonstrate examples from TEM imaging of Wistar rat, where we also correlated this image with the schematic diagram of the microscopic structure of the thyroid gland.

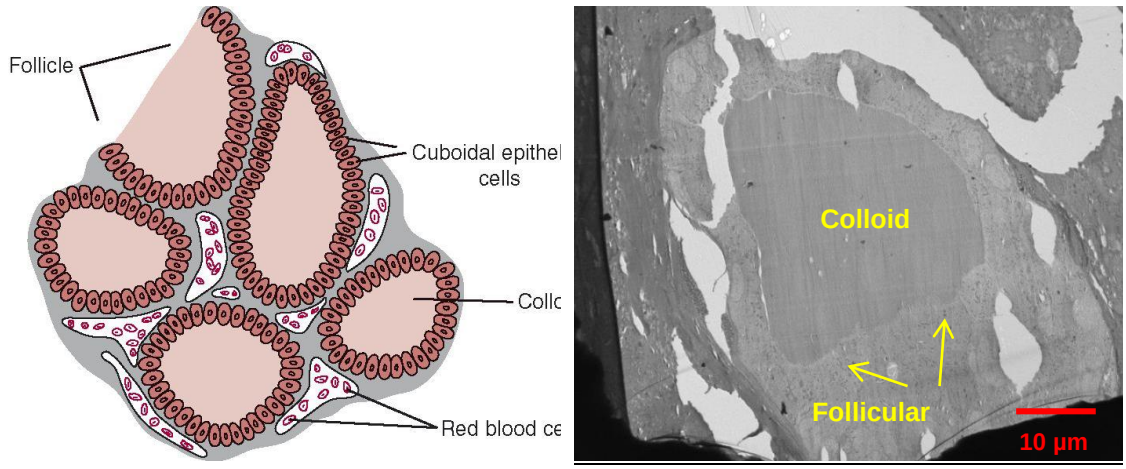

Figure 5-16 (Left) Schematic diagram of microscopic appearance of thyroid gland - modified from (Hall, 2015) (Right) TEM Image of our sample – a healthy female Wistar Rat (1500x)

A TEM image from normal Wistar rat thyroid sample is shown in figure 5-16. The colloid diameter was approximately 30 to 40 µm; follicular cell dimension was 5-7 µm. However, it was not possible to lower magnification in order to obtain several follicles due to a technical problem of the microscope. To localise the elemental map, the STEM/HAADF and EDX spectra were used as shown in figure 5-17.

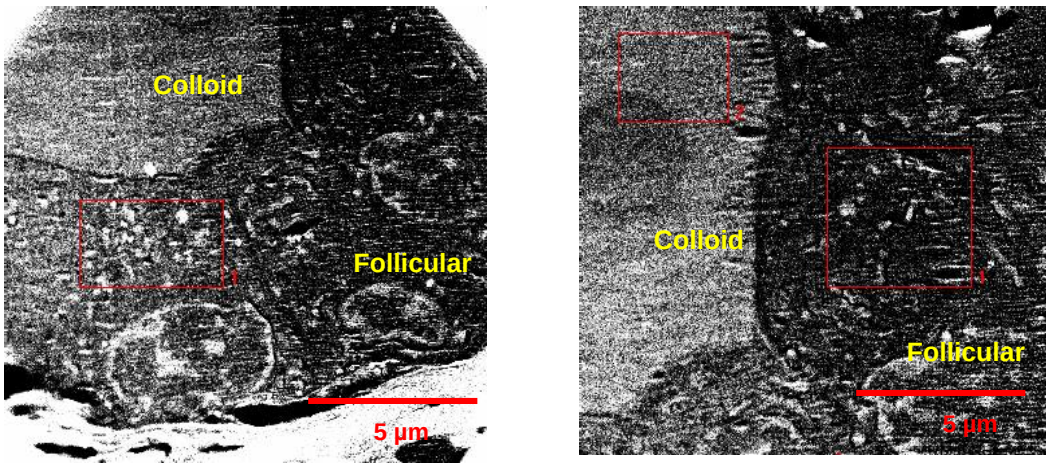

Figure 5-17 Images were acquired with HAADF technique which the contrast depending on the average atomic number, the red rectangular area shows the region of interest for obtaining the spectra for elemental analysis

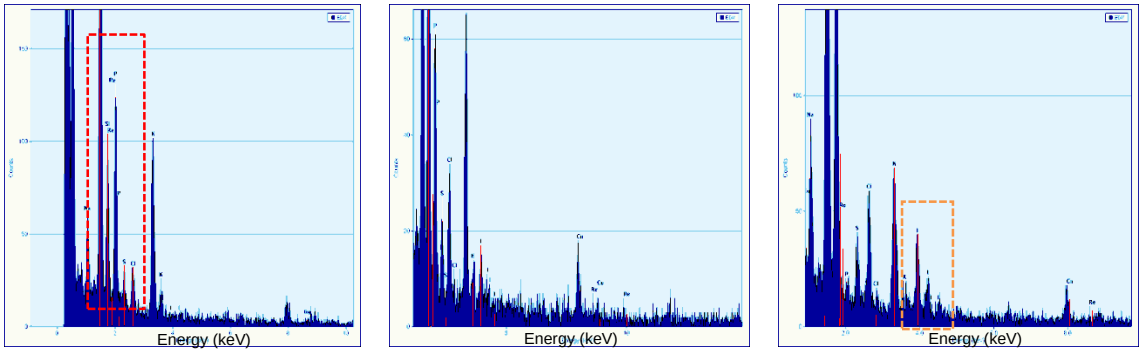

(A) (B) (C)

Figure 5-18 The data generated by EDX technique showed several spectra corresponding to the elements making up the composition of the sample being analysed (figure 5-18 A and B) correspond to rectangular ROI 1 in figure 5-17 which are follicular cell (figure 5-18 C) correspond to rectangular ROI 2 in figure 5-17 which is colloid. The rectangular red-dashed (figure 5-18 A) shown the primary peak of rhenium that located at a similar position as the endogenous phosphorus. The rectangular orange-dashed (figure 5-18 C) area presented the iodine spectrum in the colloid area but not found in the follicular cell.

The spectra of copper, potassium, sulfur, chlorine and phosphorus were observed in thyroid follicles, suggesting these to be natural elements in the thyroid. However, the sprectrum of rhenium could not be confirmed in both folicle and colloid due to this peak being located in close proximity to the peak of endogenous phosphorus. Additionaly, iodine was detected only in the colloid but not in thyrocyte areas which correlated well with the study by Champion et al. and this confimed our initial hypothesis that most iodine is located in the colloid and not in the follicular cells (Champion et al., 2007a). However, the cost of this technique is high as it requires costly dedicated equipment.

Further investigations are needed in order to confirm that rhenium is solely located in thyrocytes and not in the colloid, hence, we will use other techniques (e.g. micro-autoradiography) in order to prove this statement in the next section.

5.3.1.3 Micro-autoradiography

The figure below shows high magnification images (400x) under the following conditions (A) silver grain from ^{99m}Tc (10 µm section of uniform source suspended in 1 % agar) (B) negative control of cold ^{99m}Tc (10 µm section of cold (10 half-lifes) ^{99m}Tc suspended in agar) and (C) negative control (10 µm section of PBS suspended in 1 % agar). The sections were mounted on the emulsion coated slide for 24 hours then developed.

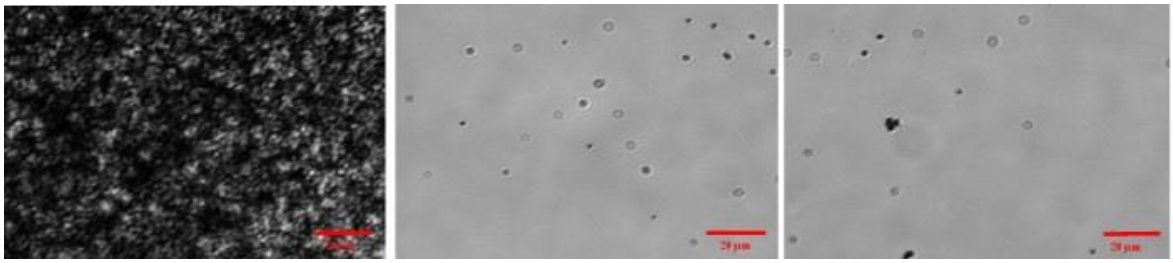

(A) (B) (C)

Figure 5-19 The sectioning of 10 um of (A) ^{99m}Tc (B) Cold ^{99m}Tc and (c) PBS suspended in 1 % agar then incubated for 24 h with emulsion coated slides (400x)

The slide in figure 5-19 (A) with ^{99m}Tc showed high density of silver grains as expected while cold ^{99m}Tc and PBS showed only a few grains visible which is likely a result from emulsion fog/background. For *in vivo* MAR, the thyroid was dissected immediately and then embedded with OCT and snap-frozen in liquid nitrogen cooled liquid propane. Sections were cut with a thickness of 10 µm in a cryostat. To confirm that we picked the right tissue, we stained our sample section with DAPI and also with H&E (haematoxylin and eosin). The section was placed on microscope slide (no emulsion coated). The image is shown in figure 5-20 below (captured by EVOS®XL).

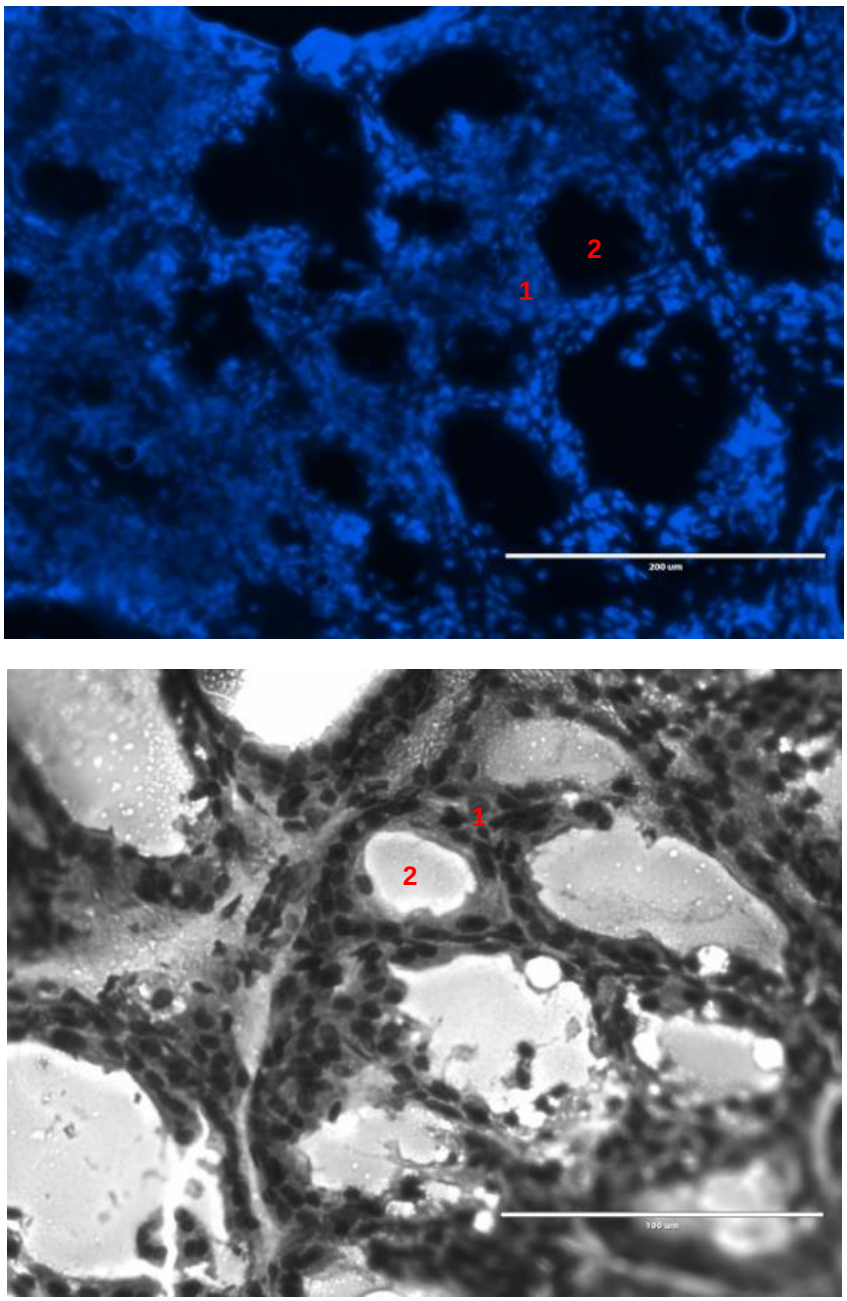

Figure 5-20 Wistar rat thyroid (Top) tissue stains with DAPI under fluorescence microscope (200x) (Bottom) H & E staining under bright field (200x). (1- Thyroidfollicular cell (thyrocyte), 2 – Colloid). It was important to note that images were from different areas.

The images in figure 5-20 (top) and (bottom) displayed the 10 µm section of thyroid with DAPI and H & E staining. DAPI and haematoxylin stain the nucleus of thyroid follicular cells. The diameter ranges of colloid were 40 – 100 µm. The wall of follicular cells was not clearly seen from staining but the estimated sizes of the nucleus were about 5 × 5 µm (width × length). The morphological dimensions of colloid and thyrocyte agreed well with our previous electron microscope study.

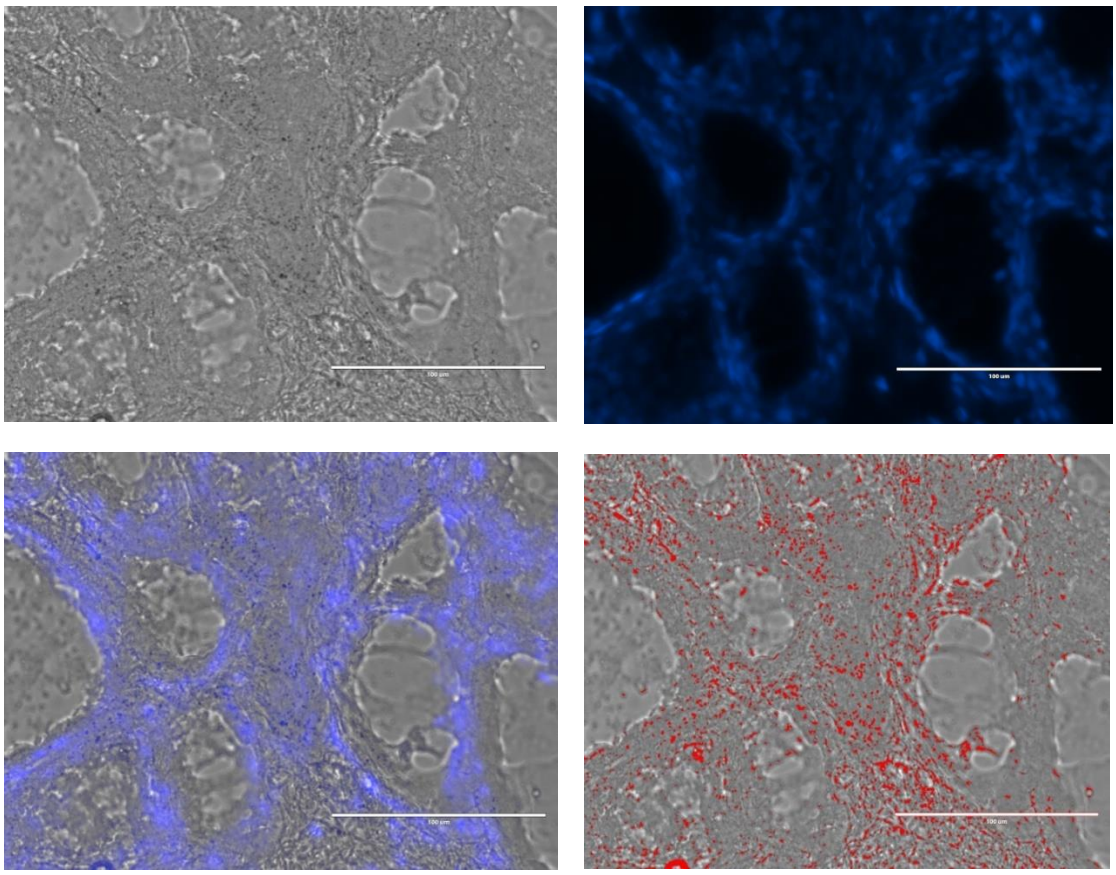

Figure 5-21. Wistar rat thyroid injected with 100 MBq of ^{99m}Tc-pertechnetate, tissue harvested at 1 h after injection. (Top Left) Micro-autoradiograph of 10 µm section, image with bright-field (200x). (Top Right) Image from similar area with DAPI under fluorescence microscope (200x). (Bottom Left) Fused image of micro-autoradiograph and DAPI. (Bottom Right) Grain enhancing from post processing technique, the red dots refer to the silver grain.

Figure 5-21 showed the thyroid autoradiograph, the tissue section was placed on the slide and then the slide was transferred to the dark room for coating process. After exposure for 24 hours, the MAR slide was developed using the protocol stated in previous sections. Additionally, we stained a sample with DAPI and also showed fusion of images in figure 5-21 (bottom left). In figure 5-21 (bottom right), the digitised red dots indicate the grains. Interestingly, silver grains were observed only in thyrocyte areas but were not present in colloid. *In vivo* MAR with ^{188}Re-perrhenate also showed similar findings (as illustrated in next figure).

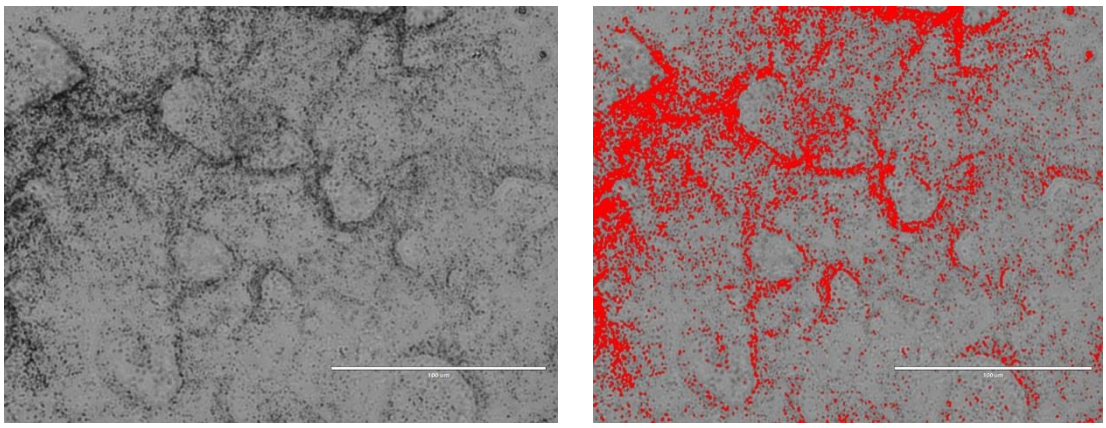

Figure 5-22 Wistar rat thyroid injected with 100 MBq of ^{188}Re-perrheate, tissue harvested at 1 hr after injection. (Left) Micro-autoradiograph of 7 µm section, image with bright-field (200x). (Right) Image from similar area with grain enhancing from post processing technique, the red dots refer to the silver grain.

Figure 5-22 presented the thyroid autoradiograph, the tissue section was placed on the slide, the section was cut thinner (from 10 µm to 7 µm) in order to yield better resolution (Puncher and Blower, 1994b). Then, the slide was transferred to the dark room for coating process. After exposure for 24 hours, the MAR slide was developed using the protocol stated in previous sections. However, the DAPI staining was not performed due to technical problem.

Based on this study, the findings support our initial hypothesis that non-metabolised tracers (e.g. pertechnetate, perrhenate) localise only in thyrocytes (not in colloid). In addition, we also performed a control experiment by mounting the non-radioactive thyroid (rat injected with 150 µl of PBS) on the emulsion coated slide. This slide was also exposed for 24 hours with similar condition and then developed using same protocol. The image is shown in the figure below.

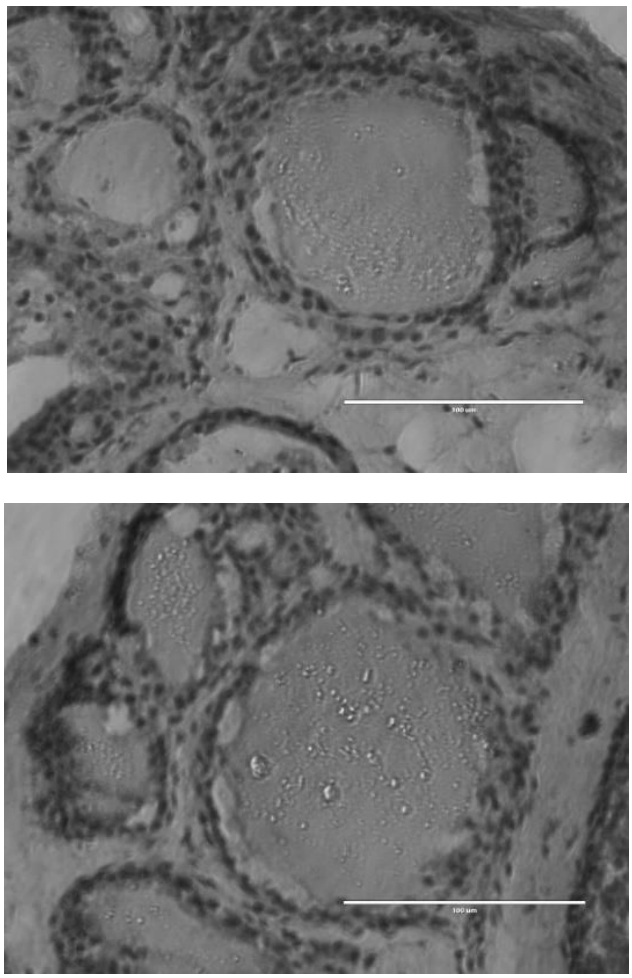

Figure 5-23 Thyroid of Wistar Rat injected with 150 µl of PBS (negative control). The tissue section was mounted on the emulsion-coated slide, then exposed and developed using similar protocol

The control experiment (as illustrated in figure 5-23) showed no silver grain in both slides. These indicated that silver grains (as seen in figure 5-21 and 5-22) were produced from secondary electrons of ^{99m}Tc-pertechnetate and ^{188}Re-perrhenate. In this study, we proved that radiotracer distribution of ^{99m}Tc-pertechnetate and ^{188}Re-perrhenate in thyroid have similar patterns. This finding was supported our initial hypothesis.

It was important to mention that according to the published literature pertechnetate provides a better resolution due to the short range of secondary electrons. As previously reported (Puncher and Blower, 1994b), ^{188}Re provided a resolution of 3.9 µm whereas ^{99m}Tc gave resolution of 2.8 µm. It was important to clarify that the resolution value of MAR is usually expressed as the distance from the edge of uniform source to the point that grain density falls to half value over the source. With reference to the principle of silver grain forming, ^{99m}Tc has no beta emissions and the process only depends on secondary emissions of electrons (Auger and internal conversions). This is similar to ^{125}I. In terms of exposure time, ^{99m}Tc has much shorter

half-life, so, exposure times longer than 24 h are meaningless. The additional advantages of ^{99m}Tc-pertechnetate include that it is cheap, available daily, imparts very low radiation dose to user (compared with ^{188}Re-perrhenate).

The poorer resolution of ^{188}Re results from its high-energy beta particles (penetrate longer range in emulsion). The thinner slide can improve the resolution, however, this was difficult to perform especially with a small tissue/organ (Puncher and Blower, 1994b). Also, we have not quantified the silver grain at this stage, this will be carried in future work. Further investigations (such as SIM-Secondary Ion Mass Spectroscopy) are needed in order to confirm this statement, also further MAR experiments ideally with ^{125}I-NaI are required to prove that there is no stable iodine present in thyrocytes at equilibrium conditions.

To conclude our assumption of tracer distribution, we need to combine the results from 2 experiments (TEM and MAR). With TEM, the primary peak of rhenium could not be unambiguously detected because this peak is located close to that of endogenous phosphorus. However, iodine was detected only in colloid but not in thyrocytes. With MAR, pertechnetate and perrhenate were found present only in thyrocyte areas while no pertechnetate/perrhenate were detected in the colloid. These information were used as an input for small-scale dosimetry.

5.3.2 Small-scale dosimetry

Graphs in figure 5-24 are plotted of the number of volume elements (no. of voxel) per bin of absorbed dose (cGy) in the distribution.

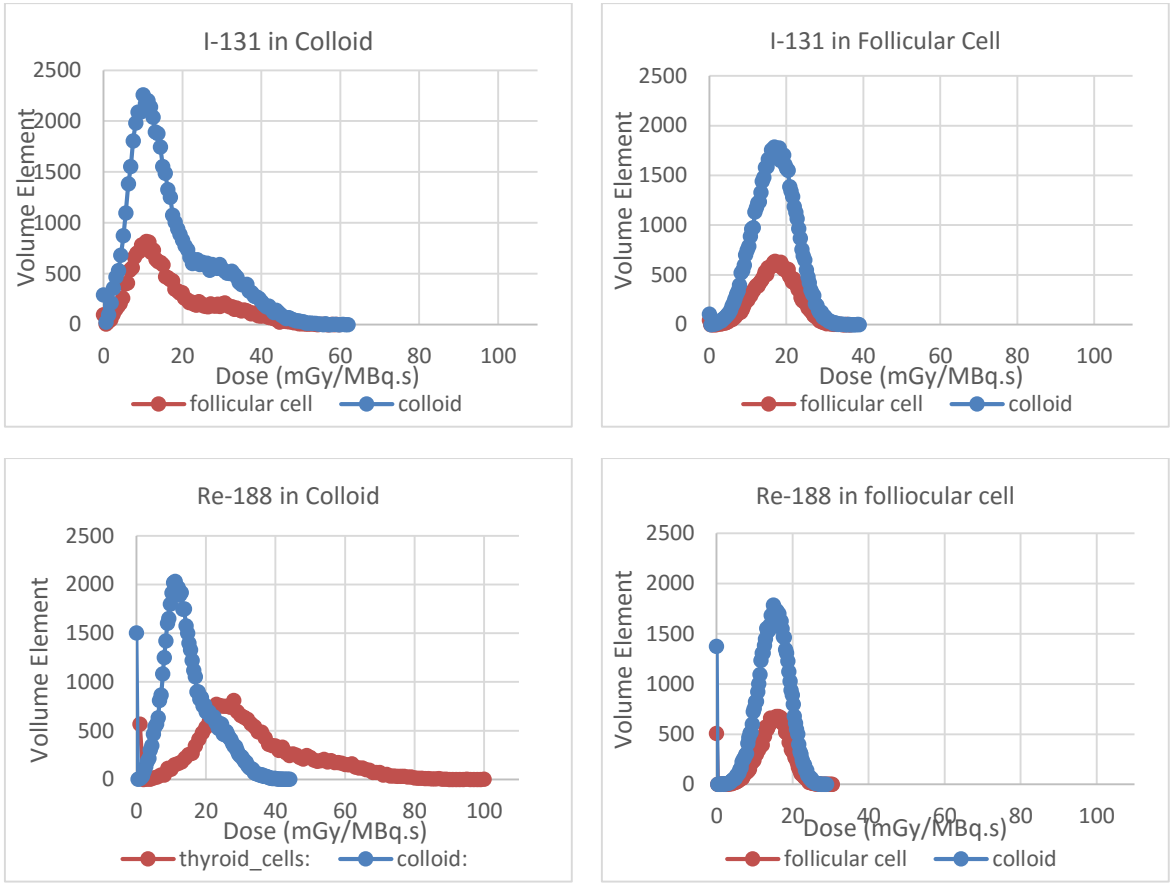

Figure 5-24. Absorbed dose distribution in thyroid section, calculated by small-scale dose modelling with MCNPx. The graphs show the population of voxels that received absorbed dose with following conditons (a) ^{131}I in colloids (top left) (b) ^{131}I in follicular cells (top right) (c) ^{188}Re in colloids (bottom left) and (d) ^{188}Re in follicular cells (bottom right). There was assumed to be no radioactive elsewhere in each condition

These graphs indicate the population of voxels that received absorbed dose from different scenarios of tracer distributions. ^{131}I in colloid and ^{188}Re in follicle are biologically realistic, as both these two conditions were experimentally demonstrated in the first part of this chapter with transmission electron microscopy and micro-autoradiography techniques along with other published studies in the literature (Champion et al., 2007a; Elbast et al., 2008b). In addition, ^{131}I located in colloid could also occur during the transition time of transferring iodide from the basal- to apical- membrane of NIS. As shown in a study by Champion et al (figure 5-10), the kinetic pattern of iodine in thyroid cells of new-born mice seems to indicate that there is no iodine observed in follicular cells at 1 hr post injection. Hence, we assumed that the transition of iodine from the outer membrane to colloid is rapid.

Based on the graph, the total elements comprised 81920 voxels (128 × 128 × 5) of which 60100 voxels (73.36 %) are assigned to colloid and 21820 voxels (26.64 %) are follicular cells. As seen from the graphs, the dose distribution spectrum was broader when the radionuclide was localised in colloid. The dose range was distributed from 0 mGy/MBq.s to 0.619, 0.457, 0.400 and 0.304 mGy/MBq.s for ^{131}I in colloid, ^{188}Re in colloid, ^{131}I in follicular cell and ^{188}Re in follicular cell respectively. The dose which most voxels were found to absorbed ("mode" of absorbed dose in colloid) were 11.26mGy/MBq.s (2202 voxels) for ^{131}I distributed in colloid, 16.93mGy/MBq.s (1785 voxels) for ^{131}I distributed in follicular cell, 11.14mGy/MBq.s (2032 voxels) for^{188}Re distributed in colloid and 14.92mGy/MBq.s (1786 voxels) for ^{188}Re distributed in follicular cell. However at this stage, we assumed that the cell nucleus is the biological target for cell killing and the nucleus is located in the follicular cell. Hence, we plot another graph (figure 5-25) to illustrate the absorbed dose distribution in follicular cells (i.e. excluding colloid voxels).

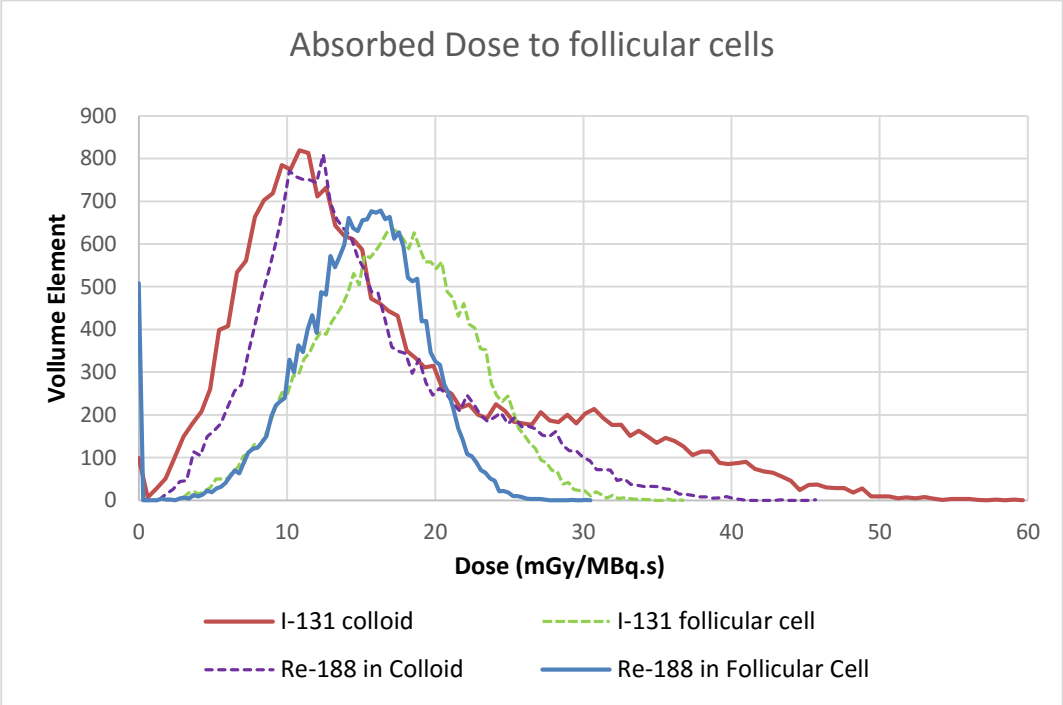

Figure 5-25 Absorbed dose distribution to follicular cells

Fig. 5-25 shows that both ^{131}I and ^{188}Re deliver higher dose to more thyrocytes if the radionuclide is located only in thyrocytes and not in colloid. However, only ^{188}Re can show this advantage because only ^{188}Re is in the thyrocytes.

Considering only biologically realistic distribution scenarios, the mode of absorbed dose to follicular cells was 16.32 mGy/MBq.s (678 voxels) and 10.85 mGy/MBq.s (819 voxels) for ^{188}Re

located in follicular cell and ^{131}I located in colloid respectively. We considered only these two scenarios as the transit time of radioiodine in cell is very fast (less than an hour after administration based on the Champion study (Champion et al., 2007a)) compared with the half-life of ^{131}I (8.01 days).

This preliminary finding indicates that most of follicular cells received high dose when ^{188}Re was located in follicular cells. Moreover, the absorbed dose spectrum from ^{188}Re was narrower when compared with ^{131}I located in the colloid.

As a measure of the broadening of the absorbed dose distribution, the width of the histogram distribution at 50% of the maximum when ^{188}Re being located in follicular cells was 10.62 – 19.86 mGy/MBq.s compared with 6.03 – 17.78 mGy/MBq.s when ^{131}I located in colloid. Broad dose distribution was observed when ^{131}I located in colloid. The volume elements of follicular cell that received more than 17.78 mGy/MBq.s was 7848 voxels (35.97 % of follicular cells) but there were 1889 voxels (8.66 % of follicular cells) which received less than 6.03 mGy/MBq.s. Conversely when ^{188}Re was located in follicular cells, 77.80% of follicular cells received absorbed dose between 10.62 -19.86 mGy/MBq.s. Lesser absorbed dose and narrower range indicate more uniformly distributed dose which should make it easier to predict the biological effect on the cell or nucleus. On the other hand, it might be difficult to predict the radiobiological effect for broad dose distribution as some cells received high absorbed dose whereas there are some areas that received low dose. Also the lower energy limit on emission energies will cause underestimation of the advantage of the radionuclide being inside the cell.

It is important to note that results of MCNPx simulations reported in this chapter are very preliminary. The main limitations of this work are the lack of rigorous validation of the simulation model in such a small region (micron level) and ideally with cross-validation with radiobiology experimental results (e.g. *in vitro* clonogenic cell survival assay) and also the fact that beta ranges from both radionuclides (^{131}I and ^{188}Re) are far beyond the simulation space even if we already propagated our histology section in X-, Y- and Z-dimensions (3.35×10^{-7} cm^3 calculated from voxel dimension of $128 \times 128 \times 5$ with voxel size of $1.6 \times 1.6 \times 1.6$ µm^3).

In addition, our simulated activity (0.01 MBq.s homogeneous distributed in the section) is generated the overestimation of activity when scaling this simulated volume (3.35×10^{-7} cm^3) to average volume of human thyroid (average of 14.4 g for female age 20-96 years and assuming density of thyroid 1.05 g/cm^3) (Pankow et al., 1985). The calculated human-equivalent activity from our simulation is 408.16 GBq whereas the clinical administered dosage ranges are 0.19 to

0.74 GBq for hyperthyroidism, 2.75 to 7.40 GBq for thyroid cancer. The initial choice of simulated activity was speculative in order to avoid issues of high noise levels though results can be scaled down to clinically applicable levels of administered activities.

There are also some aspects where a deeper understanding of the biological and physical mechanisms are required in this simulation, for example, effects of radiation on colloid, loss of follicular structure in thyroid cancer, threshold dose for killing the cell or to produce DNA double strand break in the nucleus and also different patterns of dose distribution in colloid and follicular cells (e.g. homogeneous, heterogeneous or at the periphery of the cell). These will be factors to note for further investigation in future work.

5.4 Conclusion

Our initial assumption was that metabolised radiotracers (e.g. ^{123}I-NaI, ^{131}I-NaI) are taken up by NIS at the apical membrane, then oxidised and organified to thyroid hormone in thyrocytes, and stored in colloid until released to the bloodstream. In contrast, non-metabolised tracers (e.g. ^{99m}Tc-pertechnetate, ^{188}Re-perrhenate) are not involved in the processes of thyroid hormone synthesis and as such are expected to be solely localised in in thyrocytes.

For tracer localisation with EM, the primary peak of rhenium cannot be detected in follicular cells due to limitations of detection sensitivity and the physical properties of rhenium (proximity of characteristic peak to other elements naturally present in the sample). Nevertheless, this work has shown the capability of EM as a tool for tracer localisation at cellular level and elemental analysis of high spatial resolution images of rat thyroid follicles.

As shown in this work, the MAR technique can be used to determine the micro-distribution of radiopharmaceuticals at cellular level. Results showed that pertechnetate/perrhenate was located only in thyrocytes but was not present in colloid.

It can therefore be concluded that non-metabolised tracers are only located in thyrocytes. To conclude our initial assumption, we need to combine the results from 2 experiments (TEM and MAR). This information was used as an input for small-scale dosimetry.

The next part of this chapter described small-scale dosimetry. The work described in this study has been carried out to estimate the absorbed dose distribution among a population of cells at cellular level using MCNPx. The modelling information (cell geometry, radionuclide distribution) were experimentally derived from real histology sections and MAR of the rat thyroid as described in the first part of this chapter. Then the data formed the input to Monte Carlo simulations using the OEDIPE platform. These initial results demonstrated that ^{188}Re-perrhenate, being localised in follicular cells, has dosimetric advantages over conventional^{131}I-NaI localised in the colloid. By assuming follicular cells are targets for cell killing, the pattern of absorbed dose when ^{188}Re distributed in follicular cells seemed to have some advantage as absorbed dose ranges were higher and also more uniform as about 80% of the cell population received dose within narrower range. On the other hand, the absorbed dose received by ^{131}I located in colloid were inhomogeneous as only 65% of the follicular cells population was exposed to a dose range within the width of the histogram distribution at 50% of the maximum, whereas some cells received high and some cells received low dose which may be difficult to predict the range of biological effects.

These pilot data seem to support the macro-dosimetric estimation of possible advantages from using ^{188}Re-perrhenate treatment of thyroid disease. However, further model validation together with deeper knowledge of radiobiological and physical modelling are needed for establishing these preliminary results for clinical translation of this tracer.

Chapter 6 Summary and Future Work

6.1 Thesis Summary

Work in this thesis investigated the isotopes ^{186}Re- and ^{188}Re- in the form of perrhenate as alternatives to conventional radionuclide ^{131}I-sodium iodide for treatment of thyroid benign disease. Also, the potential of using these isotopes in non-thyroidal tumours has been discussed in this work.

A general introduction of the sodium iodide symporter, basic anatomy, histology, physiology and system description of our preclinical scanners (nanoScan SPECT/CT and nanoScan PET/CT) were presented in chapter 1. The published literature relevant to the sodium iodide symporter (NIS), NIS in nuclear medicine, NIS radiotracers and the role of nuclear medicine imaging in the management of thyroid disease were also reviewed in the first chapter.

The first experimental part of this thesis reported on basic performance characteristics (uniformity, linearity, calibration factor) of the nanoScan SPECT/CT. In this chapter, we critically investigated the quantification accuracy of preclinical nanScan SPECT/CT (with ^{99m}Tc, ^{123}I and ^{188}Re) and nanoScan PET/CT (with ^{18}F) using the mouse size micro-hollow sphere phantom relevant to the *in vivo* imaging intended in this research project. The effects of object size, acquisition time and reconstruction parameters (number of iterations) on the image-based quantitative accuracy were examined. We also inspected the quantification accuracy with 3 different methods; (a) large VOI with integral activity (b) large VOI with SUV_{max} and (c) automatic VOI with 42% thresholding SUV_{mean}. The large VOI approach with integral activity within the entire organ seems the most suitable method for our *in vivo* experiments aiming at determining relative organ uptake. Subsequently, this work attempted to assess PVE from this method and correct for its effects using phantom-derived correction factors. Quantification results with ^{188}Re showed poorest accuracy especially with the smallest phantom compartment (3.9 mm diameter sphere). However, our normalised results indicated that across different isotopes the influence of PVE remained comparable. Therefore, the poorer performance of ^{188}Re compared with ^{99m}Tc and ^{123}I is likely to be caused by other factors; physical properties of ^{188}Re (scatter photon, septal penetration, Bremsstrahlung, low-abundant photons), limitations of instrument and reconstruction software (lack of high energy multi-pinhole collimation, no attenuation and scatter correction, unclear energy dependency of PSF model used during image reconstruction). For the effects of acquisition time and reconstruction iterations, varying acquisition time did not alter the

quantification accuracy for ^{99m}Tc and ^{123}I, however, ^{188}Re was more affected when acquiring shorter time frames and the effect was stronger in smaller spheres. Additionally, the quantification accuracy improved when changing from 6 to 9 iterations. When changing from 9 to 24 iterations, quantification accuracy depended on acquisition time (count levels). Hence, these errors are likely to be related to the influence of number of counts per projection. Furthermore, the quantification accuracy in the smallest microsphere was affected most strongly by the reconstructing parameters and acquisition times. In the later part of chapter 2, the quantification results from nanoScan SPECT/CT were compared with ^{18}F data from the nanoScan PET/CT. The quantification of small objects from nanoScan PET/CT was more accurate than nanoScan SPECT/CT. Our PVE results were found to be somehow contradicting with the scanner spatial resolution as according to system specifications, the nanoScan SPECT/CT has a better spatial resolution than the nanoScan PET/CT. Therefore, the quantification of small objects from nanoScan PET/CT should be subject to stronger PVE than nanoScan SPECT/CT. However, this might be mainly due to the correction processes of attenuation, scatter and dead-time which are employed only in nanoScan PET/CT. Hence, these data are important to note when comparing results across different modalities.

In chapter 3, we presented a series of *in vivo* spatio-temporal quantification measurements with available SPECT NIS-radiotracers (^{99m}Tc-pertechnetate, ^{123}I-NaI, ^{131}I-NaI and ^{188}Re-perrhenate) in normal healthy and non-thyroidal NIS bearing tumour model. We also presented kinetic data to support a forthcoming clinical PET radiotracer ^{18}F-BF_4. This information afforded a side by side comparison of NIS radiotracers. In a healthy mouse model, we demonstrated distinct differences of uptake patterns in thyroid between metabolised (^{123}I- and ^{131}I-NaI) and non-metabolised tracers (^{18}F-tetrafluoroborate, ^{99m}Tc-pertechnetate and ^{188}Re-perrhenate), and also subtle differences between the supposedly non-metabolised tracers. In salivary glands, similar patterns of uptake were observed for all tracers with uptake increasing gradually over time then remaining steady and slowly washing out. Stomach uptake was high compared with other organs (thyroid, salivary glands, and urinary bladder) perhaps due to its large size and effect of anaesthesia. The uptake in stomach peaked at 4 h for metabolised radiotracers. In contrary, peak uptake in stomach was found at 8 h for non-metabolised radiotracers, except for ^{18}F-BF_4 which showed peak values at around 3 h after injection (as we collected data only up to 4 h). The activities in the urinary bladder indicated the excretion of radioisotopes via the genitourinary system. The maximum bladder activity was mostly observed

at 4 hr post injection because all animals were anesthetised during the imaging session then mice were awakened from anaesthesia and urinated. Activity in muscle (not expressing-NIS) and left ventricle (representing blood activity) was low and remained so over time for all tracers. In this chapter, we demonstrated the capabilities of the dedicated high-resolution preclinical systems which clearly distinguished and quantified the radioactivity accumulated in small organs such as the thyroid and salivary glands. The later part of this chapter described *in vivo* spatio-temporal quantification in a xenograft model. All radiotracers detected the tumour with high target to background ratio. However, perrhenate uptake in tumour was significantly low when compared with pertechnetate or iodide, with percentage uptake per gram of tumour at about 5 - 12 %ID/g for ^{188}Re-perrhenate, 45-55 % ID/g for ^{99m}Tc-pertechnetate and 42-62 % ID/g for ^{123}I-NaI). This work also showed kinetic data of the forthcoming PET radiotracer ^{18}F-BF_4 for imaging NIS-expressing tumours, showing that ^{18}F-tetrafluoroborate accumulated in tumour at about 4-8 % ID/g. This chapter has described the ability of ^{188}Re-perrhenate for imaging with appealing therapeutic properties (shorter half-life, higher beta energy and lower energy gamma emission compared with ^{131}I-NaI). However, it also brought up challenges with imaging ^{188}Re such as increased image background.

The human-equivalent effective dose for diagnostic and therapeutic use of NIS radiotracers (^{18}F-tetrafluroborate, ^{99m}Tc-pertechnetate, ^{123}I-iodide, ^{131}I-iodide and ^{186}Re- and ^{188}Re-perrhenate) have been reported in chapter 4 using the spatio-temporal data from chapter 3. In the present work, the dose comparison studies were conducted on the same strain sex- and age-matched animals to allow approximate comparison of radiation dose for tracer development. Estimation of effective doses from our study varied from the ICRP and this can be attributed mainly to the bio-kinetic models used as a basis for the calculations. Nevertheless, these estimated values can still be practically useful for initial estimates and dosimetric comparison in the development of new radiotracers. For illustration, the findings from this work indicated the effective dose for ^{18}F-BF_4 as an initial approach for a forthcoming clinical trial of the radiotracer in thyroid disease. Based on our human-equivalent estimation, the effective dose from this new PET tracer was lower than conventional imaging agents (^{123}I-iodide and ^{131}I-iodide). However, the ^{18}F-BF_4 estimated dose was still higher when compared with ^{99m}Tc-pertechnetate a long-established SPECT tracer. In the later part of the chapter, we presented the dosimetric feasibility of using rhenium isotopes (^{186}Re- and ^{188}Re-perrhenate) in treatment of benign nodular thyroid disease and non-thyroidal NIS-expressing tumours compared with conventional ^{131}I-NaI. The preclinical

dosimetric estimation demonstrated that rhenium isotopes were equally effective when excluding uptake in stomach and urinary bladder (due to large variations affected by subject conditions such as food consumption and anaesthesia). Our results indicate that radionuclide therapy of thyroid benign disease with rhenium isotopes appears promising and worthy for further investigation in humans. This study is the first *in vivo* kinetic study that provided dosimetry estimations and compared the therapeutic efficiency in treating thyroid benign disease. The higher beta energies and longer range of rhenium isotopes may improve treatment efficacy when treating larger benign nodules in which radioiodine therapy may be less effective due to the shorter particle range. The lower abundance of gamma photons emitted by ^{186}Re and ^{188}Re is more favourable than those produced by ^{131}I, reducing radiation dose to whole body and to other people (members of family, staff, general public) and thus reducing or eliminating the need for isolation. Based on our study, effective dose per administered activity from ^{186}Re and ^{188}Re was lower than conventional radioiodine. Also red marrow absorbed dose was about 1.5 and 3 times (for ^{186}Re and ^{188}Re respectively) lower than that produced by radioiodine. Furthermore, treatments might therefore be offered on outpatient basis at great cost saving, and patients could return to normal lifestyle earlier. These factors make perrhenate promising therapeutic substrates for the sodium/iodine symporter. In xenograft bearing non-thyroidal NIS adenocarcinoma tumour (hNIS-engineered model), our data indicated that both rhenium isotopes delivered higher absorbed dose to the tumour (6.33 and 8.68 times higher for ^{186}Re and ^{188}Re) compared to ^{131}I-NaI. Additionally, the therapy indexes (tumour to effective dose and tumour to thyroid ratio) for both rhenium isotopes were greater than ^{131}I-NaI. Tumour to effective dose ratio for rhenium isotopes were about 5 - 7 times higher whereas tumour to thyroid ratio of both rhenium isotopes were about 7 – 9 time higher than ^{131}I-NaI . The red-marrow absorbed doses produced by rhenium were lower than those produced by radioiodine (~ 0.27 times for ^{186}Re and 0.50 times for ^{188}Re) so for the same effective dose to the whole-body, rhenium can deliver more dose to the tumour. It was also demonstrated in this chapter that the quantification accuracy and partial volume effect in preclinical research can be evaluated and corrected for by using standard geometrical phantom data (MHS quantification data from Chapter 2). Data presented in this work show the impact of quantification accuracy and partial volume effect on dosimetry calculations in small organs (e.g. thyroid, salivary glands) and also its influence on the whole-body effective dose which should not be ignored.

An investigation of the radionuclide distribution at the microscopic level in thyroid was critically examined in Chapter 5. It has long been hypothesised that metabolised radiotracers (e.g. ^{123}I-NaI, ^{131}I-NaI) are taken up by NIS to thyrocytes, and stored in colloid until released to the bloodstream. In contrast, non-metabolised tracers (e.g. ^{99m}Tc-pertechnetate, ^{188}Re-perrhenate) are expected to be localised only in thyrocytes. In this thesis, we used electron microscopy (EM) and micro-autoradiography (MAR) to study the tracer distribution at cellular level. With the EM technique, the spectra of copper, potassium, sulfur, chlorine and phosphorus were observed in thyroid follicles, suggesting these to be natural elements in the thyroid. Spectra of iodine were detected only in the colloid but not in thyrocytes. However, the primary peak of rhenium cannot be detected in follicular cells due to limitations of detection sensitivity and the physical properties of rhenium. This experiment has demonstrated the competence of EM as a tool for tracer localisation and elemental analysis at cellular level although rhenium is problematic. In the latter part of this chapter, the MAR technique was used to prove our hypothesis that non-metabolised tracers are present only in thyrocytes but not in the colloid. The results from this experiment indicated that pertechnetate/perrhenate was present only in thyrocyte areas while there was no pertechnetate detected in the colloid. It can therefore be concluded from these two techniques (EM, MAR) that non-metabolised tracers are only located in thyrocytes. This information can be used as an input for small-scale dosimetry. In the last part of this thesis, simulation work has been carried out to estimate the absorbed dose at cellular level using MCNPx. The modelling information (cell geometry, radionuclide distribution) was experimentally acquired from real histology section and MAR of rat thyroid, then the data input to Monte Carlo using the OEDIPE platform. By assuming follicular cells are the target for cell killing, the pattern of absorbed dose when ^{188}Re distributed in follicular cells showed higher and also more uniform dose distribution as about 80% of the cell population received dose within narrower range. On the other hand, the absorbed dose delivered by ^{131}I located in the colloid was more inhomogeneous as only 65% of the follicular cells population was exposed to a dose range within the width of the histogram distribution at 50% of the maximum, whereas some cells received high and some cells received low dose which may be difficult to predict the range of biological effects. These pilot data support the macro-dosimetric estimation from chapter 4 for using ^{188}Re-perrhenate in treatment of thyroid diseases. The results suggested that both ^{131}I and ^{188}Re would be more effective if localised within thyrocytes, but this advantages is not available to ^{131}I as only ^{188}Re is actually located within thyrocytes.

In conclusion, the initial preclinical work and small-scale dosimetry have proved the hypothesis that the radioisotopes of rhenium (^{186}Re- and ^{188}Re-) in the form of perrhenate can be used as alternatives therapeutic radionuclide to conventional ^{131}I-NaI. Although it is difficult to estimate the human dosimetry by scaling from animal data the preclinical dosimetric study in this thesis has formed an important step for initial estimates of the therapeutic potential and application of these radiotracers clinically and in support of methodology for performing kinetic data of ^{99m}Tc-pertechnetate and ^{188}Re-perrhenate in order to estimate preliminary dosimetric data in humans.

6.2 Recommendation for Future Work

Although results presented here have demonstrated the capabilities of preclinical scanners in quantification, dosimetric profile estimation and the potential of using rhenium isotopes in benign thyroid disease, as well as the tracer distribution at cellular level and small-scale dosimetry in the thyroid model, these issues could be further investigated and developed in a number of ways:

- **Attenuation correction for nanoScan SPECT/CT and ^{188}Re scatter correction**

We did not correct for photon attenuation in our SPECT data. Hence, SPECT attenuation correction could be performed in order to improve the quantification accuracy in preclinical SPECT. In addition, ^{188}Re scatter correction needs further investigation with the development of software applicable to multi-pinhole reconstruction. Triple-energy window, Monte Carlo simulation using GATE or the convolution method with Matlab/IDL would lead to a better image quality and reduce scatter. Furthermore, the high energy multi-pinhole collimator could be employed to reduce septal penetration (Bernsen et al., 2014).

- **Improve accuracy of image-based VOI**

In order to improve the accuracy of image-based VOI analysis, alternative imaging techniques such as SPECT/MR or PET/MR should be investigated since those techniques can provide an improved soft tissue contrast which should make it easier to identify and distinguish the boundaries of small organs (e.g. thyroid, salivary glands) on the MRI images. Also, thyroid volume could be precisely estimated with preclinical 3D ultrasonography (Freesmeyer et al., 2014; Nagarajah et al., 2011).

- **Tracer localisation at cellular level and quantification of micro-autoradiography**

As mentioned earlier, tracer localisation at cellular level is the key to understand small-scale dosimetry. Further investigations with other techniques (such as SIM-Secondary Ion Mass Spectroscopy, or Confocal Fluorescence microscopy) are needed in order to improve the resolution and sensitivity (Koike et al., 2015; Tessier et al., 2012). In addition, further MAR experiments should be extended to cover silver grain quantification technique which may improve the realistic dose map for small-scale dosimetry (Lund Nielsen and Halkjær Nielsen, 2005; Puncher and Blower, 1994b).

- **In vitro- and in vivo treatment response of ^{188}Re-perrhenate versus ^{131}I-NaI**

In vitro dose validation using conventional clonogenic assays and *in vivo* treatment response (measuring level of thyroid hormones, determining thyroid/tumour volume and histopathological changing for pre- and post-treatment) need further work before using this rhenium isotope in human.

- **Small-scale dosimetry, Role of Auger electrons in small-scale dosimetry**

We performed pilot small-scale dosimetry with MCNPx in this thesis. However, small-scale dosimetry can also be performed with other platforms for example PENELOPE, GATE, GEANT4. Additional comparison of simulation results should be also considered because different simulation platforms have different assumptions and physics processes (e.g. choice of tissue compartment, energy spectrum of radionuclide and cut-off simulation energy).

Also due to limited time and resources, we did not validate our MCNPx simulation at such a small-scale. Further model validation together with deeper knowledge of radiobiological and physical modelling are needed for using this preliminary results for clinical translation. In addition, we did not include Auger electrons in our simulation due to the limitation of energy cut-off in MCNPx. This could be addressed by using the PENELOPE, GEANT4 or Monte Carlo 4 (MC4) (Fourie et al., 2015; Paquet et al., 2013).

Appendix A. Accuracy Calibration of Radionuclide Activity Calibrator

In this study, the radionuclide activity calibrator was used as a standard measurement throughout the thesis. It is important to calibrate this equipment in order to ensure that the radionuclide calibrator provides a correct reading of activity within the required accuracy levels (Busemann Sokole et al., 2010). In the UK, the accuracy of radionuclide activity calibrator is calibrated against the NPL (National Physics Laboratory) as national standard using the MGPG 9317 (Measurement Good Practice Guide No. 9317) as a guideline. The recommended accuracy deviation limit for high energy radionuclide (energy ≥ 100 keV) as stated by NPL is ± 2% from secondary standard source (Gadd et al., 2006).

The radionuclide activity calibrators in the Department of Imaging Sciences and Biomedical engineering were annually calibrated using a standard source directly traceable to NPL. The calibration sources are sent to NPL immediately after completion of measurements with a number of calibrators, including at least one of the calibrators in the department Imaging Sciences and Biomedical Engineering. As NPL recommended, the radionuclide activity calibrator is checked and calibrated with at least two reference sources and local practice is to include ^{99m}Tc every year while varying the radionuclide of the second source. For example, in 2013, the calibration was performed on 31st July 2013 with ^{99m}Tc and ^{67}Ga (as illustrated in figure A-1 and A-2)

Calibrator NPL Tracable standard test - All calibrators

Please contact the Qrep or EQCO if this form needs updating. (Yellow cells are locked.)

Medicial Physics Quality System
version 1.5, 25-Jul-11.

Tests performed by	SMG
Isotope	Tc-99m
Reference time	12:00 GMT
Reference activity (MBq)	116.20
Reference date	31-Jul-13
Measurements taken in	BST

Tc-99m half-life (hours) = 6.02
Reference time (GMT) = 12:00

Calibrator	Setting	Date	Time on watch	Calibrator Readings (MBq) 1st	2nd	3rd	Back-ground	Average - Backgd (MBq)	Time (GMT)	Time diff. (hours decimal)	Decay corrected MBq	% diff. (actual - measured)
STH CRC-712M sn 77012, Im Sci Hot Lab	preset	31-Jul-13	09:33	174.7	174.6	174.6	0.1	174.53	08:33	3.45	172.87	0.96
STH CRC-712M sn 77012, Im Sci Hot Lab	dial	31-Jul-13	09:34	174.6	174.2	174.2	0.1	174.23	08:34	3.43	172.54	0.98
												0.94
												0.68

Figure A-1 The accuracy calibration of radionuclide activity calibrator with ^{99m}Tc in year of 2013. The reference standard source was obtained from NPL

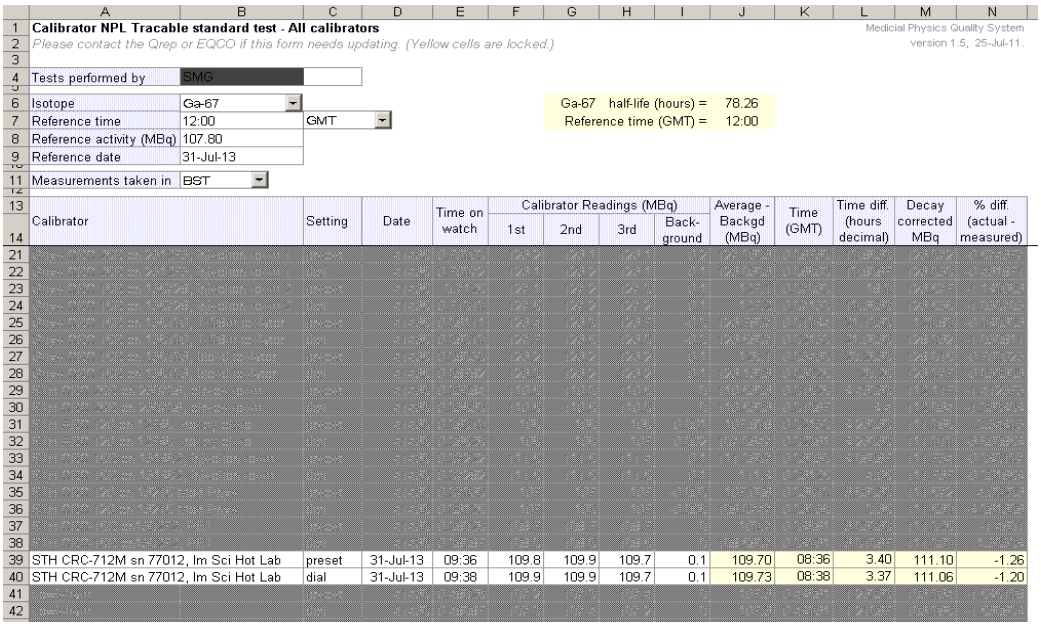

Calibrator NPL Tracable standard test - All calibrators

Medicial Physics Quality System
version 1.5, 25-Jul-11.

Please contact the Qrep or EQCO if this form needs updating. (Yellow cells are locked.)

Tests performed by	SMG
Isotope	Ga-67
Reference time	12:00 GMT
Reference activity (MBq)	107.80
Reference date	31-Jul-13
Measurements taken in	BST

Ga-67 half-life (hours) = 78.26
Reference time (GMT) = 12:00

Calibrator	Setting	Date	Time on watch	Calibrator Readings (MBq) 1st	2nd	3rd	Back-ground	Average - Backgd (MBq)	Time (GMT)	Time diff. (hours decimal)	Decay corrected MBq	% diff. (actual - measured)
STH CRC-712M sn 77012, Im Sci Hot Lab	preset	31-Jul-13	09:36	109.8	109.9	109.7	0.1	109.70	08:36	3.40	111.10	-1.26
STH CRC-712M sn 77012, Im Sci Hot Lab	dial	31-Jul-13	09:38	109.9	109.9	109.7	0.1	109.73	08:38	3.37	111.06	-1.20

Figure A-2 The accuracy calibration of radionuclide activity calibrator with ^{67}Ga in year of 2013. The reference standard source was obtained from NPL

The test was performed in 2 modes of measurement; “preset” and “dial” (a manual mode allows the user to “dial in” conversion factors not available on the preset button). The percentage deviations of measurement from reference standard source for ^{99m}Tc and ^{67}Ga were 0.96 and -1.26 for “preset” setting and 0.98 and -1.20 for “dial” setting. Hence, the results showed that our radionuclide activity calibrator were within ± 2 % as recommended by NPL.

References

. Basic Physics of Nuclear Medicine/Patient Dosimetry.

(2004). New Internal Radiation Dose and Modeling Software; FDA Approves Commercial MIRDOSE Successor. Journal of Nuclear Medicine *45*, 26N.

Ahn, B.-C. (2012). Sodium iodide symporter for nuclear molecular imaging and gene therapy: from bedside to bench and back. Theranostics *2*, 392-402.

Akabani, G., and Zalutsky, M.R. (1997). Microdosimetry of Astatine-211 Using Histological Images: Application to Bone Marrow. Radiation Research *148*, 599-607.

Alan, E.N. (1996). Microdosimetry and radiocurability: modelling targeted therapy with emitters. Physics in Medicine and Biology *41*, 1957.

Amin I, K. (2008). Therapeutic Radionuclides: Biophysical and Radiobiologic Principles. Seminars in Nuclear Medicine *38*, 358-366.

Andersson, M., Johansson, L., Minarik, D., Leide-Svegborn, S., and Mattsson, S. (2014). Effective dose to adult patients from 338 radiopharmaceuticals estimated using ICRP biokinetic data, ICRP/ICRU computational reference phantoms and ICRP 2007 tissue weighting factors. EJNMMI Physics *1*, 9.

Archambault, L., Beaulieu, L., Carrier, J.F., Castrovillari, F., Chauvie, S., Foppiano, F., Ghiso, G., Guatelli, S., Incerti, S., Lamanna, E.*, et al.* (2003). Overview of Geant4 applications in medical physics. Paper presented at: Nuclear Science Symposium Conference Record, 2003 IEEE.

Argyrou, M., Valassi, A., Andreou, M., and Lyra, M. (2013). Rhenium-188 Production in Hospitals, by W-188/Re-188 Generator, for Easy Use in Radionuclide Therapy. International Journal of Molecular Imaging *2013*, 7.

Aschebrook-Kilfoy, B., Ward, M.H., Sabra, M.M., and Devesa, S.S. (2010). Thyroid Cancer Incidence Patterns in the United States by Histologic Type, 1992–2006. Thyroid *21*, 125-134.

Attix, F.H. (2007). Dosimetry Fundamentals. In Introduction to Radiological Physics and Radiation Dosimetry (Wiley-VCH Verlag GmbH), pp. 264-291.

Aurlien, R.H.L., G. Akabani, D. R. Olsen, M. R. Zalutsky, Ø. S. Bruland, E. (2000). Exposure of human osteosarcoma and bone marrow cells to tumour-targeted α-particles and γ-irradiation: analysis of cell survival and microdosimetry. International Journal of Radiation Biology *76*, 1129-1141.

Bai, B., Bading, J., and Conti, P.S. (2013). Tumor quantification in clinical positron emission tomography. Theranostics *3*, 787-801.

Bailey, D.L., and Willowson, K.P. (2013). An evidence-based review of quantitative SPECT imaging and potential clinical applications. Journal of Nuclear Medicine *54*, 83-89.

Bardies, M., and Pihet, P. (2000). Dosimetry and Microdosimetry of Targeted Radiotherapy. Current Pharmaceutical Design *6*, 1469-1502.

Behr, T.M., Sharkey, R.M., Sgouros, G., Blumenthal, R.D., Dunn, R.M., Kolbert, K., Griffiths, G.L., Siegel, J.A., Becker, W.S., and Goldenberg, D.M. (1997). Overcoming the nephrotoxicity of radiometal-labeled immunoconjugates. Cancer *80*, 2591-2610.

Berger, M.J. (1970). BETA-RAY DOSIMETRY CALCULATIONS WITH THE USE OF POINT KERNELS. In Other Information: From Medical Radionuclides: Radiation Dose and Effects Symposium, Oak Ridge, Tenn, Dec 8--11, 1969 UNCL Orig Receipt Date: 31-DEC-70, pp. Medium: X.

Berger, M.J., and Seltzer, S.M. (1973). ETRAN Monte Carlo code system for electron and photon transport through extended media. Radiation Shielding Information Center (RSIC) Report CCC-107, Oak Ridge National Laboratory, Oak Ridge, TN *75*.

Berman, M., Braverman, L., Burke, J., De Groot, L., McCORMACK, K., Oddie, T., Rohrer, R., Wellman, H., and Smith, E. (1975). Summary of current radiation dose estimates to humans from 1231, 124i 1251, 126i, 130I, 131I and 1321 as sodium iodide. J Nucl Med *16*, 857-860.

Bernsen, M., Vaissier, P.B., Van Holen, R., Booij, J., Beekman, F., and de Jong, M. (2014). The role of preclinical SPECT in oncological and neurological research in combination with either CT or MRI. Eur J Nucl Med Mol Imaging *41*, 36-49.

Błażewicz, A., Dolliver, W., Sivsammye, S., Deol, A., Randhawa, R., Orlicz-Szczęsna, G., and Błażewicz, R. (2010). Determination of cadmium, cobalt, copper, iron, manganese, and zinc in thyroid glands of patients with diagnosed nodular goitre using ion chromatography. Journal of Chromatography B *878*, 34-38.

Blower, P., Kettle, A., O'doherty, M., Coakley, A., and Knapp Jr, F. (2000). 99mTc (V) DMSA quantitatively predicts 188Re (V) DMSA distribution in patients with prostate cancer metastatic to bone. European journal of nuclear medicine *27*, 1405-1409.

Bolch, W.E., Bouchet, L.G., Robertson, J.S., Wessels, B.W., Siegel, J.A., Howell, R.W., Erdi, A.K., Aydogan, B., Costes, S., Watson, E.E.*, et al.* (1999). MIRD Pamphlet No. 17: The Dosimetry

of Nonuniform Activity Distributions—Radionuclide S Values at the Voxel Level. Journal of Nuclear Medicine *40*, 11S-36S.
Bousis, C., Emfietzoglou, D., Hadjidoukas, P., and Nikjoo, H. (2009). A Monte Carlo study of cellular S -factors for 1 keV to 1 MeV electrons. Physics in Medicine and Biology *54*, 5023.
Brady, W.L., Altschuler, M.D., Smith, A.R., Bloch, P., Heilmann, H.P., Bova, F.J., Brahme, A., Buchsbaum, D.J., Chen, G.T.Y., and Fessenden, P. (2013). Radiation Therapy Physics (Springer Berlin Heidelberg).
Brandt, M.P., Kloos, R.T., Shen, D.H., Zhang, X., Liu, Y.-Y., and Jhiang, S.M. (2012). Micro–Single-Photon Emission Computed Tomography Image Acquisition and Quantification of Sodium-Iodide Symporter–Mediated Radionuclide Accumulation in Mouse Thyroid and Salivary Glands. Thyroid *22*, 617-624.
Busemann Sokole, E., Płachcínska, A., Britten, A., Lyra Georgosopoulou, M., Tindale, W., and Klett, R. (2010). Routine quality control recommendations for nuclear medicine instrumentation. European journal of nuclear medicine and molecular imaging *37*, 662-671.
Champion, C., Elbast, M., Wu, T.-D., and Colas-Linhart, N. (2007a). Thyroid cell irradiation by radioiodines: a new Monte Carlo electron track-structure code. Brazilian Archives of Biology and Technology *50*, 135-144.
Champion, C., Elbast, M., Wu, T.-D., and Colas-Linhart, N. (2007b). Thyroid cell irradiation by radioiodines: a new Monte Carlo electron track-structure code. Brazilian Archives of Biology and Technology *50*, 135-144.
Champion, C., Zanotti-Fregonara, P., and Hindié, E. (2008). CELLDOSE: A Monte Carlo Code to Assess Electron Dose Distribution—S Values for 131I in Spheres of Various Sizes. Journal of Nuclear Medicine *49*, 151-157.
Chang, C.-H., Chang, Y.-J., Lee, T.-W., Ting, G., and Chang, K.-P. (2012). Dosimetric evaluation of nanotargeted 188Re-liposome with the MIRDOSE3 and OLINDA/EXM programs. Ann Nucl Med *26*, 419-425.
Charles, M.W. (2008). ICRP Publication 103: Recommendations of the ICRP†. Radiation Protection Dosimetry *129*, 500-507.
Chauvie, S., Francis, Z., Guatelli, S., Incerti, S., Mascialino, B., Moretto, P., Nieminen, P., and Pia, M.G. (2007). Geant4 Physics Processes for Microdosimetry Simulation: Design Foundation and Implementation of the First Set of Models. Nuclear Science, IEEE Transactions on *54*, 2619-2628.
Chen, J. (2008). A compilation of microdosimetry for uniformly distributed Auger emitters used in medicine. International Journal of Radiation Biology *84*, 1027-1033.
Cherry, S.R., Sorenson, J.A., and Phelps, M.E. (2012). Physics in Nuclear Medicine (Elsevier Health Sciences).
Chin, B.B., Kronauge, J.F., Femia, F.J., Chen, J., Maresca, K.P., Hillier, S., Petry, N.A., James, O.G., Oldan, J.D., Armor, T.*, et al.* (2014). Phase-1 Clinical Trial Results of High-Specific-Activity Carrier-Free 123I-Iobenguane. Journal of Nuclear Medicine *55*, 765-771.
Chouin, N., Bernardeau, K., Davodeau, F., Chérel, M., Faivre-Chauvet, A., Bourgeois, M., Apostolidis, C., Morgenstern, A., Lisbona, A., and Bardiès, M. (2009). Evidence of Extranuclear Cell Sensitivity to Alpha-Particle Radiation Using a Microdosimetric Model. I. Presentation and Validation of a Microdosimetric Model. Radiation Research *171*, 657-663.
Chung, J.-K. (2002). Sodium iodide symporter: its role in nuclear medicine. Journal of Nuclear Medicine *43*, 1188-1200.
Chung, J.-K., Youn, H., Kang, J., Lee, H., and Kang, K. (2010a). Sodium Iodide Symporter and the Radioiodine Treatment of Thyroid Carcinoma. Nuclear Medicine and Molecular Imaging *44*, 4-14.
Chung, J.-K., Youn, H.W., Kang, J.H., Lee, H.Y., and Kang, K.W. (2010b). Sodium iodide symporter and the radioiodine treatment of thyroid carcinoma. Nuclear medicine and molecular imaging *44*, 4-14.
Coleman, R.E., Stubbs, J.B., Barrett, J.A., de la Guardia, M., LaFrance, N., and Babich, J.W. (2009). Radiation dosimetry, pharmacokinetics, and safety of ultratrace™ iobenguane I-131 in patients with malignant pheochromocytoma/paraganglioma or metastatic carcinoid. Cancer Biotherapy and Radiopharmaceuticals *24*, 469-475.
Cooper, D.S., Doherty, G.M., Haugen, B.R., Kloos, R.T., Lee, S.L., Mandel, S.J., Mazzaferri, E.L., McIver, B., Sherman, S.I., and Tuttle, R.M. (2006). Management Guidelines for Patients with Thyroid Nodules and Differentiated Thyroid Cancer: The American Thyroid Association Guidelines Taskforce. Thyroid *16*, 109-142.
Cucinotta, F.A., Nikjoo, H., and Goodhead, D.T. (1998). The Effects of Delta Rays on the Number of Particle-Track Traversals per Cell in Laboratory and Space Exposures. Radiation Research *150*, 115-119.

Cyr, J.E., Pearson, D.A., Wilson, D.M., Nelson, C.A., Guaraldi, M., Azure, M.T., Lister-James, J., Dinkelborg, L.M., and Dean, R.T. (2007). Somatostatin Receptor-Binding Peptides Suitable for Tumor Radiotherapy with Re-188 or Re-186. Chemistry and Initial Biological Studies. Journal of Medicinal Chemistry *50*, 1354-1364.
Dadachova, E. (2010). Rhenium-188 and rhenium-186 for treatment of tumors expressing a Na+/I− symporter (Google Patents).
Dadachova, E., Bouzahzah, B., Zuckier, L., and Pestell, R. (2002). Rhenium-188 as an alternative to Iodine-131 for treatment of breast tumors expressing the sodium/iodide symporter (NIS). Nuclear medicine and biology *29*, 13-18.
Dadachova, E., and Carrasco, N. (2004). The Na+/I− symporter (NIS): imaging and therapeutic applications. Seminars in Nuclear Medicine *34*, 23-31.
Dadachova, E., Nguyen, A., Lin, E.Y., Gnatovskiy, L., Lu, P., and Pollard, J.W. (2005). Treatment with rhenium-188-perrhenate and iodine-131 of NIS-expressing mammary cancer in a mouse model remarkably inhibited tumor growth. Nuclear medicine and biology *32*, 695-700.
De la Vieja, A., Dohan, O., Levy, O., and Carrasco, N. (2000). Molecular Analysis of the Sodium/Iodide Symporter: Impact on Thyroid and Extrathyroid Pathophysiology. Physiological Reviews *80*, 1083-1105.
Deleye, S., Van Holen, R., Verhaeghe, J., Vandenberghe, S., Stroobants, S., and Staelens, S. (2013). Performance evaluation of small-animal multipinhole μSPECT scanners for mouse imaging. European journal of nuclear medicine and molecular imaging *40*, 744-758.
Dohán, O., and Carrasco, N. (2003a). Advances in Na+/I− symporter (NIS) research in the thyroid and beyond. Molecular and Cellular Endocrinology *213*, 59-70.
Dohán, O., and Carrasco, N. (2003b). Advances in Na< sup>+</sup>/I< sup>−</sup> symporter (NIS) research in the thyroid and beyond. Molecular and cellular endocrinology *213*, 59-70.
Dohán, O., De la Vieja, A., Paroder, V., Riedel, C., Artani, M., Reed, M., Ginter, C.S., and Carrasco, N. (2003). The Sodium/Iodide Symporter (NIS): Characterization, Regulation, and Medical Significance. Endocrine Reviews *24*, 48-77.
Eary, J., Durack, L., Williams, D., and Vanderheyden, J. (1990). Considerations for imaging Re-188 and Re-186 isotopes. Clinical nuclear medicine *15*, 911-916.
Elbast, M., Wu, T.-D., Guiraud-Vitaux, F., Petiet, A., Hindié, E., Champion, C., Croisy, A., Guerquin-Kern, J.-L., and Colas-Linhart, N. (2008a). Cinétique intracolloïdale de l'iode dans la thyroïde de rat nouveau-né. Imagerie directe par microscopie ionique analytique. Comptes Rendus Biologies *331*, 13-22.
Elbast, M., Wu, T.-D., Guiraud-Vitaux, F., Petiet, A., Hindié, E., Champion, C., Croisy, A., Guerquin-Kern, J.-L., and Colas-Linhart, N. (2008b). [Kinetics of intracolloidal iodine within the thyroid of newborn rats. Direct imagery using secondary ion mass spectrometry]. Comptes rendus biologies *331*, 13-22.
Erlandsson, K., Buvat, I., Pretorius, P.H., Thomas, B.A., and Hutton, B.F. (2012). A review of partial volume correction techniques for emission tomography and their applications in neurology, cardiology and oncology. Physics in medicine and biology *57*, R119.
Eskandari, S., Loo, D.D., Dai, G., Levy, O., Wright, E.M., and Carrasco, N. (1997a). Thyroid Na+/I− symporter Mechanism, stoichiometry, and specificity. Journal of Biological Chemistry *272*, 27230-27238.
Eskandari, S., Loo, D.D.F., Dai, G., Levy, O., Wright, E.M., and Carrasco, N. (1997b). Thyroid Na+/I− Symporter: MECHANISM, STOICHIOMETRY, AND SPECIFICITY. Journal of Biological Chemistry *272*, 27230-27238.
Farragi, M., Gardin, I., de Labriolle-Vaylet, C., Moretti, J.-L., and Bok, B. (1994). The influence of tracer localization on the electron dose rate delivered to the cell nucleus. Journal of Nuclear Medicine *35*, 113-119.
Ferro-Flores, G., and Arteaga de Murphy, C. (2008a). Pharmacokinetics and dosimetry of 188Re-pharmaceuticals. Advanced Drug Delivery Reviews *60*, 1389-1401.
Ferro-Flores, G., and Arteaga de Murphy, C. (2008b). Pharmacokinetics and dosimetry of< sup> 188</sup> Re-pharmaceuticals. Advanced drug delivery reviews *60*, 1389-1401.
Ferro-Flores, G., and de Murphy, C.A. (2008). Pharmacokinetics and dosimetry of 188 Re-pharmaceuticals. Advanced drug delivery reviews *60*, 1389-1401.
Filetti, S., Bidart, J., Arturi, F., Caillou, B., Russo, D., and Schlumberger, M. (1999). Sodium/iodide symporter: a key transport system in thyroid cancer cell metabolism. European Journal of Endocrinology *141*, 443-457.
Finucane, C.M., Murray, I., Sosabowski, J.K., Foster, J.M., and Mather, S.J. (2011). Quantitative Accuracy of Low-Count SPECT Imaging in Phantom and In Vivo Mouse Studies. International Journal of Molecular Imaging *2011*, 8.

Fourie, H., Newman, R.T., and Slabbert, J.P. (2015). Microdosimetry of the Auger electron emitting 123 I radionuclide using Geant4-DNA simulations. Physics in Medicine and Biology *60*, 3333.
Franc, B.L., Acton, P.D., Mari, C., and Hasegawa, B.H. (2008). Small-Animal SPECT and SPECT/CT: Important Tools for Preclinical Investigation. Journal of Nuclear Medicine *49*, 1651-1663.
Franck, D., De Carlan, L., Pierrat, N., Broggio, D., and Lamart, S. (2007). OEDIPE: a new graphical user interface for fast construction of numerical phantoms and MCNP calculations. Radiation protection dosimetry *127*, 262-265.
Franken, P., Guglielmi, J., Vanhove, C., Koulibaly, M., Defrise, M., Darcourt, J., and Pourcher, T. (2010). Distribution and Dynamics of 99m Tc-Pertechnetate Uptake in the Thyroid and Other Organs Assessed by Single-Photon Emission Computed Tomography in Living Mice. Thyroid *20*, 519-526.
Freesmeyer, M., Wiegand, S., Schierz, J.-H., Winkens, T., and Licht, K. (2014). Multimodal Evaluation of 2-D and 3-D Ultrasound, Computed Tomography and Magnetic Resonance Imaging in Measurements of the Thyroid Volume Using Universally Applicable Cross-Sectional Imaging Software: A Phantom Study. Ultrasound in Medicine & Biology *40*, 1453-1462.
Freudenberg, L.S., Antoch, G., Jentzen, W., Pink, R., Knust, J., Görges, R., Müller, S.P., Bockisch, A., Debatin, J.F., and Brandau, W. (2004). Value of ¹²⁴I-PET/CT in staging of patients with differentiated thyroid cancer. European Radiology *14*, 2092-2098.
Freudenberg, R., and Kotzerke, J. (2010). Cellular dosimetry using the Geant4 Monte Carlo toolkit. Journal of Nuclear Medicine *51*, 1488-1489.
Fruhwirth, G.O., Diocou, S., Blower, P.J., Ng, T., and Mullen, G.E. (2014). A whole-body dual-modality radionuclide optical strategy for preclinical imaging of metastasis and heterogeneous treatment response in different microenvironments. Journal of Nuclear Medicine *55*, 686-694.
Fuster, B.M., Falcon, C., Tsoumpas, C., Livieratos, L., Aguiar, P., Cot, A., Ros, D., and Thielemans, K. (2013). Integration of advanced 3D SPECT modeling into the open-source STIR framework. Medical Physics *40*, 092502.
Gadd, R., Baker, M., Nijran, K., Owens, S., Thomson, W., Woods, M., and Zananiri, F. (2006). Measurement good practice guide no. 93: protocol for establishing and maintaining the calibration of medical radionuclide calibrators and their quality control. Teddington: National Physical Laboratory.
Gardin, I., Faraggi, M., Huc, E., and Bok, B.D. (1995). Modelling of the relationship between cell dimensions and mean electron dose delivered to the cell nucleus: application to five radionuclides used in nuclear medicine. Physics in Medicine and Biology *40*, 1001.
Ghorbani, M., Salahshour, F., Haghparast, A., Moghaddas, T.A., and Knaup, C. (2014). Effect of tissue composition on dose distribution in brachytherapy with various photon emitting sources. Journal of contemporary brachytherapy *6*, 54.
Giap, H.B., Macey, D.J., Bayouth, J.E., and Boyer, A.L. (1995). Validation of a dose-point kernel convolution technique for internal dosimetry. Physics in Medicine and Biology *40*, 365.
Goddu, S.M., and Budinger, T.F. (2003). MIRD cellular S. values: self-absorbed dose per unit cumulated activity for selected radionuclides and monoenergetic electron and alpha particle emitters incorporated into different cell compartments (Society of Nuclear Medicine).
Goddu, S.M., Rao, D.V., and Howell, R.W. (1994). Multicellular dosimetry for micrometastases: dependence of self-dose versus cross-dose to cell nuclei on type and energy of radiation and subcellular distribution of radionuclides. Journal of Nuclear Medicine *35*, 521-521.
Goldstein, J., Newbury, D.E., and Williams, D.B. (2012). X-ray spectrometry in electron beam instruments (Springer Science & Business Media).
Goodhead, D.T. (1982). An Assessment of the Role of Microdosimetry in Radiobiology. Radiation Research *91*, 45-76.
Grewal, R.K., Larson, S.M., Pentlow, C.E., Pentlow, K.S., Gonen, M., Qualey, R., Natbony, L., and Tuttle, R.M. (2009). Salivary Gland Side Effects Commonly Develop Several Weeks After Initial Radioactive Iodine Ablation. Journal of Nuclear Medicine *50*, 1605-1610.
Häggström, M. (2014). Medical gallery of Mikael Hggstrm 2014. Wikiversity J Med *1*.
Hall, J.E. (2015). Guyton and Hall textbook of medical physiology (Elsevier Health Sciences).
Haymart, M.R., Banerjee, M., Stewart, A.K., Koenig, R.J., Birkmeyer, J.D., and Griggs, J.J. (2011). Use of Radioactive Iodine for Thyroid Cancer. JAMA: The Journal of the American Medical Association *306*, 721-728.
Hoffman, E.J., Huang, S.-C., and Phelps, M.E. (1979). Quantitation in positron emission computed tomography: 1. Effect of object size. Journal of computer assisted tomography *3*, 299-308.

Hong, R., Halama, J., Bova, D., Sethi, A., and Emami, B. (2007). Correlation of PET standard uptake value and CT window-level thresholds for target delineation in CT-based radiation treatment planning. International Journal of Radiation Oncology* Biology* Physics *67*, 720-726.
Howell, R.W., Wessels, B.W., Loevinger, R., In collaboration with the Mird Committee, S.o.N.M.E.E.W.W.E.B.A.B.B.N.D.C.D.R.F.M., and Wessels, B.W. (1999). The MIRD Perspective 1999. Journal of Nuclear Medicine *40*, 3S-10S.
Hudson, H.M., and Larkin, R.S. (1994). Accelerated image reconstruction using ordered subsets of projection data. Medical Imaging, IEEE Transactions on *13*, 601-609.
Hume, S.P., Gunn, R.N., and Jones, T. (1998). Pharmacological constraints associated with positron emission tomographic scanning of small laboratory animals. European Journal of Nuclear Medicine *25*, 173-176.
Humm, J., Roeske, J., Fisher, D., and Chen, G. (1993a). Microdosimetric concepts in radioimmunotherapy. Medical physics *20*, 535-541.
Humm, J.L., Roeske, J.C., Fisher, D.R., and Chen, G.T.Y. (1993b). Microdosimetric concepts in radioimmunotherapy. Medical Physics *20*, 535-541.
Hwang, A.B., Franc, B.L., Gullberg, G.T., and Hasegawa, B.H. (2008). Assessment of the sources of error affecting the quantitative accuracy of SPECT imaging in small animals. Physics in medicine and biology *53*, 2233.
ICRP (2008). Radiation Dose to Patients from Radiopharmaceuticals - Addendum 3 to ICRP Publication 53. In ICRP 106.
J.L, H. (1987). A microdosimetric model of astatine-211 labeled antibodies for radioimmunotherapy. International Journal of Radiation Oncology*Biology*Physics *13*, 1767-1773.
Jaszczak, R.J., Coleman, R.E., and Whitehead, F.R. (1981). Physical factors affecting quantitative measurements using camera-based single photon emission computed tomography (SPECT). Nuclear Science, IEEE Transactions on *28*, 69-80.
Jauregui-Osoro, M., Sunassee, K., Weeks, A., Berry, D., Paul, R., Cleij, M., Banga, J., O'Doherty, M., Marsden, P., Clarke, S.*, et al.* (2010a). Synthesis and biological evaluation of [¹⁸F]tetrafluoroborate: a PET imaging agent for thyroid disease and reporter gene imaging of the sodium/iodide symporter. European Journal of Nuclear Medicine and Molecular Imaging *37*, 2108-2116.
Jauregui-Osoro, M., Sunassee, K., Weeks, A.J., Berry, D.J., Paul, R.L., Cleij, M., Banga, J.P., O'Doherty, M.J., Marsden, P.K., and Clarke, S.E. (2010b). Synthesis and biological evaluation of [18F] tetrafluoroborate: a PET imaging agent for thyroid disease and reporter gene imaging of the sodium/iodide symporter. European journal of nuclear medicine and molecular imaging *37*, 2108-2116.
Jentzen, W., Balschuweit, D., Schmitz, J., Freudenberg, L., Eising, E., Hilbel, T., Bockisch, A., and Stahl, A. (2010). The influence of saliva flow stimulation on the absorbed radiation dose to the salivary glands during radioiodine therapy of thyroid cancer using 124I PET (/CT) imaging. European journal of nuclear medicine and molecular imaging *37*, 2298-2306.
Jeong, J.M., and Chung, J.-K. (2003). Therapy with 188Re-Labeled Radiopharmaceuticals: An Overview of Promising Results from Initial Clinical Trials. Cancer Biotherapy & Radiopharmaceuticals *18*, 707-717.
Jeong, J.M., Kim, Y.J., Lee, Y.S., Ko, J.I., Son, M., Lee, D.S., Chung, J.-K., Park, J.H., and Lee, M.C. (2001). Lipiodol solution of a lipophilic agent, 188 Re-TDD, for the treatment of liver cancer. Nuclear medicine and biology *28*, 197-204.
Jeong, J.M., and Knapp Jr, F. (2008a). Use of the Oak Ridge National Laboratory tungsten-188/rhenium-188 generator for preparation of the rhenium-188 HDD/lipiodol complex for trans-arterial liver cancer therapy. Paper presented at: Seminars in nuclear medicine (Elsevier).
Jeong, J.M., and Knapp Jr, F.F. (2008b). Use of the Oak Ridge National Laboratory Tungsten-188/Rhenium-188 Generator for Preparation of the Rhenium-188 HDD/Lipiodol Complex for Trans-Arterial Liver Cancer Therapy. Seminars in Nuclear Medicine *38*, S19-S29.
Johansson, L., Leide-Svegborn, S., Mattsson, S., and Nosslin, B. (2003). Biokinetics of iodide in man: refinement of current ICRP dosimetry models. Cancer Biotherapy and Radiopharmaceuticals *18*, 445-450.
Johansson, L., Mattsson, S., and Nosslin, B. (1984). Effective dose equivalent from radiopharmaceuticals. European journal of nuclear medicine *9*, 485-489.
Johnström, P., Fryer, T., Bird, J., Richards, H., and Davenport, A. (2012). Dynamic In Vivo Imaging of Receptors in Small Animals Using Positron Emission Tomography. In Receptor Binding Techniques, A.P. Davenport, ed. (Humana Press), pp. 221-237.
Kang, J.H., Chung, J.-K., Lee, Y.J., Shin, J.H., Jeong, J.M., Lee, D.S., and Lee, M.C. (2004). Establishment of a Human Hepatocellular Carcinoma Cell Line Highly Expressing Sodium Iodide Symporter for Radionuclide Gene Therapy. Journal of Nuclear Medicine *45*, 1571-1576.

Kassis, A.I. (2010). Molecular and cellular radiobiological effects of Auger emitting radionuclides. Radiation protection dosimetry, ncq385.
Kassis, A.I. (2011). Molecular and cellular radiobiological effects of Auger emitting radionuclides. Radiation Protection Dosimetry *143*, 241-247.
Kazy, S.K., D'Souza, S., and Sar, P. (2009). Uranium and thorium sequestration by a Pseudomonas sp.: mechanism and chemical characterization. Journal of hazardous materials *163*, 65-72.
Kellerer, A.M. (1981). Criteria for the Equivalence of Spherical and Cylindrical Proportional Counters in Microdosimetry. Radiation Research *86*, 277-286.
Kellerer, A.M., and Chmelevsky, D. (1975). Criteria for the Applicability of LET. Radiation Research *63*, 226-234.
Khalil, M.M., Tremoleda, J.L., Bayomy, T.B., and Gsell, W. (2011). Molecular SPECT imaging: an overview. International journal of molecular imaging *2011*.
Kirschner, A.S., Ice, R.D., and Beierwaltes, W.H. (1973). Radiation Dosimetry of 131I-19-Iodocholesterol. Journal of Nuclear Medicine *14*, 713-717.
Klutz, K., Russ, V., Willhauck, M.J., Wunderlich, N., Zach, C., Gildehaus, F.J., Göke, B., Wagner, E., Ogris, M., and Spitzweg, C. (2009). Targeted Radioiodine Therapy of Neuroblastoma Tumors following Systemic Nonviral Delivery of the Sodium Iodide Symporter Gene. Clinical Cancer Research *15*, 6079-6086.
Kogai, T., Schultz, J.J., Johnson, L.S., Huang, M., and Brent, G.A. (2000). Retinoic acid induces sodium/iodide symporter gene expression and radioiodide uptake in the MCF-7 breast cancer cell line. Proceedings of the National Academy of Sciences *97*, 8519-8524.
Koike, M., Yutoku, Y., and Koike, A. (2015). Dynamic changes in subcellular localization of cattle XLF during cell cycle, and focus formation of cattle XLF at DNA damage sites immediately after irradiation. Journal of Veterinary Medical Science *advpub*.
Konijnenberg, M., Melis, M., Valkema, R., Krenning, E., and de Jong, M. (2007). Radiation dose distribution in human kidneys by octreotides in peptide receptor radionuclide therapy. Journal of Nuclear Medicine *48*, 134-142.
Kramer, G.H., Chamberlain, M.J., and Yiu, S. (1997). A study of thyroid radioiodine monitoring by Monte Carlo simulations: implications for equipment design. Physics in medicine and biology *42*, 2175.
Krisanat Chuamsaamarkkee, L.L., Philip J. Blower (2014). Dosimetric Estimation of F-18 Tetrafluoroborate (BF4) using Preclinical Spatio-Temporal Data: A Dose Comparison with other NIS-radiotracers in Normal Subjects. Paper presented at: World Molecular Imaging Congress 2014 (Seoul, South Korea).
Krisanat Chuamsaamarkkee, S.D., Greg Mullen, Lefteris Livieratos, Phil Blower (2013a). In vitro and Quantitative In vivo Dynamic Study of 188Re-perrhenate for Imaging and Treatment in NIS-expressing Tumour. Paper presented at: The Sixth World Molecular Imaging Conference (Georgia, USA).
Krisanat Chuamsaamarkkee, S.D., Greg Mullen, Lefteris Livieratos, Phil Blower (2013b). Spatio-Temporal Quantification of Sodium Iodide Symporter (NIS) Radiotracers using pre-clinical SPECT/CT and PET/CT: A Study in Healthy Scid/Beige Mouse. Paper presented at: The Sixth World Molecular Imaging Conference (Georgia, USA.).
Larsen, R.H., Akabani, G., Welsh, P., and Zalutsky, M.R. (1998). The Cytotoxicity and Microdosimetry of Astatine-211-Labeled Chimeric Monoclonal Antibodies in Human Glioma and Melanoma Cells In Vitro. Radiation Research *149*, 155-162.
Larsson, E., Meerkhan, S.A., Strand, S.-E., and Jönsson, B.-A. (2012). A small-scale anatomic model for testicular radiation dosimetry for radionuclides localized in the human testes. Journal of Nuclear Medicine *53*, 72-81.
Lazar, V., Bidart, J.-M., Caillou, B., Mahé, C., Lacroix, L., Filetti, S., and Schlumberger, M. (1999). Expression of the Na+/I− Symporter Gene in Human Thyroid Tumors: A Comparison Study with Other Thyroid-Specific Genes. Journal of Clinical Endocrinology & Metabolism *84*, 3228-3234.
Lee, S.L., Mandel, S.J., Mazzaferri, E.L., McIver, B., Sherman, S.I., and Tuttle10, R.M. (2006). Management guidelines for patients with thyroid nodules and differentiated thyroid cancer. Thyroid *16*.
Leong, L.K., Kruger, R.L., and O'Connor, M.K. (2001). A Comparison of the Uniformity Requirements for SPECT Image Reconstruction Using FBP and OSEM Techniques. Journal of Nuclear Medicine Technology *29*, 79-83.
Li, S., Liu, J., Zhang, H., Tian, M., Wang, J., and Zheng, X. (2001). Rhenium-188 HEDP to treat painful bone metastases. Clinical nuclear medicine *26*, 919-922.
Liu, B., Huang, R., Kuang, A., Zhao, Z., Zeng, Y., Wang, J., and Tian, R. (2011). Iodine kinetics and dosimetry in the salivary glands during repeated courses of radioiodine therapy for thyroid cancer. Medical physics *38*, 5412-5419.

Loncol, T., Cosgrove, V., Denis, J.M., Gueulette, J., Mazal, A., Menzel, H.G., Pihet, P., and Sabattier, R. (1994). Radiobiological Effectiveness of Radiation Beams with Broad LET Spectra: Microdosimetric Analysis Using Biological Weighting Functions. Radiation Protection Dosimetry *52*, 347-352.
Lund Nielsen, J., and Halkjær Nielsen, P. (2005). Advances in Microscopy: Microautoradiography of Single Cells. In Methods in Enzymology (Academic Press), pp. 237-256.
Luster, M., Clarke, S., Dietlein, M., Lassmann, M., Lind, P., Oyen, W., Tennvall, J., and Bombardieri, E. (2008). Guidelines for radioiodine therapy of differentiated thyroid cancer. European journal of nuclear medicine and molecular imaging *35*, 1941-1959.
Makrigiorgos, G., Adelstein, S.J., and Kassis, A.I. (1990). Auger electron emitters: Insights gained from in vitro experiments. Radiation and Environmental Biophysics *29*, 75-91.
Makrigiorgos, G.M., Adelstein, S.J., and Kassis, A.I. (1989). Limitations of Conventional Internal Dosimetry at the Cellular Level. Journal of Nuclear Medicine *30*, 1856-1864.
Mannheim, J.G., Judenhofer, M.S., Schmid, A., Tillmanns, J., Stiller, D., Sossi, V., and Pichler, B.J. (2012). Quantification accuracy and partial volume effect in dependence of the attenuation correction of a state-of-the-art small animal PET scanner. Physics in medicine and biology *57*, 3981.
Marine, D. (1922). THE PRESENT STATUS OF THE FUNCTIONS OF THE THYROID GLAND. Physiological Reviews *2*, 521-551.
Matthews, P.M., Coatney, R., Alsaid, H., Jucker, B., Ashworth, S., Parker, C., and Changani, K. Technologies: preclinical imaging for drug development. Drug Discovery Today: Technologies.
Mattsson, S., Johansson, L., Leide-Svegborn, S., Liniecki, J., Nosske, D., Riklund, K., Stabin, M., and Taylor, D. (2011). Current activities in the ICRP concerning estimation of radiation doses to patients from radiopharmaceuticals for diagnostic use. Paper presented at: Journal of Physics: Conference Series (IOP Publishing).
McElroy, D.P., MacDonald, L.R., Beekman, F.J., Wang, Y., Patt, B.E., Iwanczyk, J.S., Tsui, B.M., and Hoffman, E.J. (2002). Performance evaluation of A-SPECT: a high resolution desktop pinhole SPECT system for imaging small animals. Nuclear Science, IEEE Transactions on *49*, 2139-2147.
McMullen, T.P.W., and Delbridge, L.W. (2009). Thyroid Embryology, Anatomy, and Physiology: A Review for the Surgeon

Endocrine Surgery. In, J. Hubbard, W.B. Inabnet, and C.-Y. Lo, eds. (Springer London), pp. 3-16.
Michael P. Brandt, R.T.K., Daniel H. Shen, Xiaoli Zhang, Yu-Yu Liu, and Sissy M. Jhiang. (2012). Micro–Single-Photon Emission Computed Tomography Image Acquisition and Quantification of Sodium-Iodide Symporter–Mediated Radionuclide Accumulation in Mouse Thyroid and Salivary Glands. Thyroid *22*, 8.
Moustapha, M.E., Ehrhardt, G.J., Smith, C.J., Szajek, L.P., Eckelman, W.C., and Jurisson, S.S. (2006). Preparation of cyclotron-produced< sup> 186</sup> Re and comparison with reactor-produced< sup> 186</sup> Re and generator-produced< sup> 188</sup> Re for the labeling of bombesin. Nuclear medicine and biology *33*, 81-89.
Nagarajah, J., Jentzen, W., Hartung, V., Rosenbaum-Krumme, S., Mikat, C., Heusner, T., Antoch, G., Bockisch, A., and Stahl, A. (2011). Diagnosis and dosimetry in differentiated thyroid carcinoma using 124I PET: comparison of PET/MRI vs PET/CT of the neck. Eur J Nucl Med Mol Imaging *38*, 1862-1868.
Nerl, H.C., Cheng, C., Goode, A.E., Bergin, S.D., Lich, B., Gass, M., and Porter, A.E. (2011). Imaging methods for determining uptake and toxicity of carbon nanotubes in vitro and in vivo. Nanomedicine *6*, 849-865.
Pacini, F. Management of differentiated thyroid cancer of the follicular epithelium. Annals of Medicine *0*, 1-5.
Pacini, F., Castagna, M., Brilli, L., and Pentheroudakis, G. (2010). Thyroid cancer: ESMO Clinical Practice Guidelines for diagnosis, treatment and follow-up. Annals of oncology *21*, v214-v219.
Pankow, B.G., Michalak, J., and McGee, M.K. (1985). Adult human thyroid weight. Health physics *49*, 1097-1104.
Paquet, F., Barbey, P., Bardiès, M., Biau, A., Blanchardon, E., Chetioui, A., Lebaron-Jacobs, L., and Pasquier, J.L. (2013). The assessment and management of risks associated with exposures to short-range Auger- and beta-emitting radionuclides. State of the art and proposals for lines of research. Journal of Radiological Protection *33*, R1.
Park, H.-M. (2002). 123I: Almost a Designer Radioiodine for Thyroid Scanning. Journal of Nuclear Medicine *43*, 77-78.
Penheiter, A.R., Russell, S.J., and Carlson, S.K. (2012). The sodium iodide symporter (NIS) as an imaging reporter for gene, viral, and cell-based therapies. Current gene therapy *12*, 33.

Pentlow, K.S., Graham, M.C., Lambrecht, R.M., Daghighian, F., Bacharach, S.L., Bendriem, B., Finn, R.D., Jordan, K., Kalaigian, H., Karp, J.S.*, et al.* (1996). Quantitative imaging of iodine-124 with PET. Journal of nuclear medicine : official publication, Society of Nuclear Medicine *37*, 1557-1562.
Portulano, C., Paroder-Belenitsky, M., and Carrasco, N. (2013). The Na+/I− symporter (NIS): mechanism and medical impact. Endocrine reviews *35*, 106-149.
Pradhan, A.S., Kim, J.L., and Lee, J.I. (2012). On the use of “effective dose” (E) in medical exposures. Journal of Medical Physics / Association of Medical Physicists of India *37*, 63-65.
Puncher, M., and Blower, P. (1994a). Radionuclide targeting and dosimetry at the microscopic level: the role of microautoradiography. European Journal of Nuclear Medicine and Molecular Imaging *21*, 1347-1365.
Puncher, M.R., and Blower, P.J. (1994b). Radionuclide targeting and dosimetry at the microscopic level: the role of microautoradiography. European journal of nuclear medicine *21*, 1347-1365.
Rapisarda, E., Bettinardi, V., Thielemans, K., and Gilardi, M. (2010). Image-based point spread function implementation in a fully 3D OSEM reconstruction algorithm for PET. Physics in medicine and biology *55*, 4131.
Riesco-Eizaguirre, G., and Santisteban, P. (2006). A perspective view of sodium iodide symporter research and its clinical implications. European journal of endocrinology *155*, 495-512.
Ritt, P., and Kuwert, T. (2013). Quantitative SPECT/CT. In Molecular Imaging in Oncology (Springer), pp. 313-330.
Roeske, J.C., Aydogan, B., Bardies, M., and Humm, J.L. (2008a). Small-Scale Dosimetry: Challenges and Future Directions. Seminars in Nuclear Medicine *38*, 367-383.
Roeske, J.C., Aydogan, B., Bardies, M., and Humm, J.L. (2008b). Small-scale dosimetry: challenges and future directions. Paper presented at: Seminars in nuclear medicine (Elsevier).
Roeske, J.C., and Stinchcomb, T.G. (1996). Relationships between Cell Survival and Specific Energy Spectra for Therapeutic Alpha-Particle Emitters. Radiation Research *145*, 268-273.
Roeske, J.C., and Stinchcomb, T.G. (2000). Tumor Control Probability Model for Alpha-Particle-Emitting Radionuclides. Radiation Research *153*, 16-22.
Rossi, H.H., and Zaider, M. (1991). Elements of microdosimetry. Medical Physics *18*, 1085-1092.
S. Murty Goddu, R.W.H., and Dandamudi V. Rao (1994). Cellular Dosimetry: Absorbed Fractions for Monoenergetic Electron and Alpha Particle Sources and S-Values for Radionuclides Uniformly Distributed in Different Cell Compartments. Journal of Nuclear Medicine *35*, 14.
Seabold, J., Ben-Haim, S., Pettit, W., Gurli, N., Rojeski, M., Flanigan, M., Ponto, J., and Bricker, J. (1993). Diuretic-enhanced I-131 clearance after ablation therapy for differentiated thyroid cancer. Radiology *187*, 839-842.
Sgouros, G. (2005). Dosimetry of Internal Emitters. Journal of Nuclear Medicine *46*, 18S-27S.
Sgouros, G., Roeske, J.C., McDevitt, M.R., Palm, S., Allen, B.J., Fisher, D.R., Brill, A.B., Song, H., Howell, R.W., Akabani, G.*, et al.* (2010). MIRD Pamphlet No. 22 (Abridged): Radiobiology and Dosimetry of α-Particle Emitters for Targeted Radionuclide Therapy. Journal of Nuclear Medicine *51*, 311-328.
Shcherbinin, S., Grimes, J., Bator, A., Cwikla, J.B., and Celler, A. (2014). Three-dimensional personalized dosimetry for 188 Re liver selective internal radiation therapy based on quantitative post-treatment SPECT studies. Physics in Medicine and Biology *59*, 119.
Shen, D., Marsee, D., Schaap, J., Yang, W., Cho, J., Hinkle, G., Nagaraja, H., Kloos, R., Barth, R., and Jhiang, S. (2004). Effects of dose, intervention time, and radionuclide on sodium iodide symporter (NIS)-targeted radionuclide therapy. Gene therapy *11*, 161-169.
Soret, M., Bacharach, S.L., and Buvat, I. (2007). Partial-Volume Effect in PET Tumor Imaging. Journal of Nuclear Medicine *48*, 932-945.
Speer, T.W. (2012). Targeted Radionuclide Therapy (Wolters Kluwer Health).
Spitzweg, C., Joba, W., Eisenmenger, W., and Heufelder, A.E. (1998). Analysis of Human Sodium Iodide Symporter Gene Expression in Extrathyroidal Tissues and Cloning of Its Complementary Deoxyribonucleic Acids from Salivary Gland, Mammary Gland, and Gastric Mucosa. Journal of Clinical Endocrinology & Metabolism *83*, 1746-1751.
Spitzweg, C., and Morris, J.C. (2009). Chapter 101 - The Sodium–Iodide Symporter (NIS): NIS-Mediated Radioiodide Therapy. In Comprehensive Handbook of Iodine, R.P. Victor, N.B. Gerard, G.N.B. Ronald WatsonA2 - Victor R. Preedy, and W. Ronald, eds. (San Diego: Academic Press), pp. 979-989.
Spitzweg, C., Zhang, S., Bergert, E.R., Castro, M.R., McIver, B., Heufelder, A.E., Tindall, D.J., Young, C.Y.F., and Morris, J.C. (1999). Prostate-specific Antigen (PSA) Promoter-driven Androgen-inducible Expression of Sodium Iodide Symporter in Prostate Cancer Cell Lines. Cancer Research *59*, 2136-2141.

Stabin, M. (2003). Developments in the internal dosimetry of radiopharmaceuticals. Radiation protection dosimetry *105*, 575-580.
Stabin, M. (2006). Nuclear medicine dosimetry. Physics in Medicine and Biology *51*, R187.
Stabin, M. (2007). Internal Dosimetry

Pediatric Nuclear Medicine/PET. In, S.T. Treves, ed. (Springer New York), pp. 513-520.
Stabin, M.G. (1996). MIRDOSE: Personal Computer Software for Internal Dose Assessment in Nuclear Medicine. Journal of Nuclear Medicine *37*, 538-546.
Stabin, M.G. (2008). Uncertainties in Internal Dose Calculations for Radiopharmaceuticals. Journal of Nuclear Medicine *49*, 853-860.
Stabin, M.G., Emmons, M.A., Segars, W.P., and Fernald, M.J. (2011). REALISTIC REFERENCE ADULT AND PAEDIATRIC PHANTOM SERIES FOR INTERNAL AND EXTERNAL DOSIMETRY. Radiation Protection Dosimetry.
Stabin, M.G., and Siegel, J.A. (2003). Physical Models and Dose Factors for Use in Internal Dose Assessment. Health Physics *85*, 294-310.
Stabin, M.G., Sparks, R.B., and Crowe, E. (2005). OLINDA/EXM: The Second-Generation Personal Computer Software for Internal Dose Assessment in Nuclear Medicine. Journal of Nuclear Medicine *46*, 1023-1027.
Stabin, M.G., Tagesson, M., Thomas, S.R., Ljungberg, M., and Strand, S.E. (1999). Radiation dosimetry in nuclear medicine. Applied Radiation and Isotopes *50*, 73-87.
Stepanek, J., Larsson, B., and Weinreich, R. (1996). Auger-Electron Spectra of Radionuclides for Therapy and Diagnostics. Acta Oncologica *35*, 863-868.
Stinchcomb, T.G., and Roeske, J.C. (1992). Analytic microdosimetry for radioimmunotherapeutic alpha emitters. Medical Physics *19*, 1385-1393.
Stokkel, M.P., Junak, D.H., Lassmann, M., Dietlein, M., and Luster, M. (2010). EANM procedure guidelines for therapy of benign thyroid disease. European journal of nuclear medicine and molecular imaging *37*, 2218-2228.
Szanda, I., Mackewn, J., Patay, G., Major, P., Sunassee, K., Mullen, G.E., Nemeth, G., Haemisch, Y., Blower, P.J., and Marsden, P.K. (2011). National Electrical Manufacturers Association NU-4 performance evaluation of the PET component of the NanoPET/CT preclinical PET/CT scanner. Journal of Nuclear Medicine *52*, 1741-1747.
Tessier, C., Suhard, D., Rebière, F., Souidi, M., Dublineau, I., and Agarande, M. (2012). Uranium microdistribution in renal cortex of rats after chronic exposure: a study by secondary ion mass spectrometry microscopy. Microscopy and Microanalysis *18*, 123-133.
Thierens, H.M., Monsieurs, M.A., Brans, B., Van Driessche, T., Christiaens, I., and Dierckx, R.A. (2001). Dosimetry from organ to cellular dimensions. Computerized Medical Imaging and Graphics *25*, 187-193.
Tuttle, R.M., Tala, H., Shah, J., Leboeuf, R., Ghossein, R., Gonen, M., Brokhin, M., Omry, G., Fagin, J.A., and Shaha, A. (2010). Estimating Risk of Recurrence in Differentiated Thyroid Cancer After Total Thyroidectomy and Radioactive Iodine Remnant Ablation: Using Response to Therapy Variables to Modify the Initial Risk Estimates Predicted by the New American Thyroid Association Staging System. Thyroid *20*, 1341-1349.
Units, I.C.o.R., and Measurements (1989). Tissue Substitutes in Radiation Dosimetry and Measurement (International Commission on Radiation Units and Measurements).
Utsunomiya, S., Kogawa, M., Kamiishi, E., and Ewing, R.C. (2011). Scanning Transmission Electron Microscopy and Related Techniques for Research on Actinide and Radionuclide Nanomaterials. In Actinide Nanoparticle Research (Springer), pp. 33-62.
Van Sande, J., Massart, C., Beauwens, R., Schoutens, A., Costagliola, S., Dumont, J.E., and Wolff, J. (2003). Anion Selectivity by the Sodium Iodide Symporter. Endocrinology *144*, 247-252.
Verburg, F.A., Brans, B., and Mottaghy, F.M. (2011). Molecular nuclear therapies for thyroid carcinoma. Methods *55*, 230-237.
Walrand, S. (2014). SPECT/CT for Dosimetry. In Clinical Applications of SPECT-CT (Springer), pp. 29-42.
Weigel, R.J. (2008). Thyroid

Surgery. In, J.A. Norton, P.S. Barie, R.R. Bollinger, A.E. Chang, S.F. Lowry, S.J. Mulvihill, H.I. Pass, and R.W. Thompson, eds. (Springer New York), pp. 1211-1228.
Willhauck, M.J., Sharif Samani, B.-R., Gildehaus, F.-J., Wolf, I., Senekowitsch-Schmidtke, R., Stark, H.-J.r., Göke, B., Morris, J.C., and Spitzweg, C. (2007). Application of 188rhenium as an alternative radionuclide for treatment of prostate cancer after tumor-specific sodium iodide symporter gene expression. The Journal of Clinical Endocrinology & Metabolism *92*, 4451-4458.
Wrixon, A.D. (2008). New ICRP recommendations. Journal of Radiological Protection *28*, 161.

Zaider, M., and Brenner, D.J. (1985). On the Microdosimetric Definition of Quality Factors. Radiation Research *103*, 302-316.
Zanzonico, P.B. (2000). Internal Radionuclide Radiation Dosimetry: A Review of Basic Concepts and Recent. J Nucl Med *41*, 297-308.
Zuckier, L.S., Dohan, O., Li, Y., Chang, C.J., Carrasco, N., and Dadachova, E. (2004). Kinetics of perrhenate uptake and comparative biodistribution of perrhenate, pertechnetate, and iodide by NaI symporter–expressing tissues in vivo. Journal of Nuclear Medicine *45*, 500-507.